# The Opacity of the Universe for high and very high energy $\gamma$-rays

Dissertation
zur Erlangung des Doktorgrades
des Department Physik
der Universität Hamburg

vorgelegt von

**Manuel Meyer**
aus Hamburg

Hamburg
2013

| | |
|---|---|
| Gutachter der Dissertation: | Prof. Dr. Dieter Horns<br>Dr. Andreas Ringwald |
| Gutachter der Disputation : | Dr. Andreas Ringwald<br>Prof. Dr. Marcus Brüggen |
| Vorsitzende des Prüfungsausschusses: | Prof. Dr. Caren Hagner |
| Vorsitzender des Promotionsausschusses: | Prof. Dr. Peter Hauschildt |
| Dekan der MIN Fakultät: | Prof. Dr. Heinrich Graener |

# Abstract

The flux of high energy (HE, energy $100\,\mathrm{MeV} \lesssim E \lesssim 100\,\mathrm{GeV}$) and very high energy (VHE, $E \gtrsim 100\,\mathrm{GeV}$) $\gamma$-rays originating from cosmological sources is attenuated due to pair production in interactions with photons at ultraviolet to infrared wavelengths of the extragalactic background light (EBL). The main components contributing to the EBL photon density are the starlight integrated over cosmic time and the starlight reprocessed by dust in galaxies. Consequently, the EBL is an integral measure of the cosmic star formation history. Depending on the source distance, the Universe should be opaque to $\gamma$-rays above a certain energy.

Nevertheless, the number of detected $\gamma$-ray sources has increased continuously in recent years. VHE emitting objects beyond redshifts of $z > 0.5$ have been detected with imaging air Cherenkov telescopes (IACTs), while HE $\gamma$-rays from active galactic nuclei (AGN) above redshifts $z \gtrsim 3$ have been observed with the Large Area Telescope (LAT) on board the *Fermi* satellite.

In this work, a large sample of VHE $\gamma$-ray spectra will be combined with data of the *Fermi*-LAT to derive upper limits on the EBL photon density at $z = 0$. Generic EBL realizations are used to correct AGN spectra for absorption, which are subsequently tested against model assumptions. The evolution of the EBL with redshift is accounted for, and a possible formation of electromagnetic cascades is considered. As a result, the EBL density is constrained over almost three orders of magnitude in wavelength, between $0.4\,\mu$m and $100\,\mu$m. At optical wavelengths, an EBL intensity above $24\,\mathrm{nW\,m^{-2}\,sr^{-1}}$ is ruled out, and between $8\,\mu$m and $31\,\mu$m it is limited to be below $5\,\mathrm{nW\,m^{-2}\,sr^{-1}}$. In the infrared, the constraints are within a factor $\sim 2$ of lower limits derived from galaxy number counts.

Additionally, the behavior of VHE spectra in the transition from the optical depth regimes $\tau_{\gamma\gamma} < 1$ to $\tau_{\gamma\gamma} \geqslant 2$ is investigated. The absorption-corrected spectra consistently show an upturn at high optical depths, significant at the $4\,\sigma$ level. A source intrinsic effect is unlikely to produce such a feature, since the transition to the $\tau_{\gamma\gamma} \geqslant 2$ regime occurs at different energies for each source. Systematic uncertainties that could mimic the effect are studied but found unlikely as a possible explanation.

A similar study is conducted for photons detected with the *Fermi*-LAT. To this end, the number of expected photons in the optical thick regime is compared to the number of photons observed with the LAT. Above $\tau_{\gamma\gamma} \geqslant 2$, three photons are associated with AGN with high confidence. Under the assumption of certain EBL models,

extrapolating the unattenuated spectrum from low to high energies results in a probability of $1.2\times10^{-4}$ to observe these photons. However, the probability for detecting the high optical depth photons when all LAT detected AGN with known redshift are considered sensitively depends on the the choice of the intrinsic spectral model.
The indication for a reduced opacity might be explained by the oscillation of photons into hypothetical axion-like particles (ALPs) in ambient magnetic fields. Such particles propagate unimpeded over cosmological distances, thereby reducing the $\gamma$-ray opacity. Photon-ALP conversions are studied in different magnetic field configurations, including intracluster and intergalactic magnetic fields, as well as the field of the Milky Way. Optimistic values of the field strength and coherence length result in lower limits on the photon-ALP coupling, $g_{a\gamma} \gtrsim 10^{-12}\,\mathrm{GeV}^{-1}$. For more realistic magnetic field parameters, couplings above $g_{a\gamma} \gtrsim 2\times10^{-11}\,\mathrm{GeV}^{-1}$ are necessary to explain the indication for the reduced opacity. The lower limits are in reach of future dedicated ALP experiments.

# KURZFASSUNG

Der Fluss der hoch- und sehr hochenergetischen (HE und SHE) Gammastrahlung von extragalaktischen Quellen wird durch Paarproduktion mit niederenergetischen Photonen des extragalaktischen Hintergrundlichts (EHL) abgeschwächt. Dieses Hintergrundlicht erstreckt sich von ultravioletten bis hin zu ferninfraroten Wellenlängen. Über die Zeit integriertes Sternenlicht sowie Sternenlicht, dass durch interstellaren Staub absorbiert und reemittiert wird, machen die Hauptbestandteile des EHL aus. Das EHL kann somit als integrales Maß für die Sternenentstehungsrate angesehen werden. Aus der Absorption ergibt sich, dass das Universum undurchsichtig für Gammastrahlung jenseits einer bestimmten, distanzabhängigen Energie sein sollte.

Ungeachtet der erwarteten Abschwächung des intrinsischen Flusses ist in den letzten Jahren die Anzahl der detektierten extragalaktischen Gammastrahlungsquellen stetig angewachsen. Quellen mit Rotverschiebungen jenseits von $z > 0.5$ wurden mit abbildenden Cherenkov-Teleskopen detektiert, aktive galaktische Kerne (AGK) konnten mit dem Large Area Telescope (LAT) an Bord des *Fermi*-Satelliten sogar über $z \gtrsim 3$ hinaus nachgewiesen werden.

In der vorliegenden Arbeit wird die bis dato größte Auswahl an SHE Spektren zusammen mit spektralen Informationen des *Fermi*-LAT benutzt, um eine obere Schranke auf die EHL-Dichte bei $z = 0$ zu bestimmen. Dazu wird eine Absorptionskorrektur aus generischen EHL-Realisierungen berechnet und auf die gemessenen Spektren angewendet. Die so erhaltenden intrinsischen Spektren werden anschließend gegen Modellvorhersagen getestet. Es wird dabei berücksichtigt, dass sich das EHL mit der Rotverschiebung ändert und sich möglicherweise elektromagnetische Kaskaden ausbilden. EHL-Intensitäten bei optischen Wellenlängen oberhalb von $24\,\mathrm{nW\,m^{-2}\,sr^{-1}}$ können ausgeschlossen werden, ebenso wie Intensitäten oberhalb von $5\,\mathrm{nW\,m^{-2}\,sr^{-1}}$ zwischen $8\,\mu$m und $31\,\mu$m. Damit sind die hier abgeleiteten oberen Grenzen bei infraroten Wellenlängen nur noch einen Faktor $\sim 2$ von unteren Grenzen entfernt, die sich aus Galaxienzählungen ergeben.

Des Weiteren wird untersucht, ob sich ein systematischer Trend in SHE Spektren im Übergang vom optisch dünnen, $\tau_{\gamma\gamma} < 1$, zum optisch tiefen Regime, $\tau_{\gamma\gamma} \geqslant 2$, feststellen lässt. Mit einer Signifikanz oberhalb von $4\,\sigma$ wird konsistent für alle untersuchten absorptionskorrigierten Spektren ein erhöhter Photonenfluss bei hohen optischen Tiefen festgestellt. Dieses Verhalten lässt sich aufgrund der großen

Spanne von untersuchten Energie- und Rotverschiebungsintervallen nur schwer mit quellintrinsischen Effekten erklären. Es stellt sich heraus, dass systematische Unsicherheiten nur unwahrscheinlich einen solchen Effekt hervorrufen können.
In ähnlicher Weise werden Beobachtungen des *Fermi*-LAT auf eine geringe Opazität hin untersucht. Hierzu wird die Anzahl der beobachteten Photonen im optisch tiefen Regime mit der theoretisch erwarteten Anzahl verglichen. Oberhalb von $\tau_{\gamma\gamma} = 2$ können drei Photonen mit hoher Sicherheit AGK zugeordnet werden. Für diese Quellen wird das unabsorbierte Spektrum aus *Fermi*-LAT-Daten bestimmt und zu hohen Energien hin extrapoliert. Unter Berücksichtigung theoretischer EHL-Modelle kann aus dieser Extrapolation die Anzahl der erwarteten Photonen bestimmt werden. Es ergibt sich eine Wahrscheinlichkeit von $1{,}2 \cdot 10^{-4}$, diese drei Photonen zu beobachten. Falls die erwarteten Photonen aller mit dem LAT detektierten AGK berücksichtigt werden, ist die Wahrscheinlichkeit jedoch stark abhängig von dem gewählten intrinsischen Spektralmodell.
Die Anzeichen für eine geringe Opazität können als Hinweise auf Oszillationen zwischen Photonen und hypothetischen axionartigen Teilchen gewertet werden. Solche Teilchen können ungehindert kosmologische Distanzen zurücklegen. Damit diese Oszillationen stattfinden, bedarf es magnetischer Felder. Es werden Magnetfelder in Galaxienhaufen, im intergalaktischen Medium und in der Milchstraße studiert, um die Stärke eines möglichen Effekts zu quantifizieren. Für optimistische Feldstärken und Kohärenzlängen kann die geringe Opazität mit einer Kopplung zwischen Photonen und axionartigen Teilchen von $g_{a\gamma} \gtrsim 10^{-12}\,\mathrm{GeV}^{-1}$ erklärt werden. Realistischere Werte führen zu einer unteren Grenze auf die Kopplung von $g_{a\gamma} \gtrsim 2 \cdot 10^{-11}\,\mathrm{GeV}^{-1}$. Die erwarteten Sensitivitäten geplanter Laborexperimente sind ausreichend, um in Zukunft gezielt nach axionartigen Teilchen mit diesen Parametern zu suchen.

*The effort to understand the universe is one of the very few things which lifts human life a little above the level of farce and gives it some of the grace of tragedy.*

---

Steven Weinberg
in “The First Three Minutes” (1993)

# Contents

**Abstract** i

**Kurzfassung** iii

**1 Introduction: Extragalactic high and very high energy $\gamma$-rays** 1
- 1.1 Active galactic nuclei: Sources of high and very high energy $\gamma$-rays 3
  - 1.1.1 Continuum emission models . . . 7
  - 1.1.2 The blazar sequence . . . 10
- 1.2 Absorption of $\gamma$-rays on background radiation fields . . . 11
  - 1.2.1 Electromagnetic cascades . . . 13
- 1.3 Detection of high and very high energy $\gamma$-rays . . . 15
  - 1.3.1 The *Fermi* satellite . . . 16
  - 1.3.2 Imaging air Cherenkov telescopes . . . 19
- 1.4 Pseudo-Nambu-Goldstone bosons . . . 23

**2 Upper limits on the extragalactic background light density in the *Fermi* era** 31
- 2.1 The extragalactic background light . . . 32
- 2.2 Absorption correction of VHE $\gamma$-ray spectra for generic EBL densities 36
- 2.3 Exclusion criteria for the EBL shapes . . . 39
  - 2.3.1 Concavity . . . 39
  - 2.3.2 Cascade emission and energy budget . . . 41
- 2.4 VHE AGN Sample . . . 45
  - 2.4.1 Sample tested against concavity criteria . . . 45
  - 2.4.2 Sample tested against intrinsic VHE luminosity . . . 48
- 2.5 Results . . . 50

**3 Indications for an anomalous propagation of $\gamma$-rays** 61
- 3.1 Statistical analysis of VHE $\gamma$-ray spectra . . . 62
  - 3.1.1 Method and results . . . 65
  - 3.1.2 Systematic effects . . . 71
- 3.2 Observations of $\gamma$-rays in the optical thick regime with the *Fermi*-LAT 78
  - 3.2.1 Sample of high optical depth photons . . . 78

3.2.2 Method for searching the anomaly . . . . . 80
3.2.3 Estimation of the background probability . . . . . 87
3.2.4 Results and systematic uncertainties . . . . . 90

**4 Interpretations of the anomalous propagation of $\gamma$-rays 101**
4.1 Electromagnetic cascades . . . . . 101
4.2 Beyond the Standard Model . . . . . 105
4.2.1 Lorentz invariance violation . . . . . 105
4.2.2 Hidden gauge bosons . . . . . 108
4.2.3 Axion-like particles . . . . . 111

**5 First lower limits on the photon-axion-like-particle coupling 113**
5.1 Photon-ALP conversion in magnetic fields . . . . . 114
5.2 Magnetic field configurations and scenarios . . . . . 117
5.2.1 Magnetic field of the Milky Way . . . . . 118
5.2.2 Intergalactic magnetic field . . . . . 120
5.2.3 Intracluster magnetic fields . . . . . 122
5.2.4 Magnetic field scenarios . . . . . 124
5.3 Probing the Opacity with VHE gamma-ray spectra . . . . . 127
5.4 Results . . . . . 129

**6 Summary and outlook 137**

**A Fit qualities for VHE $\gamma$-ray spectra in the optical thick regime 145**

**B Galactic VHE $\gamma$-ray spectra used to cross check the PPA 151**

**C Light curves of AGN associated with a high optical depth photon 153**

**D Solution to the equation of motion of photon-ALP oscillations 159**

**E Theoretical bound on the photon survival probability in photon-ALP oscillations 161**

**F The Galactic magnetic field in heliocentric spherical coordinates 163**

**Publication list 167**

**Acknowledgements 171**

**Bibliography 173**

# 1 Introduction: Extragalactic high and very high energy $\gamma$-rays

Astronomy is one of the oldest scientific disciplines, and the systematic study of the sky dates back to the ancient Babylonian astronomers. In the modern era, the progress in astronomy was accompanied by technological developments such as the invention of the telescope in the 17$^{\text{th}}$ century or the photographic plate in the 19$^{\text{th}}$ century. Since the 20$^{\text{th}}$ century, the wavelength range accessible for astronomers, hitherto limited to the optical spectrum, has been extended dramatically. For instance, the first detection of extraterrestrial radio waves was made by Jansky (1933) and Penzias & Wilson (1965) discovered the cosmic microwave background (CMB), the relic radiation of the *Big Bang*. Charged particles from outer space, today referred to as cosmic rays, were first measured by Hess in 1912 with balloon flight experiments.

With the advancement in satellite technology, the emission at very short wavelengths, usually absorbed by the Earth's atmosphere, could be efficiently examined for the first time. *Uhuru*, the first X-ray satellite, was launched in 1970 and detected 339 sources in an all-sky survey (Giacconi *et al.*, 1971). The frequency range was further extended to $\gamma$-ray energies with the $\gamma$-ray satellites SAS-2 and COS-B (Fichtel *et al.*, 1975; Hermsen *et al.*, 1977), with the latter giving the first $\gamma$-ray map of the galaxy. The two instruments operated in the energy ranges between 20 MeV and 1 GeV and 2 keV to 5 GeV, respectively[1]. Several years later in 1989, the first source at very high $\gamma$-ray energies (VHE; energy $E \gtrsim 100\,\text{GeV}$) was discovered with the Whipple imaging air Cherenkov telescope (IACT; Weekes *et al.*, 1989, see Section 1.3.2 for a review of the instrumentation technique and current experiments).

The broad multi-wavelength coverage from radio frequencies to VHE opened the window to the analyses of *non-thermal* radiation processes, i.e., processes in which the observed flux does neither follow the spectrum of a black body nor the spectrum of thermal bremsstrahlung[2] (e.g., Longair, 2011). The observation of non-thermal

[1] Throughout this work, energies are frequently given in units of eV (electron volts), with $1\,\text{eV} \approx 1.602 \times 10^{-19}\,\text{J}$, see also Table 1.2 on page 30. See Table 1.4 on the same page for the prefixes of units.

[2] Thermal bremsstrahlung describes the radiation of electrons in a plasma that are deflected in coulomb interactions with plasma ions (e.g., Longair, 2011).

emission at high energies (HE, $100\,\mathrm{MeV} \gtrsim E \gtrsim 100\,\mathrm{GeV}$) and VHE probes the most powerful accelerators in the Universe, since particles at relativistic speeds are required to produce it (see Section 1.1.1 for an overview of the possible acceleration and emission processes, including synchrotron radiation and inverse Compton scattering). Such sources with very different morphologies have been successfully identified in the Milky Way (see, e.g., Rieger *et al.*, 2013, for a recent review). The majority of extragalactic $\gamma$-ray sources are active galactic nuclei (AGN, see Section 1.1) and their identification as efficient $\gamma$-ray emitters at HE was pioneered with the Energetic Gamma Ray Experiment Telescope (EGRET) on board the *Compton Gamma Ray Observatory* (CRGO) satellite (Thompson *et al.*, 1993). The third EGRET catalog release contains more than 66 associated AGN (Hartman *et al.*, 1999). This number has grown tremendously with the operations of the Large Area Telescope (LAT) on board the *Fermi* satellite which was launched in 2008 (see Section 1.3.1 for a description of the instrument). The 2 year *Fermi* catalog (Nolan *et al.*, 2012, henceforth 2FGL) lists 1,298 associated sources of which 1,017 have an AGN association. The sensitivity of spaceborne instruments is usually insufficient to detect sources at VHE (see Section 1.3). Therefore, the first extragalactic source was detected with the ground-based Whipple IACT (Punch *et al.*, 1992). Since then, the number of VHE emitting extragalactic objects[3] has increased to more than 50. Photon energies beyond the reach of the Large Hadron Collider have been observed from these sources (e.g., in the observation of Markarian 501; Aharonian *et al.*, 1999b). Their distances[4] range from a few Mpc up to several Gpc corresponding to redshifts beyond $z = 0.5$. At high energies, the LAT has detected AGN with distances up to redshifts $z \gtrsim 3$.

Given the cosmological distances of AGN, the observations of IACTs and the *Fermi*-LAT offer a unique opportunity to investigate the propagation of HE and VHE $\gamma$-rays. As shown in Section 1.2, the interaction of $\gamma$-rays with background radiation fields omnipresent in the Universe can lead to an absorption of the emitted $\gamma$-ray flux. The diffuse radiation field most important for the attenuation at HE and VHE is the isotropic extragalactic background light (EBL) that stretches from ultraviolet (UV) to infrared wavelengths and is very difficult to observe directly (see Section 2.1 for a review). Knowledge about the EBL is essential in order to understand, e.g., the evolution of the star formation rate and the dust content in galaxies, since the main contributors to the EBL are the integrated starlight and the starlight absorbed and reemitted by dust. In this work, observations of IACTs and the *Fermi*-LAT together with assumptions on the emitted spectrum are combined to derive upper limits on the EBL photon density over a broad wavelength range (Chapter 2)

[3] See, e.g., `http://tevcat.uchicago.edu/` for a VHE source catalog.

[4] Extragalactic distances are often given in redshift, the shift in wavelength of a photon due to the cosmic expansion, $z = (\lambda - \lambda_0)/\lambda_0$, with $\lambda$ the observed and $\lambda_0$ the emitted wavelength (e.g., Peebles, 1993). The redshift can be related to the so-called luminosity distance by means of Eq. (2.20). Table 1.2 gives the SI value for a parsec (pc).

that can in turn be used to constrain the cosmic star formation rate (Raue & Meyer, 2012).
Moreover, the growing number of detected AGN with IACTs and the *Fermi*-LAT allows to investigate the question whether the current understanding of the opacity of the Universe for HE and VHE $\gamma$-rays is correct (Chapter 3). Interestingly, an indication is found that the opacity is lower than expected from current EBL models. This includes EBL predictions that closely follow lower limits on the EBL photon density which results in a minimal guaranteed attenuation of the $\gamma$-ray flux. This result can be interpreted in a number of scenarios which also involve physics beyond the Standard Model of particle physics (Chapter 4). An intriguing interpretation is given by the oscillation of photons into hypothetical pseudo-Nambu-Goldstone bosons in the presence of ambient magnetic fields, reviewed in Section 1.4 and 5.1. These bosons are a common prediction in the compactification in string theory (e.g., Cicoli *et al.*, 2012). If the indication for a reduced opacity is regarded as evidence for such a mechanism, VHE $\gamma$-ray spectra can be used to constrain the parameters of these particles (Chapter 5). This demonstrates that the propagation of HE and VHE $\gamma$-rays can be used to probe fundamental physics. Obviously, all of the above analyses require assumptions on the emitted spectrum of an AGN. The current understanding of these objects is summarized in the next Section. The work concludes with an outlook in Chapter 6.
Major parts of this thesis are already published in peer-reviewed journals and conference proceedings which are listed on page 167.

## 1.1 Active galactic nuclei: Extragalactic sources of high and very high energy $\gamma$-rays

Observational evidence suggests that galaxies harbor a super-massive black hole (SMBH) with masses $10^6 M_\odot \lesssim M_\bullet \lesssim 10^9 M_\odot$ at their center, with $M_\odot$ being the solar mass (see Table 1.2). This conclusion is drawn, e.g., from inferred high densities in galactic centers and high velocities of stars in central regions of nearby galaxies (e.g., Rees, 1998). In contrast to inactive galaxies, AGN often show one or more of the following characteristics: They have a compact core with a luminosity exceeding that of galaxies with the same classification in the Hubble sequence; they show non-thermal, sometimes variable, continuous emission from the infrared to X-rays for which the emitted flux per unit frequency interval $[\nu, \nu + \mathrm{d}\nu]$ follows a power-law shape, $F_\nu \propto \nu^{-\alpha}$; their spectra encompass a wide range of ionization emission lines that cannot be attributed to stellar photoionization (e.g., Unsöld & Baschek, 2002; Tadhunter, 2008). Only a limited fraction of galaxies have an active nucleus: For instance, Martini *et al.* (2007) find an average value of $\sim 5\,\%$ in the observation of galaxy clusters and there is an ongoing discussion if and how the AGN fraction is influenced by their environment (e.g., Pimbblet *et al.*, 2013, and

references therein). The small fraction suggests that the activity is likely episodic on timescales of $\sim 10^7$–$10^8$ years (Di Matteo *et al.*, 2005) and might be initiated by galaxy merger events (Barnes & Hernquist, 1991) or internal galaxy processes (Krawczynski & Treister, 2013, and references therein).
Active galactic nuclei belong to the most luminous objects in the Universe, their power originating from the release of gravitational energy during the accretion of matter onto the SMBH. The first optical observations were reported by Fath (1909, noting strong emission lines in NGC 1068) and Curtis (1918, commenting on a ray-like feature emanating from the core of M 87, later to be identified as the jet, see below), and a first systematic study of active spiral galaxies was carried out by Seyfert (1943). The structure of AGN is displayed in Figure 1.1. Emission can be observed from several regions of the AGN (e.g., Urry & Padovani, 1995):

Accretion disk. The emission from the hot disk stretches from optical and UV wavelengths to soft X-rays and is possibly responsible for the "blue bump" feature observed in some AGN spectra (e.g., Sun & Malkan, 1989).

Corona. Hot interstellar material can upscatter the high energy tail of the disk emission via Comptonization (see Section 1.1.1) to hard X-ray energies.

Broad and narrow line regions. Fast dense gravitationally bound clouds of interstellar medium in the proximity of the SMBH (at a distance of several light days) can emit broad emission lines mainly at UV and optical wavelengths (broad line region, BLR). At larger distances, slower less dense clouds give rise to narrow emission lines (narrow line region, NLR).

Torus. The BLR can be obscured by a dusty torus or warped disk which is heated by the core emission and reemits it in the infrared wavelength band.

Jet. Perpendicular to the accretion disk, collimated outflows (jets) of relativistic particles occur. The inner jet region is believed to be the zone from which the broadband continuum emission ranging to HE and VHE originates. Models for the continuum emission are discussed in the following Section. Radio observations of jets in AGN have revealed substructures (knots and hotspots) that show an apparent speed exceeding the speed of light. Such apparent superluminal motions are attributed to the relativistic beaming of the outflowing plasma if the angle $\theta_\mathrm{j}$ between the jet axis and the line of sight is small. With the bulk speed $\beta_\mathrm{j} = v_\mathrm{j}/c$ of the plasma, the bulk Lorentz factor $\Gamma_\mathrm{L}$ is (see, e.g., the appendix in Urry & Padovani, 1995, for the formulas below)

$$\Gamma_\mathrm{L} = \left(1 - \beta_\mathrm{j}^2\right)^{-1/2} . \tag{1.1}$$

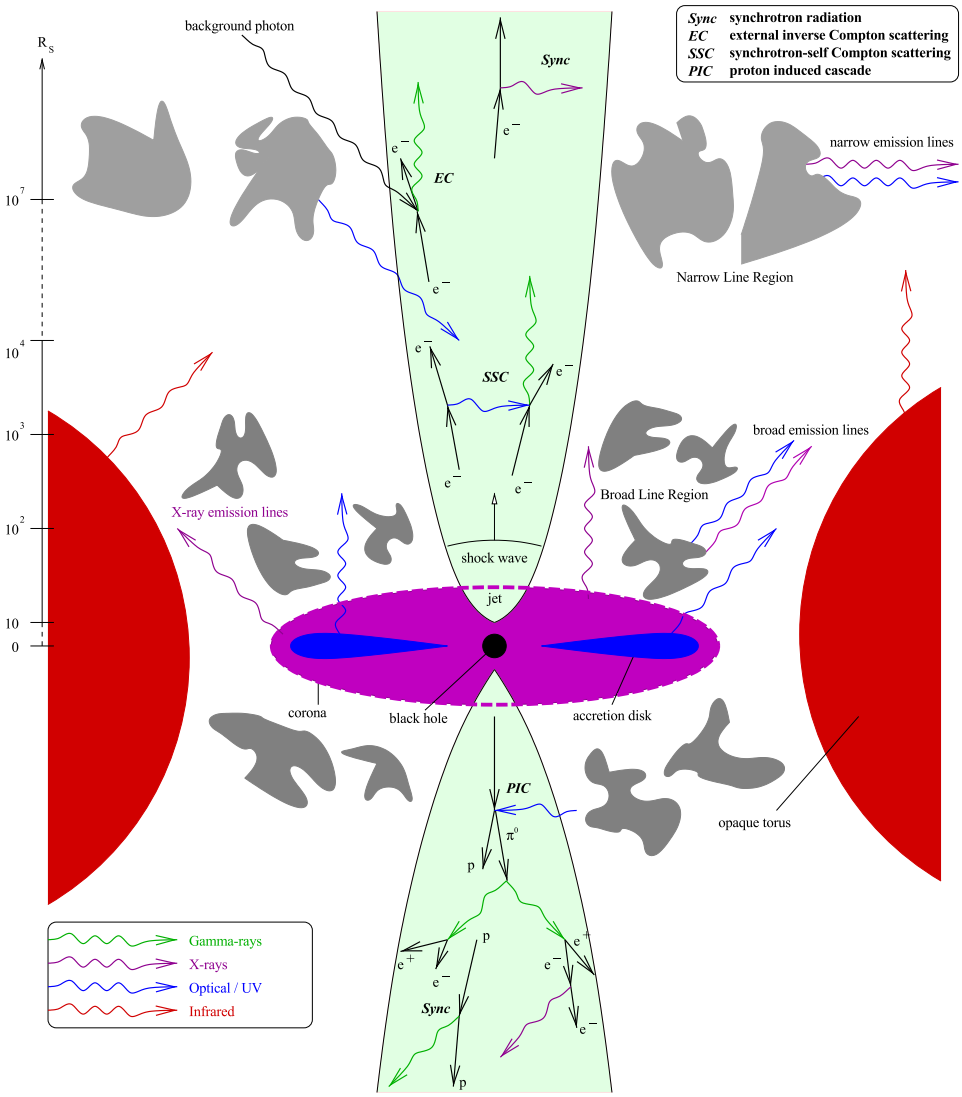


**FIGURE 1.1:** Structure of an AGN (not to scale; Figure courtesy of Max Kastendieck). Distances are given in units of Schwarzschild radii, $R_s = 2GM_\bullet/c^2 \approx 2.95 M_\bullet/M_\odot$ km.

The emission from the jet is then boosted with the Doppler factor $\delta_\mathrm{D}$,

$$\delta_\mathrm{D} = \left[\Gamma_\mathrm{L}(1 - \beta_\mathrm{j}\cos\theta_\mathrm{j})\right]^{-1}. \tag{1.2}$$

The observed apparent speed is given by

$$\beta_\mathrm{apparent} = \frac{\beta_\mathrm{j}\sin\theta_\mathrm{j}}{1 - \beta_\mathrm{j}\cos\theta_\mathrm{j}}. \tag{1.3}$$

Radio observations of 135 compact radio sources with the Very Long Baseline Array (VLBA) have revealed bulk Lorentz factors in the range $1 \lesssim \Gamma_{\mathrm{L}} \lesssim 40$ (Savolainen *et al.*, 2010). An open question in the understanding of AGN is the exact mechanism responsible the formation and collimation of the jet and for the necessary extraction of angular momentum from the accretion disk. One possibility is that material from the accretion disk follows open magnetic field lines that emerge from the disk. The field lines are co-rotating with the disk leading to an acceleration of the matter by centrifugal forces and a collimation into bipolar jets (Blandford & Payne, 1982). This process could also be accompanied by the conversion of rotational energy of a spinning black hole in the magnetic field of the disk into electromagnetic energy (Blandford & Znajek, 1977).

Within the general picture sketched in Figure 1.1, the different types of observed AGN can be explained solely by the different viewing angles $\theta_{\mathrm{j}}$ (Urry & Padovani, 1995). For large viewing angles, the accretion disk and the BLR are obscured by the torus and only weak continuum emission and narrow emission lines can be observed. Such objects can be further divided into radio-quiet and radio-loud objects, meaning the ratio of the flux at 5 GHz and in the optical *B*-band (the ratio exceeds $\sim 10$ for radio-loud objects). Seyfert type II galaxies fall into the former (radio-quiet) and Fanaroff-Riley (FR) type I and II (Fanaroff & Riley, 1974) into the latter category (also generically referred to as radio galaxies). Type I and II FR galaxies are distinguished by their morphology: FR I luminosities peak in the core and decline towards the jets, whereas FR II galaxies peak in the radio lobes of the extended jets and are on average more luminous than FR I type sources. At lower values of $\theta_{\mathrm{j}}$, the BLR becomes visible, and in this case radio-quiet objects are referred to as Seyfert I galaxies or, for higher luminosities, as quasi-stellar objects (QSOs)[5]. Steep and flat spectrum radio quasars (SSRQs and FSRQs, respectively) are the radio-loud counterparts, distinguished by the spectral slope at radio frequencies, $\alpha \lesssim 0.5$ for FSRQs. For viewing angles $\theta_{\mathrm{j}} \lesssim 10°$, the emission of AGN is dominated by the continuum emission that is strongly enhanced by relativistic beaming (cf. Section 1.1.1). Under this condition, radio-loud objects that lack broad emission lines (equivalent line width $< 5$ Å) are called BL Lac objects (named after the AGN BL Lacertae) otherwise they are referred to as FSRQs. Taken together, these objects are generically referred to as *blazars*.

Before describing models for the continuum emission, other (potential) extragalactic HE and VHE $\gamma$-ray sources are mentioned for completeness: Two starburst galaxies are confirmed VHE $\gamma$-ray emitters; NGC 265 (Acero *et al.*, 2009) and M 82 (VERITAS Collaboration *et al.*, 2009) which are also listed in the 2FGL. These galaxies show a high starformation and supernova rate, as well as high gas densities. Very bright $\gamma$-ray sources are gamma-ray bursts (GRBs), that occur on very short timescales and can outshine all other $\gamma$-ray sources in the sky (see, e.g.,

[5]The extragalactic nature of QSOs was not confirmed until 1963 when Schmidt determined the redshift of the QSO 3C 273 to be $z = 0.158$.

Mészáros, 2013, for a review). They have been detected up to redshifts of $z \sim 9.4$ (Cucchiara *et al.*, 2011). At the time of writing, 32 GRBs are listed in the *Fermi*-LAT GRB catalog[6]. Certain scenarios also predict VHE $\gamma$-ray emission (e.g., Asano & Inoue, 2007) but, so far, no GRB has been observed at these energies. Further potential VHE $\gamma$-ray sources include galaxy clusters, normal nearby and ultraluminous infrared galaxies (see, e.g., Hinton & Hofmann, 2009, and references therein).

### 1.1.1 Continuum emission models

In the following, models for the continuum emission are summarized (this Section follows the review of Böttcher, 2010). The high luminosities, the superluminal motion, and the variability suggest that the continuum emission is produced in a compact region of the jet. An upper limit on the size $R'$ of the emission zone (primed values denote the comoving frame) can be inferred from the observed time variability[7] $\Delta t$ due to causality arguments (e.g., Dermer & Menon, 2009): $R' \lesssim c\Delta t\delta_{\mathrm{D}}/(1+z)$, where the time dilation due to the relativistic movement implies $\Delta t = \Delta t'(1+z)/\delta_{\mathrm{D}}$. It is commonly assumed for simplicity that the emission zone is a sphere of radius $R'$ ("blob") filled isotropically with magnetic fields and a relativistic plasma which moves with the bulk Lorentz factor $\Gamma_{\mathrm{L}}$.
The spectral energy distribution (SED), the frequency weighted flux per unit frequency interval, $\nu F_\nu$, of the continuum emission exhibits two distinct bumps at high and low energies (see Figure 1.2). The low energy part is usually attributed to synchrotron emission of relativistic electrons and positrons (henceforth referred to as electrons) that are deflected in the magnetic field and loose their energy $E$ at a rate

$$-\dot{E} = -m_e c^2 \dot{\gamma} = \frac{4}{3}\sigma_{\mathrm{T}} c \beta^2 \gamma^2 U_B, \tag{1.4}$$

where $\gamma$ is the Lorentz factor of the electron with a speed $\beta$, $\sigma_{\mathrm{T}}$ denotes the Thomson cross section (see Table 1.2), and $U_B = B^2/(8\pi)$ is the magnetic field energy (the process is labeled "Sync" in Figure 1.1).
The high energy part of the SED is either modeled with purely leptonic or lepto-hadronic models. In the former case, photons are upscattered by electrons by means of the inverse Compton (IC) process (see the upper jet in Figure 1.1). The seed photons can originate from the synchrotron radiation generated in the emission zone itself (self-synchrotron Compton, SSC, Marscher & Gear, 1985; Maraschi *et al.*, 1992; Bloom & Marscher, 1996) or external photon fields (external Compton, EC). External target photons can be supplied by the accretion disk radiation (Dermer *et al.*, 1992; Dermer & Schlickeiser, 1993), optical / UV emission, e.g., from the BLR (Sikora *et al.*, 1994; Blandford & Levinson, 1995; Ghisellini & Madau, 1996;

[6] `http://fermi.gsfc.nasa.gov/ssc/observations/types/grbs/grb_table/`
[7] The variability time scale can be defined in several ways, e.g., the time it takes for the observed flux to double.

Dermer *et al.*, 1997), the infrared emission of the torus (Błażejowski *et al.*, 2000), or other synchrotron emission regions inside the jet (Georganopoulos & Kazanas, 2003; Ghisellini & Tavecchio, 2008). Two distinct regimes can be distinguished in IC scattering (see, e.g., Blumenthal & Gould, 1970, for a detailed review): If, on the one hand, the initial photon energy in the rest frame of the electron[8] is much less than the electron's rest mass, the scattering occurs in the Thomson regime. In this case, the scattering cross section is independent of energy and the electron will loose its energy continuously, according to

$$-\dot{E} = -m_e c^2 \dot{\gamma} = \frac{4}{3}\sigma_{\mathrm{T}} c \gamma^2 U_{\mathrm{rad}}, \tag{1.6}$$

for an isotropic photon energy density $U_{\mathrm{rad}}$ in the electron's rest frame. In this case, the average photon energy after scattering, $\langle\epsilon_1\rangle$, is simply

$$\langle\epsilon_1\rangle = \frac{4}{3}\gamma^2\langle\epsilon\rangle, \tag{1.7}$$

for an average photon energy $\langle\epsilon\rangle$ before scattering. On the other hand, if the initial photon energy is much higher than the electron rest mass, the scattering takes place in the Klein-Nishina (KN) regime. The energy loss of the electron can no longer be treated as continuous, since the electron looses a large amount of its initial energy in a single scattering event. Neglecting cooling of the electron spectrum, the resulting instantaneous photon spectrum will steepen in comparison to the Thomson regime (Blumenthal & Gould, 1970).

In the above mentioned leptonic models an ad-hoc electron spectrum is often assumed without discussing how the particles were accelerated in the first place (e.g., Böttcher, 2010, for a discussion). One possible scenario is the acceleration of particles on shock fronts that are formed due to plasma instabilities in the jet (see, e.g., Begelman *et al.*, 1984, for a review and the sketch in Figure 1.1). Relativistic particles scatter off of turbulent magnetic fields and are isotropized on both sides of the shock. Each time a particle crosses the shock, it gains energy of the order $\Delta E/E \propto u/c$, where $u$ is the bulk plasma velocity upstream of the shock. For each crossing, there is a finite probability that the particle escapes downstream of the shock and the competition of acceleration and escape probabilities leads to a power-law shape of the particle distribution (this process was originally proposed by Fermi in 1949, in order to explain the origin of cosmic rays; today it is referred to

[8] In the rest frame of the electron traveling with a speed $v = \beta c$ and corresponding Lorentz factor $\gamma = (1-\beta^2)^{-1/2}$ in the lab frame, the photon energy $\epsilon'$ is given by (e.g., Blumenthal & Gould, 1970)

$$\epsilon' = \gamma\epsilon(1 - \beta\cos\theta), \tag{1.5}$$

where $\epsilon$ is the photon energy and $\theta$ the angle between the photon and electron momenta, both measured in the lab frame.

as first-order Fermi acceleration, reviewed, e.g., in Longair, 2011, or Kirk & Duffy, 1999). In principle, the electron distribution should be obtained from a solution of the Fokker-Planck equation taking into account the injection of particles and the adiabatic and radiative cooling (e.g., Böttcher, 2010). However, such solutions can, in general, only be found numerically.

Leptonic models are usually very successful in describing the broad-band SEDs of AGN and the intra-day time variability due to the short cooling time scales of synchrotron emission, $t_{\mathrm{sync}} = |\dot{\gamma}|^{-1}$, see Eq. (1.4). This is more difficult to achieve in lepto-hadronic models (see the lower jet in Figure 1.1). In these scenarios, the low energy part of the SED is still attributed to synchrotron radiation of electrons, whereas the high energy end is caused by proton induced cascades (PIC; Mannheim & Biermann, 1992; Mannheim, 1993) accompanied by synchrotron radiation of protons and secondary muons and mesons, as well as photo-pion production (Rachen & Mészáros, 1998; Aharonian, 2000; Mücke & Protheroe, 2000, 2001; Mücke *et al.*, 2003). The PIC is initiated by protons with energies $E_p \gtrsim 10^{19}\,\mathrm{eV}$, exceeding the threshold for pion production, $p + \gamma \rightarrow p + \pi^0$ or $p + \gamma \rightarrow n + \pi^+$. Neutral pions quickly decay with a mean life time of $\sim 10^{-16}\,\mathrm{s}$ almost exclusively through the $\pi^0 \rightarrow \gamma + \gamma$ channel or through decays involving additional $e^+e^-$ pairs (Beringer *et al.*, 2012). This initiates an electromagnetic pair cascade (see Section 1.2.1). The high proton energies require high magnetic fields of the order of $\mathcal{O}(10\,\mathrm{G})$ to confine the protons to the emission region. Since the cooling times for protons through, e.g., synchrotron emission are large, it is difficult to account for the short-time variability observed in some blazars.

Regardless of the emission model, the produced $\gamma$-rays have to be able to escape the source. This could be prohibited by pair production $\gamma + \gamma \rightarrow e^+ + e^-$ in intense radiation fields in the emission zone. The zone is transparent for $\gamma$-rays (assuming the Thomson regime) if the compactness, $\ell_c = (L'/R')(\sigma_{\mathrm{T}}/m_e c^3)$, of the source is smaller than $\sim 40$ (e.g., Dondi & Ghisellini, 1995; Urry & Padovani, 1995), where $L'$ is the intrinsic source luminosity. This is another argument in favor of Doppler boosted emission: The relativistic beaming leads to an enhancement of the observed flux, $F_\nu(\nu) = \delta_{\mathrm{D}}^3 F'_{\nu'}(\nu')$, or equivalently of the integrated flux $F = \delta_{\mathrm{D}}^4 F'$ (e.g., Dermer & Menon, 2009). The same holds for the luminosity $L$, with $F = \delta_{\mathrm{D}}^4 L'/(4\pi d_{\mathrm{L}}^2)$, where $d_{\mathrm{L}}$ is the luminosity distance of the source [see Eq. (2.20)]. Using the relation $R' \propto \delta_{\mathrm{D}} \Delta t$, results in the compactness

$$\ell_c \propto \delta_{\mathrm{D}}^{-5} \frac{L}{\Delta t} \frac{\sigma_{\mathrm{T}}}{m_e c^4}, \tag{1.8}$$

up to a redshift factor. Thus, relativistic beaming significantly reduces the compactness and from the above limit on $\ell_c$ a lower limit on $\delta_{\mathrm{D}}$ can be derived from the observed luminosity and time variability.

### 1.1.2 The blazar sequence

The majority of AGN detected at HE and VHE $\gamma$-rays are blazars (see, e.g., the 2FGL and `http://tevcat.uchicago.edu/`). Thus, it is worthwhile to search for an underlying physical mechanism that connects the two subclasses of blazars, BL Lacs and FSRQs. Fossati *et al.* (1998) searched for correlations in a set of blazar observations selected from radio, X-ray, and $\gamma$-ray surveys. The blazars were binned according to their radio luminosity and average SEDs were derived in each bin from simple one-zone SSC models (see Figure 1.2 for a recent version by Ghisellini 2011, with a binning according to the $\gamma$-ray luminosity). They found a clear anti-correlation between the peak synchrotron frequency $\nu_{\mathrm{p}}^{\mathrm{sync}}$ and (1) the integrated luminosity and (2) the $\gamma$-ray dominance, i.e., the ratio of the $\gamma$-ray luminosity, $L_\gamma$, to the peak synchrotron luminosity. Furthermore, a positive correlation between the two peak frequencies at low and high energies was found. Hence, blazars with a low synchrotron peak frequency (LSPs), $\nu_{\mathrm{p}}^{\mathrm{sync}} < 10^{14}\,\mathrm{Hz}$, have the highest luminosities, strongest $\gamma$-ray dominance and the high energy component of the SED at lower energies. This changes for intermediate peaked blazars (ISPs, $10^{14}\,\mathrm{Hz} < \nu_{\mathrm{p}}^{\mathrm{sync}} < 10^{15}\,\mathrm{Hz}$) and high synchrotron peaked blazars (HSP, $\nu_{\mathrm{p}}^{\mathrm{sync}} > 10^{15}\,\mathrm{Hz}$). The latter class has the lowest luminosity and $\gamma$-ray dominance but make up the majority of blazars detected at VHE, as the $\gamma$-ray peak frequency occurs at higher energies. This *blazar sequence* can also be recovered if the average SEDs are binned according to their $\gamma$-ray luminosity (e.g., Ghisellini, 2011). However, it is discussed if the anti-correlation between $\nu_{\mathrm{p}}^{\mathrm{sync}}$ and luminosity is simply due to selection effects, i.e., mainly bright sources enter the analyzed samples (Giommi *et al.*, 2012). However, as pointed out by Finke (2013), the $\gamma$-ray dominance (and a related quantity, the Compton dominance, the ratio of the peak luminosities in the synchrotron and $\gamma$-ray regimes) is independent of redshift and $\nu_{\mathrm{p}}^{\mathrm{sync}}$ is only weakly dependent on the redshift with $(1 + z)$. Including sources with unknown redshift, Finke (2013) finds a clear anti-correlation between the Compton dominance and $\nu_{\mathrm{p}}^{\mathrm{sync}}$ and concludes that this is likely because of a physical origin rather than selection effects.

The differences between FSRQs and BL Lacs could also be due to a difference in the accretion flow (e.g., Ghisellini, 2011): In this picture, a low accretion rate results in less ionizing radiation from the accretion disk and consequently lower luminosities from the BLR are expected. This could then also lead to a reduced Compton dominance as less seed photons are available for the IC process in EC scenarios. The reduced radiative cooling due to IC scattering allows the electrons in the jet to reach higher energies, and the peak frequencies of the two SED bumps are shifted to higher frequencies. Thus, a low accretion rate would result in a BL Lac and a high accretion rate in an FSRQ. Although compelling, no firm evidence exists for this theory at the moment (Krawczynski & Treister, 2013).

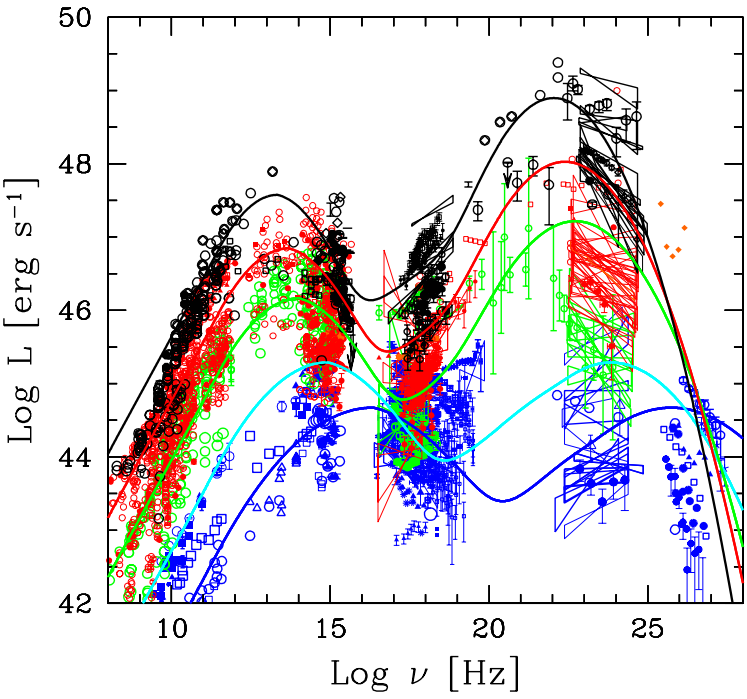


**FIGURE 1.2:** The blazar sequence (taken from Ghisellini, 2011). Shown are average phenomenological SEDs binned according to their $\gamma$-ray luminosity between 0.1 GeV and 10 GeV (see caption of Figure 2 in Ghisellini, 2011): $\log_{10} L_\gamma < 45.5$ (blue), $45.5 < \log_{10} L_\gamma < 46.5$ (green), $46.5 < \log_{10} L_\gamma < 47.5$ (red), and $\log_{10} L_\gamma > 48.5$ (black).

## 1.2 Absorption of $\gamma$-rays on background radiation fields

As mentioned in the previous section, HE and VHE $\gamma$-rays can undergo pair production with radiation fields in the source. The same process can occur in the intergalactic medium, leading to an attenuation of the $\gamma$-ray flux emitted by the AGN (Nikishov, 1962; Jelley, 1966; Gould & Schréder, 1966, 1967). Let $\Phi_{\rm obs}(E) \equiv {\rm d}N_{\rm obs}/{\rm d}E$ denote the observed spectrum (photons flux per unit energy interval) at observed energy $E$ emitted by a source at redshift $z_0$. The interaction between a $\gamma$-ray and a background photon, $\gamma + \gamma_{\rm bkg} \rightarrow e^+ + e^-$, leads to an exponential suppression of the intrinsic differential photon flux $\Phi(E')$, $E' = E(1+z)$, commonly denoted as

$$\Phi_{\rm obs}(E) = \exp\left[-\tau_{\gamma\gamma}(E, z_0)\right] \Phi(E'), \tag{1.9}$$

where $\tau_{\gamma\gamma}$ is the optical depth. It is a threefold integral over the line of sight $\ell$, the cosine of the angle between the photon momenta, $\mu$, and the energy $\epsilon$ of the

background radiation field[9] (e.g., Dwek & Krennrich, 2005),

$$\tau_{\gamma\gamma}(E, z_0) = \int_0^{z_0} \mathrm{d}\ell(z) \int_{-1}^{+1} \mathrm{d}\mu \frac{1-\mu}{2} \int_{\epsilon'_{\mathrm{thr}}}^{\infty} \mathrm{d}\epsilon' n_\epsilon(\epsilon', z) \sigma_{\gamma\gamma}(E', \epsilon', \mu). \tag{1.10}$$

Pair production is energetically possible above the threshold energy,

$$\epsilon_{\mathrm{thr}}(E, \mu) = \frac{2(m_e c^2)^2}{E(1-\mu)}, \tag{1.11}$$

with $\epsilon'_{\mathrm{thr}} = \epsilon_{\mathrm{thr}}(E', \mu)$. The comoving photon number density of the background radiation field in the interval $\epsilon'$ and $\epsilon' + \mathrm{d}\epsilon'$ at redshift $z$ is denoted by $n_\epsilon(\epsilon', z)$. The cross section for pair production is given by (e.g., Heitler, 1954)

$$\sigma_{\gamma\gamma}(E, \mu, \epsilon) = \frac{3\sigma_{\mathrm{T}}}{16}\left(1-\beta^2\right)\left[2\beta\left(\beta^2-2\right) + \left(3-\beta^4\right)\ln\left(\frac{1+\beta}{1-\beta}\right)\right], \tag{1.12}$$

$$\beta(E, \mu, \epsilon) = \sqrt{1 - \frac{\epsilon_{\mathrm{thr}}}{\epsilon}}. \tag{1.13}$$

The integration over the line of sight can be substituted for an integration over redshift, $\mathrm{d}\ell(z) = |\mathrm{d}\ell/\mathrm{d}z|\mathrm{d}z$, with the Jacobian (e.g., Peacock, 1999)

$$\frac{\mathrm{d}\ell}{\mathrm{d}z} = c\frac{\mathrm{d}t}{\mathrm{d}z} = \frac{c}{H_0(1+z)E(z)}, \tag{1.14}$$

$$E(z) = \left\{(1+z)^2(\Omega_m z + 1) + z(2+z)\left[(1+z)^2\Omega_r - \Omega_\Lambda\right]\right\}^{1/2}, \tag{1.15}$$

where $\Omega_m$ and $\Omega_r$ are the matter and radiation density, respectively, normalized to the critical density, $\Omega_{r,m} = \rho_{r,m}/\rho_c$, with $\rho_c = 3H_0^2/(8\pi G)$, and $\Omega_\Lambda = \Lambda/(3H_0^2)$ corresponds to the energy density attributed to the cosmological constant. The present day Hubble constant is denoted by $H_0 = 100h\,\mathrm{km\,s^{-1}\,Mpc^{-1}}$, with the Hubble parameter $h$. In a flat universe one has $\Omega_r + \Omega_m + \Omega_\Lambda = 1$. These equations are derived within the standard cosmological model parametrization including a cosmological constant and cold Dark Matter ($\Lambda$CDM model, see, e.g., Beringer *et al.*, 2012, for a review and Section 1.4 for a short discussion of observational evidence for Dark Matter and Dark Matter candidates). Measured values can be found in Beringer *et al.* (2012) and values including data from the *Planck* satellite are given in Planck Collaboration *et al.* (2013).

The cross section for pair production multiplied by the velocity $v = \beta c$ and averaged over $\mu$ is shown for different $\gamma$-ray energies as a function of wavelength of the

[9] If the integrations over $\epsilon$ and $\mu$ are swapped in Eq. (1.10), the integration over $\epsilon'$ runs over $[m_e c^2/E; \infty)$ while the integration over $\mu$ runs from $-1$ to $1 - 2(m_e c^2)^2/(E\epsilon')$ (e.g., Mirizzi & Montanino, 2009).

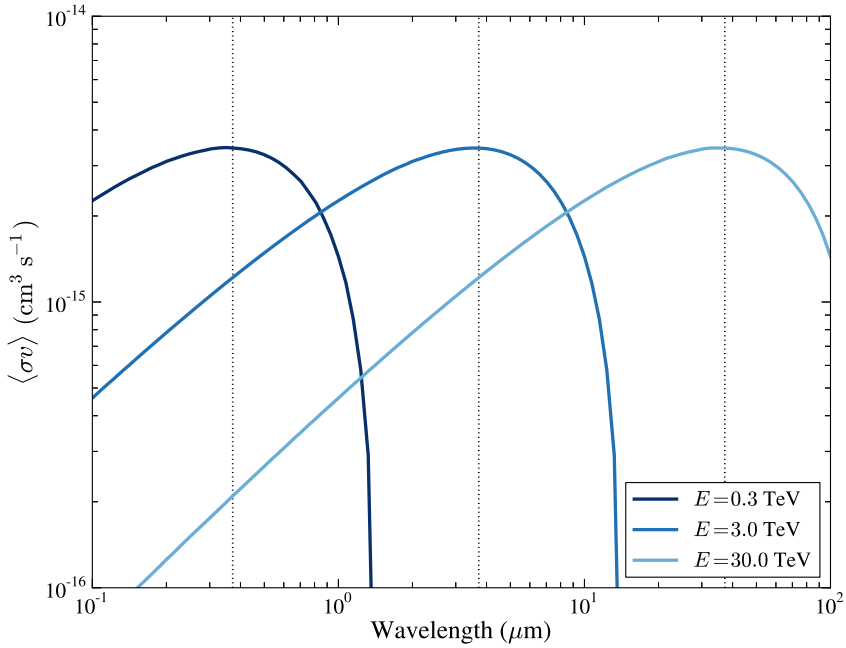


**Figure 1.3:** The velocity averaged pair production cross section for different $\gamma$-ray energies $E$. The maxima are given by Eq. (1.16) and are shown as dashed lines.

background photon in Figure 1.3. It is strongly peaked at a wavelength $\lambda_*$, evaluated numerically to be (e.g., Guy *et al.*, 2000)

$$\lambda_* = \frac{hc}{\epsilon_*} \approx 1.24 \left( \frac{E}{\text{TeV}} \right) \mu\text{m}. \tag{1.16}$$

The most intense background radiation field is the CMB, peaking at an energy $\epsilon_{\text{CMB}} = 634\,\mu\text{eV}$ or a wavelength of $\approx 2\,\text{mm}$ at $z = 0$. Consequently, the pair production peaks for photon energies $E \approx 1.6\,\text{PeV}$ and can be safely neglected here, as the maximum energy measured from an AGN is of the order of 20 TeV. In the energy range covered with the *Fermi*-LAT and IACTs, HE and VHE $\gamma$-rays predominantly interact with soft photons with optical / UV to far-infrared wavelengths. The background radiation at these wavelengths is the EBL, reviewed in Section 2.1.

### 1.2.1 Electromagnetic cascades

The relativistic $e^+e^-$ pairs produced in the interaction between $\gamma$-rays and EBL photons (see the previous Section) can generate HE and VHE emission by upscattering CMB photons by means of the IC process and initiate an electromagnetic cascade,

as these photons can again undergo pair production (e.g., Svensson, 1987; Protheroe & Stanev, 1993; Aharonian *et al.*, 1994; Dai *et al.*, 2002; Dolag *et al.*, 2009; Kachelrieß *et al.*, 2012). The amount of cascade radiation that comes from the same line of sight as the primary emission depends on the field strength $B_{\mathrm{IGMF}}$ of the intergalactic magnetic field (IGMF) and its correlation length $\lambda^c_{\mathrm{IGMF}}$. The values of $B_{\mathrm{IGMF}}$ and $\lambda^c_{\mathrm{IGMF}}$ are unknown and only upper and lower limits exist (e.g., Neronov & Semikoz, 2009, for a compilation of limits and Section 5.2 for a more detailed discussion). If the field strength is large or the correlation length is small compared to the IC cooling length, $ct_{\mathrm{IC}} = c/|\dot{\gamma}|$ [see Eq. (1.6)], the pairs are quickly isotropized and extended halos of $\gamma$-ray emission form around the initial source (e.g., Aharonian *et al.*, 1994; Dai *et al.*, 2002; Elyiv *et al.*, 2009; Dolag *et al.*, 2009). The time delay of the cascade emission compared to the primary emission also depends on $B_{\mathrm{IGMF}}$ and $\lambda^c_{\mathrm{IGMF}}$. High energy and VHE $\gamma$-rays need to be produced for a sufficiently long period, so that the reprocessed radiation is observable (e.g., Dermer *et al.*, 2011).

In the following, a simplified treatment to calculate the cascade spectrum will be presented. The broadening of the beam due to the deflection of the pairs in the IGMF will be neglected and only the first generation of the cascade is included (see also Section 2.3.2). This corresponds to the case that the VHE spectra of blazars cut off immediately after the highest measured energy point. For a $E = 10\,\mathrm{TeV}$ primary $\gamma$-ray, the electrons will have a Lorentz factor $\gamma \approx E/(2m_e c^2) \approx 10^7$. Using Eq. (1.7), the upscattered CMB photons have an energy of $\sim 85\,\mathrm{GeV}$. For all detected extragalactic VHE sources and current EBL models (see Section 2.1), the optical depth is $\tau_{\gamma\gamma} < 1$ at these energies and, thus, it suffices to include only the first generation of pairs in the cascade. Furthermore, it will be assumed that the pairs predominantly loose their energy in IC scattering and not through plasma instabilities heating the intergalactic medium (Broderick *et al.*, 2012; Schlickeiser *et al.*, 2012, see the discussion in Section 4.1).

With these simplifications, the cascade spectrum can be obtained by solving the corresponding kinetic equation for the electron distribution $N(\gamma)$ in the steady state limit (Tavecchio *et al.*, 2011a),

$$N(\gamma) = \frac{1}{|\dot{\gamma}|} \int_{\gamma}^{\infty} \mathrm{d}\gamma' Q(\gamma'), \tag{1.17}$$

with $|\dot{\gamma}|$ the energy loss of electrons due to IC scattering, see Eq. (1.6). The injection rate, $Q(\gamma)$, is the difference between observed and emitted photon flux,

$$Q(\gamma) = \left(e^{\tau_{\gamma\gamma}(E,z)} - 1\right) \Phi_{\mathrm{obs}}(E). \tag{1.18}$$

The cascade energy spectrum at energy $\epsilon$ is then calculated to be (Blumenthal &

Gould, 1970; Dermer *et al.*, 2011)

$$\begin{aligned} F_\epsilon(\epsilon) &= \frac{9}{64}\frac{\epsilon\, m_e c^2}{u_{\rm CMB}(z=0)} \\ &\times \int\limits_{\max\left[\sqrt{\epsilon/4\epsilon_{\rm CMB}},\gamma_{\rm dfl},\gamma_{\rm eng}\right]}^{\infty} \frac{{\rm d}\gamma}{\gamma^6} \int\limits_{2m_e c^2\gamma}^{\infty} {\rm d}E \left(e^{\tau_{\gamma\gamma}(E,z)}-1\right)\Phi_{\rm obs}(E) \\ &\times \int\limits_0^{\infty} {\rm d}\epsilon' \frac{n_{\rm CMB}(\epsilon', z=0)}{\epsilon'^{\,2}} F_{\rm T}^{\rm IC}(\epsilon,\epsilon',\gamma), \end{aligned} \tag{1.19}$$

where $u_{\rm CMB}(z=0) = 0.26$ eV cm$^{-3}$, $\epsilon_{\rm CMB}(z=0) = 634\,\mu$eV and $n_{\rm CMB}(\epsilon', z)$ denote the energy density, mean energy, and differential photon number density of the CMB, respectively. The inverse Compton kernel for scattering on an isotropic photon field in the Thomson regime is

$$F_{\rm T}^{\rm IC}(\epsilon,\epsilon',\gamma) = 4\epsilon'\gamma\left(2\hat{\epsilon}\ln\hat{\epsilon} + \hat{\epsilon} + 1 - 2\hat{\epsilon}^2\right), \tag{1.20}$$

with $0 \leq F_{\rm T}^{\rm IC} \leq 1$ and $\hat{\epsilon} = \epsilon/(4\epsilon'\gamma^2)$. Klein-Nishina effects can be safely neglected at the considered energies. It follows from Eq. (1.5) that the maximum photon energy in the electron's rest frame is $\epsilon'_{\rm max} \approx 2\gamma\epsilon$. For $\gamma \approx 10^7$ and $\epsilon = \epsilon_{\rm CMB}$, one finds $\epsilon'_{\rm max} \ll m_e c^2$. The lower limit for the integration over $\gamma$ is the maximum of three different constraints on $\gamma$. The first one stems from kinematic constraints of Compton scattering. The second one denotes the $\gamma$ factor for which the electrons are deflected outside the opening cone of the blazar jet with an opening angle $\theta_{\rm cone} \sim 1/\Gamma_{\rm L}$, with $\Gamma_{\rm L}$ the bulk Lorentz factor of the plasma of the jet. And finally, the third factor gives the minimum possible Lorentz factor if the source is active for a certain time (see Dermer *et al.*, 2011, for further details). The quantities $\gamma_{\rm dfl}$ and $\gamma_{\rm eng}$ are calculated by Dermer *et al.* (2011) under the approximation of small deflections and small observing angles. In the case of isotropic emission, i.e., $B_{\rm IGMF} \approx 10^{-13}$ G and a lifetime of the source of $\Delta t \gtrsim 10^6$ years (cf. Section 2.3.2), this approximation no longer holds and the lower integration-limit is replaced by $\sqrt{\epsilon/4\epsilon_{\rm CMB}}$.
For an analysis of the induced time delay and angular spread of the beam, as well as for spectra that extend above $\sim 10$ TeV Monte-Carlo simulations are necessary. Examples for such models can be found in, e.g., Taylor *et al.* (2011) and Kachelrieß *et al.* (2012).

## 1.3 Detection of high and very high energy $\gamma$-rays

Data taken with the *Fermi*-LAT and IACTs are used in this work to study the propagation of HE and VHE $\gamma$-rays through the intergalactic medium. First, the detection

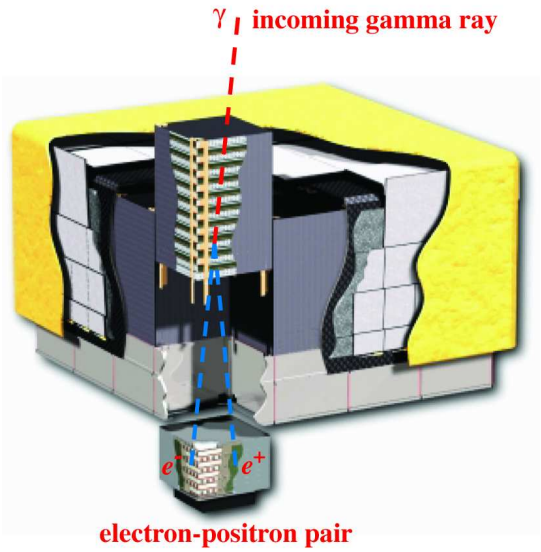


**FIGURE 1.4:** Schematic structure of the LAT. As an example, a $\gamma$-ray is shown that converts into an $e^+e^-$ pair in the tracker module. The energy of the pair is measured in the calorimeter.

of $\gamma$-rays with the *Fermi*-LAT will be reviewed. Thereafter, the imaging Cherenkov technique is discussed and current experiments are summarized.

### 1.3.1 THE *Fermi* SATELLITE

The *Fermi* satellite was launched into orbit on June 11, 2008 and began science operations on August 13, 2008 (if not cited otherwise, the detailed description of Atwood *et al.*, 2009, is followed here). The satellite orbits the Earth at an $\sim$ 565 km altitude with a period of $\sim$ 1.5 hours. Two main instruments are supported by the spacecraft: The Gamma-ray Burst Monitor (GBM) and the Large Area Telescope (LAT). In the following, the focus is on the LAT, a pair-conversion telescope with a broad field of view (FoV) of 2.4 sr at 1 GeV, which covers a nominal energy range from about 20 MeV to more than 300 GeV. For most of the observation time, the *Fermi*-LAT is in the all-sky survey mode: The boresight of the satellite alternates each orbit between the northern and southern hemisphere covering the whole sky every three hours.

A schematic view of the LAT is shown in Figure 1.4. An incident $\gamma$-ray enters one of the tracker modules and converts into an $e^+e^-$ pair preferentially in one of the 16 tungsten foils (with a high atomic number $Z = 74$). The mean free path of photons for pair production is $7/9X_0$, where $X_0$ is the radiation length, conventionally given

in units of $\mathrm{g\,cm^{-2}}$ (Beringer *et al.*, 2012),

$$X_0 = \frac{716.4\,A}{Z(Z+1)\ln(287/\sqrt{Z})}\,\mathrm{g\,cm^{-2}}, \tag{1.21}$$

with the atomic mass $A$ in $\mathrm{g\,mol^{-1}}$. It is also the characteristic amount of matter traversed by electrons and positrons for bremsstrahlung. The tungsten foils are interleaved with 18 two-layered single sided silicon strip detectors (SSDs) that measure the tracks of the charged particles.

The probability distribution function (pdf) of the reconstructed arrival direction from a point source is referred to as point spread function (PSF). The reconstruction of the arrival direction improves if the incident $\gamma$-ray converts in one of the first tungsten foils because the $e^+e^-$ tracks are recorded by several SSDs. For a 100 MeV $\gamma$-ray, missing one of the first foils deteriorates the resolution by a factor of $\sim 2$. As a compromise between resolution at low energies limited by multiple Coulomb scattering (with a $\sim 1/E$ dependence) and high energies requiring converter material, the tracker is divided into a *front* and *back* part: The first 12 converter foils have a thickness of 0.03 radiation lengths while the last 4 layers are approximately 6 times thicker. A photon from a point source will be reconstructed with a 68 % probability into a circle of radius $r_{68}$. This is the radius for which the integral of the PSF over the scaled-angular deviation (the difference between the true and reconstructed arrival direction) is equal to 0.68[10]. The PSF also depends on the photon energy, the inclination angle $\theta$ (angle between the arrival direction and the LAT's $z$ axis), the conversion type (front or back converted events), and the chosen event class (see below). The left panel of Figure 1.5 shows $r_{68}$ as a function of the $\gamma$-ray energy for the in-flight PSF which is derived from in-orbit data and is independent of the inclination angle. At 1 GeV, $r_{68}$ is twice as large for back converted events compared to front converted ones.

In the electromagnetic calorimeter, the $e^+e^-$ pair will loose energy predominantly through bremsstrahlung and the emitted photons produce further pairs, thus initiating an electromagnetic cascade. This continues until ionization losses dominate over cooling via bremsstrahlung. The energy loss is equal for the two processes at the critical energy (Beringer *et al.*, 2012)

$$E_c = \frac{800\,\mathrm{MeV}}{Z+1.2} \tag{1.22}$$

below which the cascade formation ceases. The calorimeter consist of 96 CsI(Tl) inorganic scintillator crystals grouped into 8 segments with a thickness of 8.6 radiation lengths at nominal incidence (10.1 radiation lengths including the tracker).

[10] Details on and the functional form of the PSF can be found under `http://fermi.gsfc.nasa.gov/ssc/data/analysis/documentation/Cicerone/Cicerone_LAT_IRFs/IRF_PSF.html`.

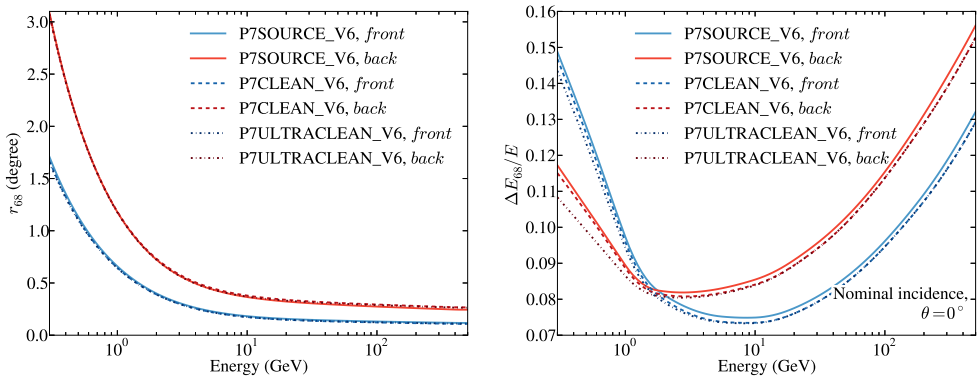


**FIGURE 1.5:** Left panel: $r_{68}$ radius of the in-flight PSF for front and back converted events and different event classes. Right panel: relative energy dispersion (68 % confidence) at nominal incidence for different classes.

The scintillation light of the crystals is measured with photodiodes at both crystal ends. This gives an estimate where in the crystal the energy was deposited. The segmentation of the calorimeter allows to measure the longitudinal shower development resulting in a successful shower energy reconstruction up to TeV energies. The transversal shower development is characterized by the Molière radius $R_M = X_0 E_s / E_c'$ in which $\sim 90\,\%$ of the shower energy is contained (Beringer *et al.*, 2012). Here, $E_s \approx 21\,\mathrm{MeV}$ and $E_c'$ is the energy for which the ionization loss per radiation length is equal to the electron energy [this definition is due to Rossi, 1952, note the difference to the definition of $E_c$ in Eq. (1.22)]. The Molière radius for the LAT calorimeter is $R_M = 3.8\,\mathrm{cm}$.

The 68 % energy uncertainty $\Delta E$ is calculated similarly to the $r_{68}$ confidence radius as an integral over the energy dispersion of the LAT which depends on the conversion type (back or front part of the tracker), the energy itself, the chosen event class (see below), and the inclination angle $\theta$ of the photon[11]. It is shown in the right panel of Figure 1.5.

Most events detected with the LAT are background events; charged cosmic rays and $\gamma$-rays from the interaction of cosmic rays with the Earth's atmosphere (the so-called Earth albedo, the *Fermi*-LAT spectrum is presented in Abdo *et al.*, 2009b). The anti-coincidence detector (ACD) is designed to deliver a rejection against charged background particles with an efficiency of at least 0.9997. It covers the entire tracking array and consists of 89 overlapping tiles of plastic scintillator and scintillating fiber ribbons, the latter covering gaps between the tiles. Each tile is coupled to a wavelength-shifting fiber and two photomultiplier tubes. The segmented design minimizes the chance of a false veto generated by the backsplash effect: Charged

[11] See `http://fermi.gsfc.nasa.gov/ssc/data/analysis/documentation/Cicerone/Cicerone_LAT_IRFs/IRF_E_dispersion.html` for further details.

particles created in the calorimeter by the shower can migrate into the ACD and cause a scintillation-light signal. Therefore, the on-board veto is disengaged if the energy deposition in the calorimeter exceeds 20 GeV.
The background is further reduced by the event-reconstruction algorithm. For example, events for which two tracks point back to the same vertex are very likely caused by $e^+e^-$ pairs created by a primary $\gamma$-ray. Furthermore, events can be discarded for which unassociated tracks are present in the tracker. Another discriminator against the background is the identification of the electromagnetic shower. Showers initiated by hadrons can be distinguished from electron and $\gamma$-ray induced showers through their different morphology. Combining data from all LAT subsystems, several parameters are defined to assess the quality of the event reconstruction and the probability that the event has been initiated by a $\gamma$-ray. These parameters are the energy reconstruction quality, the directional reconstruction quality, and the $\gamma$-ray probability derived from tracker, calorimeter, and ACD data (Ackermann *et al.*, 2012b). Different cuts on these parameters define different event classes, and tighter cuts will result in lower background contamination and a higher probability that the candidate event is indeed a $\gamma$-ray. In the *Pass 7* release of the *Fermi*-LAT data these classes are called (sorted by increasingly tighter cuts) P7V6_TRANSIENT, P7V6_SOURCE, P7V6_CLEAN, and P7V6_ULTRACLEAN[12]. The event classes take into account on-orbit data and compare the event classification with detailed Monte-Carlo simulations (Ackermann *et al.*, 2012b). Since the background rejection influences the sensitivity of the instrument, the instrumental response functions (IRFs) also depend on the event classes. The instrument's response is canonically factored into the already introduced PSF, the energy dispersion, and the effective area (e.g., Rando, 2009). The latter is the product over the cross-sectional geometrical collection area, the $\gamma$-ray conversion probability, and the efficiency of an event selection, given by the event classes above (Ackermann *et al.*, 2012b). For tighter constraints on the $\gamma$-ray probability of an event, the effective area will decrease. The LAT can detect fluxes from point sources at the galactic north pole with a power-law type spectrum $\mathrm{d}N/\mathrm{d}E \propto E^{-\Gamma}$ with an index $\Gamma = 2$ down to $\sim 10^{-12}\,\mathrm{erg\,cm^{-2}\,s^{-1}}$ at $\sim 1\,\mathrm{GeV}$ after 3 years of observation[13].

### 1.3.2 Imaging air Cherenkov telescopes

The flux sensitivity of the *Fermi*-LAT considered at the end of the previous Section of $\nu F_\nu = E^2\mathrm{d}N/\mathrm{d}E = 10^{-12}\,\mathrm{erg\,cm^{-2}\,s^{-1}}$ at 1 GeV corresponds to roughly 200 photons per year and $\mathrm{m}^2$ above this energy, assuming again a power law for the differential photon flux with an index $\Gamma = 2$. Above 1 TeV, only $\sim 2$ photons every 10

[12] See also `http://fermi.gsfc.nasa.gov/ssc/data/analysis/documentation/Cicerone/Cicerone_LAT_IRFs/IRF_overview.html`.

[13] See `http://www.slac.stanford.edu/exp/glast/groups/canda/lat_Performance.htm` for plots and discussion of the effective area and the point source sensitivity.

years and $m^2$ are expected. At these energies, the sensitivity of the *Fermi*-LAT is, in general, not sufficient to provide adequate statistics in order to analyze the spectral or temporal behavior of the source (e.g., Rieger *et al.*, 2013). A significant increase in the effective area is required to compensate for the reduced flux beyond these energies, and it seems unlikely that a space mission can meet this requirement in the foreseeable future. Fortunately, the ground based imaging air Cherenkov technique has proven viable to study the VHE regime. It exploits the fact that VHE $\gamma$-rays initiate electromagnetic cascades in the atmosphere and the produced relativistic $e^+e^-$ pairs emit Cherenkov radiation. This radiation can be detected on ground across hundreds of meters guaranteeing effective areas beyond $10^4\,m^2$ (e.g., Rieger *et al.*, 2013). In the following, the technique and currently operating IACT arrays are summarized (adopted from the review by Aharonian *et al.*, 2008e).

Primary VHE $\gamma$-rays interact with the atoms of the atmosphere[14] and produce $e^+e^-$ pairs at a mean free path of $7/9X_0$ [see Eq. (1.21)], with $X_0 \approx 36.6\,g\,cm^{-2}$, the atmospheric radiation length. Hence, the Earth's atmosphere acts as a calorimeter with the same working principle as the calorimeter on board the *Fermi*-LAT: The pairs loose their energy predominantly through bremsstrahlung and an extensive electromagnetic air shower (EAS) starts to develop in the atmosphere. The cascade will die out once ionization losses start to dominate for electrons and positrons at the energy $E = E_c$, given in Eq. (1.22). The amount of matter traversed in the atmosphere, $x$ (again measured in $g\,cm^{-2}$), is given by the integral over the density of the atmosphere, which has an exponential profile[15], $\rho(z) = \rho_0 \exp(-z/h)$, at height $z$, with $h = 8.5\,km$ and $\rho_0 \approx 1.21 \times 10^{-3}\,g\,cm^{-3}$. The total thickness of the atmosphere is $\sim 30X_0$. A simulated EAS for a 300 GeV primary $\gamma$-ray is shown in Figure 1.6. The shower maximum is reached at $x_{max} = X_0 \ln(E/E_c)$ with $E$ the initial energy of the $\gamma$-ray. Showers fluctuate due to differences of the depth of the first interaction. The probability that a primary $\gamma$-ray traverses $N$ atmospheric radiation lengths is $P(N) = \exp(-9/7N)$.

Once the shower develops, electrons (and positrons) propagating with velocities larger than the speed of light in air, $\beta > 1/n$, where $n = n(z)$ is the refractive index of air, will emit Cherenkov light into a cone with opening angle

$$\cos\theta_c(z) = \frac{1}{\beta n(z)}. \tag{1.23}$$

The refractive index in air scales exponentially with the height in the atmosphere, $n(z) = 1 + \eta_0 \exp(-z/h_0)$, with $h_0 = 7250\,m$ and $\eta_0 = 2.9 \times 10^{-4}$. An electron will continue to emit Cherenkov radiation as long as it's Lorentz factor $\gamma > \gamma_0$ with

[14] The main atmospheric components are $N_2$ (78.08 %, with atomic number $Z = 7$ and mass number $A = 14$ for nitrogen N) and $O_2$ (20.95 %, with $Z = 8$ and $A = 16$ for oxygen O), see, e.g., `http://nssdc.gsfc.nasa.gov/planetary/factsheet/earthfact.html`

[15] The profile follows from an isothermal slab model: The pressure on both sides of the slab is balanced by the gravitational force on the slab.

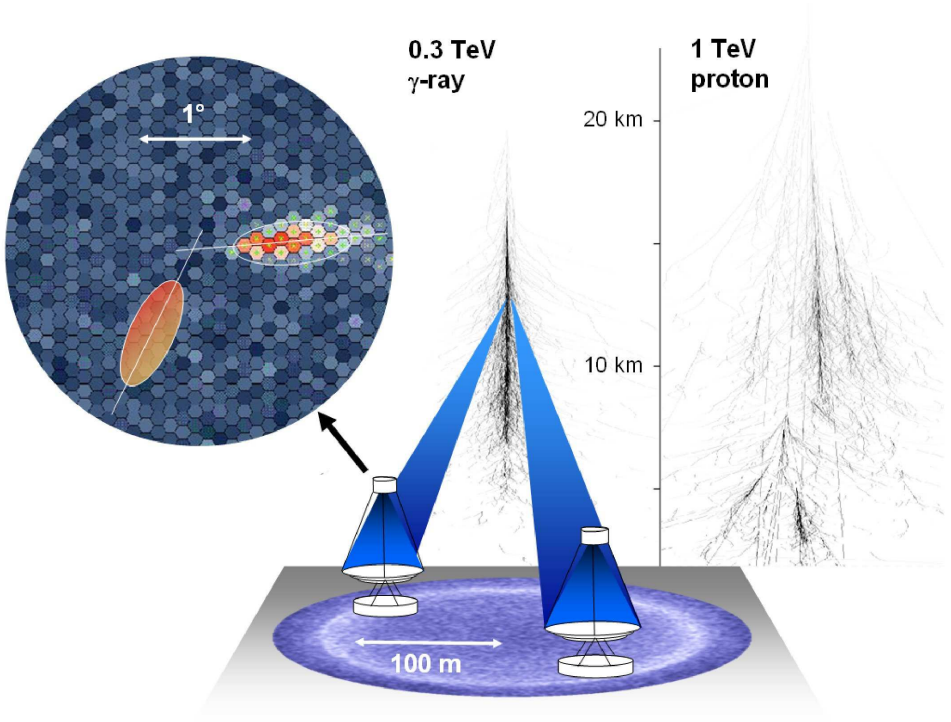


**Figure 1.6:** Working principle of IACTs: primary $\gamma$-rays initiate an air shower and the particles emit Cherenkov radiation, which is recorded by the cameras. A simulated shower initiated by a proton is also shown (image taken from Hinton & Hofmann, 2009).

$\gamma_0 = n(z)/\sqrt{n^2(z)-1}$, which decreases from $\gamma_0 \approx 87$ at $z = 10\,\mathrm{km}$ to $\gamma_0 \approx 48$ at sea level. Equivalently, $\theta_c$ decreases with increasing height, and typically a cone with radius $\sim 120\,\mathrm{m}$ is illuminated on the ground, sketched in Figure 1.6. The emitted spectrum and is given by

$$\frac{\mathrm{d}^2N}{\mathrm{d}x\,\mathrm{d}\lambda} = \frac{2\pi\alpha}{\lambda^2}\sin^2\theta_c = \frac{2\pi\alpha}{\lambda^2}\left(1-\frac{1}{\beta^2 n^2(z)}\right). \tag{1.24}$$

The refractive index changes with wavelength and the emission at wavelengths shorter than UV is absorbed by the atmosphere. Thus, the Cherenkov spectrum is strongly peaked in the UV / optical band.

Unfortunately, the atmosphere is far from being an ideal calorimeter. Cherenkov radiation is subject to Rayleigh scattering (scattering off of particles much smaller than the photon wavelength), Mie scattering (particles with sizes comparable to the photon wavelength, e.g., aerosols), and scattering off of water vapor. Furthermore, Cherenkov photons can be absorbed by the ozone process, $O_3 + \gamma \rightarrow O_2 + O$.

Air showers initiated by cosmic rays constitute the main background for IACTs (a shower initiated by a 1 TeV proton is shown in Figure 1.6). Cosmic rays pen-

etrating the Earth's atmosphere are constituted mainly of protons (87 %), Helium nuclei (12 %), and heavier nuclei as well as anti-protons, electrons, positrons, and neutrinos (e.g., Longair, 2011). A proton interacting with a nucleus will produce fragment nuclei, anti-nuclei, and pions, thus initiating a nucleonic cascade (e.g., Longair, 2011). Neutral pions predominantly decay via $\pi^0 \rightarrow \gamma + \gamma$ (also initiating electromagnetic cascades), while charged pions mainly decay into muons and muon neutrinos, $\pi^+ \rightarrow \mu^+ + \nu_\mu$ and $\pi^- \rightarrow \mu^- + \overline{\nu}_\mu$. Muons will emit Cherenkov light resulting in ring or arc images in the camera. However, for large distances from the telescope, the images will be compact, mimicking $\gamma$-ray air shower images. This poses an irreducible background for single telescope systems (e.g., Hinton & Hofmann, 2009). Observations with IACTs are always background dominated, since the $\gamma$-ray to cosmic-ray flux is as low as $\sim 10^{-4}$ even for the brightest $\gamma$-ray sources[16]. Consequently, an efficient background rejection is mandatory. Fortunately, cosmic-ray and $\gamma$-ray induced cascades can be distinguished through differences in the camera images of the showers (see below).

Imaging air Cherenkov telescopes record the short flashes of Cherenkov light utilizing large reflectors and high speed cameras in the focal plane. The Davies-Cotton design (Davies & Cotton, 1957) of tessellated mirrors is commonly used and the camera consists of an array of photomultiplier tubes (PMTs), each PMT being one camera pixel with exposure times $\lesssim 30$ ns. The cameras need to have a sufficiently large field of view (FoV), so that even those showers are contained in the camera for which the telescope is on the edge of the Cherenkov light pool. A $\gamma$-ray shower image as recorded with the camera is shown in Figure 1.6. The major axis of the ellipse is a projection of the shower axis on the plane of the sky and the intensity of the ellipse scales with the energy of the primary $\gamma$-ray. Parameters are defined which further characterize the shape of the ellipse and are used to reject showers induced by cosmic rays (Hillas, 1985). Images of $\gamma$-ray showers will have a compact elliptic shape, whereas a cosmic-ray image will have a complex structure due to the hadronic interactions. Cuts in the parameter space of the image parameters allow to reject the background events with a high probability. Furthermore, the angular resolution of IACTs of typically $\lesssim 0.1^\circ$ allows to select air showers that have arrived from the direction of the observed source. For instance, Benbow (2005) simulated $\gamma$-ray showers for a Crab-like $\gamma$-ray spectrum observed with a H.E.S.S. type array and found a residual cosmic-ray contamination in the data of 0.024 % after applying image and angular cuts. With the same cuts, 40 % of all simulated $\gamma$-rays were retained.

Images will only be taken if some particular trigger criteria are met. Typically, it is required that the photocurrent in a number of pixels (usually 2 to 4) exceeds a

[16] The all-particle cosmic-ray spectrum is $\phi(E) \approx 2.5 \times 10^{-8} (E/1000\,\mathrm{GeV})^{-2.7}\,\mathrm{cm}^{-2}\,\mathrm{s}^{-1}\,\mathrm{sr}^{-1}\,\mathrm{GeV}^{-1}$ (e.g., Aharonian *et al.*, 2008e), resulting in an integral flux of $\sim 9 \times 10^{-8}\,\mathrm{cm}^{-2}\,\mathrm{s}^{-1}$ above 1 TeV and a field of view of 5°. Compared to the integral flux of the Crab nebula measured by H.E.S.S. of $2.26 \times 10^{-11}\,\mathrm{cm}^{-2}\,\mathrm{s}^{-1}$ (Aharonian *et al.*, 2006d), this results in a ratio of $\sim 3 \times 10^{-4}$.

**TABLE 1.1:** Selection of currently operating IACT arrays.

| Experiment (site) | | location and altitude | $N_{\text{tel}}$ [a] | $A_{\text{mirror}}$ ($m^2$) [b] | FoV | Camera pixels times pixel size |
|---|---|---|---|---|---|---|
| H.E.S.S. [c] | Phase I | 23°S, 17°E | 4 | 108 | 5° | $960 \times 0.16°$ |
| (Namibia) | Phase II | 1800 m | 4+1 | 614 | 3.2° | $2048 \times 0.07°$ |
| MAGIC [d] (La Palma) | Phase I | 28°N, 19°W | 1 | 234 | 4° | $397 \times 0.1°$ $+180 \times 0.2°$ |
| | Phase II | 2230 m | 1+1 | 246 | 3.5° | $1039 \times 0.1°$ |
| VERITAS [e] (Arizona, USA) | | 32°N, 111°W 1268 m | 4 | 106 | 3.5° | $499 \times 0.15°$ |

[a] Number of telescopes.
[b] Mirror area per telescope.
[c] High Energy Stereoscopic System (e.g., Hinton, 2004; Vincent, 2005), see `http://www.mpi-hd.mpg.de/hfm/HESS/`.
[d] Major Atmospheric Gamma-ray Imaging Cherenkov Telescopes (e.g., Baixeras *et al.*, 2004; Tridon *et al.*, 2010), see `http://magic.mppmu.mpg.de/` .
[e] Very Energetic Radiation Imaging Telescope Array System (e.g., Maier *et al.*, 2008), see `http://veritas.sao.arizona.edu/`.

threshold value in a small time window (of the order of 3 ns to 25 ns). Additionally, it is often required that the triggered pixels are adjacent to each other or are within the same topological camera sector.
A selection of currently operating IACTs and their instrumental parameters are listed in Table 1.1 and are shown in Figure 1.7[17]. All are operating in stereoscopic mode, meaning that at least two telescopes observe the same air showers. Requiring coincident detection of the air shower by several telescopes within a fixed time window reduces the background of single muons, helps to reject false triggers caused by fluctuations in the night-sky background and cosmic ray initiated showers due to their irregular time structure. Moreover, stereoscopy results in a better reconstruction of the shower core position.

## 1.4 Probing physics beyond the standard model: The case of pseudo-Nambu-Goldstone bosons

The observation of HE and VHE $\gamma$-rays offers an opportunity to search for physics beyond the Standard Model (SM) of particle physics, complementary to laboratory experiments. One prominent example is the indirect search for Dark Matter (DM).

[17] Image credits: H.E.S.S.: `http://www.mpi-hd.mpg.de/hfm/HESS/pages/press/2012/HESS_II_first_light/images/Image_18.JPG`; MAGIC telescopes: `http://magic.mppmu.mpg.de/physics/recent/M87-PR/Fig3_left.jpg`; VERITAS: `http://ecuip.lib.uchicago.edu/multiwavelength-astronomy/images/gamma-ray/science/New_Array.jpg`.

**Figure 1.7:** Images of the IACT arrays listed in Table 1.1. From top to bottom: H.E.S.S., MAGIC telescopes, and VERITAS. See footnote in main text for image credits.

Several observations suggest that about 25 % of the total energy density of the Universe are due to non-baryonic matter that only scarcely interacts with SM particles and is mainly traced through its gravitational interactions (see, e.g., Bertone *et al.* 2005, for a review, and Planck Collaboration *et al.* 2013 for a recent value of the DM density including data from the *Planck* satellite). Evidence is derived from, e.g., large-scale structure formation in the Universe, gravitational lensing data of galaxy clusters, and rotation curves of galaxies.

A natural DM candidate is a weakly interacting massive particle (WIMP). Thermally produced in the early Universe, such particles with masses at the TeV scale could naturally account for the observational evidences, their high mass ensuring that they are sufficiently non-relativistic (or cold) in order not to hinder structure

formation. Candidates for such particles are provided by the lightest supersymmetric particle (for a review see, e.g., Jungman *et al.*, 1996) or SM extensions involving extra dimensions such as Kaluza-Klein models (e.g., Hooper & Profumo, 2007, for a review). If WIMPs are self-annihilating, this process will eventually also involve $\gamma$-rays that could be detected with IACTs or the *Fermi*-LAT. Indeed, recently an indication for a $\gamma$-ray line in the vicinity of the Galactic center has been found in *Fermi*-LAT data that can be interpreted as an indication for a WIMP with a mass of $\sim$ 130 GeV (Weniger, 2012). However, an analysis conducted by the *Fermi*-LAT collaboration (Ackermann *et al.*, 2013) resulted in a line feature at 133 GeV with a global significance of $1.6\,\sigma$, only.

Physics beyond the SM has already been confirmed at small mass scales with the detection of neutrino masses (e.g., Strumia & Vissani, 2006, for a review). More generally, extensions of the SM predict additional broken symmetries and consequently the existence of pseudo-Nambu-Goldstone bosons (pNGBs) associated with these broken symmetries (see, e.g., Jaeckel & Ringwald, 2010, for a review). Probably the most extensively studied pNGB is the axion that solves the strong CP problem in quantum chromodynamics (QCD). In general, QCD allows for a term in the Lagrangian that violates the simultaneous charge conjugation and parity transformation (CP),

$$\mathcal{L}_{\mathrm{CP}} = \frac{\alpha_s}{4\pi}\theta\,\mathrm{Tr}\left[G^{\mu\nu}\tilde{G}_{\mu\nu}\right], \tag{1.25}$$

where $\alpha_s$ is the fine structure constant of the strong interactions, $G_{\mu\nu}$ is the gluon field tensor and its dual $\tilde{G}_{\mu\nu} = 1/2\epsilon^{\mu\nu\rho\sigma}G_{\rho\sigma}$, (throughout this Section, natural units will be used, i.e., $\hbar = c = 1$) and $\theta$ is a free parameter expected to be of order unity (see, e.g., Peccei, 2008, for a review). This term would lead to an electric dipole moment of the neutron with a strength $d_n = 10^{-16}|\bar{\theta}|e\,\mathrm{cm}$, where $e$ is the electric charge and $\bar{\theta} = \theta + \arg\det\mathcal{M}$, with $\mathcal{M}$ the quark mass matrix. Current limits on $d_n$ imply that $|\bar{\theta}| \lesssim 10^{-10}$. The smallness of this parameter constitutes an unnatural fine-tuning, also referred to as the strong CP problem. A solution was provided by Peccei & Quinn (1977) by introducing an additional global $U(1)$ symmetry, promoting $\theta$ to the dynamical field connected to it. The field relaxes to zero if the symmetry is spontaneously broken at the scale $f_a$. The broken symmetry gives rise to a pNGB, the axion (Weinberg, 1978; Wilczek, 1978). Its mass is connected to the scale of the symmetry breaking, $m_a = 6\,\mathrm{meV}\,(10^9\,\mathrm{GeV}/f_a)$. Axions couple to photons described with the Lagrangian

$$\mathcal{L}_{a\gamma} = -\frac{1}{4}g_{a\gamma}F^{\mu\nu}\tilde{F}_{\mu\nu}a = g_{a\gamma}\mathbf{E}\cdot\mathbf{B}a, \tag{1.26}$$

with the electromagnetic field tensor $F_{\mu\nu}$ and its dual $\tilde{F}_{\mu\nu}$. The last equality follows from an explicit calculation. The coupling constant is also related to the symmetry

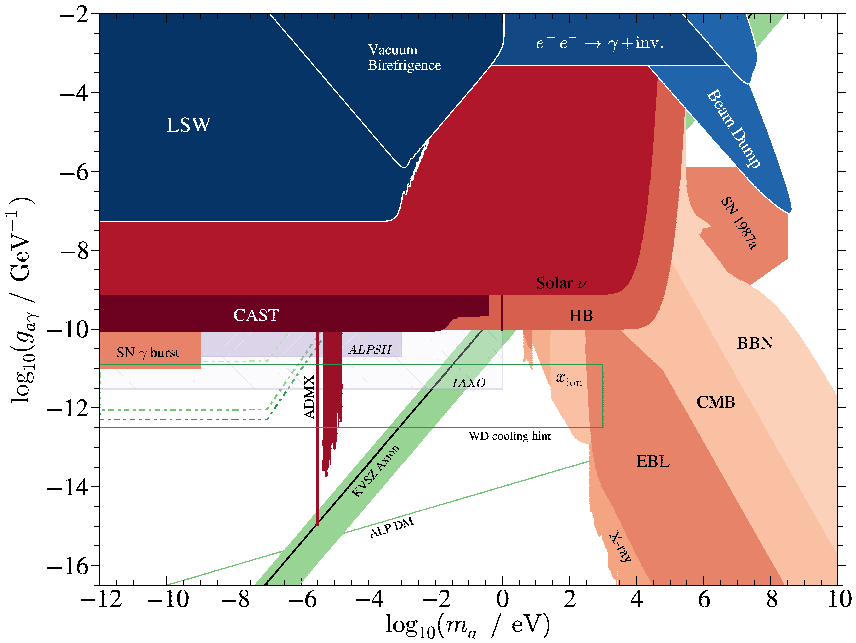


**Figure 1.8:** The ALP parameter space adopted from Hewett *et al.* (2012) with updates from Javier Redondo (private communication). Current bounds from laboratory experiments are shown in blue, limits from astrophysical and cosmological observations in red. Theoretical preferred regions are depicted in green and future experiment sensitivities as purple hatched and cross-hatched regions. See text for details.

breaking scale

$$g_{a\gamma} = \frac{\alpha}{2\pi}\frac{\mathcal{N}}{f_a}, \tag{1.27}$$

with $\mathcal{N}$ a model-dependent factor of the order unity. Thus, for axions, the mass and coupling to photons are related. This is not the case for axion-like particles (ALPs) that share the coupling to photons, but $m_a$ and $g_{a\gamma}$ are independent from each other. Such particles naturally arise in the compactification of string theories (e.g., Cicoli *et al.*, 2012). From the Lagrangian in Eq. (1.26) it is clear that photons can oscillate into ALPs and vice versa in the presence of ambient magnetic fields. As ALPs do not interact with background radiation fields, their flux is not attenuated. The effect on the propagation of VHE $\gamma$-rays will be studied in Chapter 5.

Current exclusions of the photon-ALP coupling are shown in Figure 1.8 in the $(m_a, g_{a\gamma})$ parameter space and are briefly summarized below (following Jaeckel & Ringwald, 2010).

Light-shining-through-a-wall (LSW) experiments shine a laser beam in a magnetic field onto an opaque wall and search for a regenerated signal behind the wall (also

in a magnetic field). The non-detection of a signal with the ALPS experiment (Any Light Particle Search; Ehret *et al.*, 2010) results in the upper bounds on $g_{a\gamma}$, labeled LSW in the Figure. It is also possible to search for a change in the polarization of a laser beam induced by the photon-ALPs oscillations. However, the sensitivity is limited due to quantum-electrodynamical effects that also change the polarization. The results are labeled "vacuum birefringence" in the plot (e.g., Zavattini *et al.*, 2008, for the PVLAS collaboration). For higher masses, one can also search for ALPs in beam dump experiments (e.g., Riordan *et al.*, 1987).

If ALPs existed they should also be produced in stellar interiors (e.g., Raffelt, 1996, 2008, for reviews). The CAST (CERN Axion Solar Telescope) experiment searches for solar ALPs by pointing a magnet towards the sun. Inside the magnet, ALPs could reconvert into photons. No signal has been detected and upper limits on the coupling were derived (Andriamonje *et al.*, 2007). The ALP production in the sun would pose an additional energy loss channel. This would lead to an enhanced production of solar neutrinos and neutrino measurements can be used to constrain this scenario (Gondolo & Raffelt, 2009, exclusion region labeled Solar $\nu$ in Figure 1.8). The extra energy loss also shortens the lifetime of stars that have reached the stage of helium burning, i.e., energy is generated by fusing helium to heavier elements in the core (Raffelt, 2008). Such stars are located on the horizontal branch (HB) in the Hertzsprung-Russell diagram and limits comparable to the CAST bounds can be derived over a broad mass range. The duration of the neutrino burst in the supernova SN1987a can also be used to derive constraints (Raffelt, 2008): The neutrino emission is delayed, since neutrinos are trapped in the neutron star produced in the core collapse supernova, and they escape at timescales of the diffuse energy transport. The emission of ALPs could be the more effective energy loss channel. The burst duration leads to the bounds labeled SN1987a. Limits from the non-observation of a $\gamma$-ray burst of the supernova SN1987a, as well as bounds from magnetic white dwarfs (dashed-dotted lines in Figure 1.8) will be discussed in Chapter 5.

Additionally, cosmological observations can be used to constrain the parameter space. For instance, the neutron to proton ratio, $n/p$, in the Universe depends on the time when the weak interaction $p + e^- \leftrightarrow n + \nu_e$ became ineffective in the primordial plasma and this time depends on the cosmic expansion. The expansion is determined from the total energy density of all particles in the plasma. The more particles, the sooner the above reaction will freeze-out, and thus ALPs would alter the $n/p$ ratio (see Cadamuro & Redondo, 2012, for a detailed discussion). The ratio can be determined by measuring today's helium abundance. The ALP decay into two photons, $a \rightarrow \gamma + \gamma$, has a lifetime of $\tau_a = 64\pi/(g_{a\gamma}^2 m_a^3)$ (e.g., Cadamuro & Redondo, 2012). If it occurs sufficiently early in the primordial plasma, the injected photons thermalize with electrons and positrons which in turn heat the primordial neutrino bath through $e^+ + e^- \rightarrow \nu + \overline{\nu}$. The caused neutrino dilution can have an observable effect, e.g., on the large-scale structure formation. Cadamuro & Redondo (2012) have combined the above arguments with further analyses to derive

the bound labeled BBN (Big Bang Nucleosynthesis). The same authors also investigated the potential impact of the energy injection through ALPs on the black body spectrum of the CMB measured with the FIRAS instrument on-board the COBE satellite (Fixsen *et al.*, 1996). A distortion of the spectrum can only be circumvented if ALPs decay very late or very early. In the latter case, the produced photons could rethermalize and no distortion of the CMB is expected. The derived constraints are labeled CMB in Figure 1.8. The CMB spectrum would also be influenced by resonant photon-ALPs oscillations in the presence of a primordial magnetic field. Limits were derived by Mirizzi *et al.* (2009a), which, however, depend on the unknown primordial field strength. Furthermore, the ALP decay should not overproduce any background radiation field such as the EBL (bounds labeled EBL in the figure are derived by Arias *et al.*, 2012). Neither must it produce line-like features in galactic spectra. Arias *et al.* (2012) used this argument together with X-ray and optical data to exclude regions in the parameter space. Finally, ALP decays could reionize neutral primordial hydrogen. The produced free electrons can scatter the CMB photons and increase the optical depth to CMB photons. Constraints can be derived by comparing the expected optical depth with measurements from WMAP (labeled $x_{\mathrm{ion}}$ in Figure 1.8 referring to the reionization fraction; Cadamuro & Redondo, 2012).

Green regions in Figure 1.8 correspond to theoretically preferred parameters. For the QCD axion, the green band labeled KVSZ shows one specific model for the axion with its order unity model uncertainties (Kim, 1979; Shifman *et al.*, 1980). Moreover, there are indications that an additional cooling mechanism is necessary to explain the observed luminosity function of white dwarfs (WD cooling hint, Isern *et al.*, 2008), see Chapter 5 for a further discussion. Interestingly, ALPs could constitute or add to the DM content of the Universe, provided that the ALP lifetime is longer than the age of the Universe (this excludes the unconstrained region of the parameter space for couplings above the BBN bound for ALP DM). Given that the ALP can have a mass below 1 eV, thermal ALP production would not lead to cold DM, required to explain the large scale structure formation. An alternative approach is the non-thermal production of ALPs via the misalignment mechanism (see, e.g., Preskill *et al.* 1983; Abbott & Sikivie 1983; Dine & Fischler 1983 for QCD axion DM and Arias *et al.* 2012 for general ALP DM). Following Arias *et al.* (2012), the general idea of this mechanism goes as follows: In the early Universe, ALP fields will have an initial random value which is fixed by expansion and evolves on timescales $t \sim m_a^{-1}$. After such time scales, the fields will start to react to their potential, minimizing their potential energy. At this time, $t = t_1$, the field strength is given by $\phi_1 = \theta_1 \mathcal{N}\alpha/(2\pi g_{a\gamma})$ if the dominant interaction is between photons and ALPs, where $\theta_1 = |\phi_1|/f_a$ is the misalignment angle, expected to be of order unity. The coherent oscillations around the minimum have the same equation of state as non-relativistic DM. The resulting DM distribution of ALPs crucially depends on when the breaking of the underlying $U(1)$ symmetry occurs. If it happens before inflation, DM will be distributed homogeneously. Otherwise, substructures will form

that will, however, average to a constant value of the DM density. Alternatively, cosmic ALP strings could form and their decay could also contribute to the DM density (e.g., Sikivie, 2008). Parameters below the line labeled ALP DM in Figure 1.8 correspond to least fine-tuned scenarios in which the ALP mass is independent of time, i.e., not subject to radiative corrections in the primordial plasma. Dark Matter from larger couplings is also possible, especially for large values of $\tilde{N}$ or fine-tuned $\theta_1$ values.

The sensitivities of future experiments (ALPS II, Bähre *et al.* 2013, and the International Axion Observatory, IAXO, Irastorza *et al.* 2011) are shown as purple hatched and cross-hatched regions in Figure 1.8. The ALPS II experiment is an LSW type laboratory experiment that will, at its final stage, use a powerful infrared laser as a photon source, sensitive super-conducting transition edge detectors to measure reconverted photons, ∼100 m long cavities on the production and regeneration side of the wall, and dipole magnets of the HERA experiment. The planned IAXO experiment is in principle an upscaled version of the CAST experiment: It consists of six vacuum bores attached to X-ray optics in a toroidal magnetic field to search for reconverted ALPs produced in the sun.

Given the rich phenomenology of ALPs, it is tantalizing to use HE and VHE $\gamma$-ray observations to search for possible effects in $\gamma$-ray spectra.

**Table 1.2:** Constants and their corresponding values used in this work (e.g., Beringer *et al.*, 2012; Unsöld & Baschek, 2002).

| Symbol | Name | Value |
|---|---|---|
| $c$ | speed of light | $2.99792458 \times 10^{8}$ m s$^{-1}$ |
| $h$ | Planck constant | $6.62606896 \times 10^{-34}$ J s |
| $\hbar \equiv h/(2\pi)$ | reduced Planck constant | $1.054571628 \times 10^{-34}$ J s |
| $e$ | electron charge | $1.602176487 \times 10^{-19}$ C |
| $m_e$ | electron mass | $9.10938215 \times 10^{31}$ kg |
| $G$ | Newtonian gravitational constant | $6.6738 \times 10^{-11}$ m$^3$ kg$^{-1}$ s$^{-2}$ |
| $\sigma_\mathrm{T}$ | Thomson cross section | 0.6652458558 barn<br>$= 0.6652458558 \times 10^{-28}$ m$^2$ |
| $\alpha$ | fine-structure constant | $1/137.035999679$ |
| $k_B$ | Boltzmann constant | $1.3806504 \times 10^{-23}$ J K$^{-1}$ |
| $M_\odot$ | solar mass | $1.989 \times 10^{30}$ kg |
| pc | parsec | $3.0856776 \times 10^{16}$ m |

**Table 1.3:** Abbreviations used throughout this work

| Abbreviation | Meaning |
|---|---|
| HE | high energy |
| VHE | very high energy |
| AGN | active galactic nucleus / nuclei |
| BLR | broad line region |
| GRB | gamma-ray burst |
| SED | spectral energy distribution |
| CMB | cosmic microwave background |
| EBL | extragalactic background light |
| LAT | large area telescope |
| PSF | point spread function |
| IACT | imaging air Cherenkov telescope |
| PPA | pair-production anomaly |
| HOP | high optical depth photon |
| ALP | axion-like particle |
| IGMF | intergalactic magnetic field |
| ICMF | intracluster magnetic field |
| GMF | Galactic magnetic field |

**Table 1.4:** Unit prefixes used in this work.

| Prefix | Name | Value |
|---|---|---|
| $\mu$ | micro | $10^{-6}$ |
| m | milli | $10^{-3}$ |
| c | centi | $10^{-2}$ |
| k | kilo | $10^{3}$ |
| M | mega | $10^{6}$ |
| G | giga | $10^{9}$ |
| T | tera | $10^{12}$ |
| P | peta | $10^{15}$ |

# 2 Upper limits on the extragalactic background light density in the *Fermi* era

High and very high energy $\gamma$-rays undergo pair production with low energy photons from background radiation fields (Nikishov, 1962; Jelley, 1966; Gould & Schréder, 1966, 1967, and Section 1.2). The cross section for this process is strongly peaked so that photons in the wavelength range $0.1\,\mu\text{m} \lesssim \lambda \lesssim 60\,\mu\text{m}$ are mainly responsible for the attenuation of $\gamma$-rays between the energies $100\,\text{GeV} \lesssim E \lesssim 50\,\text{TeV}$ [see Eq. (1.16) and Figure 1.3]. This is the wavelength regime of the extragalactic background light (EBL), the diffuse and isotropic radiation field from ultraviolet to far-infrared wavelengths, see Section 2.1 for a review. Its direct detection is extremely difficult due to prominent foreground emission (Hauser *et al.*, 1998, see below).

The observations of very high energy (VHE; energy $E \gtrsim 100\,\text{GeV}$) $\gamma$-rays from extragalactic sources, mostly active galactic nuclei (AGN), with imaging atmospheric Cherenkov telescopes (IACTs) has opened a new window to constrain the EBL density. If assumptions are made about the properties of the intrinsic spectrum emitted by the source, a comparison with the observed spectrum allows to place upper limits on the EBL intensity (e.g. Stecker *et al.*, 1992). In this context, the spectra of Markarian (Mkn) 501 during an extraordinary flare (Aharonian *et al.*, 1999b) and of the blazar H 1426+482 (Aharonian *et al.*, 2003b) resulted in the first constraints of the EBL density from mid- to far-infrared (MIR and FIR) wavelengths. With the new generation of IACTs, constraints could be derived from a number of spectra. At near-infrared (NIR) wavelengths, the observations 1ES 1101-232 and H 2356-309 (Aharonian *et al.*, 2006a) and 1ES 0229+200 (Aharonian *et al.*, 2007g) were used, and the MAGIC observation of 3C 279 (Albert *et al.*, 2008b) lead to bounds at optical wavelengths. A sample of all at that time known blazars was tested against a large number of different EBL shapes by Mazin & Raue (2007, henceforth MR07) who derived robust constraints over a broad wavelength range, $1\,\mu\text{m} \gtrsim \lambda \gtrsim 80\,\mu\text{m}$. The authors excluded EBL densities that produce VHE spectra, characterized by $\text{d}N/\text{d}E \propto E^{-\Gamma}$, with $\Gamma < \Gamma_{\text{limit}}$ (being $\Gamma_{\text{limit}} = 1.5$ for realistic and $\Gamma_{\text{limit}} = 2/3$ for extreme scenarios) or an exponential pile-up at highest energies.

With the advent of the Large Area Telescope (LAT) on board the *Fermi* satellite (see Section 1.3.1 and Atwood *et al.*, 2009) and its unprecedented sensitivity at high energies (HE, $100\,\mathrm{MeV} \lesssim E \lesssim 100\,\mathrm{GeV}$), further possibilities arose to confine the EBL density. Bounds can be derived either by considering solely *Fermi*-LAT observations of AGN and gamma-ray bursts (Abdo *et al.*, 2010b; Raue, 2010) or by combining HE with VHE spectra (e.g., Georganopoulos *et al.*, 2010; Orr *et al.*, 2011). Recently, the *Fermi*-LAT and H.E.S.S. collaborations published independently the detection of the imprint of the EBL on $\gamma$-ray spectra (Ackermann *et al.*, 2012c; H.E.S.S. Collaboration *et al.*, 2013, respectively). It has also been proposed that the *Fermi*-LAT can, in principle, measure the EBL photons upscattered by electrons in lobes of radio galaxies directly (Georganopoulos *et al.*, 2008). Attenuation limits can also be estimated by modeling the entire spectral energy distribution (SED) of blazars in order to forecast the intrinsic VHE emission (Krawczynski *et al.*, 2002; Mankuzhiyil *et al.*, 2010).

In this Chapter, results from the *Fermi* two year source catalog (Nolan *et al.*, 2012, henceforth 2FGL) together with a comprehensive sample of VHE spectra are used to place upper limits on the EBL density, incorporating the evolution of the EBL with redshift and the formation of electromagnetic cascades. The approach relies on minimal assumptions about the intrinsic spectra. The VHE sample is composed of spectra measured with different IACTs, thereby ensuring that the results are not influenced by the possible systematic bias of an individual instrument or observation.

After shortly reviewing the sources, measurements, and models of the EBL (based on the reviews of Hauser & Dwek, 2001; Kashlinsky, 2005; Dwek & Krennrich, 2013), the calculations for the absorption correction of observed VHE $\gamma$-ray spectra with model-independent EBL shapes are presented in Section 2.2. The resulting intrinsic spectra are subsequently described with analytical functions. Section 2.3 outlines in detail the different approaches to constrain the EBL before the selection of VHE spectra is addressed in Section 2.4. The combination of VHE and HE spectra of variable sources will also be discussed. The results are presented in Section 2.5. Throughout this Chapter a standard $\Lambda$CDM cosmology is assumed with $\Omega_m = 0.3$, $\Omega_\Lambda = 0.7$, and $h = 0.72$ (see Section 1.2). The calculations and results presented here have been published in Meyer *et al.* (2012b).

## 2.1 The extragalactic background light

Starlight integrated over all epochs and starlight emission reprocessed by interstellar dust constitute the main contributions to the EBL. These two distinct components lead to two maxima in the SED of the EBL, the first at $\sim 1\,\mu$m (starlight) and the second at $\sim 100\,\mu$m (dust), see Figure 2.1. Narrow spectral features like absorption lines are smeared out in the integration over redshift, leading to a smooth shape

of the EBL at $z = 0$. Further contributions may come from diffuse emission from galaxy clusters (Chelouche *et al.*, 2007), unresolved AGN (Matute *et al.*, 2006), the first (Population III) stars (e.g., Raue *et al.*, 2009), or exotic sources like Dark Matter powered stars in the early universe (Maurer *et al.*, 2012). This renders the EBL an important probe of the formation and evolution of stars, the history of dust formation and distribution in galaxies, as well as the metal production with cosmic time. Its frequency weighted spectral intensity at redshift $z$ and observed frequency $\nu$ is given by an integration over the luminosity density $\mathcal{L}_\nu$ of all contributing sources up to a maximal redshift $z_{\mathrm{max}}$ at which star formation started (Peebles, 1993)

$$\nu I_\nu(z) = \nu \frac{c}{4\pi} \int_z^{z_{\mathrm{max}}} \mathcal{L}_{\nu'}(z') \left| \frac{\mathrm{d}t'}{\mathrm{d}z'} \right| \mathrm{d}z', \tag{2.1}$$

with $\nu' = \nu(1 + z')/(1 + z)$. The EBL is, furthermore, connected to several other cosmological backgrounds: The cosmic X-ray background is mainly due to dust obscured AGN (Mushotzky *et al.*, 2000). The heated dust radiates predominantly at MIR wavelengths contributing to the EBL (e.g., Franceschini *et al.*, 2002). Star-forming regions show a correlation between radio and IR emission due to massive stars that, on the one hand, heat the interstellar medium to produce thermal IR radiation, and on the other hand, end their lives in core-collapse supernovae and the remnants are sources of radio synchrotron emission (e.g., Helou *et al.*, 1985). This connects the EBL with the cosmic radio background (e.g., Dwek & Barker, 2002). At the same time, the energy release in core-collapse supernovae is mostly in form of neutrinos. Thus, the EBL can also be used to probe the cosmic neutrino background (Horiuchi *et al.*, 2009).

Direct detections of the EBL are technically challenging since a precise absolute calibration of the instrument is necessary, and any emission from the instrument components and the Earth's atmosphere has to be eliminated. Furthermore, direct measurements are severely impeded (especially in the infrared) by prominent foreground sources such as sunlight scattered, absorbed, and reradiated by interplanetary dust (zodiacal light) and emission from stars and the interstellar medium (Hauser *et al.*, 1998). These foreground sources have to be carefully subtracted and often only upper limits are given instead of direct measurements. A compilation of data points is shown in Figure 2.1 in which the two maxima of the SED are visible.

The EBL density can also be probed with integrated galaxy number counts as done with, e.g., the *Hubble Space Telescope* in the optical (Madau & Pozzetti, 2000) and the *Spitzer* telescope in the infrared (Fazio *et al.*, 2004) [the data points are also shown in Figure 2.1]. Even in these deep surveys that have reached convergence[1],

[1] Convergence is a necessary condition for integrated galaxy number counts, meaning that the slope $\alpha$ of galaxy counts per unit flux $S$, $\mathrm{d}N/\mathrm{d}S \propto S^{-\alpha}$ is larger than 2, ensuring that the integral $\int S^2(\mathrm{d}N/\mathrm{d}S)\mathrm{d}S$ is finite (e.g., Dwek & Krennrich, 2013).

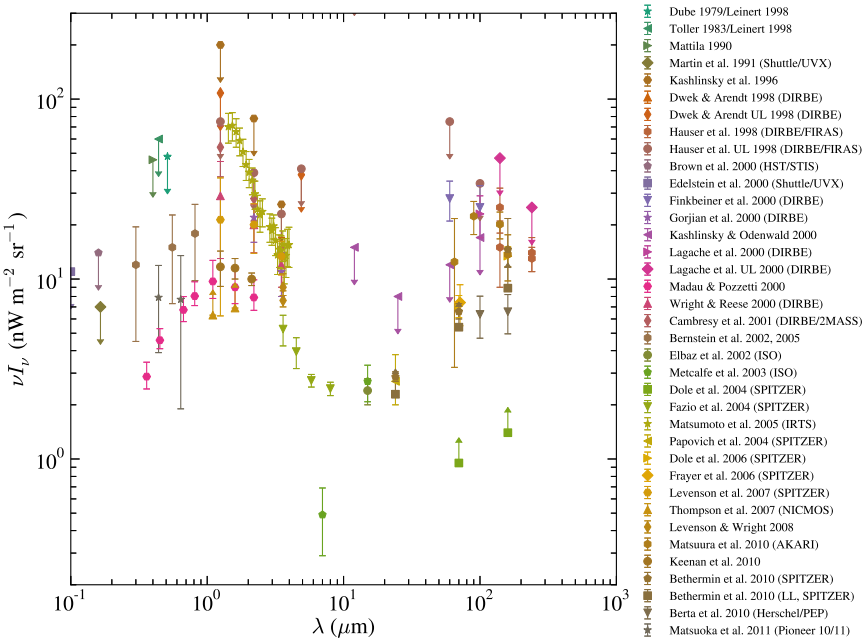


**Figure 2.1:** Limits on and measurements of the EBL density. Figure and references adapted from Mazin & Raue (2007) and Raue & Mazin (2011).

it is not guaranteed that all faint sources are resolved. Furthermore, truly diffuse emission that might contribute to the overall EBL density cannot be accounted for by this method. Thus, the cumulative brightness of galaxies is a firm lower limit on the EBL density.

In the future, the *James Webb Space Telescope* (JWST, Gardner *et al.*, 2006) with a planned launch date in 2018 will make important contributions to the understanding of the EBL. It will be equipped with a 6.5 m mirror and science instruments primarily sensitive at NIR wavelengths [Near Infrared Camera (NIRCam) sensitive between 0.6 $\mu$m and 5 $\mu$m and Mid-Infrared Instrument (MIRI) between 5 $\mu$m and 28 $\mu$m]. Moreover, the spectroscopy of solar absorption lines of zodiacal light can improve the subtraction of this foreground emission (Kutyrev *et al.*, 2008).

Several authors have modeled the EBL in the past with different approaches that can roughly be divided into backward evolution (BE), forward evolution (FE), cosmic chemical evolution (CE), and semi-analytical (SA) models (e.g., Dwek & Krennrich, 2013): In BE models, one fits the present luminosity density $\mathcal{L}_\nu(z = 0)$ to observations of galaxies in the local universe and evolves this quantity backwards in time using different prescriptions for the different galaxy morphologies. Recent versions are given in, e.g., Franceschini *et al.* (2008) and Domínguez *et al.* (2011). Forward evolution models, on the other hand, use numerical codes for the stellar

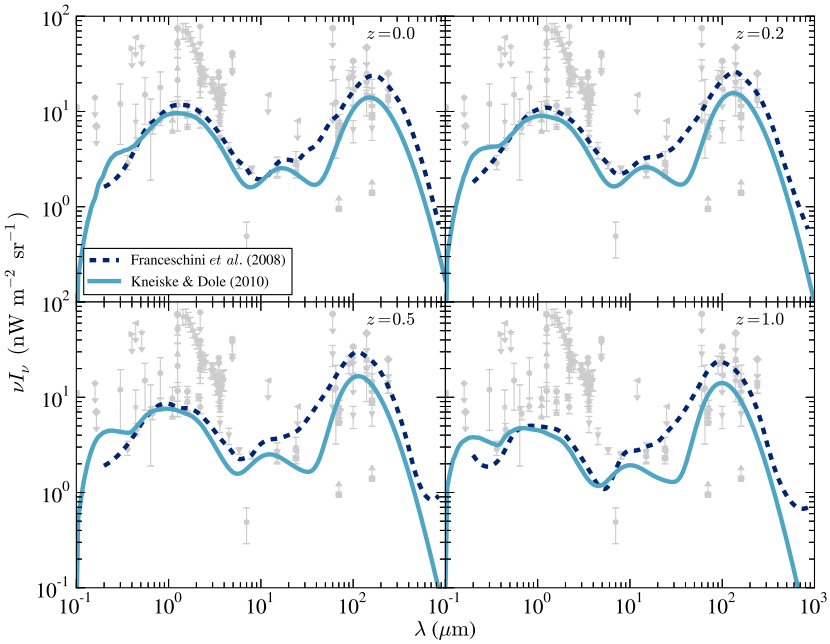


**FIGURE 2.2:** EBL model predictions for the FE model of Kneiske & Dole (2010) and the BE model of Franceschini *et al.* (2008) for different redshifts. For orientation, the data points (for $z = 0$) presented in Figure 2.1 are shown in gray.

evolution and take the cosmic star formation rate, the stellar initial mass function (the number of stars per unit mass interval collectively born in one event; Kroupa *et al.*, 2011) and a simple stellar population as input parameters. Furthermore, these models need to incorporate the absorption and reemission of starlight by dust, which depends on the dust composition and size distribution, its scattering and absorption properties, its relative spatial distributions, etc. (e.g., Hauser & Dwek, 2001). The input parameters are tuned to reproduce observations. Examples of these models are provided by, e.g., Razzaque *et al.* (2009); Finke *et al.* (2010); and Kneiske & Dole (2010, based on Kneiske *et al.* 2002) who fitted their model to the lower limits from galaxy number counts to provide a model of guaranteed attenuation of VHE $\gamma$-rays. In CE models, chemical evolution equations are used to self-consistently describe average stellar, gaseous, and radiative contents of galaxies and their evolution (see Pei *et al.*, 1999, for an example of a CE model). The most ambitious approach is given by SA models that use structure-formation frameworks to predict the formation and evolution of galaxies and the EBL (e.g., Somerville *et al.*, 2012; Gilmore *et al.*, 2012; Inoue *et al.*, 2012, for recent model versions). These models depend on a large number of parameters and processes and hence require large amount of

input data. As examples, the predictions for the EBL SED at different redshifts in two model frameworks are shown in Figure 2.2.

## 2.2 Absorption correction of VHE $\gamma$-ray spectra for generic EBL densities

The intrinsic energy spectrum $\mathrm{d}N_{\mathrm{int}}/\mathrm{d}E$ of a source at redshift $z_0$ at the measured energy $E$ differs from the observed spectrum $\mathrm{d}N_{\mathrm{obs}}/\mathrm{d}E$ due to the interaction of source photons with the photons of the EBL which is most commonly expressed as

$$\frac{\mathrm{d}N_{\mathrm{obs}}}{\mathrm{d}E} = \frac{\mathrm{d}N_{\mathrm{int}}}{\mathrm{d}E} \times \exp\left[-\tau_{\gamma\gamma}(E, z_0)\right]. \tag{2.2}$$

The strength of the attenuation is given by the optical depth $\tau_{\gamma\gamma}$ defined in Eq. (1.10) with $n_\epsilon(\epsilon, z)$ the comoving EBL photon number density in the energy interval $[\epsilon, \epsilon + \mathrm{d}\epsilon]$. It is connected with the EBL SED through the relation $\epsilon^2 n_\epsilon(\epsilon, z) = (4\pi/c)\nu I_\nu(z)$. The comoving EBL photon density is described here by splines (MR07):

$$\nu I_\nu = \sum_{i=0}^{k} w_i s_{i,p}(\epsilon), \tag{2.3}$$

with the B-Splines $s_{i,p}$ (de Boor, 1978),

$$s_{i,0}(\epsilon) = \begin{cases} 1 & \epsilon_i \le \epsilon < \epsilon_{i+1} \text{ and } \epsilon_i < \epsilon_{i+1}, \\ 0 & \text{otherwise,} \end{cases} \tag{2.4}$$

$$s_{i,p}(\epsilon) = \frac{\epsilon - \epsilon_i}{\epsilon_{i+1} - \epsilon_i} s_{i,p-1}(\epsilon) + \frac{\epsilon_{i+p+1} - \epsilon}{\epsilon_{i+p+1} - \epsilon_{i+p}} s_{i+1,p-1}(\epsilon), \tag{2.5}$$

and the order $p = 2$. This ensures independence of EBL model assumptions and allows for a great variety of EBL shapes to be tested. The usage of splines drastically reduces the effort to numerically compute the complete threefold integral of Eq. (1.10) as shown in MR07. Each spline is defined by a set of $k$ knot points $\epsilon_i = hc/\lambda_i$, $i = 0, \ldots, k$, and weights $w_i$ from a grid in the ($\lambda$,$\nu I_\nu$)-plane. The grid is bound by a minimum and a maximum shape, shown in Figure 2.3. The setup of grid points is taken from MR07. The minimum tested shape is set to reproduce the lower limits from the galaxy number counts from *Spitzer* (Fazio *et al.*, 2004), while the maximum shape roughly follows the upper limits derived from measurements. To reduce the computational costs, the extreme cases considered by MR07 of the EBL density in the optical and near-infrared (NIR) are not tested. With current VHE spectra the EBL intensity is only testable up to a wavelength $\lambda \approx 100\,\mu$m, so no additional grid points beyond this wavelength are used. In total, this range of knots and weights allows for 1,920,000 different EBL shapes. A much smaller

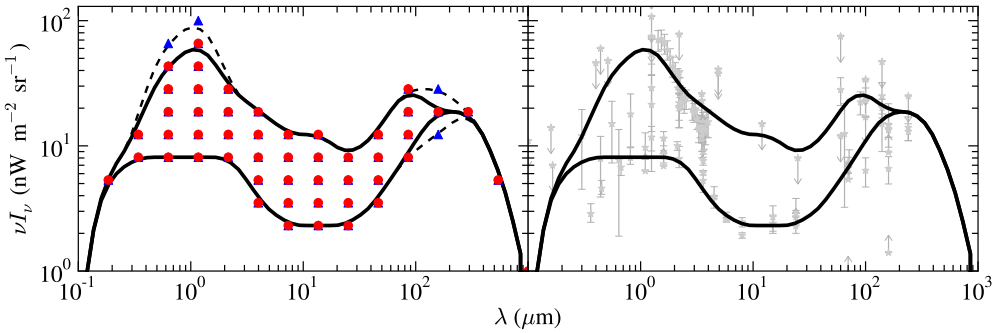


**FIGURE 2.3:** Left panel: Grid in wavelength versus the energy density of the EBL used to construct the EBL shapes for testing (red bullets). Also shown are the minimum and maximum shape tested (solid lines) and the same for the grid of MR07 (blue triangles; dashed lines). Right panel: Minimum and maximum EBL shape tested versus EBL limits and measurements (gray symbols, see Figure 2.1).

spacing of the grid points is not meaningful as small structures are smeared out in the calculation of $\tau_{\gamma\gamma}$ and the EBL can be understood as a superposition of black bodies that are not arbitrarily narrow in wavelength (MR07; Raue, 2007).

In most previous studies, no EBL evolution with redshift is assumed when computing EBL upper limits using VHE $\gamma$-ray observations. Neglecting the evolution leads to an overestimation of the optical depth between 10 % ($z = 0.2$) and 35 % ($z = 0.5$) (Raue & Mazin, 2008) and too rigid upper limits (see Section 2.5). Without evolution, the effective cosmological photon number density is connected with the EBL density of Eq. (2.3) through (Franceschini *et al.*, 2008)

$$n_\epsilon(\epsilon, z) = \frac{4\pi}{c\epsilon^2}(1+z)^2 \nu I_\nu(\epsilon = h\nu). \tag{2.6}$$

In this study, the evolution is accounted for by a phenomenological ansatz (e.g., Raue & Mazin, 2008), i.e., the scaling $(1+z)^2$ is changed to $(1+z)^{2-f_{\rm evo}}$. For a value of $f_{\rm evo} = 1.2$ a good agreement is found between this simplified approach and complete EBL model calculations for redshifts $z \lesssim 0.7$ (Raue & Mazin, 2008). Generally, including the redshift evolution of the EBL decreases the attenuation compared to the no-evolution case and, therefore, weaker EBL limits are expected.

The intrinsic $\gamma$-ray spectrum for a given EBL shape and measured spectrum is reconstructed by solving Eq. (2.2) for $\mathrm{d}N_{\rm int}/\mathrm{d}E$. For a spectrum with $n$ energy bins the relation reads

$$\left(\frac{\mathrm{d}N_{\rm int}}{\mathrm{d}E}\right)_i = \left(\frac{\mathrm{d}N_{\rm obs}}{\mathrm{d}E}\right)_i \times \exp\left[\tau_{\gamma\gamma}(E_i, z_0)\right], \quad i = 1, \ldots, n, \tag{2.7}$$

**Table 2.1:** Comparison between the optical depth at the logarithmic bin center of the highest energy bin and the averaged value over the bin width. The HEGRA spectrum is used for Mkn 501 (see Table 2.3 for the references).

| Source | Minimum EBL shape tested | | | Maximum EBL shape tested | | |
|---|---|---|---|---|---|---|
| | $\tau_{\gamma\gamma}$ | $\langle\tau_{\gamma\gamma}\rangle$ | $\langle\tau_{\gamma\gamma}\rangle/\tau_{\gamma\gamma}$ | $\tau_{\gamma\gamma}$ | $\langle\tau_{\gamma\gamma}\rangle$ | $\langle\tau_{\gamma\gamma}\rangle/\tau_{\gamma\gamma}$ |
| 3C 279 | 3.48 | 3.34 | 0.96 | 18.33 | 17.61 | 0.96 |
| H 1426+428 | 2.54 | 2.53 | 0.99 | 12.61 | 12.48 | 0.99 |
| 1ES 1101-232 | 2.69 | 2.68 | 1.00 | 13.62 | 13.57 | 1.00 |
| Mkn 501 | 3.27 | 3.21 | 0.98 | 11.86 | 11.67 | 0.98 |

where the energy of the logarithmic bin center is denoted by $E_i$. A systematic error is introduced by using $\tau_{\gamma\gamma}$ calculated for the energy at the bin center, since the attenuation can change dramatically within relatively wide energy bins and the mean attenuation actually depends on the intrinsic spectral shape in the energy bin (Stecker & Scully, 2009). The introduced error is studied by comparing $\tau_{\gamma\gamma}$ with an averaged value of the optical depth over the highest energy bin for the spectra that are attenuated most. These spectra are described with an analytical function $f(E)$ (a power or broken power law, cf. Table 2.2) and the averaged optical depth $\langle\tau_{\gamma\gamma}\rangle$ is found to be

$$\langle\tau_{\gamma\gamma}\rangle = \frac{\int\limits_{\Delta E} \tau_{\gamma\gamma}(E,z)\, f(E)\,\mathrm{d}E}{\int\limits_{\Delta E} f(E)\,\mathrm{d}E}. \tag{2.8}$$

The results are summarized in Table 2.1. The ratios $\langle\tau_{\gamma\gamma}\rangle/\tau_{\gamma\gamma}$ are close to, but always smaller than, one and the optical depth is overestimated by $< 5\,\%$. Thus, the simplified approach adds marginally to the uncertainties of the upper limits.

The intrinsic spectra will be described by analytical functions in order to test the fit parameters for their physical feasibility. The parameters are determined by fitting a series of functions listed in Table 2.2. A $\chi^2$-minimization algorithm (utilizing the MINUIT package routines for `python`, see James, 1998) is employed, starting with the first function of the table, a simple power law. The fit is not considered valid if the corresponding probability is $p_{\mathrm{fit}}(\chi^2) < 0.05$. In this case the next function with a larger number of model parameters $m$ from Table 2.2 is evaluated. For a given energy spectrum of $n$ data points, only functions are examined with $n - m - 1 > 0$. If more than one fit results in an acceptable fit probability, an $F$-Test is used to determine the preferred hypothesis (e.g., Brandt, 1999). The parameters of the model with more fit parameters are examined if the test results in a 95 % probability that the description of the data has improved.

**TABLE 2.2:** Analytical functions fitted to the deabsorbed spectra.

| Description | Name | Formula $\mathrm{d}N_{\mathrm{int}}/\mathrm{d}E$ | $m$ |
|---|---|---|---|
| Power law | PL | $PL_1$ | 2 |
| Broken power law with transition region | BPL | $PL_1 \times CPL_{12}$ | 4 |
| Broken power law with transition region and super-exponential pile-up | SEBPL | $PL_1 \times CPL_{12} \times Pile$ | 6 |
| Double broken power law with transition region | DBPL | $PL_1 \times CPL_{12} \times CPL_{23}$ | 6 |
| Double broken power law with super-exponential pile-up | SEDBPL | $PL_1 \times CPL_{12} \times CPL_{23} \times Pile$ | 8 |

*Notes:* The functions (with $m$ free fit parameters) are a power law, a curved power law and a super-exponential pile-up defined as

$$PL_i = N_0\, E^{-\Gamma_i},\ CPL_{ij} = \left[1 + \left(E/E_i^{\mathrm{break}}\right)^{f_i}\right]^{(\Gamma_i-\Gamma_j)/f_i},\ Pile = \exp\left[\left(E/E_{\mathrm{pile}}\right)^{\beta}\right],$$

respectively, where all energies are normalized to 1 TeV. The smoothness parameters $f_i$ are held constant and the break energies $E_i^{\mathrm{break}}$ are forced to be positive. Only positive pile-up, i.e. $E_{\mathrm{pile}} > 0$, is tested.

## 2.3 Exclusion criteria for the EBL shapes

In the following, arguments to exclude EBL shapes will be presented. While the first criteria are based on the expected concavity of the intrinsic VHE spectra, the second set of criteria relies on the integral of the intrinsic VHE emission.

### 2.3.1 Concavity

Observations have led to the commonly accepted picture that particles are accelerated in jets of AGN thereby producing non-thermal radiation. As discussed in Chapter 1, the HE and VHE emission of blazars can be explained within leptonic or hadronic emission scenarios which commonly describe the measured data satisfactorily. These models neither predict a spectral hardening in the transition from HE to VHE nor one within the VHE band[2]. This is also confirmed by observations of nearby sources. On the contrary, the spectral slope is thought to become softer

[2] A spectral hardening is to be understood as a decreasing power-law index with increasing energy.

with energy, due to a possible cut-off in the spectrum of accelerated particles and Klein-Nishina effects in leptonic scenarios.
However, in more specific scenarios a spectral hardening is possible. If mechanisms like, e.g., second order inverse Compton (IC) scattering (Bloom & Marscher, 1996), internal photon absorption (Aharonian *et al.*, 2008f), comptonization of low frequency radiation by a cold ultrarelativistic wind of particles (Aharonian *et al.*, 2002b), or multiple HE and VHE $\gamma$-ray emitting regions in the source (Lefa *et al.*, 2011b) contribute significantly to the overall spectrum, convex curvature or an exponential pile-up can indeed occur. Nevertheless, none of these features has been observed with certainty at VHE in nearby sources where EBL absorption is negligible. Furthermore, it would imply serious fine-tuning if such components appeared in all examined sources in the transition from the optical thin, i.e. $\tau_{\gamma\gamma} < 1$, to optical thick regime, $\tau_{\gamma\gamma} \geq 1$. This seems unlikely, considering the large number of EBL shapes tested. Consequently, EBL shapes leading to an intrinsic VHE spectrum which is not concave will be excluded. This expectation is formulated through three test criteria:

*Fermi*-LAT SPECTRUM AS AN UPPER LIMIT. With the launch of the *Fermi* satellite and the current generation of IACTs, there is an increasing number of broad-band AGN energy spectra measured in the HE and VHE domains. Thus, the least model dependent approach is to test spectra against a convex curvature in the transition from HE to VHE by regarding the spectral index measured by *Fermi*, $\Gamma_{\mathrm{HE}}$, as a limit on the reconstructed intrinsic index at VHE, $\Gamma$. Hence, the intrinsic VHE spectrum is regarded as unphysical if the following condition is met,

$$\Gamma + \sigma_{\mathrm{stat}} + \sigma_{\mathrm{sys}} < \Gamma_{\mathrm{HE}} - \sigma_{\mathrm{HE,\ stat}}. \tag{2.9}$$

The statistical error $\sigma_{\mathrm{stat}}$ is estimated from the fit of an analytical function to the intrinsic spectrum whereas the systematic uncertainty $\sigma_{\mathrm{sys}}$ is used that is estimated by the respective instrumental team. The statistical uncertainty $\sigma_{\mathrm{HE,\ stat}}$ of the *Fermi*-LAT spectral index is given by the 2FGL or the corresponding publication, see Section 2.4. This exclusion criterion will be referred to as *VHE-HEIndex* criterion in the following. Note that this is *not* the same criterion as used by Orr *et al.* (2011). They assume that the VHE index should be *equal* to the index measured with the *Fermi*-LAT.

SUPER-EXPONENTIAL PILE-UP. Furthermore, shapes will be excluded that lead to an intrinsic VHE spectrum that piles up super-exponentially at highest energies. This is the case if it is best described by the analytical functions abbreviated SEBPL or SEDBPL, see Table 2.2, and the pile-up energy is positive within a $1\sigma$ confidence,

$$E_{\mathrm{pile}} - \sigma_{\mathrm{pile}} > 0. \tag{2.10}$$

This additional independent exclusion criterion relies solely on VHE observations which are subject to attenuation in contrast to *Fermi*-LAT observations. It will be denoted as *PileUp* criterion.

VHE CONCAVITY. In the case that the intrinsic spectrum is best described by either a BPL or a DBPL, it is considered as convex if the following inequalities are *not* fulfilled,

$$\begin{aligned} & \Gamma_1 - \sigma_1 \leqslant \Gamma_2 + \sigma_2 \\ \textit{and} \quad & \Gamma_2 - \sigma_2 \leqslant \Gamma_3 + \sigma_3 \text{ (DBPL)}, \end{aligned} \tag{2.11}$$

and the corresponding EBL shape will be rejected. Again, $1\sigma$ uncertainties of the fitting procedure are used. This criterion will be referred to as *VHEConcavity*. It is very similar to the *PileUp* argument formulated above, as intrinsic spectra that show an exponential rise may often be equally well described by a BPL or DBPL. However, with the *VHEConcavity* criterion, also intrinsic spectra can be excluded that show only mild convexity.

### 2.3.2 CASCADE EMISSION AND ENERGY BUDGET

In this Section, two new approaches are introduced that are based on the integrated intrinsic emission. These methods rely on a number of parameters, whose values are so far not accurately determined by observations or for which only upper and lower limits exist. Therefore, the following two criteria have to be regarded as a theoretically motivated possibility to constrain the EBL in the future. As it will be shown in Section 2.5, the final upper limits are not improved by these criteria and are, thus, independent of the model parameters chosen here.

CASCADE EMISSION. EBL photons that interact with VHE $\gamma$-rays produce $e^+e^-$ pairs which can in turn upscatter cosmic microwave background (CMB) photons and initiate an electromagnetic cascade (see Section 1.2.1). The cascade emission has been used to place lower limits on the intergalactic field, $B_{\rm IGMF}$, and its correlation length, $\lambda^c_{\rm IGMF}$, under the assumption of a certain EBL model, since the radiation that reaches Earth depends on the deflection of the $e^+e^-$ pairs in the ambient magnetic field (Neronov & Vovk, 2010; Tavecchio *et al.*, 2010, 2011a; Dermer *et al.*, 2011; Dolag *et al.*, 2011; Taylor *et al.*, 2011; Huan *et al.*, 2011). Conversely, one can place upper limits on the EBL density under the assumption of a certain magnetic field strength. This novel approach is followed here, whereas, in previous studies, the cascade emission is neglected when deriving upper limits on the EBL density. A higher EBL density leads to a higher production rate of $e^+e^-$ pairs and to a higher cascade emission that is potentially detectable with the *Fermi*-LAT. If the predicted cascade emission exceeds the observations of the *Fermi*-LAT, the corresponding

EBL shape can be excluded. Conservative upper limits are derived if the following assumptions are made: (i) The HE emission of the source is entirely due to the cascade. (ii) The observed VHE spectrum is fitted with a power law with a super-exponential cut-off at the highest measured energy of the spectrum. This minimizes the reprocessed emission and allows to consider only the first generation of the cascade. (iii) The $e^+e^-$ pairs are isotropized in the intergalactic magnetic field, minimizing the reprocessed emission. This condition is equal to the demand that the deflection angle $\vartheta$ of the particles in the magnetic field is $\approx \pi$. Assuming $\lambda^c_{\mathrm{IGMF}} \gg ct_{\mathrm{IC}}$, with $t_{\mathrm{IC}} = |\dot{\gamma}|^{-1}$ the cooling time of the pairs for IC scattering [see Eq. (1.6)], the deflection angle for electrons with an energy $\gamma mc^2 \approx E/2$, where $E$ is the energy of the primary $\gamma$-ray, can be approximated by (Tavecchio *et al.*, 2010; Neronov & Vovk, 2010)

$$\vartheta \approx \frac{ct_{\mathrm{IC}}}{R_{\mathrm{L}}} = 1.17 \left(\frac{B_{\mathrm{IGMF}}}{10^{-15}\,\mathrm{G}}\right)(1+z_r)^{-4}\left(\frac{\gamma}{10^6}\right)^{-2}, \tag{2.12}$$

with $z_r$ the redshift where the IC scattering occurs and $R_{\mathrm{L}}$ the Larmor radius. The IC scattered $e^+e^-$ pairs give rise to $\gamma$-rays with energy

$$\epsilon \approx \gamma^2 h\nu_{\mathrm{CMB}} \approx 0.63(E/\mathrm{TeV})^2\,\mathrm{GeV}, \tag{2.13}$$

with $h\nu_{\mathrm{CMB}} = 634\,\mu\mathrm{eV}$ the peak energy of the CMB [cf. Eq. (1.7)]. The $\gamma$ factor in Eq. (2.12) can be eliminated in favor of $\epsilon$, and, solving for $B_{\mathrm{IGMF}}$, the pairs are isotropized if

$$B_{\mathrm{IGMF}} \approx 4.2 \times 10^{-15}\,(1+z_r)^4(\epsilon/\mathrm{GeV})\,\mathrm{G} \approx 5 \times 10^{-13}\,\mathrm{G} \tag{2.14}$$

for $\epsilon = 100\,\mathrm{GeV}$, the maximum energy measured with the *Fermi*-LAT considered here and the maximum redshift where the IC scattering can occur, i.e., the redshift of the source[3]. This value of $B_{\mathrm{IGMF}}$ is in accordance with all experimental bounds (see, e.g., Neronov & Semikoz, 2009, especially Figures 1 and 2). For correlation lengths $\lambda^c_{\mathrm{IGMF}} \gg ct_{\mathrm{IC}} \approx 0.65(E/\mathrm{TeV})^{-1}(1+z_r)^{-4}\,\mathrm{Mpc} \approx O(\mathrm{Mpc})$ the most stringent constraints come from Faraday rotation measurements (Kronberg & Simard-Normandin, 1976; Blasi *et al.*, 1999) which limit $B_{\mathrm{IGMF}} \lesssim 10^{-9}\,\mathrm{G}$. Furthermore, the adopted value cannot be excluded neither with possible observations of deflections of ultra-high energy cosmic rays (Lee *et al.*, 1995) nor with constrained simulations of magnetic fields in galaxy clusters, both setting an upper limit on $B_{\mathrm{IGMF}} \lesssim 10^{-12}\,\mathrm{G}$ (Dolag *et al.*, 2005; Donnert *et al.*, 2009).

For this value of $B_{\mathrm{IGMF}}$, the cascade emission is detectable if a steady $\gamma$-ray emission of the source for the last $\Delta t \approx 10^6$ years is assumed (Dermer *et al.*, 2011; Tavecchio *et al.*, 2011a). Other energy loss channels apart from IC scattering like synchrotron radiation or plasma instabilities (Broderick *et al.*, 2012; Schlickeiser *et al.*, 2012, see also the discussion in Section 4.1) are neglected. However, if the latter are present,

[3] Accordingly, this $B$-field value ensures isotropy regardless were the IC scattering occurs.

the field strength is even higher, or the lifetime of the VHE source is shorter, no significant cascade emission is produced or it has not reached Earth so far.
The flux of the cascade emission, $F_\epsilon(\epsilon)$, is calculated with Eq. (1.19) following Tavecchio *et al.* (2011a) and Dermer *et al.* (2011). For isotropy, the observed cascade emission has to be further modified with the solid angle $\Omega_c \approx \pi\theta^2_{\rm cone}$ into which the intrinsic blazar emission is collimated, where $\theta_{\rm cone}$ is the semi-aperture of the irradiated cone. For blazars one has $\theta_{\rm cone} \sim 1/\Gamma_{\rm L}$ where $\Gamma_{\rm L}$ is the bulk Lorentz factor of the plasma of the jet. The observed emission is then found to be (Tavecchio *et al.*, 2011a)

$$F_{\epsilon,\rm obs}(\epsilon) = 2\frac{\Omega_c}{4\pi}F_\epsilon(\epsilon), \tag{2.15}$$

where the factor of 2 accounts for the contribution of both jets in the isotropic case. The exclusion criterion for an EBL shape at the $2\sigma$ level reads

$$F_{\epsilon,\rm obs}(\epsilon_{\rm meas}) > F_{\epsilon,\rm meas} + 2\sigma_{\rm meas}, \tag{2.16}$$

where $\epsilon_{\rm meas}$, $F_{\epsilon\rm meas}$, $\sigma_{\rm meas}$ are the measured energy, flux, and statistical uncertainty reported in the 2FGL, respectively. In the case that the source is not detected, $F_{\rm meas} = 0$, and $\sigma_{\rm meas}$ represents the $1\,\sigma$ upper limit on the flux. As an example, Figure 2.4 shows the observed and intrinsic VHE spectrum for a specific EBL shape of the blazar 1ES 0229+200 together with the *Fermi* upper limits (Tavecchio *et al.*, 2010). The different model curves demonstrate the degeneracy between the different parameters entering the calculation. The EBL shape used to calculate the intrinsic VHE spectrum is not excluded in the isotropic case since the emission does not overproduce the *Fermi* upper limits. This is contrary to the case of $B_{\rm IGMF} = 10^{-20}$ G and $\Delta t = 3$ years where the predicted cascade flux exceeds the *Fermi*-LAT upper limits in the 1–10 GeV range. Only the isotropic case is assumed in the following, i.e., $B_{\rm IGMF} = 5 \times 10^{-13}$ G in order to obtain conservative upper limits on the EBL. This implies that the source has to be steady for a lifetime of $\Delta t \gtrsim 10^6$ years. Furthermore, a Lorentz factor of $\Gamma_{\rm L} = 10$ is generically assumed for all sources.

Total energy budget. The jets of AGN, the production sites for HE and VHE emission, are powered by the accretion of matter onto a central black hole (see Section 1.1). If the radiation escapes isotropically from the black hole, the balancing of the gravitational and radiation force leads to the maximum possible luminosity due to accretion, the Eddington luminosity, (e.g., Dermer & Menon, 2009)

$$L_{\rm edd}(M_\bullet) \approx 1.26 \times 10^{38}\ \frac{M_\bullet}{M_\odot}\ \text{ergs s}^{-1}, \tag{2.17}$$

where $M_\bullet$ is the black-hole mass normalized to the mass of the sun, $M_\odot$. Assuming that the total emission of an AGN is not super-Eddington, the Eddington luminosity is the maximum power available for the two jets, $P_{\rm jet} \leq L_{\rm edd}/2$. The jet power

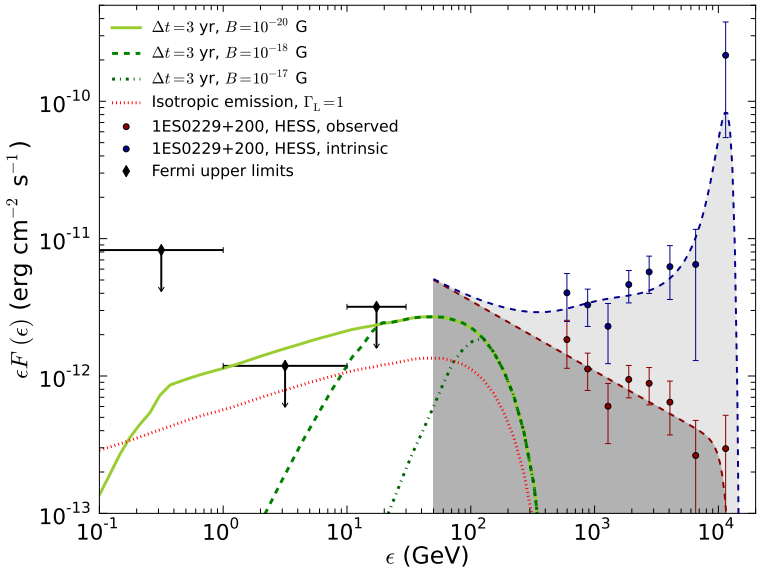


**Figure 2.4:** Cascade emission for a certain EBL shape and the VHE spectrum of 1ES 0229+200 (Aharonian *et al.*, 2007g). The observed spectrum (dark red points and line) is fitted with a power law with an exponential cut-off and corrected for the EBL absorption (dark blue dashed line and points). The green lines show the cascade emission resulting from the reprocessed flux (light gray shaded area) for a constant emission over the last three years and different magnetic field strengths. The red dotted line shows the reprocessed emission if the $e^+e^-$ pairs are isotropized. The latter does not overproduce the *Fermi* upper limits (black diamonds; Tavecchio *et al.*, 2010) and hence the corresponding EBL shape is not excluded. The light and dark gray area together are equal to the integrated flux that is compared to the Eddington luminosity.

is a sum of several contributions which all can be represented as (e.g., Celotti & Fabian, 1993; Bonnoli *et al.*, 2011) $P_i = \pi R'^2 \Gamma_L^2 \beta c U'_i$, in the case that the radiation is emitted by an isotropically radiating relativistic plasma blob in the comoving frame. The blob of radius $R'$ in the comoving frame moves with a bulk Lorentz factor $\Gamma_L$ and corresponding speed $\beta c$, and $U'_i$ is the comoving energy density. The energy density of the produced radiation is $U'_{\rm rad} = L'/(4\pi R'^2 c) = L/(4\pi \delta_D^4 R'^2 c)$. The last equality connects the comoving luminosity with the luminosity in the lab frame via the Doppler factor given in Eq. (1.2), $\delta_D \approx 2\Gamma_L/[(1+z)(1+\theta_j^2\Gamma_L^2)]$ where $\theta_j$ is the angle between the jet axis and the line of sight. The approximation holds for $\theta_j \ll 1$ and $\Gamma_L \gg 1$. Assuming $\theta_j \approx \theta_{\rm cone}$, the Doppler factor and the bulk Lorentz factor are equal up to the redshift factor $1+z$, $\delta_D \approx \Gamma_L$. The power produced in radiation is a robust lower limit for the entire power of the jet (e.g., Bonnoli *et al.*,

2011),

$$P_{\rm rad} \approx L/(4\Gamma_{\rm L}^2) < P_{\rm jet} \leq L_{\rm edd}/2. \tag{2.18}$$

Solving the inequality for the observed luminosity, one arrives at an additional exclusion criterion for EBL shapes, namely, if the intrinsic energy flux at VHE is larger than the associated Eddington energy flux,

$$(1+z)^{2-\Gamma_{\rm int}} \int_{E_{\rm min}}^{E_{\rm max}} \frac{{\rm d}N_{\rm int}}{{\rm d}E}{\rm d}E > \frac{\Gamma_{\rm L}^2 L_{\rm edd}(M_\odot)}{2\pi d_{\rm L}^2} \tag{2.19}$$

with $E_{\rm min}$ and $E_{\rm max}$ the minimum and maximum energy of the intrinsic VHE spectrum which is described with a power law with index $\Gamma_{\rm int}$. The the factor $(1+z)^{2-\Gamma_{\rm int}}$ accounts for the K-correction and $d_{\rm L}$ is the luminosity distance given by

$$d_{\rm L} = \frac{(1+z)\,c}{H_0} \int_0^z \frac{{\rm d}z'}{\sqrt{\Omega_m (1+z')^3 + \Omega_\Lambda}}, \tag{2.20}$$

where $H_0$ is today's Hubble constant. For a conservative estimate, $M_\bullet + \sigma_{M_\bullet}$ is used in the calculation of $L_{\rm edd}$. The assumption of a non-super-Eddington luminosity is, however, somewhat speculative as super-Eddington emission has been observed, e.g., in the variable source 3C 454.3 (Abdo *et al.*, 2011a). For this reason, only steady sources (listed in Table 2.4) will be considered for this criterion. In Section 2.5, it will be shown that the capability of the Eddington criterion to exclude EBL shapes is extremely limited. Here, it is only emphasized that it is in principle possible to constrain the EBL with this argument.
Excluding EBL shapes with cascade emission [Eq. (2.16)] and the total energy budget of the source [Eq. (2.19)], will be referred to as the *IntVHELumi* (short for intrinsic VHE luminosity) criterion.

## 2.4 VHE AGN Sample

In the past four years, the number of discovered VHE emitting AGN has more than doubled. In this section, samples of VHE spectra are defined that are evaluated with the *VHE-HEIndex*, *PileUp*, and *VHEConcavity* criteria (Section 2.4.1) and with the *IntVHELumi* criterion (Section 2.4.2).

### 2.4.1 Sample tested against concavity criteria

For this part of the analysis, 22 VHE spectra from 19 different sources are used. AGN are included in the sample only if their redshift is known, there is no confusion with other sources, and they are listed in the 2FGL. This excludes the known VHE

sources 3C 66A and 3C 66B, 1ES 0229+200, PG 1553+113, and S 50716+714. Two spectra from the same source are only considered if they cover different energy ranges. The radio galaxies Centaurus A and M 87 are not included since they are too close and measured at too low energies to yield any constraints on the EBL density. Spectra that are a combination of several IACTs are not included due to possible systematic uncertainties. If two or more spectra are available for a variable source, the VHE spectrum is chosen that is measured simultaneously with *Fermi*-LAT observations. If the *Fermi*-LAT spectrum is best described with a logarithmic parabola, the spectral index determined at the pivot energy is used for the comparison with the intrinsic VHE spectra. The entire AGN sample is listed in Table 2.3 together with the redshift, the energy range, the spectral index at VHE energies, the index measured with the *Fermi*-LAT, the variability index given in the 2FGL (see below), and the corresponding references.
AGN are known to be variable sources with time both in overall flux and spectral index. This poses a problem for the *VHE-HEIndex* criterion, as it relies on the comparison of *Fermi*-LAT and IACT spectra. This issue is addressed by dividing the overall source sample into three categories:

1. *Steady sources in the* Fermi*-LAT energy band.* In this category, all sources are assembled that show a variability index $< 41.64$ in the 2FGL which corresponds to a probability of more than 1 % that the sources are steady. For these AGN, simultaneous measurements are not required regardless if they are steady (like 1ES 1101-232, Aharonian *et al.* 2007c) or variable (for instance H 1426+428, see below) at VHE. This does not affect the upper limits derived here because the *Fermi*-LAT index remains valid as a lower limit independent of the VHE index. These sources are marked as “steady” in the last column of Table 2.3.

2. *Variable sources with simultaneous measurements.* Some of the variable sources were observed simultaneously with the *Fermi*-LAT and IACTs in multiwavelength campaigns, namely PKS 2155-304 with HESS (Aharonian *et al.*, 2009c), and PKS 1222+21 with MAGIC (Aleksić *et al.*, 2011a). Instead of the spectral slopes given in the 2FGL, the *Fermi*-LAT spectra from these particular observations are used to test the EBL shapes. These sources are marked as “simul” in the last column in Table 2.3. Note, however, that the observation times might not be equal for the individual instruments since the sensitivities for the *Fermi*-LAT and IACTs are different. Nevertheless, the arising systematic uncertainty is negligible for the sources under consideration. In the case of PKS 2155-304, the source was observed in a quiescent state where no fast flux variability is expected. PKS 1222+21 was observed in a HE flaring state and *Fermi*-LAT observations are not available during the 30 minutes of MAGIC observations. Instead, Aleksić *et al.* (2011a) derive the *Fermi* spectrum from 2.5 hours of data encompassing these 30 minutes. This

**TABLE 2.3:** VHE AGN spectra used to derive upper limits on the EBL density.

| Source | Redshift | Experiment | Energy Range (TeV) | VHE Slope $\Gamma \pm \sigma_{\rm stat} \pm \sigma_{\rm sys}$ | *Fermi* Slope $\Gamma \pm \sigma_{\rm stat}$ | Variability Index | Reference | Comments |
|---|---|---|---|---|---|---|---|---|
| Mkn 421 | 0.031 | H.E.S.S. | 1.75 – 23.1 | 2.05 ± 0.22 | 1.77 ± 0.01 | 112.8 | (1) | hardest index |
| Mkn 501 | 0.034 | MAGIC | 0.17 – 4.43 | 2.79 ± 0.12 | 1.64 ± 0.09 | 72.33 | (2) | hardest index |
| Mkn 501 | 0.034 | HEGRA | 0.56 – 21.45 | 1.92 ± 0.03 ± 0.20 | 1.64 ± 0.09 | 72.33 | (3) | hardest index |
| 1ES 2344+514 | 0.044 | MAGIC | 0.19 – 4.00 | 2.95 ± 0.12 ± 0.20 | 1.72 ± 0.08 | 28.13 | (4) | steady |
| Mkn 180 | 0.045 | MAGIC | 0.18 – 1.31 | 3.25 ± 0.66 | 1.74 ± 0.08 | 19.67 | (5) | steady |
| 1ES 1959+650 | 0.048 | HEGRA | 1.52 – 10.94 | 2.83 ± 0.14 ± 0.08 | 1.94 ± 0.03 | 52.30 | (6) | hardest index |
| 1ES 1959+650 | 0.048 | MAGIC | 0.19 – 2.40 | 2.58 ± 0.18 | 1.94 ± 0.03 | 52.30 | (7) | hardest index |
| BL Lacertae | 0.069 | MAGIC | 0.16 – 0.70 | 3.6 ± 0.5 | 2.11 ± 0.04 | 267.0 | (8) | hardest index |
| PKS 2005-489 | 0.071 | H.E.S.S. | 0.34 – 4.57 | 3.20 ± 0.16 ± 0.10 | 1.90 ± 0.06 | 68.86 | (9) | hardest index |
| RGB J0152+017 | 0.080 | H.E.S.S. | 0.31 – 2.95 | 2.95 ± 0.36 ± 0.20 | 1.79 ± 0.14 | 27.73 | (10) | steady |
| PKS 2155-304 | 0.116 | H.E.S.S. | 0.25 – 3.20 | 3.34 ± 0.05 ± 0.10 | 1.81 ± 0.11 | 262.9 | (11) | simul |
| RGB J0710+591 | 0.125 | VERITAS | 0.42 – 3.65 | 2.69 ± 0.26 ± 0.20 | 1.53 ± 0.12 | 29.86 | (12) | steady |
| H 1426+428 | 0.129 | HEGRA | 0.78 – 5.37 | ... | 1.32 ± 0.12 | 22.16 | (13) | steady |
| 1ES 0806+524 | 0.138 | MAGIC | 0.31 – 0.63 | 3.6 ± 1.0 ± 0.3 | 1.94 ± 0.06 | 37.80 | (14) | steady |
| H 2356-309 | 0.165 | H.E.S.S. | 0.23 – 1.71 | 3.06 ± 0.15 ± 0.10 | 1.89 ± 0.17 | 20.19 | (15) | steady |
| 1ES 1218+304 | 0.182 | MAGIC | 0.09 – 0.63 | 3.0 ± 0.4 | 1.71 ± 0.07 | 40.00 | (16) | steady |
| 1ES 1218+304 | 0.182 | VERITAS | 0.19 – 1.48 | 3.08 ± 0.34 ± 0.20 | 1.71 ± 0.07 | 40.00 | (17) | steady |
| 1ES 1101-232 | 0.186 | H.E.S.S. | 0.18 – 2.92 | 2.88 ± 0.17 | 1.80 ± 0.21 | 25.74 | (18) | steady |
| 1ES 1011+496 | 0.212 | MAGIC | 0.15 – 0.59 | 4.0 ± 0.5 | 1.72 ± 0.04 | 48.05 | (19) | hardest index |
| 1ES 0414+009 | 0.287 | H.E.S.S. | 0.17 – 1.13 | 3.44 ± 0.27 ± 0.20 | 1.98 ± 0.16 | 15.56 | (20) | steady |
| PKS 1222+21 | 0.432 | MAGIC | 0.08 – 0.35 | 3.75 ± 0.27 ± 0.20 | 1.95 ± 0.21 | 13030 | (21) | simul |
| 3C 279 | 0.536 | MAGIC | 0.08 – 0.48 | 4.1 ± 0.7 ± 0.20 | 2.22 ± 0.02 | 2935 | (22) | hardest index |
| 1ES 0229+200 | 0.140 | H.E.S.S. | 0.60 – 11.45 | 2.50 ± 0.19 ± 0.10 | ... | ... | (23) | ... |

*Notes:* If not stated otherwise in the text, the *Fermi* slope and variability index are taken from the 2FGL. See the text for details on the *Comments* column.
*References:* (1) Tluczykont (2011); (2) Abdo *et al.* (2011b); (3) Aharonian *et al.* (1999b); (4) Albert *et al.* (2007c); (5) Albert *et al.* (2006b); (6) Aharonian *et al.* (2003a); (7) Albert *et al.* (2006e); (8) Albert *et al.* (2007a); (9) HESS Collaboration *et al.* (2010b); (10) Aharonian *et al.* (2008d); (11) Aharonian *et al.* (2009c); (12) Acciari *et al.* (2010b); (13) Aharonian *et al.* (2003c); (14) Acciari *et al.* (2009a); (15) HESS Collaboration *et al.* (2010a); (16) Albert *et al.* (2006a); (17) Acciari *et al.* (2009d); (18) Aharonian *et al.* (2006a); (19) Albert *et al.* (2007b); (20) H.E.S.S. Collaboration *et al.* (2012); (21) Aleksić *et al.* (2011a); (22) Albert *et al.* (2008b); (23) Aharonian *et al.* (2007g)

is justified, since the source remained in this high flux state for several days with little spectral variations (cf. Figure 2 in Tanaka *et al.*, 2011). Accordingly, for the observations to be considered simultaneous here, the maximum time lag must not exceed $\sim 1$ hour.

3. *Variable sources not simultaneously measured.* For some variable sources, no simultaneous data are available, namely 1ES 1011+496, 1ES 1959+650, 3C 279, BL Lacertae, the flare spectra of Mkn 501 and Mkn 421, as well as PKS 2005-489 (see Table 2.3 for the references). In these cases, the literature is examined for dedicated *Fermi*-LAT analyses of the corresponding sources in order to find the hardest spectral index published. In the cases of 1ES 1011+496, 1ES 1959+650, PKS 2005-489 and Mkn 421 the indices reported in the 2FGL are the hardest published so far. The hardest indices for BL Lacertae and Mkn 501 are obtained by Abdo *et al.* (2010d) and Abdo *et al.* (2011c), respectively, see Table 2.3 for the corresponding values. The distant quasar 3C 279 was observed with the *Fermi*-LAT during a $\gamma$-ray flare in 2009 and the measured spectral indices vary between $\sim 2$ and $\sim 2.5$ (compare Figure 1 in Abdo *et al.*, 2010a). Thus, the catalog index of $2.22 \pm 0.02$ is appropriate to use. Table 2.3 refers to all the spectra discussed here as "hardest index" in the last column.

Additional uncertainties are introduced for those VHE observation with a maximum time lag between the measurement and the launch of the *Fermi* satellite, which is the case for Mkn 501 and H 1426+428. In the case of H 1426+428, no detection has been reported after the HEGRA measurement in 2002 at VHE suggesting that the source is now in a quiescent state. The 2002 spectrum with an observed spectral index of $\Gamma = 1.93 \pm 0.47$ is used in this study. The hard spectrum promises stronger limits with the *VHE-HEIndex* criterion than the 2000 spectrum which has a spectral slope of $\Gamma = 2.79 \pm 0.33$. The source showed a change in flux by a factor of 2.5 between the 1999/2000 and 2002 observation runs (Aharonian *et al.*, 2003c). Additionally, the *Fermi*-LAT index of $1.32 \pm 0.12$ is the hardest of the entire sample and, in summary, it is chosen to include the source in the study. As for Mkn 501, the spectrum of the major outbreak was measured up to 21 TeV and, consequently, it is a promising VHE spectrum to constrain the EBL density at FIR wavelengths. As it turns out, it excludes most shapes due to the *PileUp* and *VHEConcavity* criteria. These criteria are independent of the *Fermi*-LAT index and are not affected by the difference in observation time.

### 2.4.2 Sample tested against intrinsic VHE luminosity

For the integral criterion presented in Section 2.3.2, only spectra from steady sources are used in order to avoid systematic uncertainties introduced by variability. Only

**TABLE 2.4:** Sources used to exclude EBL shapes with the *IntVHELumi* criterion. The black hole masses $M_\bullet$ are taken from Wagner (2008) except for RGB J0710+591 and 1ES 0414+009 for which the masses are given in Woo *et al.* (2005) and Urry *et al.* (2000), respectively. No measurements of the central black hole masses of 1ES 1101-232 and RGB J0152+017 are available, which is why a fiducial value of $M_\bullet = 10^9 M_\odot$ is used here.

| Source | Black-hole mass $\log_{10}(M_\bullet/M_\odot)$ |
|---|---|
| 1ES 0229+200 | 9.16 ± 0.11 |
| 1ES 0414+009 | 9.3 |
| 1ES 1101-232 | 9 |
| 1ES 1218+304 | 8.04 ± 0.24 |
| H 1426+428 | 8.65 ± 0.13 |
| H 2356-309 | 8.08 ± 0.23 |
| RGB J0152+017 | 9 |
| RGB J0710+591 | 8.25 ± 0.22 |

spectra are examined which suffer from large attenuations and are measured at energies beyond several TeV. These spectra are the most promising candidates for constraints, as they show the highest values of integrated intrinsic emission. Note that the spectrum of 1ES 0229+200 which has been reanalyzed by Tavecchio *et al.* (2010) can be tested against the *IntVHELumi* condition as upper limits on the HE flux suffice and no spectral information from the *Fermi*-LAT is required for this criterion. Otherwise, the same selection criteria apply as for the sample tested against concavity (known redshift, etc.). The VHE spectra evaluated with the *IntVHE-Lumi* criterion together with the central black-hole masses of the corresponding sources are summarized in Table 2.4.

The final upper limits on the EBL density are derived by calculating the envelope shape of all *allowed* EBL shapes. The influence of the different exclusion criteria is examined by inspecting the envelope shape due to the *VHE-HEIndex* argument alone and successively adding the other criteria and reevaluating the resulting upper limits. Furthermore, the impact of the VHE spectra responsible for the most stringent limits in the optical, MIR, and FIR will be investigated by excluding these spectra from the sample and inspect the change in the upper limits.

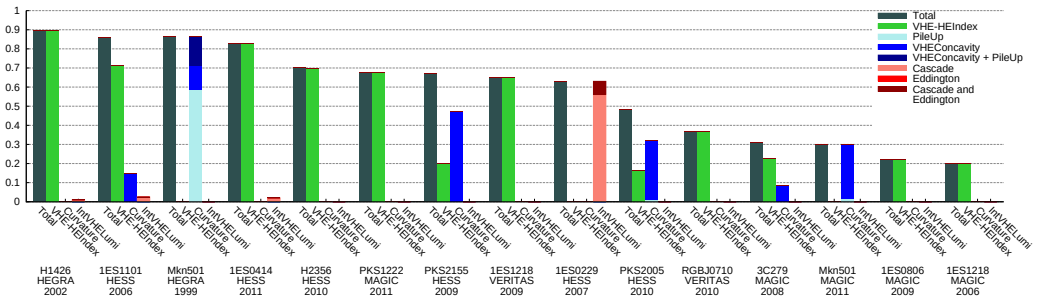


**FIGURE 2.5:** Histogram of the fraction of excluded shapes of the different VHE spectra. The columns show the total fraction of rejected shapes as well as the fraction excluded by the different criteria. The column labeled "Curvature" combines the *VHEConcavity* and *PileUp* criteria. Spectra that allow more than 90 % of all shapes are not shown.

## 2.5 RESULTS

Figure 2.5 shows a histogram of the fractions of rejected shapes by each VHE spectrum, where the different colors represent the different criteria that lead to the exclusion of an EBL shape. It should be noted that individual shapes can be rejected by several criteria at the same time, and, therefore, the different columns may add up to a number larger than indicated by the total column. Results for spectra that exclude no (BL Lacertae, 1ES 2344+514, and Mkn 180) or less than 10 % of all EBL shapes (the MAGIC spectrum of 1ES 1959+650, the HESS spectrum of RGB J0152+017 and Mkn 421, as well as the HEGRA spectrum of 1ES 1959+650) are not shown. Most EBL shapes are excluded by the VHE spectra of H 1426+428, 1ES 1101-232, and Mkn 501. The influence of H 1426+428 and Mkn 501 on the limits in the MIR and FIR and of 3C 279 together with PKS 1222+21 in the optical will be examined by excluding these spectra from the sample. These sources provide strong constraints in the respective wavelength bands. Interestingly, removing 1ES 1101-232 from the source sample does not change the upper limits since a number of sources with comparable redshifts exclude the same EBL shapes, e.g., 1ES 0414+009, the VERITAS spectrum of 1ES 1218+304, H 2356-309, and PKS 2005-489.

Different combinations of exclusion criteria are shown in the panels of Figure 2.6. Each panel depicts the limits for the complete spectrum sample and, additionally, the resulting EBL constraints if the spectra discussed above are omitted. By itself, the *VHE-HEIndex* criterion gives strong upper limits in the optical and MIR on the EBL density if all spectra are included (top-left panel of Figure 2.6). In the optical, the limits are dominated by the spectra of 3C 279 and PKS 1222+21, as the restrictions are significantly weaker without these spectra (dashed line in Figure 2.6). The spectra are influenced most by changes of the EBL density in the optical which is inferred from the maximum energies of 480 GeV and 350 GeV for 3C 279 and PKS 1222+21, respectively. They translate into a maximum cross sections for

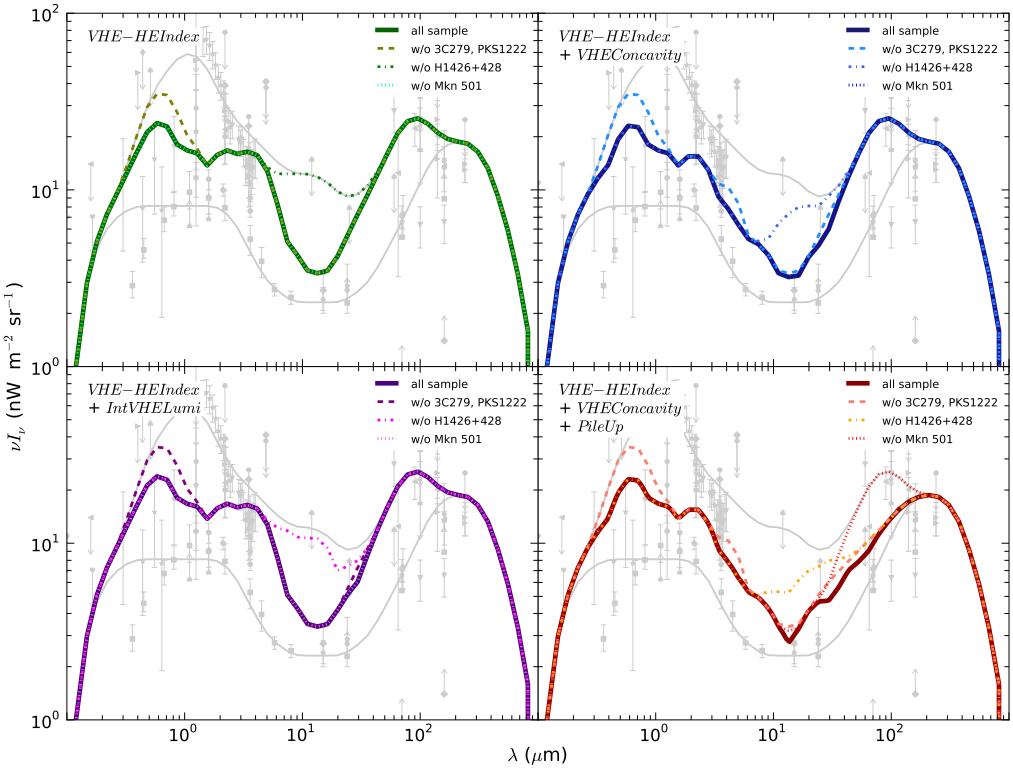


**FIGURE 2.6:** Limits on the EBL density for different exclusion criteria and excluding different sources from the sample. See text for details.

pair production at 0.6 $\mu$m (3C 279) and 0.43 $\mu$m (PKS 1222+21), see Eq. (1.16). The constraints are almost unaltered if only one of these spectra is excluded from the sample. In the MIR, the spectrum of H 1426+428 provides firm limits on the EBL density whereas hardly any EBL shape is rejected due to the spectrum of Mkn 501 with the *VHE-HEIndex* criterion.

The combination of the *VHE-HEIndex* and *VHEConcavity* criterion strengthens the upper limits between 2 $\mu$m and 10 $\mu$m, as shown in the top-right panel of Figure 2.6. Convex intrinsic spectra are the result of an EBL density with a positive gradient between lower and higher wavelengths, but a combination with the *VHE-HEIndex* criterion is necessary to exclude shapes with a high EBL density that are rather constant in wavelength. Therefore, on their own, neither the *PileUp* nor the *VHEConcavity* criterion provide strong upper limits. Combining the *PileUp* and *VHEHEIndex* arguments results in very similar limits as the combination of the *VHEHEIndex* and *VHEConcavity* criterion. This degeneracy between the *PileUp* and *VHEConcavity* criterion is also demonstrated in Figure 2.7. Corrected with a certain EBL shape, the spectrum of Mkn 501 shows a strong exponential rise at highest energies but is best described with a double broken power law. The combination of the *PileUp* and *VHEConcavity* together with the *VHE-HEIndex* criterion yields

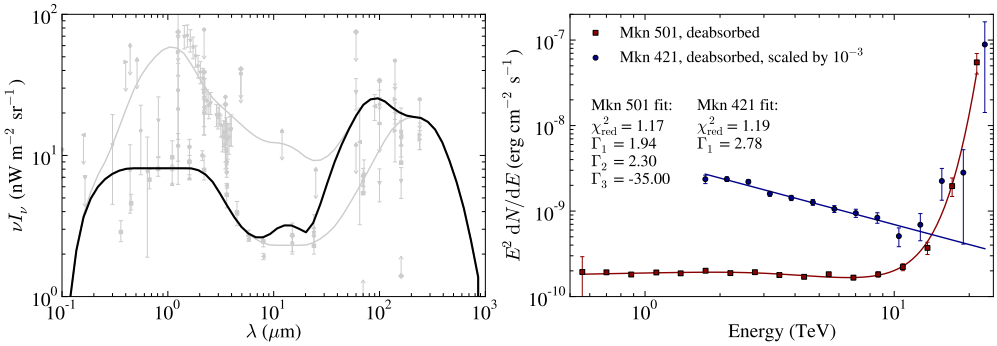


**FIGURE 2.7:** Left panel: Example of an EBL shape excluded by Mkn 501 with the *VHE-Concavity* criterion. Right panel: The spectra of Mkn 501 and Mkn 421 corrected with this particular EBL shape. The flux of the latter is scaled by $10^{-3}$ for better visibility. For Mkn 501, a double broken power law provides the best description with a spectral index $\Gamma_3 = -35$ at highest energies, the maximum value tested in the fitting procedure. In the case of Mkn 421, a simple power law suffices.

robust upper limits in the FIR as displayed in the bottom-right panel of Figure 2.6. The constraints in the FIR are entirely due to the spectrum of Mkn 501 although the spectrum of Mkn 421 is also measured beyond 20 TeV and both sources have a comparable redshift. However, the spectrum of Mkn 421 rejects far less shapes than Mkn 501. An exponential rise is observed in intrinsic spectra of Mkn 421 for certain EBL realizations (e.g., the corrected Mkn 421 spectrum in the right panel of Figure 2.7) but a power law is found to be the best description of the spectrum.

Compared to the *VHE-HEIndex* criterion alone, the combination with the *IntVHE-Lumi* criterion leads to minor improvements in the MIR (bottom-left panel of Figure 2.6). Most shapes are rejected by the VHE spectrum of 1ES 0229+200 which is also the sole spectrum which excludes a very limited number of shapes with the Eddington luminosity argument. Remarkably, the spectrum excludes more than 60 % of all shapes. The *IntVHELumi* criterion has the most substantial effect in the infrared part of the EBL density, as the highest energies of the spectrum of 1ES 0229+200 contribute most to the integral flux. The maximum energy measured in the spectrum is 11.45 TeV and, thus, the limits are most sensitive to changes in the EBL around 14 $\mu$ m. The influence of the choice of the bulk Lorentz factor $\Gamma_\mathrm{L}$ (and hence of the Doppler factor $\delta_\mathrm{D}$ since $\Gamma_\mathrm{L} \approx \delta_\mathrm{D}$ is assumed) on the envelope shape can be seen from Figure 2.8 where the upper limits are shown for $\Gamma_\mathrm{L} = 5$, 10, and 50. As $\Gamma_\mathrm{L}$ enters quadratically into the calculation of the flux [cf. Eq. (2.15)] and for the Eddington luminosity [Eq. (2.19)], the choice of the value of $\Gamma_\mathrm{L}$ is critical for the number of rejected EBL shapes. The bulk Lorentz factor is unknown for the sources tested with the *IntVHELumi* criterion, and for the combination with the other criteria $\Gamma_\mathrm{L} = 10$ is generically chosen. However, even with this oversimplified choice

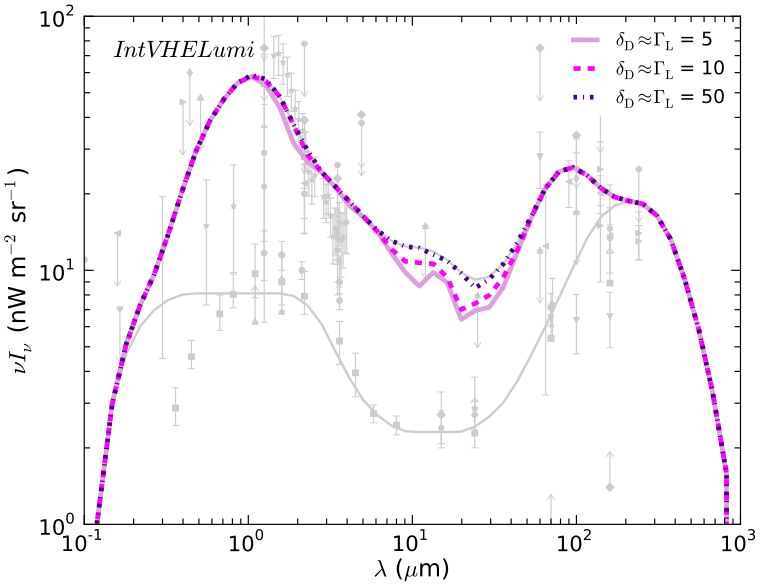


**FIGURE 2.8:** Upper limits solely due to the *IntVHELumi* criterion for different values of the bulk Lorentz factor $\Gamma_L$ and the Doppler factor $\delta_D$ of the emitting region. With increasing Lorentz and Doppler factor, respectively, the limits become worse [see Eq. (2.15) and (2.19)].

of $\Gamma_L$, the *IntVHELumi* criterion does not lead to improvements of the upper limits compared to the combination of the *VHE-HEIndex*, *VHEConcavity*, and *PileUp* criteria. Conversely, this implies that the final upper limits will not depend on the specific choice of model parameters and assumptions that enter the evaluation of the *IntVHELumi* criterion.

The final result for the upper limits is the combination of all criteria and all VHE spectra, shown in Figure 2.9. It is the envelope shape of all allowed EBL realizations (cf. top-left panel of Figure 2.9), which itself is excluded by several VHE spectra and it should not be regarded as a possible level of the EBL density. For the maximum energy of all VHE spectra of 23.1 TeV, the cross section for pair production peaks at a wavelength of the EBL photons of $\lambda_* \approx 29\,\mu$m. More than half of the interactions occur in a narrow interval $\Delta\lambda = (1 \pm 1/2)\lambda_*$ around the peak wavelength (e.g., Aharonian *et al.*, 2006a) and hence the constraints are not extended beyond $100\,\mu$m. Albeit including the evolution of the EBL with redshift, the derived upper limits are below $5\,\mathrm{nW\,m^{-2}\,sr^{-1}}$ in the range from $8\,\mu$m to $31\,\mu$m. A comparison of the constraints with previous works is shown in the top-right panel of Figure 2.9. Above $30\,\mu$m, the constraints are consistent with those derived in MR07. For wavelengths between $1\,\mu$m and $4\,\mu$m, the limits are in accordance with the results of Aharonian *et al.* (2006a, 2007g) and Albert *et al.* (2008b). The strong limits of Albert *et al.* (2008b) who utilized the spectrum of 3C 279 are not reproduced.

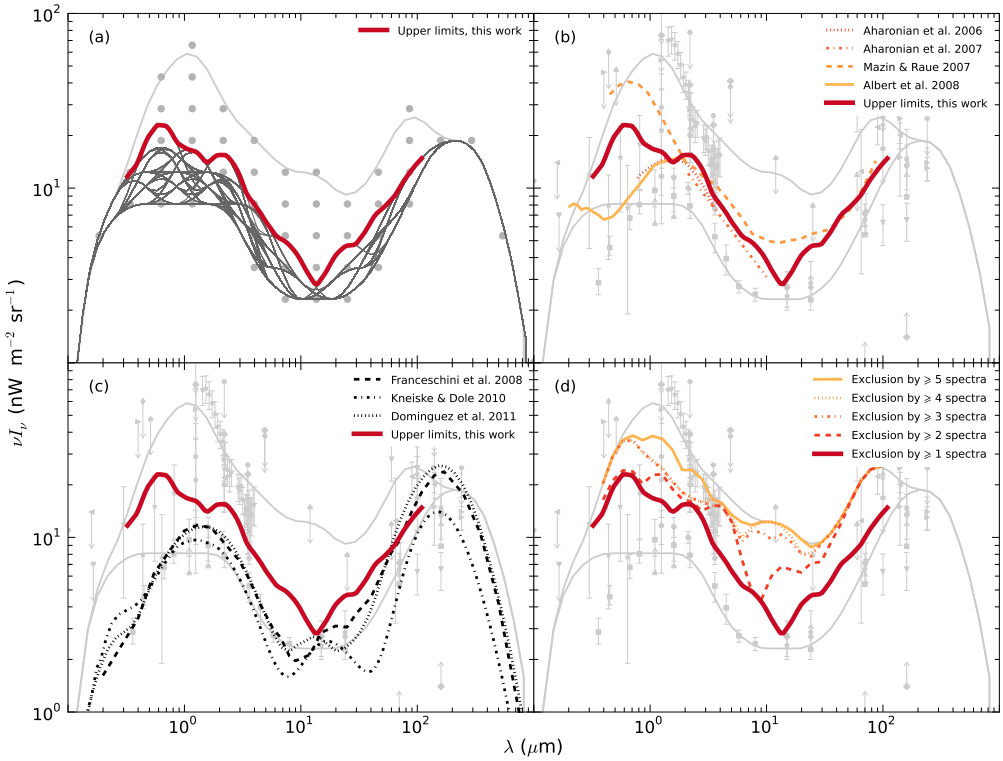


**FIGURE 2.9:** Upper limits derived in this study. (a) The envelope shape (upper limits) of all allowed shapes (dark gray lines). Also shown are the grid points as light gray bullets. (b) The constraints compared to the the upper limits of MR07, Aharonian *et al.* (2006a, 2007g), and Albert *et al.* (2008b). (c) Upper limits of this study together with three EBL models (Franceschini *et al.*, 2008; Kneiske & Dole, 2010; Domínguez *et al.*, 2011). (d) Upper limits requiring different minimum numbers of VHE spectra that exclude one EBL shape.

These limits are derived by changing certain free parameters (e.g., the fraction of UV emission escaping the galaxies) of the EBL model of Kneiske *et al.* (2002) while the current approach allows for generic EBL shapes. An EBL shape with a high density at UV / optical wavelengths followed by a steep decline towards optical and NIR wavelengths produces a soft intrinsic spectrum of 3C 279 that cannot be excluded by any criterion. Furthermore, an inspection of the spectrum of 3C 279 shows that the fit will be dominated by the first two energy bins due to the smaller error bars. Thus, a convex spectrum is often still sufficiently described with a soft power law. In general, it should be underlined that all of the above limits from recent studies use a theoretically motivated bound on the intrinsic spectral slope of $\Gamma = 1.5$. This value is under debate, as a harder index can be possible, for instance, if the underlying population of relativistic electrons is very narrow (Katarzyński

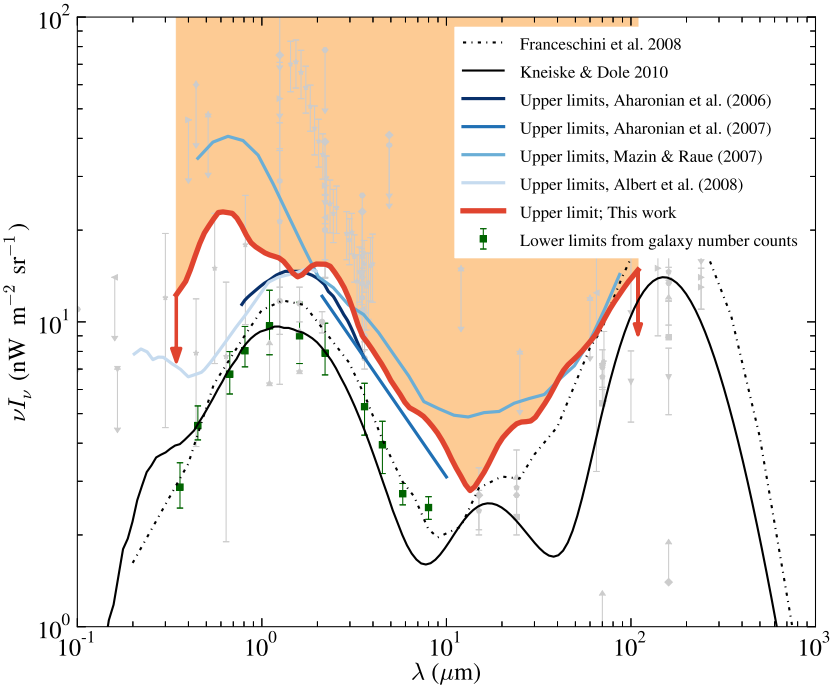


**FIGURE 2.10:** Upper limits of this work together with previous limits and EBL models and measurements.

*et al.*, 2006; Tavecchio *et al.*, 2009; Lefa *et al.*, 2011a), particles are accelerated at relativistic shocks (e.g., Stecker *et al.*, 2007), in the case of internal photon absorption (Aharonian *et al.*, 2008f), or in proton-synchrotron models (e.g., Aharonian, 2000; Zacharopoulou *et al.*, 2011).

The upper limits derived here are not in conflict with the EBL model calculations of Franceschini *et al.* (2008), Kneiske & Dole (2010), and Domínguez *et al.* (2011) and are compatible with the lower limit galaxy number counts derived from *Spitzer* measurements (see the bottom-left panel of Figure 2.9). In the FIR, the models of Franceschini *et al.* (2008) and Domínguez *et al.* (2011) lie above the derived upper limits, but the EBL limit at these wavelengths relies on a single spectrum (Mkn 501). Between $\sim 1\,\mu$m and $\sim 14\,\mu$m there is a convergence between the upper limits and model calculations and at $13.4\,\mu$m the EBL is constrained below $2.7\,\mathrm{nW\,m^{-2}\,sr^{-1}}$, just above the EBL models. This leaves not much room for additional components such as Population III stars or dark stars and implies that the direct measurements of Matsumoto *et al.* (2005) are foreground dominated as discussed in Dwek *et al.* (2005). The EBL models, the upper limits from previous works, and the results derived here are shown together in Figure 2.10.

In general, most of the tested EBL shapes are excluded by more than one spectrum

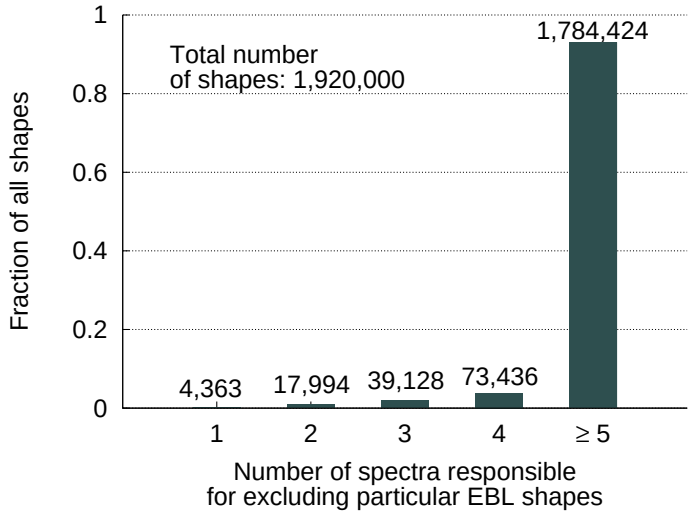


**FIGURE 2.11:** Percentage of all shapes excluded by at least a certain number of spectra. The majority of rejected shapes is not allowed by more than five spectra.

(Figure 2.11). While 0.23 % of all EBL shapes are excluded by only one of the spectra in the sample, the majority of shapes (93 %) is rejected by five spectra or more. The bottom-right panel of Figure 2.9 shows the limits for different minimum numbers of VHE spectra that rule out an EBL shape. From NIR to MIR wavelengths, the limits are only slightly worsened if at least two spectra are required to exclude EBL shapes. If at least five spectra are ought to reject an EBL shape, the EBL density remains confined below 40 $\mathrm{nW\,sr^{-1}\,m^{-2}}$ in the optical. Thus, from optical to MIR wavelengths, the limits are robust against individual spectra that possibly have a peculiar intrinsic shape due to one of the mechanisms discussed in Section 2.3.1. Especially in the MIR and FIR, however, the limits are weakened as they mainly depend on two spectra, H 1426+428 and Mkn 501. This underlines the need for more spectra measured beyond several TeV in order to draw conclusions about the EBL density in the MIR and FIR from VHE blazar measurements.

The effect of the evolution of the EBL density with redshift is studied with three of the most constraining spectra, namely 1ES 1101-232, H 1426+428, and Mkn 501, as well as 3C 279 which is the source with the largest redshift of $z = 0.536$ in the sample. The four spectra are tested against the *VHE-HEIndex*, *PileUp*, and *VHEConcavity* criteria and the envelope shape is determined with and without the evolution with redshift discussed in Section 2.2. Not surprisingly, the EBL density is less confined if the evolution is accounted for, as seen from Figure 2.12. The differences are most pronounced in the optical, where the influence of 3C 279 is the strongest (light blue shaded region in Figure 2.12). Without taking the evolution into account, the limits are overestimated by up to 40 % at 0.6 $\mu$m. At higher wavelengths, the difference is not as distinct as in the optical. This outcome emphasizes

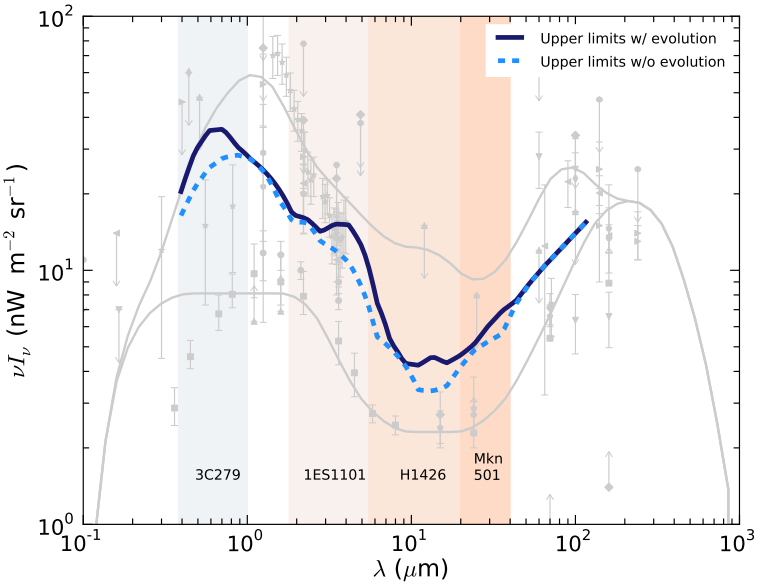


**FIGURE 2.12:** Upper limits with and without evolution for four VHE spectra. The individual spectra have the strongest influence in the correspondingly shaded regions.

that the evolution of the EBL density with redshift has a non-negligible effect on upper limits, especially for sources with a large redshift.

Given the similarities in procedures used here and in MR07, the systematic uncertainties of the limits derived here are similar to the ones derived in MR07 (see also Raue, 2007; Raue & Meyer, 2012). They have been estimated to be 31 % in optical to near infrared and 32 - 55 % in mid to far infrared wavelengths, mainly from the grid spacing and the uncertainties on the absolute energy scale of ground based VHE instruments which is taken to be 15 %. However, Meyer *et al.* (2010) achieved a cross-calibration between the *Fermi*-LAT and IACTs using the broadband SED of the Crab Nebula, reducing the uncertainty of the absolute energy scale to $\sim 5$ %. Additional uncertainties arise from the phenomenological description of the EBL evolution ($< 4$ % for a redshift $z = 0.2$ and $< 10$ % for $z = 0.5$, Raue & Mazin 2008). Uncertainties in the calculation of the cascade emission are caused by the choice of the model parameters which are, however, difficult to quantify. The same applies for the assumption that steady sources do not show super-Eddington luminosities. Since the most stringent limits do not rely on these exclusion criteria, these uncertainties do not affect the final results of the upper limits.

Additionally, the measurement capabilities of the *Fermi*-LAT affect the *VHE-HE-Index* criterion and hence the upper limits. While the 2FGL does not quote the systematic errors on the individual spectral indices, it gives a number of sources of

systematic uncertainties: the effective area, the diffuse emission model, and the handling of front and back converted events. The systematic error on the effective area is estimated to be between 5 % and 10 %, while the errors on the diffuse emission model mainly affect sources inside the galactic plane. Furthermore, the isotropic emission for front and back converted events is assumed to be equal. This leads to underestimation of the flux below 400 MeV and might produce harder source spectra. As harder spectra in the *Fermi*-LAT band weaken the upper limits, the results derived here can, again, be regarded as conservative.

Certain mechanisms are discussed in the literature that effectively reduce the attenuation of $\gamma$-rays due to pair production. For instance, if cosmic rays produced in AGN are not deflected strongly in the intergalactic magnetic field, they could interact with the EBL and produce VHE $\gamma$-rays that contribute to the VHE spectrum (Essey & Kusenko, 2010; Essey *et al.*, 2010, 2011, and Chapter 4). Other suggestions are the conversion of photons into axion-like particles (e.g., de Angelis *et al.*, 2007; Mirizzi & Montanino, 2009, and Chapter 5) or the violation of Lorentz invariance (e.g., Jacob & Piran, 2008, and Chapter 4).

Future simultaneous observations of extragalactic blazars with the *Fermi*-LAT and IACTs have the potential to further constrain the EBL density. Furthermore, the projected energy threshold for the recently inaugurated phase II of the H.E.S.S. experiment is about 30 GeV in mono and $\sim$ 50 GeV in stereo mode (Becherini *et al.*, 2012b), enabling the simultaneous observation of intrinsic and absorbed blazar spectra. The same opportunity holds for the planned Cherenkov Telescope Array (CTA; Mazin *et al.*, 2013).

To conclude this chapter, the main results are summarized below.

- VHE $\gamma$-ray spectra from a sample of 19 AGN with redshifts in the range from 0.031 to 0.536 are used in conjunction with *Fermi*-LAT spectra to constrain the EBL density.

- A large number of generic EBL realizations is investigated, allowing for possible features, e.g., from Population III stars.

- The evolution of the EBL density is accounted for, using a phenomenological prescription (e.g., Raue & Mazin, 2008).

- The EBL density is constrained by testing the absorption-corrected spectra for their physical feasibility, employing, in principle, two criteria: (1) The intrinsic spectrum is not convex neither in the transition from HE to VHE nor in the VHE regime alone and (2) the absorbed emission reprocessed in an electromagnetic cascade does not overshoot the *Fermi*-LAT measurements, and the total intrinsic VHE emission does not exceed the Eddington luminosity. The second criterion depends on the integral flux of the intrinsic spectrum.

- The resulting upper limits stretch over a broad wavelength range between $0.4\,\mu$m and $100\,\mu$m, limiting the EBL density below $5\,\mathrm{nW\,m^{-2}\,sr^{-1}}$ at MIR wavelengths.
- The large number of used sources guarantees robust upper limits even if individual spectra are removed from the sample. This is, however, not true at FIR wavelengths, where solely the spectrum of Mkn 501 results in strong constraints.

# 3 Indications for an anomalous propagation of $\gamma$-rays from high and very high energy observations

High and very high energy $\gamma$-rays undergo pair production with the photons of the extragalactic background light (EBL), leading to an exponential suppression of the source-intrinsic flux with the optical depth $\tau_{\gamma\gamma}$ (see Section 1.2 and Nikishov, 1962; Jelley, 1966; Gould & Schréder, 1966, 1967). The optical depth is a monotonously increasing function with the observed photon energy $E$, the source redshift $z$, and the EBL photon density [see Eq. (1.10)]. As discussed in the previous Chapter, direct measurements of the EBL are difficult due to the contamination with foreground emission, and only firm upper and lower limits can be derived from direct observations. The upper limits derived in the last Chapter from the combination of very high energy (VHE; energy $E \gtrsim 100\,\mathrm{GeV}$) $\gamma$-ray spectra with observations of the Large Area Telescope (LAT) on board the *Fermi* satellite suggest a low EBL density, especially in the infrared. Evidence for a low opacity of the Universe for VHE $\gamma$-rays has also been inferred from the observations of distant blazars (e.g., Aharonian *et al.*, 2006a, 2007g; Albert *et al.*, 2008b) or the lack of a correlation between the redshift and the spectral index (de Angelis *et al.*, 2011). In principle, the spectral index should become softer with the redshift, as the EBL absorption increases. The imprint of the EBL on high and VHE spectra has also been observed with the *Fermi*-LAT (Ackermann *et al.*, 2012c) and H.E.S.S. (H.E.S.S. Collaboration *et al.*, 2013) in data sets dominated by photons of the *optical thin regime* (i.e., photons for which $\tau_{\gamma\gamma} < 1$).

A low opacity of the Universe for $\gamma$-rays could also be interpreted in terms of an indication for a *pair-production anomaly* (PPA): The observations of sources in the *optical thick regime* (i.e., the photon energy and source redshift result in $\tau_{\gamma\gamma} > 1$) offer the unique opportunity to probe mechanisms that affect the propagation of VHE $\gamma$-rays over cosmological distances. In this regime, the primary $\gamma$-ray flux is strongly attenuated, decreasing the probability to observe the source. Thus, even minute effects that change the propagation of $\gamma$-rays and occur with a low probability can have a substantial impact on the observed flux. Several theories exist which predict a change in the effective opacity compared to the standard picture outlined

in Section 1.2. Within the Standard Model of particle physics, $\gamma$-ray emission beyond $\tau_{\gamma\gamma} > 1$ might be the result of electromagnetic cascades. In such scenarios, either photons or cosmic rays interact with background radiation fields (the EBL or the cosmic microwave background, CMB) and produce secondary $\gamma$-rays via the upscattering of CMB photons or photo-pion production (e.g., Protheroe & Stanev, 1993; Essey & Kusenko, 2010). Alternatively, certain theories beyond the Standard Model affect the photon propagation. These include Lorentz invariance violation (LIV; Coleman & Glashow, 1999; Kifune, 1999), oscillations into hidden sector bosons (Okun, 1982), or the conversion into pseudo Nambu-Goldstone bosons such as axion-like particles (Csáki *et al.*, 2003; de Angelis *et al.*, 2007). These mechanisms will be further discussed in the Chapters 4 and 5. Little data is available in the high optical depth regime due to the exponential suppression of the $\gamma$-ray flux. Thus, the accordance between data and EBL model predictions, and in particular, the question if the Universe appears more transparent in the optical thick regime, can only be investigated with large samples of high and very energy $\gamma$-rays observations of the *Fermi*-LAT and imaging air Cherenkov telescopes (IACTs).
In principle, any observation of high energy (HE; $100\,\mathrm{MeV} \lesssim E \lesssim 100\,\mathrm{GeV}$) and VHE $\gamma$-rays from environments for which a high optical depth is expected can be used to search for a PPA. For example, Tavecchio *et al.* (2012) used the MAGIC observations of the FSRQ PKS 1222+21 to investigate the possibility of photon-ALP oscillations facilitating the escape of VHE $\gamma$-rays from the source. The observed short-term variability (Aleksić *et al.*, 2011a), suggests a compact emission region. If this region was located inside the broad line region, the $\gamma$-ray absorption would be severe (Tavecchio *et al.*, 2011b).
In the first part of this Chapter, a non-parametric test will be introduced that relies on as little model assumptions as possible and uses all available VHE $\gamma$-ray spectra to search for deviations from EBL model expectations in the transition from the optical thin to the optical thick regime. The results for the EBL model of Kneiske & Dole (2010, henceforth KD model) have been published in Horns & Meyer (2012), and the analysis of further models has been presented in Meyer *et al.* (2012c). In the second part of the Chapter, photons detected with the *Fermi*-LAT are associated with active galactic nuclei (AGN) with known redshift. Under the assumptions of certain EBL models, the probability will be assessed to observe photons whose energy and redshift correspond to the optical thick regime. A preliminary analysis of the results presented here has been published in (Meyer *et al.*, 2012a).

## 3.1 Statistical analysis of VHE $\gamma$-ray spectra

All published VHE spectra are included in the search for a PPA for which the source redshift is unambiguously determined and larger than 0.01. The latter constraint leads to an exclusion of the spectra of the radio galaxies M 87 and Centaurus A.

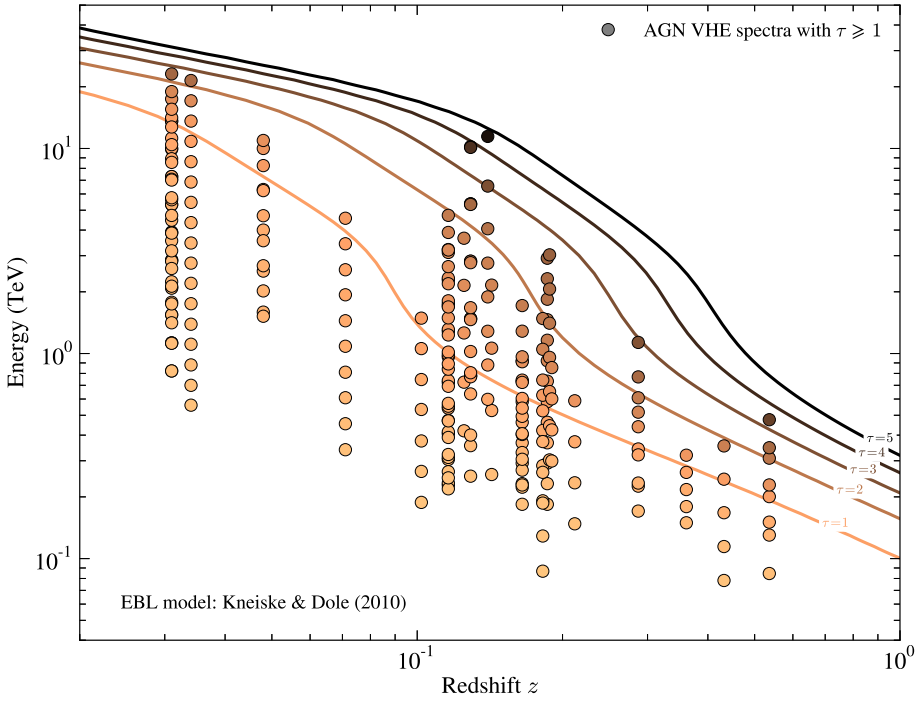


**FIGURE 3.1:** Fazio-Stecker relation for the KD model with energy bins of VHE spectra that have points in the regime $\tau_{\gamma\gamma} \geqslant 1$. Also shown are isocontours for constant values of the optical depth $\tau_{\gamma\gamma} = 1, \ldots, 5$.

These spectra do not extent to high enough energies to investigate the attenuation of $\gamma$-rays. All remaining sources are blazars. The sample of VHE spectra is listed in Table 3.1 together with the energy ranges ($E_{\mathrm{min}} - E_{\mathrm{max}}$), the source redshift, the number of energy bins in the regimes $\tau_{\gamma\gamma} < 1$, $1 \leqslant \tau_{\gamma\gamma} < 2$, and $2 \leqslant \tau_{\gamma\gamma}$, and the corresponding references. The optical depth is computed from the KD model with a $\tau_{\gamma\gamma}$ normalization of $\alpha = 1$, a conservative choice to investigate an enhanced transparency, since this model results in a minimum attenuation of VHE $\gamma$-rays at TeV energies. The sample spans a broad range of energies (0.08 TeV – 23.1 TeV) and redshifts (0.031 – 0.536). This can also be seen from Figure 3.1 which shows the energy bins of VHE $\gamma$-ray spectra plotted against the source redshift (this representation is sometimes referred to as the Fazio-Stecker relation; Fazio & Stecker, 1970; Kneiske *et al.*, 2004).
In the following, two statistical tests are introduced to search for an anomalous propagation.

**Table 3.1:** Table of VHE spectra used to search for a PPA, sorted by ascending redshift $z$.

| $i$[1] | AGN | Instrument | $z$ | $E_{\min} - E_{\max}$ (TeV) | $N_{\tau_{\gamma\gamma}<1}$ | $N_{1\leqslant\tau_{\gamma\gamma}<2}$ | $N_{2\leqslant\tau_{\gamma\gamma}}$ |
|---|---|---|---|---|---|---|---|
| 1 | 3C 66B | MAGIC | 0.021 | 0.11 – 1.85 | 4 | 0 | 0 |
| 2 | Markarian 421 | HEGRA | 0.031 | 0.82 – 13.59 | 9 | 1 | 0 |
| 3 | Markarian 421 | HEGRA | 0.031 | 0.82 – 13.59 | 9 | 1 | 0 |
| 4 | Markarian 421 | MAGIC | 0.031 | 0.13 – 1.84 | 7 | 0 | 0 |
| 5 | Markarian 421 | MAGIC | 0.031 | 0.45 – 4.24 | 6 | 0 | 0 |
| 6 | Markarian 421 | WHIPPLE | 0.031 | 0.38 – 8.23 | 9 | 0 | 0 |
| 7 | Markarian 421 | HEGRA | 0.031 | 0.56 – 6.86 | 12 | 0 | 0 |
| 8 | Markarian 421 | H.E.S.S. | 0.031 | 1.12 – 17.44 | 11 | 2 | 0 |
| 9 | Markarian 421 | H.E.S.S. | 0.031 | 1.75 – 23.10 | 11 | 2 | 1 |
| 10 | Markarian 501 | VERITAS | 0.034 | 0.26 – 3.80 | 8 | 0 | 0 |
| 11 | Markarian 501 | VERITAS | 0.034 | 0.27 – 3.86 | 8 | 0 | 0 |
| 12 | Markarian 501 | HEGRA | 0.034 | 0.56 – 21.45 | 14 | 2 | 1 |
| 13 | Markarian 501 | VERITAS | 0.034 | 0.25 – 3.89 | 7 | 0 | 0 |
| 14 | Markarian 501 | MAGIC | 0.034 | 0.17 – 4.43 | 7 | 0 | 0 |
| 15 | Markarian 501 | VERITAS | 0.034 | 0.22 – 1.90 | 6 | 0 | 0 |
| 16 | Markarian 501 | MAGIC | 0.034 | 0.10 – 1.76 | 7 | 0 | 0 |
| 17 | Markarian 501 | VERITAS | 0.034 | 0.25 – 3.81 | 7 | 0 | 0 |
| 18 | Markarian 501 | CAT | 0.034 | 0.40 – 10.00 | 8 | 0 | 0 |
| 19 | 1ES 2344+514 | MAGIC | 0.044 | 0.19 – 4.00 | 7 | 0 | 0 |
| 20 | Markarian 180 | MAGIC | 0.045 | 0.18 – 1.31 | 4 | 0 | 0 |
| 21 | 1ES 1959+650 | HEGRA | 0.048 | 1.59 – 10.00 | 4 | 1 | 0 |
| 22 | 1ES 1959+650 | HEGRA | 0.048 | 1.52 – 10.94 | 6 | 2 | 0 |
| 23 | 1ES 1959+650 | MAGIC | 0.048 | 0.19 – 2.40 | 6 | 0 | 0 |
| 24 | 1ES 1959+650 | MAGIC | 0.048 | 0.19 – 1.53 | 5 | 0 | 0 |
| 25 | PKS 0548-322 | H.E.S.S. | 0.069 | 0.34 – 3.52 | 5 | 0 | 0 |

[1] *References*: 1: Aliu *et al.* (2009); 2: Aharonian *et al.* (2002a); 3: Aharonian *et al.* (2002a); 4: Albert *et al.* (2007d); 5: Aleksić *et al.* (2010); 6: Krennrich *et al.* (2002); 7: Aharonian *et al.* (1999a); 8: Horns (2005); 9: Tluczykont (2011); 10: Gall & for the VERITAS Collaboration (2009); 11: Gall & for the VERITAS Collaboration (2009); 12: Aharonian *et al.* (1999b); 13: Abdo *et al.* (2011b); 14: Abdo *et al.* (2011b); 15: Gall & for the VERITAS Collaboration (2009); 16: Anderhub *et al.* (2009b); 17: Abdo *et al.* (2011b); 18: Djannati-Atai *et al.* (1999); 19: Albert *et al.* (2007c); 20: Albert *et al.* (2006b); 21: Aharonian *et al.* (2003a); 22: Aharonian *et al.* (2003a); 23: Tagliaferri *et al.* (2008); 24: Albert *et al.* (2006e); 25: H. E. S. S. collaboration : F. Aharonian *et al.* (2010); 26: Albert *et al.* (2007a); 27: HESS Collaboration *et al.* (2010b); 28: HESS Collaboration *et al.* (2010b); 29: Aharonian *et al.* (2008d); 30: Acciari *et al.* (2008a); 31: Acciari *et al.* (2009b); 32: Aharonian *et al.* (2005c); 33: Aharonian *et al.* (2005d); 34: Aharonian *et al.* (2007a); 35: Aharonian *et al.* (2009c); 36: Aleksić *et al.* (2012); 37: Acciari *et al.* (2010b); 38: Aharonian *et al.* (2003c); 39: Acciari *et al.* (2009a); 40: Aharonian *et al.* (2007g); 41: Aharonian *et al.* (2006a); 42: Aharonian *et al.* (2006c); 43: HESS Collaboration *et al.* (2010a); 44: Aliu *et al.* (2011); 45: Albert *et al.* (2006a); 46: Acciari *et al.* (2009d); 47: Aharonian *et al.* (2006a); 48: Aharonian *et al.* (2007e); 49: Aliu *et al.* (2012a); 50: Albert *et al.* (2007b); 51: H.E.S.S. Collaboration *et al.* (2012); 52: Aliu *et al.* (2012b); 53: Wagner & H.E.S.S. Collaboration (2010); 54: Aleksić *et al.* (2011a); 55: Albert *et al.* (2008b); 56: Aleksić *et al.* (2011b)

| | | | | | | | |
|---|---|---|---|---|---|---|---|
| 26 | BL Lacertae | MAGIC | 0.069 | 0.16 – 0.70 | 5 | 0 | 0 |
| 27 | PKS 2005-489 | H.E.S.S. | 0.071 | 0.23 – 2.27 | 9 | 0 | 0 |
| 28 | PKS 2005-489 | H.E.S.S. | 0.071 | 0.34 – 4.57 | 9 | 1 | 0 |
| 29 | RGB J0152+017 | H.E.S.S. | 0.080 | 0.31 – 2.95 | 6 | 0 | 0 |
| 30 | W Comae | VERITAS | 0.102 | 0.26 – 1.15 | 5 | 0 | 0 |
| 31 | W Comae | VERITAS | 0.102 | 0.19 – 1.49 | 6 | 1 | 0 |
| 32 | PKS 2155-304 | H.E.S.S. | 0.116 | 0.23 – 2.28 | 6 | 3 | 0 |
| 33 | PKS 2155-304 | H.E.S.S. | 0.116 | 0.23 – 3.11 | 6 | 4 | 0 |
| 34 | PKS 2155-304 | H.E.S.S. | 0.116 | 0.22 – 4.72 | 8 | 9 | 0 |
| 35 | PKS 2155-304 | H.E.S.S. | 0.116 | 0.25 – 3.20 | 3 | 2 | 0 |
| 36 | B3 2247+381 | MAGIC | 0.119 | 0.24 – 0.93 | 4 | 0 | 0 |
| 37 | RGB J0710+591 | VERITAS | 0.125 | 0.42 – 3.65 | 2 | 3 | 0 |
| 38 | H 1426+428 | HEGRA,CAT, WHIPPLE | 0.129 | 0.25 – 10.12 | 6 | 4 | 2 |
| 39 | 1ES 0806+524 | MAGIC | 0.138 | 0.31 – 0.63 | 4 | 0 | 0 |
| 40 | 1ES 0229+200 | H.E.S.S. | 0.140 | 0.60 – 11.45 | 1 | 4 | 3 |
| 41 | H 2356-309 | H.E.S.S. | 0.165 | 0.18 – 0.92 | 6 | 2 | 0 |
| 42 | H 2356-309 | H.E.S.S. | 0.165 | 0.22 – 0.91 | 6 | 2 | 0 |
| 43 | H 2356-309 | H.E.S.S. | 0.165 | 0.23 – 1.71 | 4 | 4 | 0 |
| 44 | RX J0648.7+1516 | VERITAS | 0.179 | 0.21 – 0.48 | 5 | 0 | 0 |
| 45 | 1ES 1218+304 | MAGIC | 0.182 | 0.09 – 0.63 | 5 | 1 | 0 |
| 46 | 1ES 1218+304 | VERITAS | 0.182 | 0.19 – 1.48 | 4 | 3 | 0 |
| 47 | 1ES 1101-232 | H.E.S.S. | 0.186 | 0.18 – 2.92 | 5 | 5 | 3 |
| 48 | 1ES 0347-121 | H.E.S.S. | 0.188 | 0.30 – 3.03 | 2 | 3 | 2 |
| 49 | RBS 0413 | VERITAS | 0.190 | 0.30 – 0.85 | 2 | 2 | 0 |
| 50 | 1ES 1011+496 | MAGIC | 0.212 | 0.15 – 0.59 | 3 | 1 | 0 |
| 51 | 1ES 0414+009 | H.E.S.S. | 0.287 | 0.17 – 1.13 | 3 | 1 | 2 |
| 52 | 1ES 0414+009 | VERITAS | 0.287 | 0.23 – 0.61 | 2 | 2 | 0 |
| 53 | PKS 1510-089 | H.E.S.S. | 0.361 | 0.15 – 0.32 | 4 | 1 | 0 |
| 54 | PKS 1222+21 | MAGIC | 0.432 | 0.08 – 0.35 | 3 | 2 | 0 |
| 55 | 3C 279 | MAGIC | 0.536 | 0.08 – 0.48 | 2 | 1 | 2 |
| 56 | 3C 279 | MAGIC | 0.536 | 0.15 – 0.35 | 1 | 1 | 1 |

### 3.1.1 Method and results

Method 1: The Kolmogorov Smirnov test. The first method compares the behavior of the spectra in the regimes $1 \leqslant \tau_{\gamma\gamma} < 2$ and $2 \leqslant \tau_{\gamma\gamma}$. The choice of $\tau_{\gamma\gamma} \geqslant 2$ is a compromise between an expected effect of mechanisms altering the optical depth and sufficient statistics. The test utilizes the Kolmogorov Smirnov (KS) test that has the advantage of rendering any prior knowledge of the underlying probability distribution function (pdf) unnecessary (e.g., Press *et al.*, 2002). Furthermore, all data points in these two regimes are taken into account, ensuring the largest data sample possible. Each observed flux point $j$ at the energy $E_{ij}$ of the $i$-th spectrum,

$\Phi_{ij}^{\mathrm{obs}}$, is corrected for absorption according to[2]

$$\Phi_{ij} = \exp[\tau_{\gamma\gamma}(E_{ij}, z_i)]\, \Phi_{ij}^{\mathrm{obs}}. \tag{3.1}$$

The following assumptions are made: (1) the part of the absorption-corrected spectrum in the optical thin regime ($\tau_{\gamma\gamma} < 1$) is a valid representation of the actual intrinsic spectrum emitted by the blazar and (2) it can be described with an analytical function $f_i$. The function is either a power law (PL), or in case the fit probability $p_{\mathrm{fit}}^{\mathrm{PL}}$ is less than 5 % a logarithmic parabola (LP),

$$f_i(E) = \begin{cases} N_0(E/1\,\mathrm{TeV})^{-\Gamma} & p_{\mathrm{fit}}^{\mathrm{PL}} \geqslant 0.05, \\ N_0(E/1\,\mathrm{TeV})^{-(\Gamma+\beta\ln(E/1\,\mathrm{TeV}))} & \text{otherwise.} \end{cases} \tag{3.2}$$

The normalization $N_0$, the spectral index $\Gamma$, and the curvature $\beta$ are determined from a $\chi^2$-minimization using the MINUIT package (James, 1998) for `python`, only requiring the spectral parameters to remain finite during the fit. These two functions are consistent with generic features expected from VHE emission models of blazars (see Section 1.1.1). In case the logarithmic parabola fit has a fit probability of $p_{\mathrm{fit}}^{\mathrm{LP}} < 0.05$, or the number of data points in the optical thin regime is less than 2 the spectrum is discarded from the analysis.
The obtained intrinsic spectra, $f_i$, are extrapolated to the data points that correspond to an optical depth $\tau_{\gamma\gamma} \geqslant 1$. The deviation between the extrapolation and the absorption corrected flux is quantified with the normalized ratio

$$R_{ij} = \frac{\Phi_{ij} - f_i(E_{ij})}{\Phi_{ij} + f_i(E_{ij})}, \tag{3.3}$$

with $R_{ij} > 0$ if the absorption corrected data point lies above the extrapolation. The set of all ratios is split into two distributions, the first one, $\mathcal{S}_{1\leqslant\tau_{\gamma\gamma}<2}$, containing all ratios in the transition from the optical thin to the optical thick regime whereas the second one, $\mathcal{S}_{2\leqslant\tau_{\gamma\gamma}}$, consist of the ratios in the optical thick regime. The KS test is used to calculate the probability $p_{\mathrm{KS}}$ that the two distributions follow the same underlying pdf. This probability is derived from the maximum distance $D_0$ of the two cumulative distribution functions (CDFs) of $\mathcal{S}_{1\leqslant\tau_{\gamma\gamma}<2}$ and $\mathcal{S}_{2\leqslant\tau_{\gamma\gamma}}$, and is equal to the probability of finding by chance a value of $D$ larger than the observed value $D_0$. It is given by (Press *et al.*, 2002)

$$p_{\mathrm{KS}}(D > D_0) = Q_{\mathrm{KS}}\left(\left[\sqrt{N_{\mathrm{eff}}} + 0.12 + 0.11/\sqrt{N_{\mathrm{eff}}}\right] D_0\right), \tag{3.4}$$

where $N_{\mathrm{eff}} = N_1 N_2/(N_1 + N_2)$ with $N_1$ being the number of ratios in $\mathcal{S}_{1\leqslant\tau_{\gamma\gamma}<2}$ and $N_2$

[2] The correction should actually be calculated as an average over each energy bin. In Chapter 2 it was shown that the difference is negligible and the introduced error is of the order of a few percent only.

being the number of ratios contained in $\mathcal{S}_{2\leqslant\tau_{\gamma\gamma}}$, and

$$Q_{\mathrm{KS}}(x) = 2\sum_{j=1}^{\infty}(-1)^{j-1}\exp(-2j^2x^2). \tag{3.5}$$

The KS test will result in a low probability especially if the two distributions are shifted against each other. It is less sensitive to detect differences in the tails of the two distributions (Press *et al.*, 2002). The statistical uncertainties $\sigma_{ij}$ (68 % confidence) on $\Phi_{ij}$ enter only through the fit to the intrinsic spectra. Interestingly, the statistical uncertainties seem to be overestimated. This can be seen from the the fit residuals, given by

$$\chi_{ij} = \frac{\Phi_{ij} - f_i(E_{ij})}{\sigma_{ij}}, \tag{3.6}$$

which should follow a (0,1) normal distribution. Using the Anderson-Darling test (basically a modified KS test; Anderson & Darling, 1954), the probability of the entire $\chi_{ij}$-distribution to be compatible with a Gaussian is only $p_{\mathrm{AD}} = 0.02$, with a mean of $\overline{\chi} = 0.06 \pm 0.04$ and a standard deviation $\sigma_\chi = 0.85 \pm 0.03$. This is merely compatible with a (0,1) normal distribution (the compatibility is found to be $5.59 \times 10^{-4}$ using the KS test), and especially the low value of $\sigma_\chi$ suggests that the statistical uncertainties of the spectra are indeed overestimated.

If the KD model describes the entire intrinsic spectrum correctly, one expects that in both distributions $\mathcal{S}_{1\leqslant\tau_{\gamma\gamma}<2}$ and $\mathcal{S}_{2\leqslant\tau_{\gamma\gamma}}$ the values of the ratios $R_{ij}$ scatter randomly around zero, and as a consequence both CDFs should be close to 0.5 for $R_{ij} \sim 0$. However, as shown in Figure 3.2, the CDFs of the two distributions are shifted against each other. All except two data points of the distribution of $\mathcal{S}_{2\leqslant\tau_{\gamma\gamma}}$ are larger than zero, indicating that the correction of the chosen EBL model is too strong at high optical depths. The maximum distance is found to be $D_0 = 0.68$ and the probability that the two underlying pdfs are equal is $p_{\mathrm{KS}} = 3.39 \times 10^{-5} = 3.89\sigma$ (one sided confidence interval). The two distributions show also a different behavior concerning the correlation between the ratios $R_{ij}$ and the corresponding optical depths $\tau_{\gamma\gamma}(z_i, E_{ij})$. The $\mathcal{S}_{1\leqslant\tau_{\gamma\gamma}<2}$ sample shows a negative correlation (using the Spearman-rank correlation coefficient, see, e.g., Press *et al.*, 2002), $cor(\mathcal{S}_{1\leqslant\tau_{\gamma\gamma}<2}) = -0.15$ with a probability of a non-zero correlation of $p_{cor}(\mathcal{S}_{1\leqslant\tau_{\gamma\gamma}<2}) = 0.11$. For the optical thick sample one finds a positive correlation of $cor(\mathcal{S}_{2\leqslant\tau_{\gamma\gamma}}) = 0.39$ and $p_{cor}(\mathcal{S}_{2\leqslant\tau_{\gamma\gamma}}) = 0.09$. This is also apparent from the scatter plot in Figure 3.3 which shows the ratios versus the optical depth and a smoothed average of the two quantities (solid black line, obtained from a LOESS average with the degree of the underlying polynomials set to 1, see Cleveland 1979).

Method 2: The *t* test. The second method relies on the *t* test which gives the probability that a measured mean of Gaussian distributed data is compatible with a

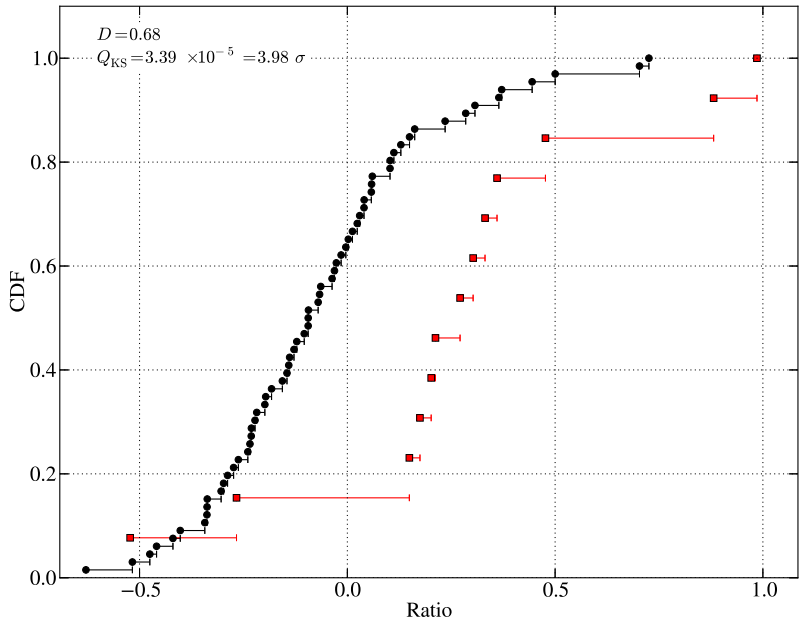


**FIGURE 3.2:** Cumulative distribution functions of the ratios $R_{ij}$ corresponding to an optical depth $1 \leqslant \tau_{\gamma\gamma} < 2$ (black bullets) and $2 \leqslant \tau_{\gamma\gamma}$ (red squares) for the EBL model of Kneiske & Dole (2010).

theoretical one. The method of computing this probability $p_t$ is similar to the one presented for the KS test above. Again, the absorption corrected spectra are fitted with the analytical functions of Eq. (3.2), this time including all data points. Hence, no extrapolation from the optical thin to the optical thick regime is required. The fit residuals are computed according to Eq. (3.6). As noted above, the fit residuals should follow a (0,1) normal distribution, and this should also be true for the subset of residuals, $\mathcal{R}_{2\leqslant\tau_{\gamma\gamma}}$, that correspond to the $N_{2\leqslant\tau_{\gamma\gamma}}$ data points in the optical thick regime, $\tau_{\gamma\gamma} \geqslant 2$. This requires the additional assumption that the distribution $\mathcal{R}_{2\leqslant\tau_{\gamma\gamma}}$ indeed follows a Gaussian with mean $\bar{\chi}$ and standard deviation $\sigma_\chi$ but allows to incorporate the statistical uncertainties self-consistently. For the null hypothesis $\bar{\chi} = 0$ (i.e., the absorption is correctly described by the KD model in the optical thick regime) the variable

$$t_0 = \frac{\bar{\chi}}{\sqrt{\sigma_\chi / N_{2\leqslant\tau_{\gamma\gamma}}}} \tag{3.7}$$

follows a $t$ distribution and the probability to find a value $t > t_0$ is defined as

$$p_t(t > t_0) = 1 - F(t_0). \tag{3.8}$$

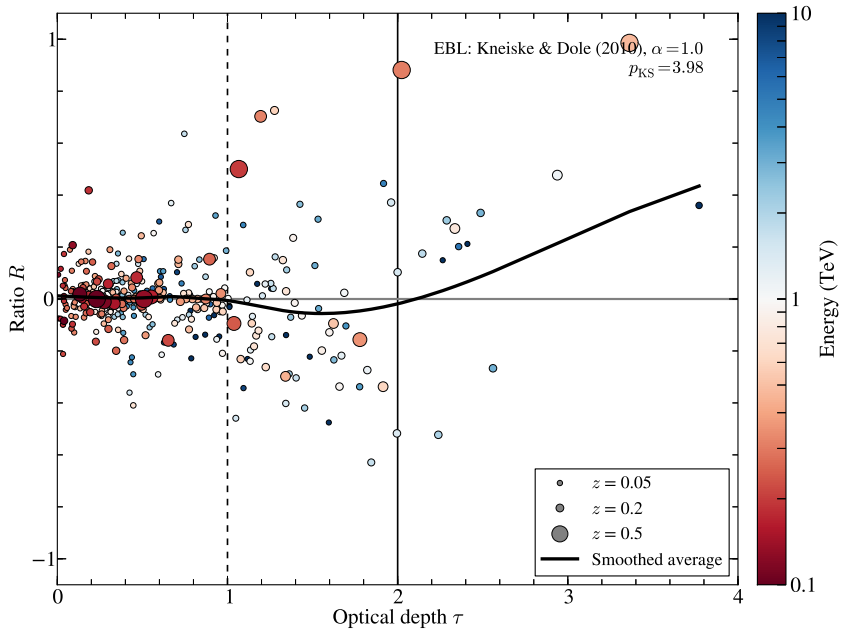


**FIGURE 3.3:** Scatter plot of the ratios $R$ versus the optical depth $\tau_{\gamma\gamma}$. The marker size corresponds to the redshift of the source, while the color coding indicates the energy of the corresponding energy bin. The ratios of the points included in the fit to determine the intrinsic spectrum ($\tau_{\gamma\gamma} < 1$) show a mild scatter around zero as expected from the $\chi^2$-minimization procedure. The scatter increases for the ratios in $\mathcal{S}_{1\leqslant\tau_{\gamma\gamma}<2}$ but on average the ratios stays close to zero, also seen by the smoothed average (solid black line). Above $\tau_{\gamma\gamma} = 2$ a clear trend towards higher values of $R$ is visible.

The cumulative distribution function $F(t)$ for $\nu = N_\chi - 1$ degrees of freedom of the Student's $t$ distribution is given by (e.g., Brandt, 1999):

$$F(t_0) = \int_{-\infty}^{t_0} f(t)\mathrm{d}t = \frac{\Gamma\left(\frac{\nu+1}{2}\right)}{\sqrt{\pi\nu}\,\Gamma\left(\frac{\nu}{2}\right)} \int_{-\infty}^{t_0} \left(1 + \frac{t}{\nu^2}\right)^{-\frac{\nu+1}{2}} \mathrm{d}t, \tag{3.9}$$

with the pdf $f(t)$ and the Gamma function $\Gamma$. A mean of the residuals in $\mathcal{R}_{2\leqslant\tau_{\gamma\gamma}}$ greater than zero indicates an overcorrection of the spectra with the tested EBL model and will result in larger values of $t_0$ and smaller values of $p_t$. Bad fit qualities, on the other hand, will lead to larger values of $\sigma_\chi$ and smaller values of $t_0$. Not discarding fits with low fit probabilities will thus lead to a conservative result for $p_t$, i.e., in accordance with the null hypothesis, and this will be done here. Similarly, if the measured uncertainties are overestimated, $\bar{\chi}$ will, by definition, tend to smaller

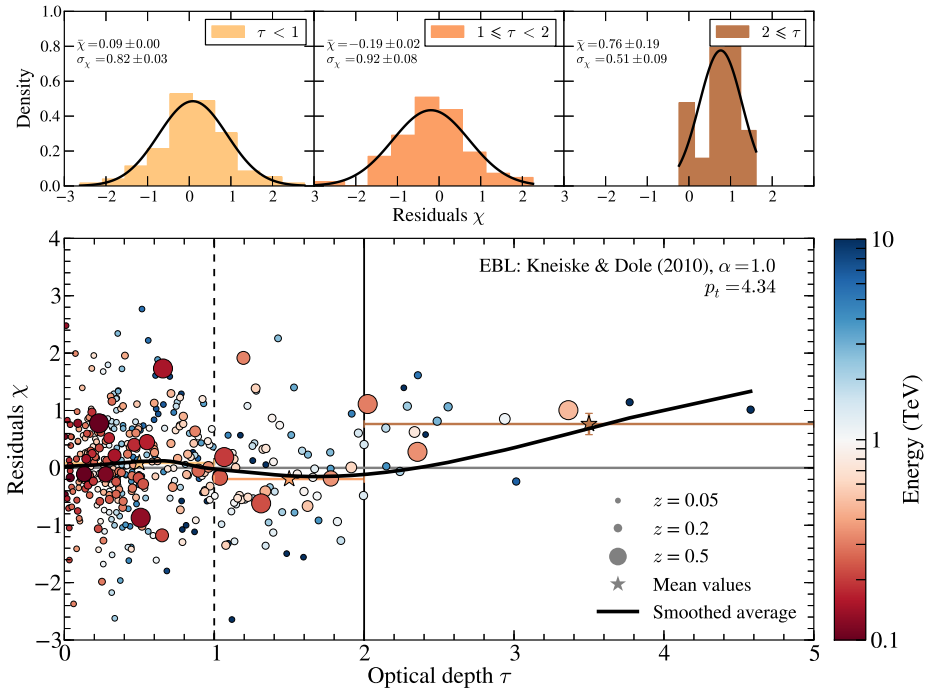


**Figure 3.4:** Same as Figure 3.3, this time showing the residuals $\chi$ versus the optical depth. Again, for $\tau_{\gamma\gamma} \geqslant 2$ the residuals increase towards positive values. The top panels show the histograms of the residual distribution for the different optical depth regimes. The mean values of the distributions are shown as stars in the scatter plot.

values and consequently also to values of $p_t$ closer to one.

With this method, one would expect a mean of $\mathcal{R}_{2\leqslant\tau_{\gamma\gamma}}$ compatible with zero if the KD model describes the data correctly. Similar to the ratios in the optical thick regime, the residuals in the $\mathcal{R}_{2\leqslant\tau_{\gamma\gamma}}$ sample show an indication for a positive correlation with the optical depth. It is found to be $cor(\mathcal{R}_{2\leqslant\tau_{\gamma\gamma}}) = 0.11$ with $p_{cor}(\mathcal{R}_{2\leqslant\tau_{\gamma\gamma}}) = 0.34$. The distribution has a mean of $\bar{\chi} = 0.76 \pm 0.19$ and a standard deviation $\sigma_\chi = 0.51 \pm 0.09$. The aforementioned Anderson-Darling test gives a probability of $p_{\mathrm{AD}} = 0.27$ that the sample follows a Gaussian distribution and the application of the $t$ test is justified. It results in a probability of $p_t = 7.23 \times 10^{-6} = 4.34\,\sigma$ for the $\bar{\chi} = 0$ hypothesis and confirms the indication found with the KS test that the KD model overcorrects the spectra in the optical thick regime. Figure 3.4 shows again a scatter plot of the residuals versus the optical depths (bottom panel) together with the histograms of the different optical depth regimes (top panel).

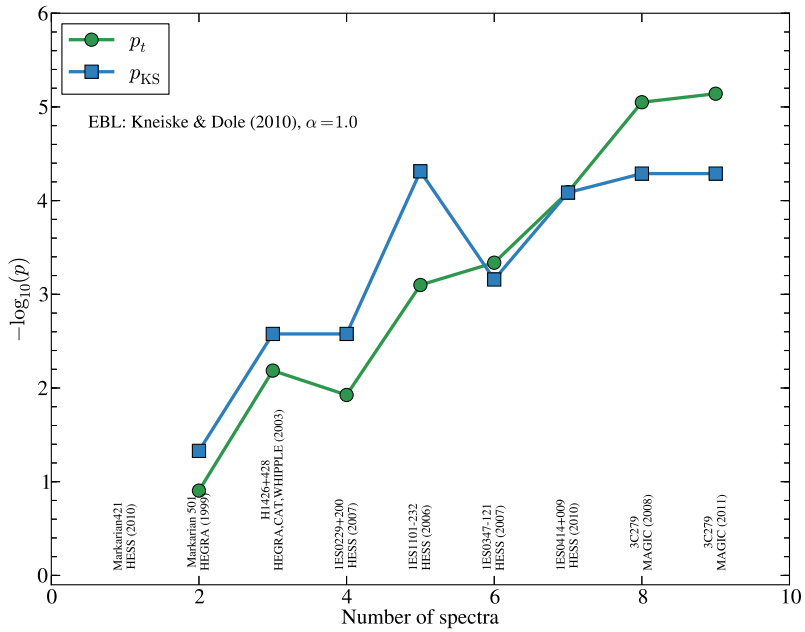


**FIGURE 3.5:** Dependence of the test significances on the spectra in the optical thick sample. For each point, the given spectrum is added to the sample (ordered by redshift). For only one spectrum, the number of data points is not sufficient to calculate the test significances.

### 3.1.2 SYSTEMATIC EFFECTS

The methods introduced above of searching for an anomalous propagation of VHE $\gamma$-rays, are subject of systematic uncertainties related to the unknown intrinsic VHE spectra, the reconstruction of the observed spectra, a potential selection bias of extragalactic VHE emitting sources, and the unknown level of the EBL density. In the following, the impact of these effects on the significance is estimated.

SOURCE RELATED EFFECTS. The indication is not caused by a single source spectrum only. This conclusion is non-trivial, as it is beforehand unknown if, e.g., the different source types such as BL Lacs or FSRQs, or the source distances introduce a bias of some sort. However, it is evident from the scatter plots (Figures 3.4 and 3.6), as different AGN at different energies and redshifts contribute to the overall significance. Sorting the sources by redshift and including them one at a time each time recalculating the *t* and KS test shows that the significance gradually increases with increasing number of data points in the optical thick sample. This is shown in the cumulative plot in Figure 3.5. For the KS test, the significance stays constant if 1ES 0229+200 and one spectrum of 3C 279 are included, since these

two spectra do not have enough data points in the optical thin regime to determine the intrinsic source spectrum. The significance decreases for 1ES 0347-121 due to the extrapolation of the two data points in the optical thin regime: All remaining data points are below the expected flux. All spectra and their corresponding fits can be found in Figure A.1 in Appendix A. The largest contribution comes from the spectrum of 1ES 1101-232. Excluding this source results in a significance of $p_{\mathrm{KS}} = 1.32 \times 10^{-3} = 3.01\,\sigma$ and $p_t = 1.34 \times 10^{-4} = 3.65\,\sigma$, respectively. In general, the sources contribute more or less equally to the overall significance, and a redshift or source-class dependent effect is not evident.

It is difficult to say how a selection bias affects the PPA significance, and this question might be answered in the future by an all-sky instrument (e.g., the High-Altitude Water Cherenkov Observatory, HAWC[3]; Sinnis *et al.* 2005). At the moment, no all-sky survey at VHE is available, and instead several search criteria are adopted to select promising AGN targets. For instance, the sources should be bright in X-rays or have a high VHE flux according to the extrapolation of their *Fermi*-LAT spectrum. Likewise, an observation might be triggered by a high state of the object at frequencies below the VHE regime. A non-detection might have a number of reasons such as the observation conditions, the intrinsic spectrum, or the activity state of the source. Blazars are known to be variable sources, and the VHE observations are carried out in different states of the sources' activity.

In principle, the overcorrection could be caused by an intrinsic spectral hardening. Such features have been observed in flaring states of several sources and theoretically discussed (see, e.g., Abdo *et al.*, 2011c; Lefa *et al.*, 2011b, for the observation and discussion of a spectral hardening at GeV energies during a flaring state of Mkn 501). Moreover, in certain emission scenarios, an exponential pile-up at the high energy end of the spectra is expected (e.g., Aharonian *et al.*, 2002b). Another possibility might be the upscattering of CMB photons in extended jets if the particles are still being accelerated to relativistic speeds on the kpc scale (Böttcher *et al.*, 2008). This mechanism would show a redshift dependence, since the energy density of the CMB scales with $(1 + z)^4$. These effects might mimic the indication found here. Except for the upscattering of CMB photons in jets, these spectral features should not depend on the redshift of the source and should thus show up at arbitrary values of the optical depth. Otherwise, this would correspond to an unnatural fine-tuning. This is also underlined in Figure 3.6, which shows the ratios and residuals, respectively, versus the corresponding energy of the data points. No systematic trend towards higher energies is seen; the distribution appears almost flat for both tests.

[3] The sensitivity of HAWC at low energies will probably not be sufficient to probe the optical thin and thick regime simultaneously. However, HAWC will potentially be able to detect transient sources, such as gamma-ray bursts at high redshift. Such observations will give further information on the significance of the PPA.

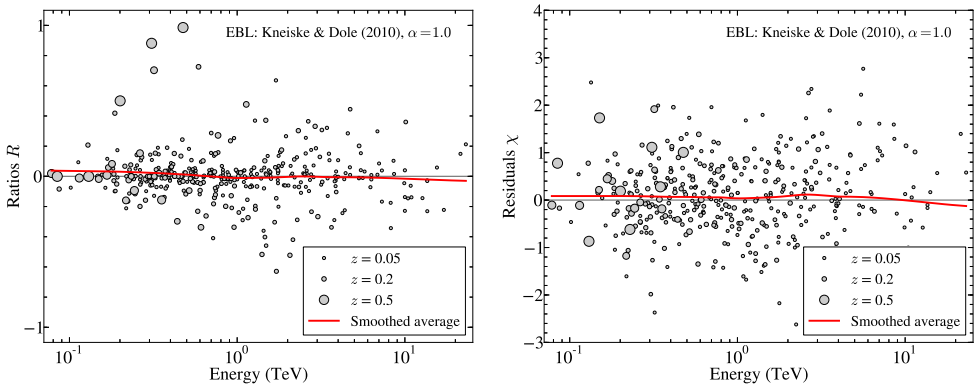


**FIGURE 3.6:** Scatter plots for the ratios (left panel) and residuals (right panel) against the corresponding energy. The point size is scaled with the redshift of the corresponding source.

ENERGY RESOLUTION. The energy resolution of IACTs is limited due to several reasons (Hofmann *et al.*, 1999, and Section 1.3.2): For instance, the localization of the shower core can be erroneously reconstructed, the shower development fluctuates due to variations of the height of the first interaction of the VHE $\gamma$-ray with the atmosphere, and the number of photoelectrons fluctuates because of the Poissonian noise in the photon signal at the photocathode. Further uncertainties are introduced by the incomplete knowledge of the telescope system that influences Monte-Carlo simulations of air showers. The limited resolution might lead to a false reconstruction of events in the highest energy bin instead of the second last one, resulting in an overestimation of the flux in the last bin (sometimes referred to as the spillover effect). Another possibility is the false reconstruction of events with energies $E > E_{\mathrm{max}}$ into the highest energy bin. As a result, the flux in the last significantly detected bin is again overestimated, and a higher energy bin that might result in a low value of the ratio or the residual falls below the detection significance. Especially soft spectra could be affected by this effect. A conservative approach to eliminate any bias introduced by the spillover effect is to remove the last energy bin of all spectra. This results in a reduced significance of $p_{\mathrm{KS}} = 1.02 \times 10^{-3} = 3.09\,\sigma$ and $p_t = 7.28 \times 10^{-3} = 2.44\,\sigma$. However, this effect should in general be accounted for in the spectral reconstruction (e.g., forward or unfolding techniques).

A systematic uncertainty, inherent of all IACT experiments, is the unknown absolute energy calibration. The relative uncertainty of the reconstructed energy of the primary $\gamma$-ray that initiated the shower is commonly estimated to be $\pm 15\,\%$ (e.g., Aharonian *et al.*, 2006d). The effect on the test results is assessed by conservatively downscaling the energies of all data points by this value. Consequently, the number of data points in the optical thick regime is reduced to 12 for both tests. The significances change to $p_{\mathrm{KS}} = 2.93 \times 10^{-4} = 3.44\,\sigma$ and $p_t = 1.18 \times 10^{-4} = 3.68\,\sigma$.

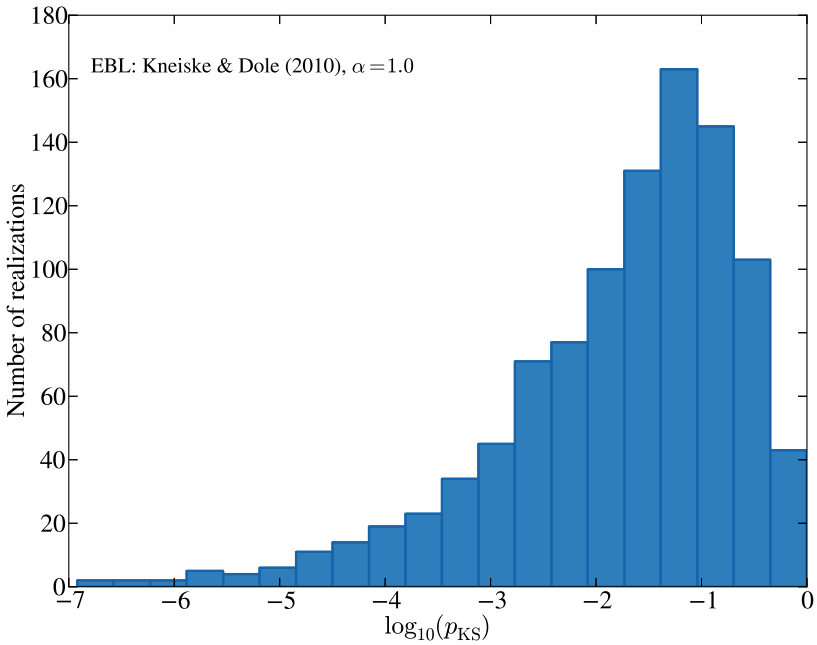


**FIGURE 3.7:** Histogram of the significances of the KS test using the mock data sample of galactic spectra.

Combining the two effects (spillover and unknown absolute energy scale) leaves only a marginal significances of the PPA of $p_{\mathrm{KS}} = 6.74 \times 10^{-3} = 2.44\,\sigma$ and $p_t = 2.33 \times 10^{-2} = 1.99\,\sigma$. Especially for the $t$ test, this value is close to the test result if no absorption correction is applied. These values are found to be $p_{\mathrm{KS}} = 0.32 = 0.47\,\sigma$ and $p_t = 3.37 \times 10^{-2} = 1.83\,\sigma$. However, a value of ±5 % for the energy uncertainty seems to be more realistic as derived from a cross calibration between IACTs and the *Fermi*-LAT (Meyer *et al.*, 2010). The *Fermi*-LAT was calibrated on ground using particle beams of accelerators (Atwood *et al.*, 2009). Thus, the corresponding results underestimate the true significances.

MOCK DATA SAMPLE. As noted above, the spectral reconstruction and the unknown absolute energy scale might cause the indication for the anomaly. An independent data set of galactic spectra is used to investigate such a potential bias (see Appendix B for a list of the used spectra). A redshift randomly drawn from the distribution of redshifts of the sources observed at VHE (see Table 3.1) is assigned to each spectrum of a galactic VHE source in order to define the samples $\mathcal{S}_{1\leqslant\tau_{\gamma\gamma}<2}$, $\mathcal{S}_{2\leqslant\tau_{\gamma\gamma}}$, and $\mathcal{R}_{2\leqslant\tau_{\gamma\gamma}}$, but the spectra are not corrected for absorption. This is repeated one thousand times and the resulting test significances are shown in Figure 3.7. The significance is below 0.01 for 33 % and above $5\,\sigma = 2.87 \times 10^{-7}$ for 0.1 % of all

realizations for the KS test. For the *t* test, no realization results in a significance smaller than 1 %. This result shows again that the *t* test is the more conservative choice, as discussed above: The galactic spectra are usually measured with high precision and small statistical uncertainties. Thus, the fit qualities are often poor, and the residual distributions are broad, giving a smaller value for *t* [cf. Eq. (3.7)] and a smaller overall significance. The KS test, on the other hand, shows a tendency to produce a slight bias in the data set. One has to keep in mind, however, that the galactic sources have different spectral properties and are measured in some cases up to $\sim 50\,\mathrm{TeV}$ in contrast to the AGN spectra. This causes the high significances with $p_{\mathrm{KS}} < 10^{-6}$: In these cases, the ratios in $\mathcal{S}_{2\leqslant\tau_{\gamma\gamma}}$ are always below 0, i.e., below the extrapolation, indicating a spectral cut-off is present in the spectra. For the *t* test, no extrapolation is necessary, so that this behavior is not encountered.

EBL DENSITY. Since the KD model closely follows the lower limits on the EBL density in the infrared, it can be expected to predict the lowest opacity of the Universe and consequently the lowest significance of the pair production anomaly. Different EBL models that result in higher values of the optical depth not only change the values of the ratios $R_{ij}$ and residuals $\chi_{ij}$, but also the number of data points that enter the different distributions used for the tests. For sufficiently high EBL densities, many data points will populate the optical thick regime, and as long as the overall fit stays reasonable the distribution $\mathcal{R}_{2\leqslant\tau}$ will be shifted closer to zero, and the PPA significance will decrease. Likewise, the cumulative distribution functions $\mathcal{S}_{1\leqslant\tau_{\gamma\gamma}<2}$ and $\mathcal{S}_{2\leqslant\tau_{\gamma\gamma}}$ will become more similar, and less points of the spectrum can be used to determine the intrinsic spectrum.
This behavior is demonstrated with the EBL model of Franceschini *et al.* (2008, henceforth FRV model). It is also allowed for an additional scaling $\alpha$ of the optical depth. A best-fit value of $\alpha = 1.27^{+0.18}_{-0.15}$ is obtained from H.E.S.S. observations for the FRV model (H.E.S.S. Collaboration *et al.*, 2013). The scatter plots of Figure 3.8 show that more data points populate the optical thick regime. The significances are $p_{\mathrm{KS}} = 1.66{\times}10^{-2} = 2.13\,\sigma$ and $p_t = 4.61{\times}10^{-3} = 2.60\,\sigma$ for $\alpha = 1$. For $\alpha = 1.3$, the tests give $p_{\mathrm{KS}} = 0.17 = 0.97\,\sigma$ and $p_t = 2.33 \times 10^{-4} = 3.50\,\sigma$. However, the same trend as with the KD model of increasing ratios and residuals with increasing optical depth is clearly visible. Especially for the KS test, the distant sources have not sufficient number of data points to determine the intrinsic spectrum. Since the *t* test does not suffer from this problem, it is better suited to probe the PPA for arbitrary EBL models. The significance is also reduced if the KD model is scaled downwards. For $\alpha = 0.7$, the indication becomes marginal, $p_{\mathrm{KS}} = 4.34 \times 10^{-3} = 2.63\,\sigma$ and $p_t = 4.23 \times 10^{-2} = 1.73\,\sigma$, and only six data points remain in the regime $\tau_{\gamma\gamma} \geqslant 2$. Below $\alpha \approx 0.6$, not enough data points are left in the optical thick regime. Such a low EBL density is, however, in strong conflict with the lower limits derived from galaxy number counts.
The significances of the different systematic checks are summarized in Table 3.2.

**Table 3.2:** Summary table of test results including different systematic uncertainties. For comparison, the test results are also shown in the last line if no absorption correction is applied to the spectra.

| Systematic check | Significance $p_{\mathrm{KS}}$ | | Significance $p_t$ | |
|---|---|---|---|---|
| -15 % energy scaling | $2.93 \times 10^{-4}$ | $3.44\,\sigma$ | $1.18 \times 10^{-4}$ | $3.68\,\sigma$ |
| Removed last energy point | $1.02 \times 10^{-3}$ | $3.09\,\sigma$ | $6.74 \times 10^{-3}$ | $2.44\,\sigma$ |
| Removed last energy point and -15 % energy scaling | $6.74 \times 10^{-3}$ | $2.44\,\sigma$ | $2.33 \times 10^{-2}$ | $1.99\,\sigma$ |
| FRV model | $1.66 \times 10^{-2}$ | $2.13\,\sigma$ | $4.61 \times 10^{-3}$ | $2.60\,\sigma$ |
| FRV model scaled by 1.3 | 0.17 | $0.97\,\sigma$ | $2.33 \times 10^{-4}$ | $3.50\,\sigma$ |
| KD model scaled by 0.7 | $4.34 \times 10^{-3}$ | $2.63\,\sigma$ | $4.23 \times 10^{-2}$ | $1.73\,\sigma$ |
| No absorption correction | 0.32 | $0.47\,\sigma$ | $3.37 \times 10^{-2}$ | $1.83\,\sigma$ |

The indication for the PPA persists if no drastic systematics are invoked (such as the downscaling of the EBL by 30 %, or an energy scaling of $-15$ % and discarding the highest energy point of each spectrum). As long as the distribution $\mathcal{R}_{2\geqslant\tau_{\gamma\gamma}}$ follows a Gaussian, the *t* test is the more reliable variant to search for the PPA, as it does not rely on an extrapolation to the optical thick regime, includes all spectra, and gives conservative results if the fit probability for a spectrum is small.
A definite answer on the indication of the PPA at VHE can only come with further measurements of the EBL and observations of VHE sources in the optical thick regime. At the moment, the sample of spectra with data points with $\tau_{\gamma\gamma} \geqslant 1$ is dominated by sources between $0.1 \lesssim z \lesssim 0.2$ with a median redshift of $\tilde{z} = 0.14$ and a median energy $\tilde{E} = 1.49$ TeV. Consequently, the tests are most sensitive to changes in the EBL at infrared wavelengths [cf. Eq. (1.16)]. Observations of nearby sources beyond tens of TeV and of distant sources beyond several hundreds of GeV will allow to probe the entire wavelength range of the EBL.

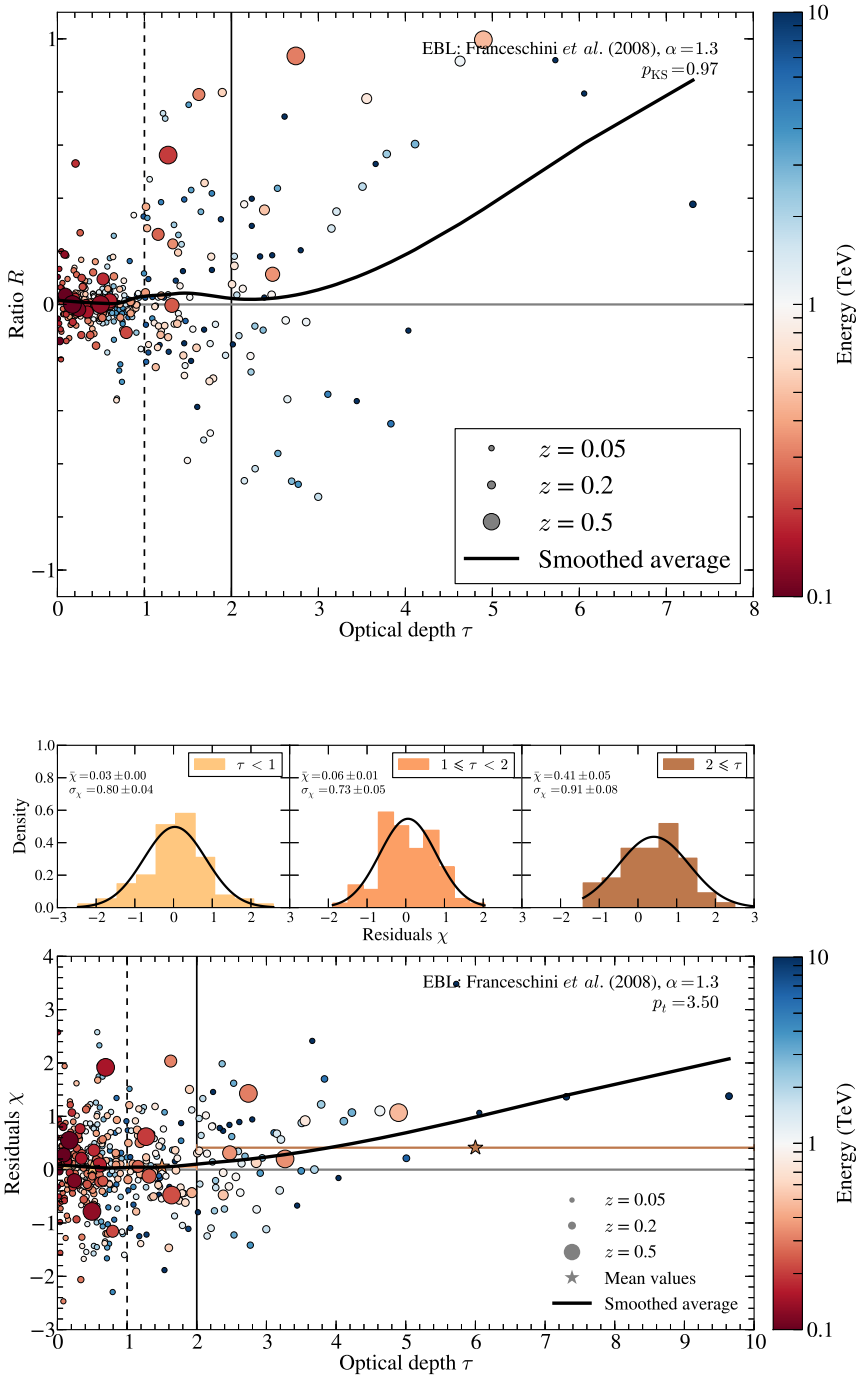


**FIGURE 3.8:** Same as Figures 3.3 (top panel) and 3.4 (bottom panel), but the EBL density is given by the model of Franceschini *et al.* (2008), which is additionally scaled upwards by $\alpha = 1.3$.

## 3.2 Observations of high energy $\gamma$-rays in the optical thick regime with the *Fermi*-LAT

Observations with the LAT on board the *Fermi* satellite enable an independent test for the indication of an anomalous propagation of $\gamma$-rays at HE. In the following, photons detected with the *Fermi*-LAT will be associated with extragalactic sources of known redshift. Events will be identified that correspond to an optical depth $\tau_{\gamma\gamma} \geqslant 1$ (high optical depth photon, HOP). These sources will be further analyzed in order to calculate the probability of detecting the associated photon under the assumption of different EBL models.
Single photons have already been used by Abdo *et al.* (2010b) with one year of *Fermi*-LAT data to constrain the opacity of the Universe, and a similar method will be utilized here. Neronov *et al.* (2012b) associated single photons with energies above 100 GeV with sources of redshifts > 0.5 to search for promising distant VHE source candidates. None of these studies, however, based their search explicitly on the optical depth regime. They have not tested the consistency of EBL predictions with these photon observations.

### 3.2.1 Sample of high optical depth photons

For each photon with an energy $E \geqslant 10$ GeV and arriving from a galactic latitude $b > 10^\circ$ observed in the first 4.3 years (until November 29, 2012) of *Fermi*-LAT operations, a counterpart is searched for among AGN. Only AGN listed in the second *Fermi*-LAT source catalog (Nolan *et al.*, 2012, henceforth 2FGL) with known redshift are considered. Additionally, the AGN identified as VHE emitters in *Fermi*-LAT data (Neronov *et al.*, 2011) are included. The redshifts are obtained from the Roma BZCAT catalog[4] (Massaro *et al.*, 2009) and Shaw *et al.* (2013), whereas the source positions are taken from the Nasa/IPAC extragalactic database[5].
The events are extracted using the *Fermi science tools* v9r27p1[6]. Besides the energy cut, photons with a zenith angle[7] $Z < 100^\circ$ are selected in order to minimize the contamination from $\gamma$-rays originating from the Earth's albedo. In addition, only photons of the P7V6_ULTRACLEAN instrumental response function (IRF) are used, ensuring the highest data quality with the least contamination from backgrounds (see Section 1.3.1). Furthermore, the standard cuts recommended by the LAT team on the time interval are made: Time periods are excluded where the Earth is either in the field of view, the rocking angle of the space craft is larger than 52°, or the data quality or LAT configuration is flagged as bad.

[4] `http://www.asdc.asi.it/bzcat/`
[5] NED, `http://ned.ipac.caltech.edu/`
[6] `http://fermi.gsfc.nasa.gov/ssc/data/analysis/`
[7] The zenith angle is the angle between the surface normal of the Earth passing through the LAT and the arrival direction of the photon.

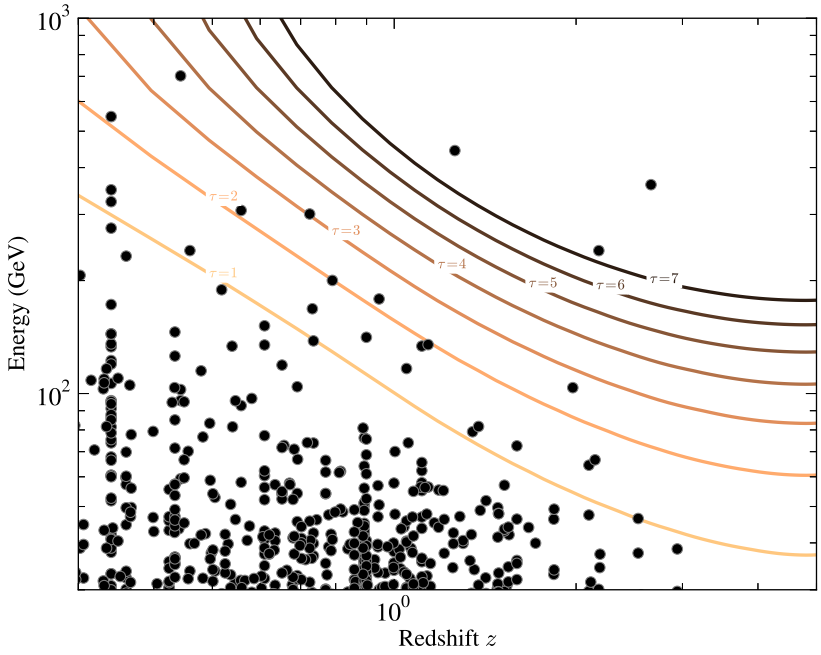


**FIGURE 3.9:** Same as Figure 3.1, this time for the all photons of the P7V6_ULTRACLEAN event class associated with AGN of known redshift and with energies above 10 GeV.

A photon will be associated with an AGN if the angular distance $d$ between the event and the source position is smaller than the 68 % confidence radius, $r_{68}$, of the photon. This confidence radius is different for each photon event. Here, the in-flight calibrated PSF is used which is constant for all inclination angles (see Section 1.3.1 for further details). If a counterpart is found, the source redshift can be used together with the photon energy to calculate the optical depth of the event. All associated photons are shown in Figure 3.9 in the Fazio-Stecker representation. In total, $N_{\mathrm{HOP}} = 23$ photons from $N_{\mathrm{src}} = 21$ sources are detected with $\tau_{\gamma\gamma} \geqslant 1$ ($N_{\mathrm{HOP}} = N_{\mathrm{src}} = 9$ for $\tau_{\gamma\gamma} \geqslant 2$) in the KD model and are listed in Table 3.3. The HOP corresponds to the highest energy photon associated with each source in all but one case, the exception being 1ES 0502+675, for which three photons with $\tau_{\gamma\gamma} \geqslant 1$ can be associated. The reconstructed energy of the highest energy photon originating from RBS 0405 is above 700 GeV and above 500 GeV for 1ES 0502+675. Consequently, only a small part of the electromagnetic shower is contained in the calorimeter (the vertical radiation length of the calorimeter is $8.6 \times X_0$), but the energy can be reconstructed from the longitudinal shower profile (Atwood *et al.*, 2009, and Section 1.3.1). However, the templates for the diffuse background emission only reach up to ∼ 511 GeV. Hence, no trustworthy reconstruction of the source

spectra up to these energies is possible, and the sources have to be excluded from further analysis. The other photons have energies from 46 GeV up to 444 GeV, and the source redshifts range from $0.34 \leqslant z \leqslant 2.661$.
Most HOPs have a relatively large $r_{68} \gtrsim 0.25^\circ$ since their first interaction occurred inside the thick layer of the *Fermi*-LAT tracker (back converted events) at the expense of a reduced angular resolution (see Section 1.3.1). The thickness of the last four tungsten foils is six times larger than that of the first 12, and thus the high energetic HOPs convert with a higher probability in this back part of the tracker.
Most sources are FSRQs that are flagged as variable in the 2FGL. The variability is confirmed in the light curves of the sources which can be found in Appendix C. The detection significances of the associated AGN range from $\sim 5.4\,\sigma$ to $\sim 104\,\sigma$, as can be seen from Table 3.3. They are roughly equal to the square root of the $TS$ values, which are the result of a log likelihood ratio test of the null hypothesis (no source) and the alternative hypothesis that a source is present at a given position (see the 2FGL). Interestingly, with these properties, most of the associated sources are not included in the analysis of Ackermann *et al.* (2012c), who restricted their sample to BL Lac objects that have been significantly detected above 3 GeV. Ackermann *et al.* (2012c) found an imprint of the EBL in 150 BL Lac spectra and a best-fit value of the EBL normalization of $\alpha = 1.02 \pm 0.23$ for the FRV model. Consequently, the analysis presented here is complementary to Ackermann *et al.* (2012c) and concentrates on the optical thick regime only.

### 3.2.2 Method for searching the anomaly in *Fermi*-LAT data

The probability of detecting each of the HOPs depends on the intrinsic source spectrum, the EBL, and the probability that the associated photon originates from diffuse background emission rather than the AGN itself.
The *Fermi*-LAT covers a broad energy range and, thus, the intrinsic (or un-attenuated) spectrum can be extracted from *Fermi*-LAT data as well. Once the intrinsic spectrum is determined, it can be extrapolated to higher energies and absorbed with a particular EBL model. The only assumption that enters is that the spectra do not harden towards higher energies. This is basically the same assumption that was already made in the previous section. It is highly unlikely that a spectral hardening or exponential pile-up occurs for all analyzed sources in the optical thick regime. The intrinsic spectrum will be described with a simple power law to ensure a conservative prediction of the number of expected photons in the optical thick regime and is determined as follows (similar to Ackermann *et al.*, 2012c): First, the spectrum between 1 GeV and 500 GeV is fitted with a power law. The fit is not extended down to, e.g., 100 MeV. For most sources, the fit would be dominated by the low energy part of the spectrum, potentially leading to an inaccurate extrapolation to high energies. The same time range, IRF, and cuts are applied to the raw data as in the previous Section. The binned likelihood analysis chain included in the `python`

**TABLE 3.3:** Associated photons that correspond to an optical depth > 1, sorted by descending $\tau_{\gamma\gamma}$.

| $i$ | Source | $E_{\mathrm{HOP}}$ (GeV) | $z$[a] | $\tau_{\gamma\gamma}$[b] | $r_{68}$ (degrees) | $d$ (degrees) | $\Delta E$[c] (GeV) | $\lambda_{\mathrm{pred}}$[d] ($\times10^{-2}$) | $p$[e] ($\times10^{-3}$) | $\lambda_{\mathrm{diff}}$[f] ($\times10^{-3}$) | $\lambda_{\mathrm{all}}$[g] ($\times10^{-2}$) | $P_{\mathrm{src}}$[h] | Source type[j] | Variability index[k] |
|---|---|---|---|---|---|---|---|---|---|---|---|---|---|---|
| 1 | TXS 0907+230 | 360.09 | 2.661 | 11.64 | 0.27 | 0.19 | 30.52 | $2.1\times10^{-6}$ | 0.36 | 0.36 | 1.01 | $2.2\times10^{-3}$ | FSRQ (LSP) | 108.18 |
| 2 | S5 1039+81 | 444.00 | 1.260 | 8.66 | 0.26 | 0.18 | 53.79 | $2.0\times10^{-8}$ | 0.14 | 0.14 | 1.07 | $1.1\times10^{-2}$ | FSRQ (LSP) | 51.87 |
| 3 | PMN J2135-5006 | 240.30 | 2.181 | 7.53 | 0.27 | 0.23 | 29.99 | $5.1\times10^{-7}$ | 9.15 | 9.19 | 2.13 | 0.11 | FSRQ (Unc.) | 35.09 |
| 4 | RBS 0405 | 702.21 | 0.443 | 3.70 | 0.26 | 0.21 | 107.87 | ... | ... | ... | ... | ... | BL Lac (HSP) | 31.62 |
| 5 | Ton 599 | 300.88 | 0.725 | 3.03 | 0.27 | 0.26 | 33.46 | 0.09 | 2.00 | 0.70 | 1.42 | 0.95 | FSRQ (LSP) | 406.93 |
| 6 | PKS 0048-071 | 103.66 | 1.975 | 2.57 | 0.29 | 0.19 | 6.85 | 0.11 | 9.25 | 7.64 | 3.93 | 0.81 | FSRQ (LSP) | 192.85 |
| 7 | S4 0218+35 | 178.65 | 0.944 | 2.22 | 0.28 | 0.15 | 21.46 | 0.91 | 18.4 | 4.92 | 3.37 | 0.98 | FSRQ (Unc.) | 157.51 |
| 8 | 1ES 0502+675 | 546.94 | 0.340 | 2.13 | 0.11 | 0.00 | 51.95 | ... | ... | 1.47 | 0.79 | ... | FSRQ (LSP) | 41.46 |
| 9 | ... | 348.99 | 0.340 | 1.25 | 0.27 | 0.02 | 40.83 | ... | ... | 1.47 | 1.49 | 1.00 | BL Lac (HSP) | 41.46 |
| 10 | ... | 324.50 | 0.340 | 1.12 | 0.27 | 0.14 | 39.94 | 26.6 | 59.4 | 1.47 | 1.49 | 1.00 | BL Lac (HSP) | 41.46 |
| 11 | GB6 J1001+2911 | 307.54 | 0.558 | 2.13 | 0.27 | 0.27 | 38.86 | 0.12 | 2.35 | 0.63 | 1.54 | 0.92 | BL Lac (ISP) | 109.00 |
| 12 | B2 2234+28A | 200.17 | 0.790 | 1.98 | 0.28 | 0.15 | 5.29 | 0.12 | 5.29 | 3.58 | 0.43 | 0.90 | FSRQ (LSP) | 379.91 |
| 13 | PKS 0426-380 | 133.79 | 1.111 | 1.85 | 0.12 | 0.01 | 12.45 | 34.9 | 402 | 0.93 | 3.76 | 1.00 | FSRQ (LSP) | 920.63 |
| 14 | PKS 1329-049 | 66.58 | 2.150 | 1.48 | 0.30 | 0.17 | 3.83 | 0.32 | 35.2 | 31.2 | 4.23 | 0.55 | FSRQ (LSP) | 322.35 |
| 15 | 4C +55.17 | 141.20 | 0.899 | 1.44 | 0.28 | 0.06 | 16.00 | 27.9 | 340 | 5.00 | 3.64 | 1.00 | FSRQ (LSP) | 23.41 |
| 16 | MG4 J000800+4712 | 64.42 | 2.100 | 1.38 | 0.13 | 0.07 | 5.17 | 18.1 | 243 | 11.8 | 9.62 | 0.99 | FSRQ (LSP) | 19.32 |
| 17 | PKS 1144-379 | 116.58 | 1.048 | 1.37 | 0.12 | 0.03 | 10.82 | 2.43 | 37.3 | 2.34 | 4.82 | 0.99 | FSRQ (LSP) | 52.88 |
| 18 | TXS 1720+102 | 168.22 | 0.732 | 1.35 | 0.12 | 0.02 | 16.23 | 0.43 | 7.73 | 1.44 | 3.04 | 0.99 | FSRQ (LSP) | 91.68 |
| 19 | B2 2114+33 | 72.54 | 1.596 | 1.21 | 0.13 | 0.07 | 3.18 | 331 | 992 | 22.4 | 6.49 | 1.00 | FSRQ (LSP) | 68.77 |
| 20 | 4C +51.37 | 81.69 | 1.379 | 1.19 | 0.13 | 0.03 | 7.03 | 1.08 | 19.4 | 3.70 | 6.63 | 0.98 | FSRQ (LSP) | 432.08 |
| 21 | MG3 J021252+2246 | 240.37 | 0.459 | 1.11 | 0.27 | 0.12 | 21.27 | 0.30 | 6.38 | 1.97 | 1.78 | 0.95 | BL Lac (HSP) | 27.48 |
| 22 | PKS 0302-623 | 79.09 | 1.348 | 1.10 | 0.29 | 0.22 | 7.01 | 0.93 | 27.5 | 14.3 | 5.66 | 0.73 | FSRQ (LSP) | 70.21 |
| 23 | B3 1343+451 | 46.44 | 2.534 | 1.00 | 0.13 | 0.03 | 3.61 | 92.4 | 746 | 10.5 | 10.3 | 1.00 | FSRQ (LSP) | 392.94 |

[a] Redshift of the source.
[b] Optical depth of the HOPs in the KD model.
[c] Energy dispersion at 68 % confidence (see Section 3.2.4).
[d] Predicted number of $\gamma$-rays detected from the source for $\alpha = 1$ (see Section 3.2.4).
[e] Poissonian probability to observe at least the detected number of photons from the source at $\alpha = 1$ (see Section 3.2.4).
[f] Expected number of background photons determined from a fit to the intrinsic spectrum (see Section 3.2.3).
[g] Expected number of background photons determined from photon counting (see Section 3.2.3).
[h] Probability that the HOP originates from the source (evaluated with `gtsrcprob`, see Section 3.2.3).
[j] Taken from the 2 year Fermi AGN catalog (see `http://www.asdc.asi.it/fermi2lac` and Ackermann *et al.*, 2011). The abbreviations in brackets refer to the frequency of the synchrotron peak of the SED, see Section 1.1.2, *Unc.* stands for uncertain.
[k] Variability index taken from the 2FGL.

tools of the *Fermi science tools* is used for the fit. The radius of the region of interest (ROI) is chosen to be 15°, and sources with an angular distance up to 30° are included in the fitting procedure. The spectral parameters of the 2FGL are used as initial values, and all parameters up to an angular distance of 4° are left free to vary during the fit. Between a distance of 4° and 8°, only the normalization is left free, and all parameters of sources with larger distances are frozen. Additionally, two background models are considered, the isotropic diffuse emission modeled with the `iso_p76clean` template and the galactic diffuse emission (`gal_2yearp7v6`) whose normalizations are left as free parameters. The best fit values are used in a second step as input parameters to determine the intrinsic spectrum between 1 GeV and the energy $E_{99}$, which is defined as the energy for which the absorption is equal to 1 %, i.e., $\exp[-\tau_{\gamma\gamma}(z, E_{99})] = 0.99$. The optical depth to calculate $E_{99}$ is taken from the KD model. It predicts a relatively high EBL density at optical and ultraviolet wavelengths and consequently a high optical depth at the energy range accessible with the *Fermi*-LAT. Thus, a low value of $E_{99}$ is obtained[8]. The same fit parameters are left free as in the determination of the spectrum of the entire energy range. The resulting intrinsic spectra of all sources are shown in Figure 3.10 together with the best fit values. Even though some sources show a clear indication for curvature, e.g. PKS 0426-380, a power law is used throughout in order to maximize the number of expected photons in the optical thick regime.

In a third step, the intrinsic spectrum is extrapolated to higher energies and attenuated with the EBL absorption $\exp(-\alpha\tau_{\gamma\gamma})$, where $\alpha \in [-0.5, 1.5]$, and the number of predicted photons above $E_{\mathrm{HOP}}$ is determined. This results in an upper bound on the number of photons if no spectral hardening is assumed. A spectral hardening for a number of blazars would correspond to less fine-tuning as in the VHE case, because a fixed energy range between 1 – 500 GeV is considered for each source. Since a little number of photons is expected in the optical thick regime, the unbinned analysis chain of the *Fermi science tools* is used, and all fit parameters are fixed to their final values of the intrinsic fit. The built-in function `NpredValue` folds the input spectrum with the instrumental response to determine the expected number of photons in the entire ROI from the source between $E_{\mathrm{HOP}}$ and 500 GeV. The number has to be scaled by a factor $c_{\mathrm{PSF}}$ to account for the fact that in the present analysis the photons are associated with a source only if the angular distance is smaller than $r_{68}$. This number should be close to $c_{\mathrm{PSF}} = 0.68$ and this value is also adopted here[9]. The expected number of photons within $r_{68}$ is denoted as $\lambda_{i,\mathrm{pred}}$. The probability to

[8] Note that the KD model is designed to predict a minimal EBL attenuation for TeV $\gamma$-rays only. Accordingly, the EBL density is minimal at infrared wavelengths but not necessarily at optical wavelengths, see Eq. (1.16) and Figure 2.2.

[9] It is also confirmed from simulations using the `gtobssim` tool. Photons from the blazar 4C +55.17 are simulated using the best-fit parameters of the intrinsic fit. Above 10 GeV, the source is found within the $r_{68}$ distance for 66.9 % of all photons.

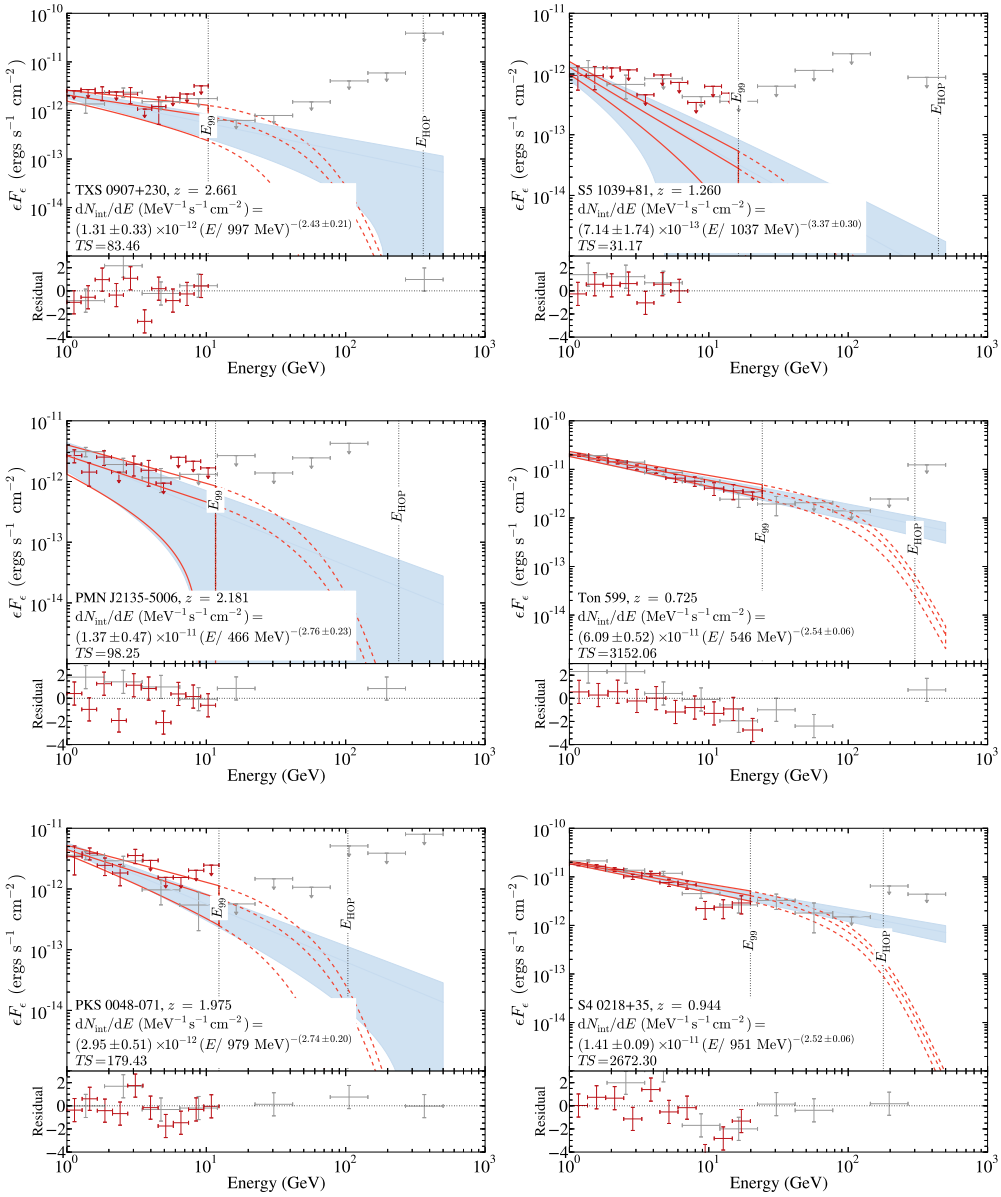


**FIGURE 3.10:** Spectral energy distributions of the sources with an associated photon in the optical thick regime. Shown are the single energy bins (red markers) for the intrinsic spectrum up to $E_{99}$ and the full energy range (from 1 GeV up to 500 GeV; gray markers) together with the best-fit power laws (red solid line for the intrinsic and blue butterfly for the full-range fit). The red dashed line shows an extrapolation of the intrinsic fit attenuated with the KD model. Some energy bins are missing since the count statistic in these bins is too small to derive a flux level or even an upper limit. All upper limits are derived for a $2\,\sigma$ confidence level.

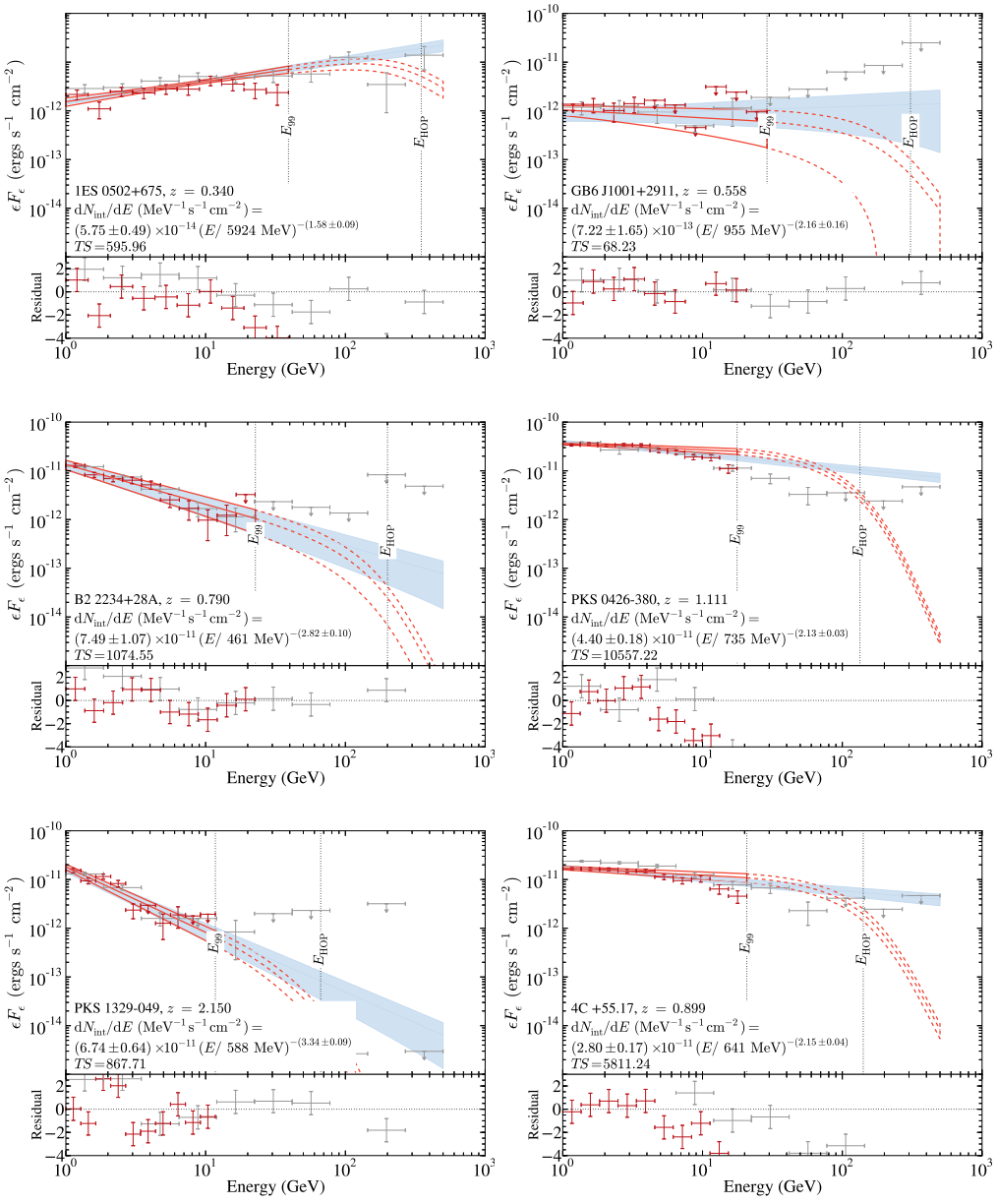


**Figure 3.10:** Continued.

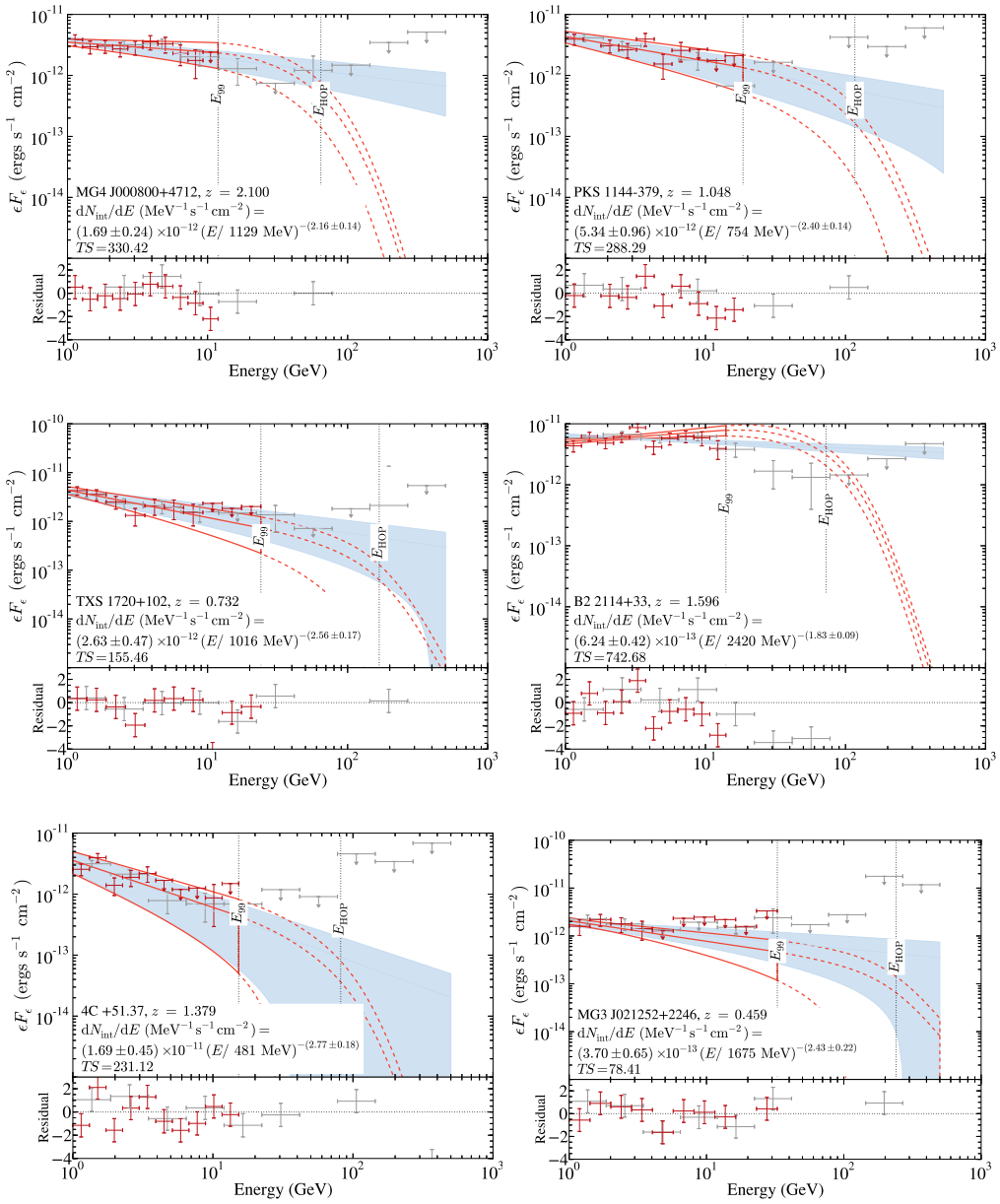


**FIGURE 3.10:** Continued.

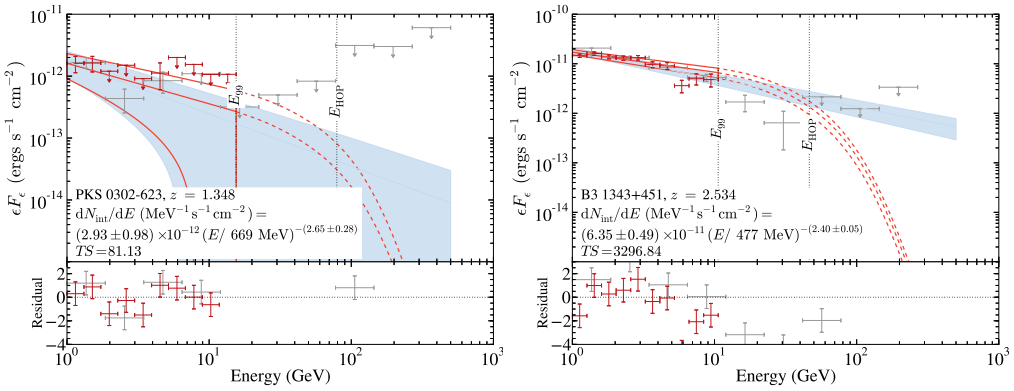


**Figure 3.10:** Continued.

observe at least the detected number of photons, $n_{0,i}$, is then calculated from

$$p_i \equiv p(n \geqslant n_{0,i}) = \sum_{k=n_{0,i}}^{\infty} \frac{\lambda_i^k}{k!} \exp(-\lambda_i) = 1 - \sum_{k=0}^{n_{0,i}-1} \frac{\lambda_i^k}{k!} \exp(-\lambda_i), \tag{3.10}$$

which is the folded Poisson statistic to measure either a photon from the source or from the background, i.e., $\lambda_i = \lambda_{i,\text{pred}} + \lambda_{i,\text{bkg}}$, where $\lambda_{i,\text{bkg}}$ is the expected number of background photons. The contribution from the backgrounds will be addressed in the next section. The index $i = 1, \ldots, N_{\text{src}}$ runs over the number of sources in the sample of Table 3.3. Each source can be regarded as an independent test of the same null hypothesis, namely that under the given EBL model and normalization $\alpha$, the probability of observing the detected photon(s) is equal or higher than a certain confidence level. Following Abdo *et al.* (2010b), the probabilities of the $p_i$ of the single sources can thus be combined using Fisher's method (Fisher, 1925): The quantity

$$X^2 = -2 \sum_{i=1}^{N_{\text{src}}} \ln p_i \tag{3.11}$$

follows a $\chi^2$-distribution with $2N_{\text{src}}$ degrees of freedom from which the probability of the hypothesis to observe the HOPs, $P_{\text{PPA}}$, can be derived. Similar to the tests in the VHE domain, $P_{\text{PPA}}$ will be calculated for the sources with $\tau_{\gamma\gamma} \geqslant 1$ and $\tau_{\gamma\gamma} \geqslant 2$ to address the significance of the PPA at different values of the optical depth.

Instead of the Poissonian probability given in Eq. (3.10), Abdo *et al.* (2010b) simulated a large number of observations under the assumption of the intrinsic source model. The probability was then calculated by comparing the number of simulations where the photon was detected to the total number of simulations. Repeating their analysis with the same sources and data sets as in Abdo *et al.* (2010b) but using the Poissonian probability yields similar results for the probability to observe

the photon. Thus, it is not necessary to derive the probabilities $p_i$ from simulations.

### 3.2.3 Estimation of the background probability

The HOPs may be falsely associated with the AGN listed in Table 3.3. Instead they could originate from background sources:

- Galactic diffuse emission. Cosmic-ray electrons and protons produce this emission in the interaction with interstellar gas and photon fields in terms of bremsstrahlung, $\pi^0$ decay, and inverse Compton (IC) scattering (see, e.g., 2FGL). It is incorporated in the fit through the spatial and spectral template `gal_2yearp7v6_v0` provided by the *Fermi*-LAT science and support center and is derived from a fit of a model to 24 months of *Fermi*-LAT data. The model is a linear combination of gas column densities and IC intensity maps in different Galactocentric rings. The IC emission is modeled with the GALPROP code[10]. Furthermore, several additional spatial components of diffuse emission, such as, e.g., the lobes north and south of the galactic plane (Su *et al.*, 2010) are included in the template.

- Isotropic diffuse emission. This background component comprises misidentified cosmic rays as well as the extragalactic $\gamma$-ray background (EGB). Even though the usage of the P7V6_ULTRACLEAN IRF guarantees the lowest background contamination, it is still possible that residual cosmic rays are present in the data sample, if, e.g., they are not rejected by the anti-coincidence detector (ACD), which cannot cover the entire area of the tracker and calorimeter due to screw holes of edge corners (Atwood *et al.*, 2009). Another background source are events which enter the calorimeter from behind and reach the thick part of the tracker, thus mimicking a signal of a $\gamma$-ray which had its first interaction in this part of the tracker. Especially for inclination angles $\theta > 65°$, the rejection of cosmic rays worsens significantly (Ackermann *et al.*, 2012a). However, only the photon associated with B2 2234+28A has a high inclination of $\theta = 73.6°$. The EGB, on the other hand, consists of $\gamma$-rays from unresolved extragalactic and truly diffuse sources (Abdo *et al.*, 2010c, and references therein). Thus, the EGB also contains the contribution of unresolved point sources. Photons that originate from point sources which are not part of the 2FGL are not included in the fitting procedure to derive the intrinsic spectrum. To overcome this, one could in principal compute *TS* maps of each region of interest (ROI) for each source (similar to what has been done in the 2FGL) to search for additional hot spots that could indicate new sources. This is, however, a computational intensive task and it is not guaranteed that the flux of potential new sources is high enough to be detected with

[10] See the 2FGL and `http://fermi.gsfc.nasa.gov/ssc/data/access/lat/Model_details/Pass7_galactic.html`

this method. A conservative estimation of the overall background can also be used instead (see below). The EGB and residual cosmic-ray components are again modeled through a template, `iso_p7v6clean`, provided by the *Fermi science and support center*, a spectral template for the diffuse all-sky emission. Most of the HOPs (15 out of 23) have arrived from a galactic latitude $|b| > 30°$, thus it is important to include this background template.

The number of expected photons from the two background templates for the entire region of interest of 15°, $N_{\mathrm{diff}}$, can be directly determined from the fit of the extrapolated data using, again, the built-in function `NpredValue`. The resulting number of predicted background photons has to be scaled from the solid angle of the region of interest, $\Omega_{\mathrm{ROI}}$, to the solid angle corresponding to the $r_{68}$ confidence radius (in general different for each photon, cf. Table 3.3), $\Omega_{68}$,

$$\lambda_{\mathrm{diff}} = N_{\mathrm{diff}} \frac{\Omega_{68}}{\Omega_{\mathrm{ROI}}} = N_{\mathrm{diff}} \frac{\int_0^{r_{68}} \mathrm{d}\vartheta \sin\vartheta}{\int_0^{r_{\mathrm{ROI}}} \mathrm{d}\vartheta \sin\vartheta} = N_{\mathrm{diff}} \frac{1-\cos r_{68}}{1-\cos r_{\mathrm{ROI}}}. \tag{3.12}$$

On the other hand, an estimation of the maximum background probability that incorporates all potential background sources can be made by photon counting. Under the assumption that the backgrounds behave similar for a constant galactic latitude, one can count all the detected photons, $N_{\mathrm{all}}$, within a band of thickness $b \pm \Delta b$ in galactic latitude and length $l \pm \Delta l$ in galactic longitude that have an energy $E_{\mathrm{HOP}} \pm \Delta E$. The 68 % energy uncertainty $\Delta E$ is calculated similarly to the $r_{68}$ confidence radius as an integral over the energy dispersion of the LAT (see Section 1.3.1). The acquired photon sample can be further enlarged by mirroring the band $(b \pm \Delta b, l \pm \Delta l)$ on the galactic plane. The number of counted photons is normalized from the solid angle of the two bands to the solid angle of the average confidence radius $\langle r_{68} \rangle$ of all photons in the sample. The expected number of background photons is found to be

$$\lambda_{\mathrm{all}} = N_{\mathrm{all}} \frac{\Omega_{\langle r_{68} \rangle}}{2\Omega_{\mathrm{band}}} = N_{\mathrm{all}} \frac{\pi\,(1-\cos\langle r_{68} \rangle)}{4\Delta l \,\sin b \sin \Delta b}. \tag{3.13}$$

The factor of 4 in the denominator stems from the 2 mirrored sheets and an additional factor of 2 from the integration over galactic latitude. The number of photons depends on the thickness $\Delta b$ and length $\Delta l$ of the sheet. As an example, Figure 3.11 shows the dependence of $\lambda_{\mathrm{all}}$ on the choice of $\Delta l$ and $\Delta b$ for the HOP associated with Ton 599. For larger $\Delta b$ the number of expected background photons increases as one approaches the Galactic plane. Thus, a small value of $\Delta b = 5°$ is chosen in order not to overestimate this already conservative approach. For $\Delta l$ it is settled on a value of 90°.

The two values for the predicted number of background photons can be found in Table 3.3. As expected, $\lambda_{\mathrm{all}} > \lambda_{\mathrm{diff}}$ for all sources. It is underlined that $\lambda_{\mathrm{all}}$ is certainly an upper limit on the true number of background photons, since known sources are also included besides the diffuse emission and unidentified point sources.

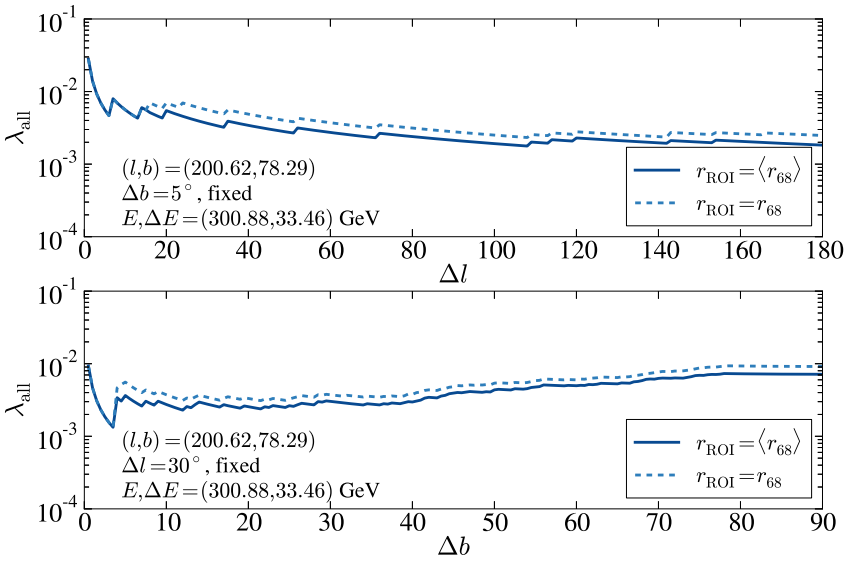


**FIGURE 3.11:** Dependence of the estimation of the expected number of background photons, $\lambda_{\rm all}$, on the length of the sheet $\Delta l$ (top panel) and thickness $\Delta b$ (bottom panel). The two lines show the different solid angles used for the normalization. The dashed line is the result if $r_{68}$ of the HOP is used, whereas for the solid line the average confidence radius of all photons in the two sheets is utilized. The photon energy and arrival direction are those of the event associated with the BL Lac Ton 599.

As an additional test, the probability $P_{\rm src}(\alpha = 0)$ can be determined that the HOP is associated with the source in the fitting procedure performed by the likelihood maximization routine. If $P_{\rm src}(\alpha = 0)$ is too small, including the effect of the EBL will only decrease the values $p_i$ defined in Eq. (3.10). The probability is calculated using the *Fermi* science tool function `gtsrcprob`, which takes the final parameters of the intrinsic spectral fit and the event file of the photons with $E \geqslant E_{\rm HOP}$ as input parameters and calculates $P_{\rm src}$ for all sources in the ROI. The sum over all $P_{\rm src}$ is equal to one. The results are also listed in Table 3.3. For the three photons with the highest $\tau_{\gamma\gamma}$, the $P_{\rm src}$-values are below $\sim 10\,\%$. So even with no absorption it is unlikely that these photons originate from the associated sources. Instead, the photons associated with PMN J2135-5006 and S5 1039+81 most probably originate from either the galactic diffuse or isotropic background with probabilities of 84% and 31 %, respectively, for the former and 5% and 50 %, respectively, for the latter component. The photon of TXS 0907+230 is assigned with 99.7 % probability to the high synchrotron peaked BL Lac RX J0908.9+2311 at a redshift $z = 0.223$. Between 1 GeV and 500 GeV, RX J0908.9+2311 has a hard spectrum described with a power law with a photon index $\Gamma = 1.54 \pm 0.12$ and a flux normalization at 5.1 GeV

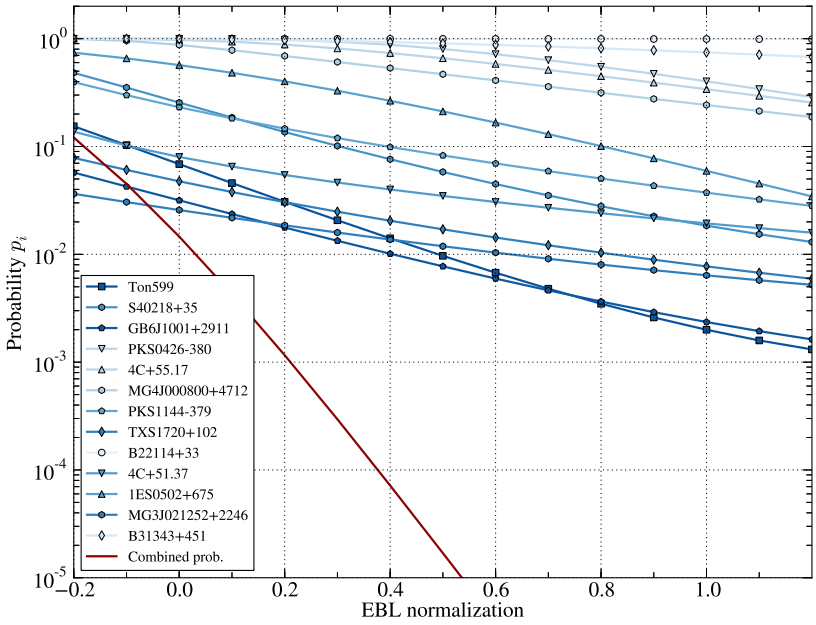


**FIGURE 3.12:** Probabilities as function of EBL normalization of observing at least the number of associated photons from each AGN. The FRV model is used to extrapolate the spectra and only those sources are included for which $P_{\mathrm{src}} > 0.9$. The number of background photons is given by $\lambda_{\mathrm{diff}}$ and the combined probability $P_{\mathrm{PPA}}$ is shown as a solid dark red line.

of $N_0 = (2.16 \pm 0.43) \times 10^{-14}\,\mathrm{MeV^{-1}s^{-1}cm^{-2}}$. The angular distance of the reconstructed photon arrival direction to RX J0908.9+2311 is 0.40° compared to 0.19° for TXS 0907+230. The 68 % confidence radius of the HOP is 0.27°. Thus, it seems likely that the photon indeed originates from this source rather than TXS 0907+230. The optical depth changes from $\tau_{\gamma\gamma} = 11.64$ to $\tau_{\gamma\gamma} = 0.74$ in the KD model, and the photon has to be discarded from the HOP sample. Without RX J0908.9+2311, the photon is associated with a $\sim 81$ % probability with TXS 0907+230 and with $\sim 8$ % ($\sim 8$ %) with the galactic (isotropic diffuse) background component. For the final results, it is conservatively required that $P_{\mathrm{src}} > 0.9$.

### 3.2.4 Results and systematic uncertainties

Similar to the VHE case, the result of the combined probability are influenced by a number of systematic uncertainties, and their impact on the final results will be discussed in the following. For brevity, the influence of the systematics is discussed for the combination of sources from which photons with $\tau_{\gamma\gamma} \geqslant 1$ are detected. The discussion is equally well applicable to the $\tau_{\gamma\gamma} \geqslant 2$ case, and all results are

summarized in Table 3.4.
For a fiducial set up, the FRV model is chosen. It predicts a low EBL density at optical and ultraviolet wavelengths and accordingly a low attenuation for the photon energies accessible with the *Fermi*-LAT. Moreover, a scaling of the optical depth of $\alpha = 1.02 \pm 0.23$ is found as a best fit for the EBL imprint on *Fermi*-LAT spectra in a large sample of BL Lacs (Ackermann *et al.*, 2012c). As discussed in the previous section, a probability of $P_{\mathrm{src}} > 0.9$ is required for a source to be included in the sample, and the background is estimated with $\lambda_{\mathrm{diff}}$. The probabilities of observing the photons with $\tau_{\gamma\gamma} \geqslant 1$ of the remaining sources are shown in Figure 3.12 as a function of the EBL normalization $\alpha$. As expected, the probabilities decrease with increasing absorption and are lower for higher optical depth photons. For $\alpha = 0$, no probability is smaller than 1 %, and they fall off by roughly an order of magnitude to $\alpha = 1$ with the exception of the sources with photons close to $\tau_{\gamma\gamma} \approx 1$. The combined probability derived with Fisher's method shows a steep decline from $P_{\mathrm{PPA}}(\alpha = 0) = 1.46 \times 10^{-2}$ to $P_{\mathrm{PPA}}(\alpha = 1) = 1.37 \times 10^{-8}$ what corresponds to a significance $5.56\,\sigma$ (using once again a one-sided confidence interval).
In this fiducial set up, photons with $\tau_{\gamma\gamma} \geqslant 2$ are detected from 3 AGN, namely from Ton 599, S4 0218+35, and GB6 J1001+2911. Combining the probabilities from these sources only results in a significance of $P_{\mathrm{PPA}}(\alpha = 1; \tau_{\gamma\gamma} \geqslant 2) = 6.57 \times 10^{-6} = 4.36\,\sigma$.

Source related effects. The various sources contribute differently to the overall significance, as visible from Figure 3.13. Interestingly, the AGN from which a photon with $\tau_{\gamma\gamma} \geqslant 2$ is observed give a strong increase in the significance similar to the trend found in the same optical depth domain at VHE energies. Conversely, the significance of observing the photons does not increase for the four sources of B2 2114+33, MG4 J00800+4712, 4C +55.17, and PKS 0426-380.
The source sample is dominated by FSRQs. Observations of the broad line region (e.g., Netzer, 2008) and the accretion disk itself (associated with the presence of a "blue bump" in the SED; Sun & Malkan, 1989) are taken as indications that $\gamma$-ray emission is due to the upscattering of photons of external radiation fields, e.g., from the accretion disk (Dermer & Schlickeiser, 1993) the broad line region (Sikora *et al.*, 1994) or a dusty torus (Błażejowski *et al.*, 2000). Depending on the location of the emission site, the external photon fields can lead to a source intrinsic attenuation of the $\gamma$-ray flux and consequently a steepening of the the spectra (e.g., Tavecchio & Ghisellini, 2008), see also Section 1.1.1. Therefore, the probability of observing the HOPs is also calculated in the case that all intrinsic spectra are described with logarithmic parabolas (LPs; dashed line in the top-right panel of Figure 3.14). Not surprisingly, the significance increases drastically, and even for $\alpha = 0$ one finds $P_{\mathrm{PPA}} = 1.24 \times 10^{-7}$. This indicates that this choice for the intrinsic spectra is not justified, as the number of expected photons is clearly underestimated. Furthermore, for most sources, the fits do not improve significantly if an LP is used

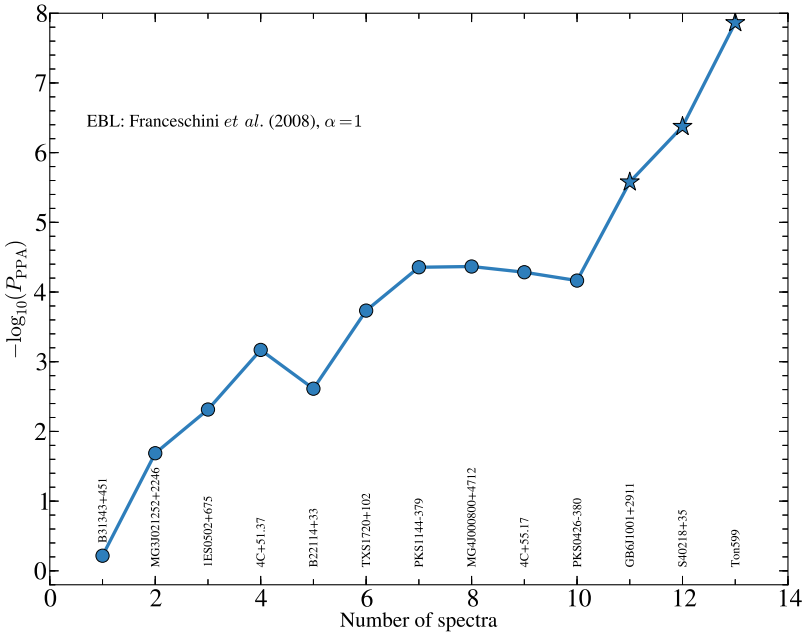


**FIGURE 3.13:** Cumulative probabilities. As in Figure 3.5, the combined probability is computed, in each step including one more spectrum (sorted in ascending order of the optical depth of the associated photon). Blazars marked with a star correspond to sources with a HOP with $\tau_{\gamma\gamma} \geqslant 2$.

to describe the intrinsic spectrum. The improvement can be quantified in terms of $TS_{\text{fit}} = -2(\log \mathcal{L}_{\text{PL}} - \log \mathcal{L}_{\text{LP}})$, where $\mathcal{L}_j$, $j = \text{PL}, \text{LP}$, are the maximum likelihood values for the power-law and logarithmic-parabola fit, respectively. Positive values of $TS_{\text{fit}}$ indicate an improvement of the fit with an LP, and the highest values are found for PKS 0426-380 ($TS_{\text{fit}} = 8.81$) and B3 1343+451 ($TS_{\text{fit}} = 8.43$) what corresponds to an improvement by almost $3\,\sigma$ (using Wilks' theorem stating that the $TS_{\text{fit}}$ values follow a $\chi^2$-distribution Wilks, 1938) . The indication for curvature can also be seen from the negative residuals of the highest energy bins in Figure 3.10. Using logarithmic parabolas for these two sources only increases the significance of the PPA to $P_{\text{PPA}}(\alpha = 1) = 5.12 \times 10^{-10} = 6.12\,\sigma$ (dash-dotted line in the top left panel of Figure 3.14, whereas the solid line shows the combined $P_{\text{PPA}}$ if the time averaged intrinsic spectra are all described with power laws).

AGN are also known to be variable sources in time both in flux and in spectral index. The light curves in the energy range 1 GeV – $E_{99}$ (Figure C.1 in Appendix C) show that most associated sources undergo periods of enhanced activity. If the HOP is emitted during such times, the number of predicted photons might be underestimated by the extrapolation of the time averaged intrinsic spectrum. Using

the normalization $N_0^{t_{\rm HOP}}$ derived from the time bin of the light curve of the intrinsic spectrum in that the HOP arrived instead of the time averaged one, $N_0$, results in the significances shown as a dotted curve in the top right panel of Figure 3.14. One finds $P_{\rm PPA}(\alpha = 1) = 5.81 \times 10^{-7} = 4.86\,\sigma$, and in contrast to the time averaged intrinsic spectrum the significance of the PPA is smaller above $\alpha \gtrsim 0.2$. The reason can be read off from the light curves in Figure C.1 that also show the arrival time of the HOP (dashed vertical line) and the value of $N_0$ with its uncertainties (gray shaded region). Photons associated with sources that contribute significantly to the combined probability (e.g., Ton 599) have often arrived during flaring periods and, consequently, $N_0^{t_{\rm HOP}} > N_0$. Thus, using $N_0^{t_{\rm HOP}}$ to extrapolate the spectrum leads to a larger number of predicted photons above $E_{\rm HOP}$ and a better accordance between the observations and EBL models.
In times of high flux states, the spectral index can also change. A spectral hardening has been observed, e.g., in Mkn 501 above 10 GeV (Abdo *et al.*, 2011c; Neronov *et al.*, 2012a). This has been investigated for Ton 599 for a 20 day time bin centered around the arrival time of the HOP. Repeating the binned analysis chain for this case results in a power law between 1 GeV and $E_{99}$ with a spectral index of $\Gamma_{t_{\rm HOP}} = 2.29 \pm 0.25$ and a normalization of $(1.65 \pm 0.65) \times 10^{-10}\,\mathrm{MeV^{-1}s^{-1}cm^{-2}}$ at 546 MeV. The normalization is about two times larger than it is for the time averaged spectrum but the spectral indices agree with each other within their $1\,\sigma$ uncertainties, the average value being $\Gamma = 2.54 \pm 0.06$ (cf. Figure 3.10). Although not significant, a spectral hardening up to $\sim 0.25$ could be hidden in the uncertainties. The EBL absorption limits the number of photons observed above $E_{99}$, and no meaningful spectrum can be derived above this energy in this time bin. For about half the spectra, only upper limits are available for the time bins corresponding to the arrival time of the HOP, and it has to be assumed that the time averaged spectrum is a good representative of the overall spectrum. However, it might still be possible that the spectra show an intrinsic hardening towards higher energies. The top-right panel of Figure 3.14 shows the effect on the overall probability if all power-law spectra become harder by one or two $\sigma_\Gamma$, which denotes the 68 % confidence interval derived from the power-law fit. Physically, this corresponds to a harder intrinsic spectrum. If all sources are affected by such a spectral change, the probability is increased by $\sim 2$ or even $\sim 4$ orders of magnitude for a spectral index of $\Gamma - \sigma_\Gamma$ and $\Gamma - 2\sigma_\Gamma$, respectively.

Energy resolution. The energy resolution of the LAT is of the order $\Delta E/E \sim 10\,\%$ for the HOPs (cf. Table 3.3). It depends on the energy and the inclination angle of the incident photon (see Section 1.3.1). The uncertainty introduced by the finite energy resolution is estimated by recalculating the predicted number of photons $\lambda_{\rm pred}$ above $E_{\rm HOP} - k\Delta E$, for $k = 1, 2$. The bottom-left panel of Figure 3.14 shows the effect of the energy resolution. If it is applied to all photons in the sample, the significance decreases by about one order of magnitude for each

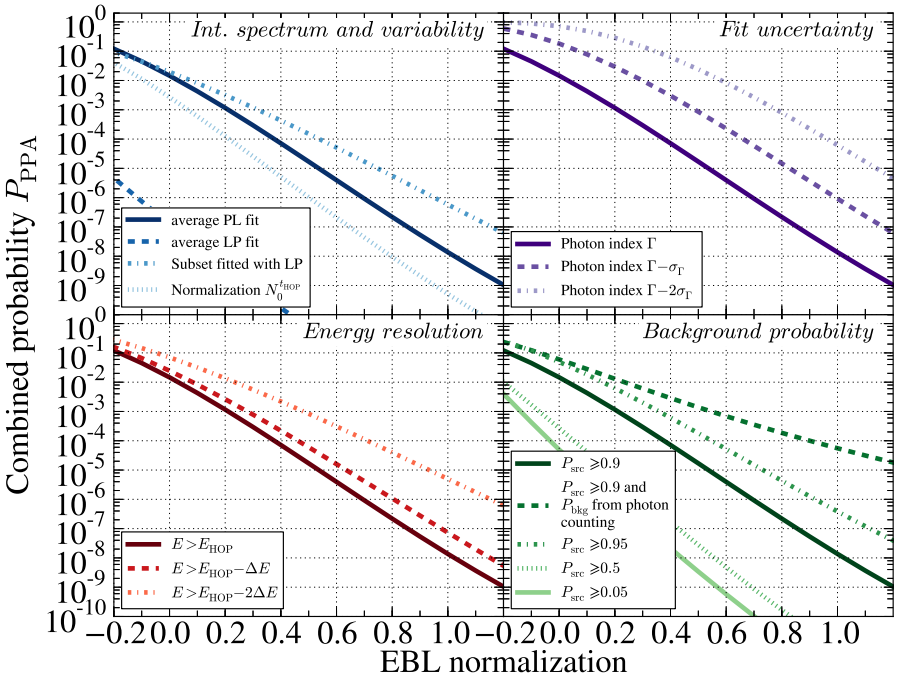


**Figure 3.14:** Influence of different systematic effects on the combined probability, $P_{\mathrm{PPA}}$. See text for details.

additional decrease of $E_{\mathrm{HOP}}$ by $\Delta E$. Interestingly, the effect is weakened due to the additional photon from 1ES 0502+675. Its energy is below 500 GeV if shifted by $k\Delta E$, and it can be included in the hypothesis test.

Source probability and expected number of background photons. If the condition $P_{\mathrm{src}} > 0.9$ is relaxed, more sources contribute to the combined probability $P_{\mathrm{PPA}}$. Doing so increases the significance of the PPA, as shown in the bottom-right panel of Figure 3.14. If the conservative photon counting method is used to calculate the expected number of background photons, $\lambda_{\mathrm{all}}$, the significance at $\alpha = 1$ decreases by $\sim 3$ orders of magnitude. Of all systematic uncertainties, the background estimation has thus the strongest impact on $P_{\mathrm{PPA}}$. As stressed before, $\lambda_{\mathrm{all}}$ certainly overpredicts the true number of background photons. Without access to the raw data of the *Fermi*-LAT, it is, however, difficult to predict the residual cosmic-ray contamination in the P7V6_ULTRACLEAN event class. A dedicated study, especially at energies $\gtrsim 13$ GeV in connection with the extragalactic $\gamma$-ray background is currently conducted by the *Fermi*-LAT collaboration that could be used in a future

analysis for a better discrimination between $\gamma$-ray and background events[11].

EBL UNCERTAINTY. The choice of a different EBL model has a negligible impact on the combined probability $P_{\mathrm{PPA}}$. Apart from the FRV model, the models of Domínguez *et al.* (2011), Inoue *et al.* (2012), and the KD model are tested. The results are comparable, although the EBL photon density and its evolution with redshift are different in each model. The highest value of the significance is found for the KD model, since the predicted EBL density is large at ultraviolet and optical wavelengths even at high redshifts (see Figure 2.2 in Chapter 2) with $P_{\mathrm{PPA}}(\alpha = 1) = 5.06 \times 10^{-9} = 5.73\,\sigma$. The lowest significance, $P_{\mathrm{PPA}} = 1.34 \times 10^{-8} = 5.56\,\sigma$, is found for the model of Inoue *et al.* (2012), marginally lower than the result for the FRV model. This might come as a surprise since the EBL density in this model is larger at $z = 0$ below $\sim 0.7\,\mu$m than the prediction of the FRV model. However, the optical depths of Ton 599 and GB6 J1001+2911 are smaller by a factor of $\sim 3/4$, giving rise to the slightly reduced significance.

TRIAL FACTORS AND FAILED DETECTIONS. Each AGN with an associated photon poses an independent hypothesis test of the same null hypothesis to detect the HOP above $\tau_{\gamma\gamma} \geqslant 1$ or $\tau_{\gamma\gamma} \geqslant 2$. A low value of $p_i$ [see Eq. (3.10)] of a single source might be caused by a statistical fluctuation and this can be accounted for by including trial factors. In this case, the number of trials is equal to the number of tested sources. In the fiducial set up discussed at the beginning of this section, the number of trials is $N_{\mathrm{trial}} = 13$ and $N_{\mathrm{trial}} = 3$, for sources with $\tau_{\gamma\gamma} \geqslant 1$ and $\tau_{\gamma\gamma} \geqslant 2$, respectively. The single $p_i$ are corrected for trials according to $p_{i,\,\mathrm{post-trial}} = 1 - (1 - p_i)^{N_{\mathrm{trial}}}$ leading to a combined probability of $P_{\mathrm{PPA,\,post-trial}}$, using again Fisher's method. The significances are reduced to $P_{\mathrm{PPA,\,post-trial}}(\alpha = 1; \tau_{\gamma\gamma} \geqslant 1) = 0.06 = 1.57\,\sigma$ and $P_{\mathrm{PPA,\,post-trial}}(\alpha = 1; \tau_{\gamma\gamma} \geqslant 2) = 1.17 \times 10^{-4} = 3.68\,\sigma$, respectively. Clearly, no indication for the PPA is present in the data for sources with $\tau_{\gamma\gamma} \geqslant 1$. However, the indication persists for AGN with $\tau_{\gamma\gamma} \geqslant 2$, similar to the VHE case with at a comparable confidence level. This finding is in agreement with the expectations of non-standard mechanisms of the photon propagation: The possible enhancement of the flux in these scenarios should be more pronounced for higher optical depths and should leave the predictions of the EBL models for $\tau_{\gamma\gamma} \approx 1$ basically unchanged (see Chapters 4 and 5 for detailed discussions).
In contrast to IACTs, with the *Fermi*-LAT and its large field of view of 2.4 sr the entire sky is surveyed about every three hours. Thus, it is possible to account for failed detections, or equivalently to calculate the probability to detect the observed number photons in the $\tau_{\gamma\gamma} \geqslant 1, 2$ regime from all AGN with known redshift in the 2FGL. For a maximum photon energy of 500 GeV, the minimal corresponding red-

[11] See the talk by M. Ackermann at the 2012 *Fermi* Symposium, `http://fermi.gsfc.nasa.gov/science/mtgs/symposia/2012/program/thu/MAckermann.pdf`

**Table 3.4:** Significance values of $P_{\mathrm{PPA}}$ including different systematic uncertainties. The values are given for sources with associated photons with $\tau_{\gamma\gamma} \geqslant 1$ and $\tau_{\gamma\gamma} \geqslant 2$, together with the corresponding confidence levels in terms of $\sigma$ (one-sided confidence interval). See text for further details.

| Cross check | $P_{\mathrm{PPA}}(\alpha = 1; \tau_{\gamma\gamma} \geqslant 1)$ | | $P_{\mathrm{PPA}}(\alpha = 1; \tau_{\gamma\gamma} \geqslant 2)$ | |
|---|---|---|---|---|
| *fiducial*[a] | $1.37 \times 10^{-8}$ | $5.56\,\sigma$ | $6.57 \times 10^{-6}$ | $4.36\,\sigma$ |
| *Intrinsic spectrum and spectral hardening* | | | | |
| LP all spectra | $5.30 \times 10^{-14}$ | $7.43\,\sigma$ | $9.69 \times 10^{-7}$ | $4.76\,\sigma$ |
| LP for $TS_{\mathrm{fit}} > 8$ | $5.12 \times 10^{-10}$ | $6.12\,\sigma$ | ... | ... |
| Intrinsic index $\Gamma - \sigma_\Gamma$ | $9.21 \times 10^{-7}$ | $4.77\,\sigma$ | $1.85 \times 10^{-5}$ | $4.16\,\sigma$ |
| Intrinsic index $\Gamma - 2\sigma_\Gamma$ | $6.21 \times 10^{-5}$ | $3.84\,\sigma$ | $6.08 \times 10^{-5}$ | $3.84\,\sigma$ |
| Normalization $N_0^{t_{\mathrm{HOP}}}$ | $5.81 \times 10^{-7}$ | $4.86\,\sigma$ | $5.15 \times 10^{-6}$ | $4.41\,\sigma$ |
| *Energy resolution* | | | | |
| $E_{\mathrm{HOP}} - \Delta E$ | $7.32 \times 10^{-8}$ | $5.26\,\sigma$ | $3.34 \times 10^{-5}$ | $3.99\,\sigma$ |
| $E_{\mathrm{HOP}} - 2\Delta E$ | $4.96 \times 10^{-6}$ | $4.42\,\sigma$ | $1.91 \times 10^{-4}$ | $3.55\,\sigma$ |
| *Source probability* $P_{\mathrm{src}}(\alpha = 0)$ *and number of background photons* | | | | |
| $P_{\mathrm{src}} = 0.95$ | $3.84 \times 10^{-7}$ | $4.94\,\sigma$ | $2.62 \times 10^{-4}$ | $3.47\,\sigma$ |
| $P_{\mathrm{src}} = 0.5$ | $7.50 \times 10^{-12}$ | $6.75\,\sigma$ | $6.96 \times 10^{-7}$ | $4.83\,\sigma$ |
| $P_{\mathrm{src}} = 0.05$ | $8.65 \times 10^{-13}$ | $7.06\,\sigma$ | $7.69 \times 10^{-8}$ | $5.24\,\sigma$ |
| $\lambda_{\mathrm{all}}$ | $5.54 \times 10^{-5}$ | $3.87\,\sigma$ | $8.13 \times 10^{-4}$ | $3.15\,\sigma$ |
| *EBL models* | | | | |
| KD model | $5.06 \times 10^{-9}$ | $5.73\,\sigma$ | $7.75 \times 10^{-6}$ | $4.32\,\sigma$ |
| Domínguez *et al.* (2011) | $1.27 \times 10^{-8}$ | $5.57\,\sigma$ | $5.90 \times 10^{-6}$ | $4.38\,\sigma$ |
| Inoue *et al.* (2012) | $1.34 \times 10^{-8}$ | $5.56\,\sigma$ | $2.41 \times 10^{-5}$ | $4.06\,\sigma$ |
| *Trial factors* | | | | |
| Including trials | 0.06 | $1.57\,\sigma$ | $1.17 \times 10^{-4}$ | $3.68\,\sigma$ |

[a] In the fiducial set up, the EBL is given by FRV model, all spectra are described by the time-averaged power laws, $P_{\mathrm{src}} = 0.9$, and $\lambda_{\mathrm{diff}}$ is used for the number of background photons.

shift in the KD model is found to be $z \gtrsim 0.2$ ($z \gtrsim 0.35$) for $\tau_{\gamma\gamma} \geqslant 1$ ($\tau_{\gamma\gamma} \geqslant 2$), resulting in $N_{\mathrm{src}} \sim 453$ ($\sim 387$) sources listed in the 2FGL. Note that this is a different hypothesis than before: Instead of calculating the probability separately for every source with an associated HOP, now the total number of observed HOPs is compared to the total number of predicted photons from all AGN in the regimes $\tau_{\gamma\gamma} \geqslant 1, 2$. This number can be calculated similarly to $\lambda_{\mathrm{pred}}$: for every source the intrinsic spectrum is determined through a power-law or LP fit which is subsequently extrapolated to higher energies. The predicted number of photons for the source in question above the energy $E_{\tau_{\gamma\gamma}=1,2}$, defined by $\tau_{\gamma\gamma}(E_{\tau_{\gamma\gamma}=1,2}, z) = 1, 2$, is obtained

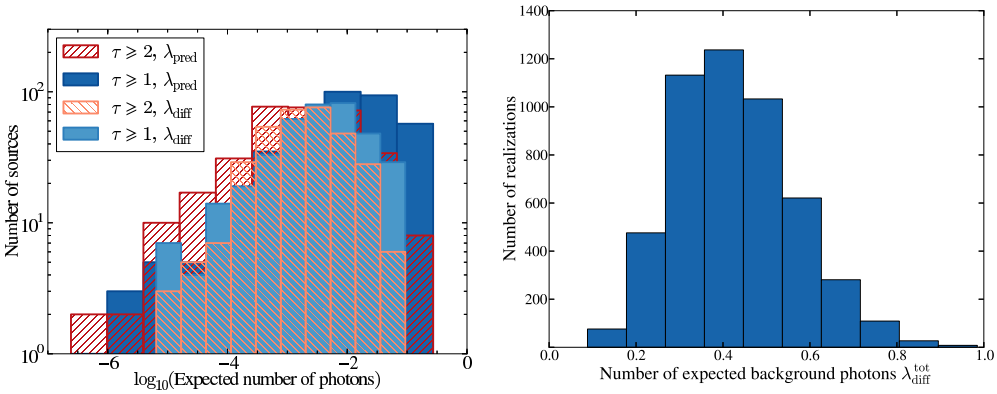


**FIGURE 3.15:** Left panel: Histogram of the expected number of photons from all AGN in the 2FGL with known redshift above $E_{\tau_{\gamma\gamma}\geq 1}$. A power law is assumed for the intrinsic spectrum for all sources. Right panel: Distribution of randomly drawn background photon numbers, $\lambda_{\rm diff}^{\rm tot}$. The same sources are used as in the left panel.

with the function `NpredValue` and scaled by $c_{\rm PSF}$. Similarly, the background components are determined. If no photon is observed in the optical thick regime, the $r_{68}$ value is calculated from the PSF for the energy $E_{\tau_{\gamma\gamma}=1,2}$. The conversion type (front or back) is randomly chosen with a probability of 54.76 % for a front converted photon. This probability corresponds to the ratio of front converted events to all detected events above 10 GeV in the first 4.3 years of *Fermi*-LAT operation. With this $r_{68}$ value, the number of background photons, $\lambda_{\rm diff}$, is calculated from Eq. (3.12). Only those sources are considered for which the intrinsic fit gives a $TS$ value larger than 25. This assures a firm source detection and determination of the intrinsic best-fit parameters. The expected numbers are shown in the histogram in the left panel of Figure 3.15 for an EBL normalization $\alpha = 1$ and the FRV model (the following discussion will focus on this choice of the EBL). In total, $\lambda_{\rm pred}^{\rm tot} = 24.60$ (3.28) photons are expected for $\tau_{\gamma\gamma} \geqslant 1$ ($\tau_{\gamma\gamma} \geqslant 2$). As before, the intrinsic spectra are also fitted with LPs. The corresponding results if the fit improves at the $TS_{\rm fit} > 8$ confidence level or if all spectra are described with a logarithmic parabola are summarized in Table 3.5.

The total number of expected background photons is calculated from a toy Monte-Carlo simulation. From the set of all AGN that are detected with $TS \geqslant 25$, single sources are drawn without replacement and for each source $i$ the number of detected photons $N_i$ is randomly determined from the Poissonian probability mass function $f(k, \lambda_i) = \exp(-\lambda_i)\lambda_i^k/k!$, where, as before, $\lambda_i = \lambda_{i,\rm pred} + \lambda_{i,\rm diff}$. If $N_i > 0$, a HOP is "detected" and the corresponding number of expected background photons, $\lambda_{i,\rm diff}$, is added to the total number of background photons, $\lambda_{\rm diff}^{\rm tot}$. Sources are drawn from the sample until the sum over all $N_i$ exceeds $N_{\rm HOP}$. This is repeated $N_{\rm sim}$ times to form

**Table 3.5:** Results for the total number of expected photons above the energies corresponding to $\tau_{\gamma\gamma} \geqslant 1, 2$ for all AGN with known redshift in the 2FGL that are firmly detected with $TS \geqslant 25$ between 1 GeV and $E_{99}$. The results utilize the FRV model with $\alpha = 1$. The intrinsic spectra are modeled with either power laws (PL) or logarithmic parabolas (LP).

| | $\tau_{\gamma\gamma} \geqslant 1$ | | | $\tau_{\gamma\gamma} \geqslant 2$ | | |
|---|---|---|---|---|---|---|
| | $\lambda_{\mathrm{pred}}^{\mathrm{tot}}$ | $\tilde{\lambda}_{\mathrm{diff}}^{\mathrm{tot}}$ | $P_{\mathrm{all}}$ | $\lambda_{\mathrm{pred}}^{\mathrm{tot}}$ | $\tilde{\lambda}_{\mathrm{diff}}^{\mathrm{tot}}$ | $P_{\mathrm{all}}$ |
| PL all | 24.60 | 0.42 | 0.87 | 3.28 | 0.04 | 0.12 |
| LP $TS_{\mathrm{fit}} > 8$ | 21.75 | 0.71 | 0.63 | 2.87 | 0.03 | 0.07 |
| LP all | 8.86 | 0.22 | $1.17 \times 10^{-3}$ | 0.98 | 0.01 | $5.59 \times 10^{-3}$ |

a distribution of $\lambda_{\mathrm{diff}}^{\mathrm{tot}}$. This method is analogous to repeating the observation of all AGN $N_{\mathrm{sim}}$ times. The distribution of $\lambda_{\mathrm{diff}}^{\mathrm{tot}}$ for $N_{\mathrm{sim}} = 5000$, $\tau_{\gamma\gamma} \geqslant 1$, and intrinsic power-law spectra is shown in the right panel of Figure 3.15. It is skewed with a tail extending to larger values $\lambda_{\mathrm{diff}}^{\mathrm{tot}}$. Thus, the median $\tilde{\lambda}_{\mathrm{diff}}^{\mathrm{tot}}$ of the distribution is used to estimate the number of expected background photons. All drawn values $\lambda_{\mathrm{diff}}^{\mathrm{tot}}$ are found to be larger than the sum over the background values of the AGN with associated HOPs. This is expected since now all background values are determined for energies for which $\tau_{\gamma\gamma} = 1$, whereas for the 21 sources, the $\tau_{\gamma\gamma}$ values are all larger than one. Consequently, for the 21 AGN the energies $E_{\mathrm{HOP}}$ are also higher, resulting in lower numbers of expected background photons. For the different $\tau_{\gamma\gamma}$ ranges and choices of intrinsic spectra, $\lambda_{\mathrm{diff}}^{\mathrm{tot}}$ is also listed in Table 3.5.
Finally, the probability $P_{\mathrm{all}}$ of observing at least $N_{\mathrm{HOP}}$ photons from all AGN above the required redshift and $TS \geqslant 25$ is again evaluated with the Poissonian probability:

$$P_{\mathrm{all}}(N \geqslant N_{\mathrm{HOP}}) = 1 - \sum_{k=0}^{N_{\mathrm{HOP}}-1} \frac{1}{k!} \left(\lambda_{\mathrm{pred}}^{\mathrm{tot}} + \tilde{\lambda}_{\mathrm{diff}}^{\mathrm{tot}}\right)^k \exp\left[-\left(\lambda_{\mathrm{pred}}^{\mathrm{tot}} + \tilde{\lambda}_{\mathrm{diff}}^{\mathrm{tot}}\right)\right]. \tag{3.14}$$

The detected number of photons is $N_{\mathrm{HOP}} = 20$ for $\tau_{\gamma\gamma} \geqslant 1$ and 6 for $\tau_{\gamma\gamma} \geqslant 2$ (the highest energy photon of 1ES 0502+675 is excluded along with the photon of RBS 0405 and TXS 0907+230). The results are summarized in Table 3.5.
Only if all spectra are described with a logarithmic parabola an indication for the PPA is found at a $3.04\,\sigma$ ($\tau_{\gamma\gamma} \geqslant 1$) and $3.26\,\sigma$ ($\tau_{\gamma\gamma} \geqslant 2$) confidence level. Otherwise, the number of expected photons exceeds the number of observed photons for $\tau_{\gamma\gamma} \geqslant 1$. This is in contrast with the previous result of the sources for which a HOP was detected (cf. Table 3.2). The expected number of photons is dominated by a handful of bright sources for which $\lambda_{i,\mathrm{pred}}$ is of the order 1 (for $\tau_{\gamma\gamma} \geqslant 1$) and most of which are best described with a power law as the intrinsic spectrum. These sources are all FSRQs or BL Lacs with a synchrotron peak at low frequencies (LSP), except one source, where the synchrotron part of the SED peaks at intermediate values. In

general, ∼ 66 % (∼ 75 %) of the sources in the tested $\tau_{\gamma\gamma} \geqslant 1$ ($\tau_{\gamma\gamma} \geqslant 2$) samples are FSRQs. As discussed above, for this source class high energy cut-offs are expected in certain emission models to which the present method is insensitive. Even though a logarithmic parabola might not be preferred in the intrinsic energy range, a cut-off is possible at higher energies.
Another possibility to explain the lack of observed photons compared to the predicted number might be the limited signal to noise ratio at these energies. In this respect, a definitive answer on the PPA from *Fermi*-LAT data might be given in the future with the updated instrumental response functions *Pass 7 Reprocessed* and *Pass 8*. The former includes reprocessed data with updated calibration constants of the various subsystems of the LAT, e.g., for the light yield of the CsI crystals of the calorimeter (Bregeon *et al.*, 2013). Preliminary results indicate a significant improvement of the PSF above 1 GeV and possible energy reconstructions and background templates up to 1 TeV (Bregeon *et al.*, 2013). An enhanced PSF will also improve the source association and the impact of the background which is scaled to the $r_{68}$ radius of the photon event [see Eqs. (3.12) and (3.13)]. The energy reconstruction to very high energies promises the detection of photons with even higher values of $\tau_{\gamma\gamma}$. In these respects, the *Pass 8* IRF will have an even larger impact. It comprises completely new algorithms to reconstruct the particle tracks in the tracker and the deposited energy in the calorimeter (Atwood *et al.*, 2013). Furthermore, events that are only detected in the tracker or in the calorimeter but not in both can be analyzed. At the moment these events are completely discarded. A further advantage will be the fact that the *Pass 8* PSF will be determined separately for each event. Consequently, a 15 % – 20 % increase in the high energy acceptance, a better overall PSF, and event reconstruction up to 3 TeV are expected (Atwood *et al.*, 2013).
Furthermore, albeit recent efforts (e.g., Shaw *et al.*, 2013), for about 50 % of the AGN included in the 2FGL, the redshift remains unknown. Both the VHE and *Fermi*-LAT analyses will benefit from future redshift determinations, as the number of sources included in the test for a PPA can be increased.
To conclude this chapter, the results for the indication of a PPA are summarized below.

- Considering all VHE spectra from AGN with known redshift, an indication for an overcorrection of EBL absorption is found in the transition from the optical thin ($\tau_{\gamma\gamma} < 1$) to the optical thick regime ($\tau_{\gamma\gamma} \geqslant 2$) at a $\sim 4\,\sigma$ confidence level. This behavior is coined pair-production anomaly (PPA). Two independent statistical tests give agreeing results. The first test is based on the Kolmogorov-Smirnov test and does not require any assumption about the underlying distribution function. The second method uses the fit residuals of the spectra and relies on the assumption that the residuals follow a (0,1) normal distribution. In the second method, no extrapolation of the spectrum to high optical depth values is necessary.

- Several systematic uncertainties are discussed to explain this indication, including a potential bias from different source classes, the energy resolution and absolute energy calibration of IACTs, and different EBL models. The test methods are checked with an independent mock data sample of Galactic VHE sources. As long as no drastic systematic effects are invoked (e.g., scaling all data points by $-15\,\%$ in energy and discarding the highest energy data point), the indication for a PPA persist (cf. Table 3.2).

- *Fermi*-LAT observations are used as a complementary test of the anomaly. Photons above 10 GeV and galactic latitudes $b \geqslant 10^\circ$ detected with the *Fermi*-LAT in the first 4.3 years of operation are associated with AGN with known redshift which are listed in the 2FGL. In case of a successful association, the optical depth for this photon is calculated, and the overall probability is determined to detect the number of observed photons with $\tau_{\gamma\gamma} \geqslant 1$ and $\tau_{\gamma\gamma} \geqslant 2$. This is achieved by an extrapolation of the source intrinsic spectra to higher energies under the assumption of a certain EBL model.

- In total, 23 photons are found that correspond to $\tau_{\gamma\gamma} \geqslant 1$. Two of these photons have an energy larger than the maximum energies of background templates required for further analysis. Moreover, one photon is probably falsely associated with a distant FSRQ, as it is most likely emitted by a closer BL Lac. The combined probability for observing the remaining 20 photons is 0.06 after excluding photons that are not associated with the AGN with more than 90 % confidence and after correcting for trials. For the three photons above $\tau_{\gamma\gamma} \geqslant 2$, the combined probability is found to be $1.17 \times 10^{-4}$ for a power-law fit of the intrinsic spectrum and the EBL model of Franceschini *et al.* (2008).

- Similarly to the VHE case, several systematic uncertainties that reduce the significance of the indication are discussed. The determination of the expected number of background photons has the strongest effect. A very conservative choice, in which the number is estimated from all detected photons, results in a reduced significance of $1.13 \times 10^{-2} = 2.28\,\sigma$ for $\tau_{\gamma\gamma} \geqslant 2$ after accounting for trials.

- An estimation of the expected number of photons from all AGN with known redshift that are firmly detected above 1 GeV does result in an indication for a PPA only if spectral curvature is assumed for all sources.

# 4 Interpretations of the anomalous propagation of $\gamma$-rays

The indication for an enhanced transparency of the Universe for very high energy (VHE; energy $E \gtrsim 100\,\mathrm{GeV}$) $\gamma$-rays found in the data at high optical depths ($\tau_{\gamma\gamma} \geqslant 2$) described in the previous Chapter can only be explained within the standard paradigm of $\gamma$-ray propagation if several systematic uncertainties are invoked simultaneously (see Section 3.1.2). Otherwise, mechanisms have to exist that alter the opacity of the Universe. The situation is less conclusive for high energy $\gamma$-rays detected with the Large Area Telescope (LAT) on board the *Fermi* satellite in the optical thick regime: Above $\tau_{\gamma\gamma} \geqslant 2$ the probability is as small as $1.2 \times 10^{-4}$ to detect the three observed photons. However, if all active galactic nuclei (AGN) with sufficiently large redshift are taken into account, the probability increases to 0.12. This result depends on the assumed intrinsic spectrum; if a logarithmic parabola is used instead of a power law to describe the intrinsic spectrum the probability is only increased to $5.6 \times 10^{-3}$.
This chapter reviews approaches discussed in the literature that can potentially ease the tension between VHE data and EBL models.

## 4.1 Electromagnetic cascades

The $e^+e^-$ pairs created in the interaction of VHE $\gamma$-rays with photons of the extragalactic background light (EBL) can upscatter low energy photons of the cosmic microwave background (CMB) via the inverse Compton (IC) process, and initiate an electromagnetic cascade (see Sections 1.2.1 and 2.3.2). This reduces the effective optical depth and might explain the indication for the pair-production anomaly (PPA).
Aharonian *et al.* (2002b) used this mechanism to quantitatively explain the increasing flux above 10 TeV in the spectrum of Markarian 501 during a major flare event in 1997 (Aharonian *et al.*, 1999b, see top-right panel of Figure A.2 in Appendix A for the spectrum). They identified several requirements for the cascade mechanism to produce the pile-up at the highest energies of the spectrum. The deflection of the pairs in the intergalactic magnetic field (IGMF) introduces a time delay of

the secondary $\gamma$-rays, $\Delta t \propto B_{\rm IGMF}^2 E^{-5/2}$, for coherence lengths $\lambda_{\rm IGMF}^c$ of the IGMF larger than the cooling length of IC scattering and $\Delta t \propto B_{\rm IGMF}^2 E^{-2}$ otherwise (Plaga, 1995; Neronov & Semikoz, 2009; Taylor *et al.*, 2011, see also the discussion of cascade emission in Chapter 2). Hence, the IGMF should not exceed $10^{-18}$ G, so that the observed variability of Markarian 501 of less than several hours is not smeared out (Aharonian *et al.*, 2002b). Even with such small values of $B_{\rm IGMF}$, the minimal variability of secondary $\gamma$-rays is of the order of $\sim$ 10 hours due to the transversal momentum spread in the cascade formation (Neronov & Semikoz, 2009) in conflict with the data. Moreover, the enhancement of the VHE $\gamma$-ray flux is only efficient up to distances of $\sim$ 100 Mpc, because of the competition of creation and absorption of $\gamma$-rays, and requires hard intrinsic spectra with spectral indices $\lesssim 2$ that extend at least up to 100 TeV (see Figures 5 and 6 in Aharonian *et al.*, 2002b). Since the luminosity distance of Markarian 501 (redshift $z = 0.034$) is $\sim$135 Mpc, the distance constraint does not apply for this source. However, the indication of the PPA discussed in this work is due to sources at a variety of distances mostly beyond 100 Mpc. Together with the requirements on the spectrum and the on the $B_{\rm IGMF}$ value, this renders the electromagnetic cascade initiated by primary $\gamma$-rays an unlikely explanation for the evidence of the PPA.

Another possibility is that the cascade is initiated by the interaction of cosmic rays with background radiation fields (Essey & Kusenko, 2010; Essey *et al.*, 2010, 2011). Cosmic rays and especially protons are believed to be accelerated in jets of AGN up to energies $E_p \sim 10^{21}$ eV (Berezinsky *et al.*, 2006). Above $\sim 3\times10^{19}$ eV, the proton flux is strongly attenuated due to the interaction with the CMB, $p + \gamma_{\rm CMB} \rightarrow p + \pi^0$ and $p + \gamma_{\rm CMB} \rightarrow n + \pi^+$ (so-called GZK cut-off; Greisen, 1966; Zatsepin & Kuz'min, 1966). Below this threshold energy, protons can transport energy efficiently over cosmological distances. They rarely interact with background photons, predominantly through the Bethe-Heitler process $p + \gamma_{\rm CMB} \rightarrow p + e^+ + e^-$ but also via $p + \gamma_{\rm EBL} \rightarrow p + \pi^0$ or $p + \gamma_{\rm EBL} \rightarrow n + \pi^+$. In the last process, the $\pi^+$ decay produces neutrinos and a detection of the neutrino flux could be used to probe this mechanism (Essey *et al.*, 2010, 2011). The other processes initiate an electromagnetic cascade (directly or via the $\pi^0 \rightarrow \gamma + \gamma$ decay). If this occurs within a distance from Earth of the order of the mean free path of $\gamma$-rays, the observed VHE flux can be enhanced by the secondary photons, as their energy is cascaded down to TeV energies (Aharonian *et al.*, 2013). This secondary component should start to dominate over the primary flux at optical depths between 1 and 3, exactly what is expected from the PPA (Essey & Kusenko, 2012). The protons only propagate towards Earth if they are not deflected substantially in the IGMF. This requires field strength of the order of $10^{-15}$ G or less in accordance with currently allowed values (Essey *et al.*, 2011). Furthermore, they should not be deflected in regions of enhanced field strength like galaxies or galaxy clusters. Berezinsky *et al.* (2002) estimated the mean free path of cosmic rays for the interaction with such magnetic bubbles and find it to be of the order (1 – 2) Gpc, sufficient for observed blazars. This argument does, however,

not apply if the AGN itself is located inside a galaxy cluster.
The deflections of protons and the created $e^+e^-$ pairs also wash out the time variability of the primary $\gamma$-rays. Prosekin *et al.* (2012) investigated the variability behavior of the cascade and concluded that at most a variability of the order of months is expected for sources with $z > 0.2$ and $\gamma$-ray energies $E > 1$ TeV for $B_{\rm IGMF} \sim 10^{-15}$ G. Interestingly, the variability should show an energy dependent behavior. Secondary $\gamma$-rays of TeV energies are created in proton interactions closer to Earth and arrive earlier with respect to $\gamma$-rays with lower energies. The latter form at later stages of a cascade that is initiated farther away from Earth. Above 1 TeV, the time delay should be roughly constant, as it is determined by the deflections of protons in the IGMF and the maximum energy of the proton acceleration and injection spectrum. For lower energies, the time delay is dominated by the transversal spread and the deflection of the particles in the cascade.
Current observations of variability at very high energies do not contradict this model. The minute scale variability of the blazar PKS 2155-304 was observed for energies $E > 200$ GeV (Aharonian *et al.*, 2007a) or optical depths $\tau_{\gamma\gamma}(z = 0.116, E > 200\,\text{GeV}) > 0.12$ (with the EBL model of Kneiske & Dole, 2010). Likewise, the flux doubling on a thirty minute time scale of Markarian 421 above 2 TeV (Horns, 2005) corresponds to an optical depth of $\tau_{\gamma\gamma}(z = 0.031, E > 2\,\text{TeV}) > 0.33$. In these $\tau_{\gamma\gamma}$ regimes, a mixture of primary and secondary $\gamma$-rays is expected, i.e., the short term variability is attributed to the primary component.
A fixed spectral shape of the secondary $\gamma$-rays is expected for sources at redshifts between $0.1 \lesssim z \lesssim 0.2$; The spectrum should be flat in $E^2$ with a modest maximum around 100 GeV and only weakly dependent on the injection spectrum (modeled as $E_p^{-\alpha_p}\Theta(E_p - E_{\rm max})$ for the proton energy $E_p$; Essey *et al.*, 2011). For large redshifts, $z > 1$, the expected spectrum shows a steep decline in flux below 1 TeV, a spectral hardening around 1 TeV, and an extension of the emission up to $\sim 10$ TeV; the exact shape depending on the injection spectrum for proton energies $E_p \lesssim 10^{18}$ eV (Aharonian *et al.*, 2013).
Typically, a spectral index of the proton spectrum of $\alpha_p = 2$ is assumed for the cascade mechanism to work efficiently (Essey & Kusenko, 2010; Essey *et al.*, 2010, 2011; Prosekin *et al.*, 2012; Essey & Kusenko, 2012; Aharonian *et al.*, 2013), in contrast to the observed cosmic-ray spectrum which has a softer index of $\alpha_{\rm CR} = 2.7$. This difference can be explained by the superposition of sources that result in a harder spectrum at low energies (Berezinsky *et al.*, 2006). For indices $\alpha_p \leqslant 2.2$, Murase *et al.* (2012) and Razzaque *et al.* (2012) point out that the isotropic jet luminosities have to be of the order of the Eddington luminosity or higher [see Eq. (2.17)]. Albeit the observation of super-Eddington luminosities in variable AGN (e.g., in 3C 454.3; Abdo *et al.*, 2011a), the energy requirements are still challenging in standard blazar emission models. This issue could be resolved if high Doppler boost factors $\delta_{\rm D} \sim 100$ of the jets are assumed (Aharonian *et al.*, 2013).
Other cooling mechanisms might dominate over the IC scattering of the $e^+e^-$ pairs,

inhibiting the formation of an electromagnetic cascade. Broderick *et al.* (2012) and Schlickeiser *et al.* (2012) consider the possibility that the $e^+e^-$ pairs constitute a cold ultrarelativistic plasma beam with typical Lorentz factors of $\gamma \sim 10^6$ propagating in the background plasma of the intergalactic medium (IGM). Here, "cold" refers to a small transversal momentum dispersion with respect to the beam propagation direction. Broderick *et al.* (2012) estimate that the transversal momentum spread is dominated by heating of the plasma due to the pair production, and that is of the order $m_e c^2 \ll p_\parallel$, with $p_\parallel$ the longitudinal momentum. In such a pair beam, the interactions of plasma waves with the beam particles can lead to the growth of plasma instabilities, and as a consequence the particles loose energy by heating the IGM instead of upscattering CMB photons. Plasma instabilities arise only if a sufficient number of pairs are present in the beam; this depends on the $\gamma$-ray (or proton) luminosity of the blazars and the optical depth for VHE $\gamma$-rays (or protons). For VHE $\gamma$-rays as the source for secondary photons, Schlickeiser *et al.* (2012) estimate that pair beam density, $n_b = 10^{-22}\mathrm{cm}^{-3} n_{22}$, must obey $n_{22} \geqslant n_c = 4.8 \times 10^{-3} T_4$ with $T_4 = 10^4 T$ the temperature of the IGM. The fastest growing instabilities are found to be the electrostatic and electromagnetic oblique two-stream instabilities (Broderick *et al.*, 2012; Schlickeiser *et al.*, 2012). Following Broderick *et al.* (2012), the two-stream instability can be envisaged as a Langmuir wave (plasma density fluctuation) that propagates parallel to the longitudinal momentum of the beam, but in opposite direction. Electrostatic fields caused by the charge separation decelerate the particles in the beam, and due to the coupling of the wave to the background plasma energy is deposited in the heating of the IGM. In the oblique instability, the Langmuir wave propagates at an angle $\theta \neq \pi$ with respect to $p_\parallel$, and the particles are not decelerated but deflected in the $E$ fields. The cooling rate of the oblique instability dominates the IC cooling rate, and the formation of the electromagnetic cascade is strongly inhibited. For weak blazars, about half of the beam energy is dissipated by heating the IGM, so the cascade formation is also suppressed to some degree (Schlickeiser *et al.*, 2012).

However, the numerical calculations performed for the cooling rate due to the instability are done for mildly relativistic beams ($\gamma \sim 3$), and not for ultrarelativistic ones. Additionally, the numerical results need to be extrapolated over many orders of magnitude in density as $n_b/n_{\mathrm{IGM}} \sim 10^{-18}$ (Broderick *et al.*, 2012), since equal densities of the beam and background plasma are assumed. Further doubts on the growth rates of the instabilities were raised by Miniati & Elyiv (2012): They find from Monte-Carlo simulations of the particles in the cascade that the transverse momentum spread can be large, and consequently only a small number of particles that are in resonance with the Langmuir wave contribute to the instability growth (Schlickeiser *et al.* 2012 and Broderick *et al.* 2012 resort to a $\delta$ approximation of the transversal momentum spread). Furthermore, scattering between pairs and background plasma ions (so-called non-linear Landau damping) can compete with the instability growth until an equilibrium is reached. This can stabilize the

plasma beam on time scales larger than the Hubble time. Plasma inhomogeneities can also contribute to this stabilization.
To conclude, proton initiated electromagnetic cascades pose an interesting possibility to explain the PPA, as the observed $\gamma$-ray flux is enhanced for optical depths $\tau_{\gamma\gamma} \gtrsim 1$ in this mechanism. The model is testable with future data due to its predictions of the spectral shape and variability. The proton cascade can only produce a seizable amount of secondary $\gamma$-rays if either the isotropic proton luminosity of the relativistic jet is close to the Eddington luminosity, or the jet is highly Doppler boosted in the observer's frame with Doppler factors $\delta_D \sim 100$. Furthermore, there is an ongoing discussion if an electromagnetic cascade is initiated at all or if, alternatively, the energy of the pairs is dissipated by heating the IGM.

## 4.2 Beyond the Standard Model

Extension of the Standard Model (SM) of particle physics can influence the propagation of VHE $\gamma$-rays. These models typically do neither require high AGN luminosities, nor do they change the intrinsic variability of the source. This comes at the "price" of, e.g., Lorentz invariance violation or the existence of non-SM particles. In the latter case, photons could oscillate into these particles and circumvent pair production.

### 4.2.1 Lorentz invariance violation

Certain quantum gravity theories that aim to unify the Standard Model with gravity predict Lorentz invariance violation (LIV) at energies near the Planck scale, $E_{\mathrm{Pl}} = \sqrt{\hbar c^5/G} \approx 1.22 \times 10^{19}\,\mathrm{GeV}$, with the reduced Planck constant $\hbar$, the speed of light $c$, and $G$ the gravitational constant entering in Newton's law (see, e.g., Shao & Ma, 2010, for a review). Examples of these theories are quantum loop (e.g., Gambini & Pullin, 1999), space-time foam (e.g., Ellis *et al.*, 2000), or double special relativity theories (e.g., Amelino-Camelia & Ahluwalia, 2002). Some classes of theories can be expressed as effective field theories by including additional terms in the Lagrangian. All renormalizable additional operators have been calculated by Colladay & Kostelecký (1998) with couplings of the order of $O(10^{-23})$. Non-renormalizable 5- or 6-dimensional operators are also possible which are, however, suppressed by $E_{\mathrm{Pl}}$ or $E_{\mathrm{Pl}}^2$ (Myers & Pospelov, 2003; Mattingly, 2008). A consequence of LIV is the modification of the dispersion relation of leptons and photons (with photon energy $E$ and three momentum $\mathbf{k}$) (Shao & Ma, 2010),

$$E^2 = k^2 \left[ 1 \pm \sum_{n=1}^{\infty} \left( \frac{E}{\xi_n E_{\mathrm{Pl}}} \right)^n \right] \tag{4.1}$$

with $c = \hbar = 1$. The scale of the quantum gravity theory is given by $\xi_n E_{\rm Pl}$, with $\xi_n > 0$ and expected of order one. From the observational point of view, the most important terms that can have measurable effects are the linear and quadratic terms in the above expansion. All higher orders are neglected from now on. For example, space-time foam models have $\xi_1 \neq 0$ and $\xi_2 = 0$, and no LIV for charged particles, whereas 6-dimensional effective field theories lead only to quadratic modifications, $\xi_1 = 0$ and $\xi_2 \neq 0$ (Shao & Ma, 2010). The "+" in the above equation corresponds to superluminal motion of photons, whereas the "−" sign results in subluminal motions (increasing or decreasing velocity of the particles with energy, respectively). Thus, also the photon changes its speed depending on its energy. Additionally, the transformation between different inertial frames are not given by Lorentz transformations any longer, making the lab frame the only accessible one.

The breakdown of Lorentz invariance has several consequences that affect the propagation of high and very high energy $\gamma$-rays from astrophysical sources. For instance, as suggested by Amelino-Camelia *et al.* (1998), $\gamma$-ray bursts (GRBs) can be used to probe LIV. These bursts occur on very short timescales and are very bright in $\gamma$-rays, and consequently detectable up to very large distances (see, e.g., Mészáros, 2013, for a recent review). The different speeds of photons with different energies induce a time lag that is enhanced by cosmological expansion. For example, the observation of a 31 GeV photon from the GRB090510 at a redshift of $z = 0.903 \pm 0.003$ with the *Fermi*-LAT is used to set a lower bound on the LIV parameter above the Planck scale, $\xi_1 > 1.22$, for subluminal motion (Abdo *et al.*, 2009a).

Most importantly in the present context, LIV results in a modification of the threshold energy for pair production. This has been utilized by several authors to explain the high energy end of the intrinsic spectra of Markarian 501 and Markarian 421 (Kifune, 1999; Stecker & Glashow, 2001; Stecker, 2003; Jacob & Piran, 2008). The modified threshold energy for head-on collisions ($\mu = -1$, cf. Eq. 1.11) at $z = 0$ for subluminal motion reads (Jacob & Piran, 2008)

$$\epsilon_{\rm thr} = \frac{m_e^2}{E} + \frac{\zeta_n}{4}\left(\frac{E}{\xi_n E_{\rm Pl}}\right)^n E, \tag{4.2}$$

with $\zeta_n$ a parameter of order one that depends on whether LIV also affects leptons. This expression is derived under the assumption that energy-momentum conservation is unaffected by LIV. For superluminal motions, the new extra term would be subtracted, which would lead to a decreased threshold and exponential cut-offs in all spectra in tension with current observations. In the subluminal case, however, the threshold follows the classical behavior until a critical energy $\omega_c$ is reached. For energies $E > \omega_c$, the threshold increases again and pair production is suppressed.

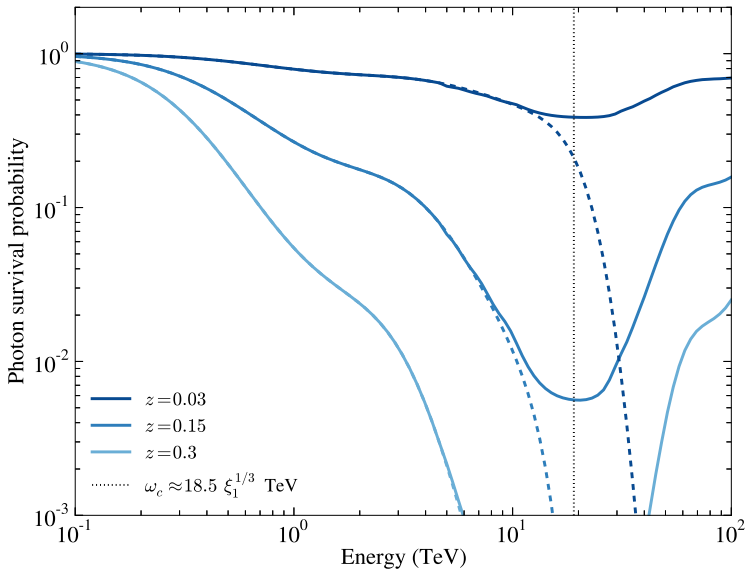


**FIGURE 4.1:** Optical depth in the presence of LIV for three different redshift values. The critical energy $\omega_c$ is shown as a dotted line and the dashed lines show the optical depth for $\xi_1 \to \infty$.

The critical energy is the energy for which $\epsilon_{\rm thr}$ becomes minimal, i.e.,

$$\left.\frac{\partial \epsilon_{\rm thr}}{\partial E}\right|_{E=\omega_c} = 0 \quad \Leftrightarrow \quad \omega_c = \left[\frac{4m_e^2(\xi_n E_{\rm Pl})^n}{(n+1)\zeta_n}\right]^{\frac{1}{n+2}}. \tag{4.3}$$

For the linear case and $\zeta_n = 1$, one finds $\omega_c \approx 18.5\xi_1^{1/3}$ TeV and $\omega_c \approx 93.9\xi_2^{1/2}$ PeV for $n = 2$. The effect on the optical depth for $n = 1$ and $\xi_n = \zeta_n = 1$ is displayed in Figure 4.1 for three different redshifts. The optical depth is derived by integrating over the EBL density $\nu I_\nu = c/(4\pi)\epsilon^2 n_\epsilon(\epsilon)$ predicted by the EBL model of Kneiske & Dole (2010). The effect of LIV clearly depends only on $\omega_c$ which evolves only weakly with redshift and the transparency of the Universe is restored at different values of the optical depth, between $\tau_{\gamma\gamma} = 1.5$ for $z = 0.031$ and $\tau_{\gamma\gamma} = 83.8$ for $z = 0.536$ (using again the EBL of Kneiske & Dole 2010). This implies that LIV is not able to explain the indication for the PPA found in the previous Chapter. The indication shows up for $\tau_{\gamma\gamma} \geqslant 2$ and thus for very different energies for the different redshifts of the VHE emitting AGN. If LIV was present a trend with energy should be visible, e.g., in Figure 3.6. On the other hand, LIV cannot be ruled out for $\xi_1 \gtrsim 1$ with the non-observation of this effect, as most blazar spectra are measured at energies below $\omega_c$. Stringent limits can be placed on $\xi_n$ by considering the non-observation of photons above energies $E \gtrsim 10^{10}$ eV. Such photons are the result of

the decay of neutral pions that are produced in the interaction of cosmic rays with the CMB. These photons are attenuated by pair production with low energy photons from the CMB and the radio background. Under the assumption of certain cosmic-ray spectra and cosmic-ray composition, Galaverni & Sigl (2008) are able to obtain the stringent constraint $\xi_1 \gtrsim 4.17 \times 10^{14}$ for both sub- and superluminal motions and $\xi_2 \gtrsim 4.17 \times 10^6$ for subluminal motions only. Maccione *et al.* (2010) extended these bounds on space-time foam theories. Further constraints and prospects for the Cherenkov Telescope Array (CTA) are reviewed by Ellis & Mavromatos (2013).

### 4.2.2 Hidden gauge bosons

Pair production can be circumvented if VHE $\gamma$-rays convert into particles that do not interact with EBL photons. Viable candidates for such particles are given in SM extensions that predict additional $U(1)$ symmetry groups under which the SM particles are uncharged (see, e.g., Jaeckel & Ringwald, 2010, for a review). Such "hidden" symmetry groups arise, e.g., in the compactification of string theories (e.g., Abel *et al.*, 2008). The hidden sector can interact with SM particles through heavy particles with masses above the electroweak scale that are charged under the SM and the additional hidden $U(1)$. The new interactions are typically suppressed by the masses of the heavy particles (Holdom, 1986). However, the photon can kinetically mix with its hidden partner, the so-called hidden or dark photon (Okun, 1982; Holdom, 1986). The Lagrangian of such mixing can be written as (e.g., Mirizzi *et al.*, 2009b)

$$\mathcal{L} \supset -\frac{1}{4}F_{\mu\nu}F^{\mu\nu} - \frac{1}{4}X_{\mu\nu}X^{\mu\nu} + \frac{\sin\chi_0}{2}F_{\mu\nu}X^{\mu\nu} + \frac{\cos^2\chi_0}{2}m_{\gamma'}^2 X_\mu X^\mu, \tag{4.4}$$

where $F_{\mu\nu}$ is the electromagnetic field tensor and $X_{\mu\nu}$ the equivalent in the hidden sector with the corresponding hidden photon field $X_\mu$. The third term denotes the kinetic mixing with a mixing angle $\chi_0$. The hidden photon $\gamma'$ can acquire a mass $m_{\gamma'}$ through a hidden Higgs or Stueckelberg mechanism (e.g., Goodsell *et al.*, 2009). Interestingly, the mass of the hidden photon can be in the sub-eV range, making it a weakly interacting sub-eV particle (WISP). Similar to neutrino oscillations, the propagation and interaction eigenstates of the photon are no longer equivalent to each other and the oscillation probability over a distance $L$ in vacuum between the photon of energy $E$ and hidden (sterile) propagation eigenstate ($\gamma_S$) is given by (e.g., Ahlers *et al.*, 2007)

$$P_{\gamma\to\gamma_S} = \sin^2(2\chi_0)\sin^2\left(\frac{m_{\gamma'}^2 L}{4E}\right). \tag{4.5}$$

The oscillation length for which the argument of the sin becomes equal to $\pi$ is

$$L_{\rm osc} = \frac{4\pi E}{m_{\gamma'}^2} \approx 8 \times 10^{-6} \left(\frac{E}{\rm TeV}\right)\left(\frac{m_{\gamma'}}{10^{-7}\,\rm eV}\right)^{-2} \rm Gpc. \tag{4.6}$$

Effects of the $\{\gamma \leftrightarrow \gamma_S\}$ oscillations can be searched for in astrophysical environments and in the laboratory. For example, the production of hidden photons would influence the stellar evolution (Raffelt, 1996; Redondo, 2008; An *et al.*, 2013a,b), or the CMB (Jaeckel *et al.*, 2008; Simha & Steigman, 2008; Mirizzi *et al.*, 2009b). In the laboratory, bounds were placed on the mixing angle by searching for alternations from the inverse distance squared behavior of Coulomb's law (Williams *et al.*, 1971; Goldhaber & Nieto, 1971; Okun, 1982; Popov, 1999) or with light-shining-through-a-wall experiments (e.g., Ehret *et al.*, 2009). For a compilation of limits, see the review by Jaeckel & Ringwald (2010, especially Figure 4) and references therein.

Hidden photons do not interact with EBL photons and thus evade pair production. If a significant part of the photon beam is in the sterile state during the propagation towards Earth, a flux enhancement is possible. This would imprint an oscillatory feature on the spectrum. In contrast to electromagnetic cascade scenarios, any source intrinsic variability would be conserved.

The parameter space relevant for photon-hidden-photon oscillations is given by two conditions, namely that (a) the oscillation length is smaller than the distance to the source, $L_{\rm osc} < d$, so that conversions can indeed occur, and (b) the oscillations are coherent. The first condition leads to a lower bound on $m_{\gamma'}$ (neglecting cosmological expansion),

$$m_{\gamma'} > 2.83 \times 10^{-10} \left(\frac{E}{\rm TeV}\right)^{1/2} \left(\frac{d}{\rm Gpc}\right)^{1/2} \rm eV \approx 10^{-9}\,eV, \tag{4.7}$$

for luminosity distances of $\sim 1\,$Gpc (equal to a redshift $z \sim 0.2$) and $E = 1\,$TeV. The second condition ensures that the wave packets of the sterile and active state have a sufficient overlap in order for the two states to mix. A quantum mechanical calculation results in the coherence length (Nussinov, 1976; Giunti & Kim, 1998; Zechlin *et al.*, 2008)

$$L_{\rm coh} = \frac{4\sqrt{2}\sigma_x E^2}{m_{\gamma'}^2} = 5.5 \times 10^{32} \left(\frac{E}{\rm TeV}\right)^2 \left(\frac{\sigma_x}{\rm pc}\right)\left(\frac{m_{\gamma'}}{10^{-7}\rm eV}\right)^{-2} \rm Gpc, \tag{4.8}$$

where $\sigma_x = \sqrt{\sigma_{x\rm P}^2 + \sigma_{x\rm D}^2}$ is quadratic the sum of the spatial uncertainties of the production ($\sigma_{x\rm P}$) and detection process ($\sigma_{x\rm D}$). Coherence is satisfied if $L_{\rm osc} < L_{\rm coh}$ and $\sigma_x < L_{\rm osc}$ (Nussinov, 1976; Giunti & Kim, 1998). The spatial uncertainty of the production is determined by the process responsible for the VHE emission in

the blazar, e.g., in leptonic scenarios, photons of synchrotron or external radiation fields upscattered by the inverse Compton process. In this case, Zechlin (2009) finds $\sigma_{x\mathrm{P}} \approx 0.16\,\mathrm{kpc}$ for the Crab nebula, much larger than the upper bound on the extension of the nebula in the VHE regime which is inferred from observations to be of the order of 1 pc (Aharonian *et al.*, 2004). At most, $\sigma_{x\mathrm{P}}$ should be equal to the size of the emission zone, which is in a blazar often assumed to be of the order of $O(0.1\,\mathrm{pc})$, the size of a relativistic plasma blob in the jet (e.g., Katarzyński *et al.*, 2001). The spatial uncertainty of the detection process is much smaller and can be neglected (Zechlin, 2009). If one conservatively sets $\sigma_x \approx 1\,\mathrm{pc}$, from $\sigma_x < L_{\mathrm{osc}}$ one arrives at an upper bound for $m_{\gamma'}$,

$$m_{\gamma'} < 8.9 \times 10^{-6} \left(\frac{E}{\mathrm{TeV}}\right)^{1/2} \left(\frac{\sigma_x}{\mathrm{pc}}\right)^{-1/2} \mathrm{eV} \approx 10^{-5}\,\mathrm{eV}. \tag{4.9}$$

For this mass range, $10^{-9} \lesssim (m_{\gamma'}/\mathrm{eV}) \lesssim 10^{-5}$, the current bounds on the mixing angle give $\chi_0 \lesssim 10^{-7}$ mainly from the searches for deviations from Coulomb's law and CMB polarization induced by hidden photons (see Figure 4 in Jaeckel & Ringwald, 2010). Hence, only a small number of photons will convert to hidden photons and no significant change in the spectra is expected. In reality, the photon beam will not propagate through vacuum but through media. Similar to the neutrino case (Kuo & Pantaleone, 1989), this leads to a modification of the oscillation probability because of the effective photon mass. The mixing angle in media, $\chi$, is related to the vacuum angle through (Redondo, 2008; Jaeckel *et al.*, 2008),

$$\sin(2\chi) = \frac{\sin\chi_0}{\sqrt{\sin^2(2\chi_0) + (\cos(2\chi_0) - \xi)^2}}, \tag{4.10}$$

with $\xi = m_\gamma/m_{\gamma'}$ the ratio between the effective photon mass and the hidden photon mass. For $\xi \gg 1$, oscillations are strongly damped and $\chi \to \pi/2$, while vacuum oscillations are recovered for $\xi \ll 1$, so that $\chi \to \chi_0$. A strong enhancement of the oscillation occurs at the resonance $m_\gamma = m_{\gamma'}$ for which the mixing becomes maximal, $\chi \to \pi/4$. Approximating the photon mass with the plasma frequency yields $m_\gamma^2 \approx \omega_{\mathrm{pl}}^2 = 4\pi\alpha n_e/m_e$, with the fine structure constant $\alpha$ and the electron number density $n_e$, so that $m_\gamma \approx 3.7 \times 10^{-11} (n_e/\,\mathrm{cm}^{-3})^{1/2}\,\mathrm{eV}$. For the resonance to occur in the desired mass range, an electron density $n_e \gtrsim 10^4\,\mathrm{cm}^{-3}$ would be required. The highest densities can be expected inside the source region where the VHE emission is produced. As an example for a quantitative treatment, the values obtained from a model fit to a multiwavelength spectral energy distribution of a quiescent state of the blazar PKS 2155-304 are used (Aharonian *et al.*, 2009c). The best-fit values are obtained with an electron density given by a double broken power law between Lorentz factors $\gamma_{\mathrm{min}} = 1$ and $\gamma_{\mathrm{max}} = 10^{6.5}$ with spectral indices $p_1 = 1.3$ between $\gamma_{\mathrm{min}}$ and $\gamma_1 = 1.4 \times 10^4$, $p_2 = 3.2$ between $\gamma_1$ and $\gamma_2 = 2.3 \times 10^5$, and $p_3 = 4.3$

above $\gamma_2$. The integrated number of electrons is found to be $N_{\rm tot} = 6.8 \times 10^{51}$ inside a plasma blob of radius $R' = 1.5 \times 10^{17}\,\mathrm{cm}$ in the comoving frame. Under the assumption of a homogeneous plasma, the average electron number density is $n_e = 0.5\,\mathrm{cm}^{-3} \ll 10^4\,\mathrm{cm}^{-3}$. Even for larger densities and / or smaller emitting regions, it is unlikely that sufficiently large number densities are reached for the electrons responsible for upscattering synchrotron photons to TeV energies, as the electron spectra are generally soft. The required Lorentz factors are of the order $\gamma \sim 10^4$ [assuming the Thomson regime for IC scattering and X-ray target photons, see Eq. (1.7)]. Nevertheless, even if resonant production was realized somewhere in the source, such high densities are not realized in the intervening interstellar, intracluster, or intergalactic media and the reconversion into photons would be suppressed. Consequently, the conversion into hidden photons cannot serve as an explanation for the indication of the PPA.

### 4.2.3 Axion-like particles

More promising WISP candidates to reduce the opacity of the Universe are pseudo-Nambu-Goldstone bosons also called axion-like particles (ALPs), which were already introduced in Chapter 1. In the presence of ambient magnetic fields, photons and ALPs can oscillate into each other and thus the photons circumvent pair production. This mechanism is used to explore the possibility to observe photons from the decay of $\pi^0$ mesons produced in the GZK cut-off (Csáki *et al.*, 2003) and the impact on VHE spectra was first discussed by Mirizzi *et al.* (2007) and de Angelis *et al.* (2007). In contrast to hidden photons, the parameter space interesting for the ALP mixing with VHE $\gamma$-rays is less constrained (see the review in Chapter 1 and Figure 1.8 for current experimental bounds). In the next Chapter, photon-ALP oscillations are discussed in detail. The photon-ALP couplings and ALP masses that reduce the significance of the PPA will be identified. In this way, the first lower limits from VHE $\gamma$-ray observations on the photon-ALP coupling will be derived.

# 5 First lower limits on the photon-axion-like-particle coupling from VHE $\gamma$-ray observations

Indications exist that the Universe is more transparent to very high energy (VHE; energy $E \gtrsim 100\,\mathrm{GeV}$) $\gamma$-rays of cosmological sources than suggested by current models of the extragalactic background light (EBL). In the standard paradigm, the reaction $\gamma_{\mathrm{VHE}} + \gamma_{\mathrm{EBL}} \rightarrow e^+ + e^-$ leads to an exponential suppression of the flux with the optical depth $\tau_{\gamma\gamma}(z, E)$ (cf. Chapter 1.2 for further details and Nikishov, 1962; Jelley, 1966; Gould & Schréder, 1966, 1967). Above a certain energy, the Universe should thus become opaque to $\gamma$-rays from sufficiently distant sources.
The observations of distant blazars with data points in the optical thick regime ($\tau_{\gamma\gamma} \geqslant 1$) (e.g., Aharonian *et al.*, 2006a, 2007g; Albert *et al.*, 2008b) and the indication for an pair-production anomaly (PPA) found in Chapter 3 point to a low opacity of the Universe for VHE $\gamma$-rays. This is also confirmed with upper limits on the EBL photon density derived in Chapter 2. In the previous Chapter, several mechanisms along with arguments against them have been summarized that attempt to explain this low opacity. An appealing alternative is the conversion of VHE $\gamma$-rays into axion-like particles (ALPs, e.g., de Angelis *et al.*, 2007; Mirizzi *et al.*, 2007; De Angelis *et al.*, 2009). ALPs are pseudo Nambu-Goldstone bosons that are created if additional global symmetries to the standard model are spontaneously broken (see, e.g., Jaeckel & Ringwald, 2010, for a review and Section 1.4). Such fields are a common prediction in compactified string theories (e.g., Cicoli *et al.*, 2012). Their phenomenology is closely related to that of axions which solve the strong CP problem in QCD (Peccei & Quinn, 1977; Weinberg, 1978; Wilczek, 1978). Most importantly in the present context, ALPs share the same coupling to photons as axions, characterized by the Lagrangian

$$\mathcal{L}_{a\gamma} = -\frac{1}{4} g_{a\gamma}\, \tilde{F}_{\mu\nu} F^{\mu\nu} a = g_{a\gamma}\, \mathbf{E} \cdot \mathbf{B}\, a, \tag{5.1}$$

where $F^{\mu\nu}$ is the electromagnetic field tensor (with electric and magnetic fields $\mathbf{E}$ and $\mathbf{B}$, respectively), $\tilde{F}^{\mu\nu}$ is its dual, $a$ is the ALP field strength, and $g_{a\gamma}$ is the photon-ALP coupling strength which has the dimension (Energy)$^{-1}$. In contrast to

the axion, the ALP mass $m_a$ is unrelated to the coupling strength. The spin mismatch between the ALP and the photon requires the existence of external magnetic fields for the conversion. The effect of photon-ALP mixing on VHE $\gamma$-ray spectra in different magnetic field settings has been extensively discussed in the literature, the basic idea being that ALPs traverse cosmological distances unimpeded and the reconversion into photons enhances the $\gamma$-ray flux observed on Earth. The case of a conversion in an intergalactic magnetic field (IGMF) was addressed by, e.g., de Angelis *et al.* (2007); Mirizzi *et al.* (2007); Mirizzi & Montanino (2009); de Angelis *et al.* (2011); Wouters & Brun (2012). The magnetic fields in and around the source were included by Sánchez-Conde *et al.* (2009); Tavecchio *et al.* (2012), and Simet *et al.* (2008) studied the back conversion of ALPs into photons in the galactic magnetic field (GMF) of the Milky Way. Recently, the photon-ALP mixing for sources located inside galaxy clusters and the reconversion in the GMF was also investigated (Horns *et al.*, 2012). Usually, previous studies used fixed values for the ALP mass and coupling close to current experimental bounds in order to maximize the effect on the $\gamma$-ray spectra.

As will be shown in the following, the photon-ALP oscillations can lead to an enhancement of the $\gamma$-ray flux for $\tau_{\gamma\gamma} \gtrsim 2$. This behavior matches the $\sim 4\,\sigma$ indication for the PPA that is evident in VHE spectra above this value of the optical depth. Additionally, ALPs do not share some of the problems of the alternative mechanisms presented in the previous chapter: photon-ALP oscillations preserve the possible intrinsic source variability and alter the spectra in a $\tau_{\gamma\gamma}$ dependent way (rather than at a fixed energy as in Lorentz invariance violation scenarios). In this Chapter, the goal is to determine the preferred region in the $(m_a, g_{a\gamma})$ parameter space that significantly minimizes the tension between data and model predictions. This allows, for the first time, to place a lower limit on the photon-ALP coupling to explain the observed transparency of the Universe for VHE $\gamma$-rays. Four different scenarios for the intervening magnetic field will be considered, including mixing in the IGMF, the intracluster magnetic field (ICMF), and the GMF of the Milky Way. In two cases, the parameters of the IGMF and ICMF will be chosen as optimistically as possible in order to derive lower limits on $g_{a\gamma}$. Additionally, a more conservative choice of *B*-field model parameters will be investigated. Furthermore, two different EBL model realizations will be studied. The results presented here have been published in *Physical Review D* (Horns *et al.*, 2012; Meyer *et al.*, 2013).

## 5.1 Photon-ALP conversion in magnetic fields

The photon-ALP interaction is described by the Lagrangian

$$\mathcal{L} = \mathcal{L}_{a\gamma} + \mathcal{L}_{\mathrm{EH}} + \mathcal{L}_a, \tag{5.2}$$

where $\mathcal{L}_{a\gamma}$ is given in Eq. (5.1). From the scalar product $\mathbf{E} \cdot \mathbf{B}$ it follows that only the external $B$-field component transversal to the photon propagation direction, $\mathbf{B}_\perp$, couples to ALPs since $\mathbf{E}$ is perpendicular to the wave vector $\mathbf{k}$ of the $E$ field (Raffelt & Stodolsky, 1988). Furthermore, it can be shown that only the component of $\mathbf{E}$ in the plane defined by $\mathbf{B}_\perp$ and $\mathbf{k}$ mixes with ALPs (e.g., de Angelis *et al.*, 2011). Thus, the photon-ALP oscillations act as a polarimeter. The second term, $\mathcal{L}_{\rm EH}$, is the effective Euler-Heisenberg Lagrangian accounting for one-loop corrections in the photon propagator (e.g., Itzykson *et al.*, 1984),

$$\mathcal{L}_{\rm EH} = \frac{2\alpha^2}{45 m_e^4}\left[\left(\mathbf{E}^2 - \mathbf{B}^2\right)^2 + 7\left(\mathbf{E}\cdot\mathbf{B}\right)^2\right], \tag{5.3}$$

with the fine structure constant $\alpha$ and $m_e$ the mass of the electron. The kinetic and mass term of the ALP are included in $\mathcal{L}_a$,

$$\mathcal{L}_a = \frac{1}{2}\partial_\mu a \partial^\mu a - \frac{1}{2} m_a^2 a^2. \tag{5.4}$$

Throughout this section, natural units will be used, i.e., $\hbar = c = 1$. For a monochromatic photon / ALP beam of energy $E$ propagating along the $x_3$ axis in a cold plasma with a homogeneous magnetic field, it can be shown that $\mathcal{L}$ leads to the following Schrödinger-like equation of motion (Raffelt & Stodolsky, 1988):

$$\left(i\frac{\mathrm{d}}{\mathrm{d}x_3} + E + \mathcal{M}_0\right)\Psi(x_3) = 0, \tag{5.5}$$

with $\Psi(x_3) = (A_1(x_3), A_2(x_3), a(x_3))^T$ where $A_1(x_3)$ and $A_2(x_3)$ describe the linear photon polarization amplitudes along $x_1$ and $x_2$, respectively, and $a(x_3)$ denotes the ALP field strength. If one chooses $\mathbf{B}_\perp$ to lie only along the $x_2$ direction, the mixing matrix $\mathcal{M}_0$ can be written as

$$\mathcal{M}_0 = \begin{pmatrix} \Delta_\perp & 0 & 0 \\ 0 & \Delta_\parallel & \Delta_{a\gamma} \\ 0 & \Delta_{a\gamma} & \Delta_a \end{pmatrix}. \tag{5.6}$$

The mixture of the photon polarization states due to Faraday rotation can be safely neglected for the energies considered here, as the effect scales with the square of the photon wavelength (see below). The matrix elements $\Delta_\parallel = \Delta_{\rm pl} + 7/2\Delta_{\rm QED}$ and $\Delta_\perp = \Delta_{\rm pl} + 2\Delta_{\rm QED}$ account for medium effects on the photon propagation, where $\Delta_{\rm pl} = -\omega_{\rm pl}/(2E)$ with the plasma frequency of the medium, $\omega_{\rm pl}$. The plasma frequency is connected to the ambient thermal electron density $n_{\rm el}$ through $\omega_{\rm pl} = 3.69\times 10^{-11}\sqrt{n_{\rm el}/\mathrm{cm}^{-3}}\,\mathrm{eV}$. The QED vacuum birefringence effect is included in $\Delta_{\rm QED} = \alpha E/(45\pi)(B_\perp/(m_e^2/e))^2$, with the electric charge $e$. The term $\Delta_a = -m_a^2/(2E)$ accounts for the ALP mass and the photon-ALP mixing is induced by the off-diagonal

element $\Delta_{a\gamma} = 1/2 g_{a\gamma} B_\perp$. The numerical values in suitable units are found to be (see, e.g., Horns *et al.*, 2012)

$$\Delta_{\rm pl} = -1.1 \times 10^{-7} \left(\frac{n_{\rm el}}{10^{-3}{\rm cm}^{-3}}\right)\left(\frac{E}{\rm GeV}\right)^{-1} \ {\rm kpc}^{-1}, \tag{5.7}$$

$$\Delta_{\rm QED} = 4.1 \times 10^{-9} \left(\frac{E}{\rm GeV}\right)\left(\frac{B_\perp}{\mu{\rm G}}\right)^{2} \ {\rm kpc}^{-1}, \tag{5.8}$$

$$\Delta_{a} = -7.8 \times 10^{-2} \left(\frac{m_a}{\rm neV}\right)^{2}\left(\frac{E}{\rm GeV}\right)^{-1} \ {\rm kpc}^{-1}, \tag{5.9}$$

$$\Delta_{a\gamma} = 1.52 \times 10^{-2} \left(\frac{g_{a\gamma}}{10^{-11}\,{\rm GeV}^{-1}}\right)\left(\frac{B_\perp}{\mu{\rm G}}\right) \ {\rm kpc}^{-1}. \tag{5.10}$$

If photons are lost due to the interaction with the EBL, the elements $\Delta_{\parallel,\perp}$ are modified to include a complex absorption term, $\Delta_{\parallel,\perp} \rightarrow \Delta_{\parallel,\perp} + i/(2\lambda_\gamma^{\rm mfp})$, where $\lambda_\gamma^{\rm mfp}$ is the mean free path for photons undergoing pair production. Equation (5.5) is solved with the transfer function $\mathcal{T}(x_3, 0; E)$, i.e., $\Psi(x_3) = e^{iEx_3}\mathcal{T}(x_3, 0; E)\Psi(0)$, with the initial condition $\mathcal{T}(0, 0; E) = 1$ (see Appendix D for further details).

Neglecting the birefringence contribution for a moment, it can be shown that the photon-ALP oscillations become maximal and independent of the energy $E$ and ALP mass $m_a$ for an energy above the critical energy

$$E_{\rm crit} \equiv E\frac{|\Delta_a - \Delta_{\rm pl}|}{2\Delta_{a\gamma}} \approx 2.5\frac{|m_a^2 - \omega_{\rm pl}^2|}{1\,{\rm neV}}\left(\frac{g_{a\gamma}}{10^{-11}{\rm GeV}^{-1}}\right)^{-1}\left(\frac{B_\perp}{1\,\mu{\rm G}}\right)^{-1} {\rm GeV}, \tag{5.11}$$

defining the so-called strong mixing regime. However, as the goal here is to constrain the $(m_a, g_{a\gamma})$ parameter space, it is generally not the case that the mixing occurs in this regime.

So far, only a polarized photon beam has been considered. As of today, the polarization of VHE $\gamma$-rays cannot be measured and one has to consider an unpolarized photon beam and reformulate the problem in terms of density matrices. The general polarization matrix is given by

$$\rho(x_3) = \begin{pmatrix} A_1(x_3) \\ A_2(x_3) \\ a(x_3) \end{pmatrix} \otimes \begin{pmatrix} A_1(x_3) & A_2(x_3) & a(x_3) \end{pmatrix}^*, \tag{5.12}$$

and the equation of motion takes the form of a von Neumann-like equation,

$$i\frac{{\rm d}\rho}{{\rm d}x_3} = [\rho, \mathcal{M}_0], \tag{5.13}$$

which is solved by $\rho(x_3, E) = \mathcal{T}(x_3, 0; E)\,\rho(0)\,\mathcal{T}^\dagger(x_3, 0; E)$. In the more general case in which $\mathbf{B}_\perp$ has an arbitrary orientation and forms an angle $\psi$ with the $x_2$ axis,

the solution can be found via a similarity transformation

$$V(\psi) = \begin{pmatrix} \cos\psi & -\sin\psi & 0 \\ \sin\psi & \cos\psi & 0 \\ 0 & 0 & 1 \end{pmatrix}, \tag{5.14}$$

so that $\mathcal{M} = V(\psi)\mathcal{M}_0 V^\dagger(\psi)$, and the solution to the modified Eq. (5.13) is

$$\mathcal{T}(x_3, 0; E; \psi) = V(\psi)\mathcal{T}(x_3, 0; E)V^\dagger(\psi). \tag{5.15}$$

If, moreover, the beam path can be split up into $n$ domains with a constant and homogeneous magnetic field in each domain but a changing orientation (and strength) from one domain to the next, the complete transfer matrix is simply given by the product over all domains,

$$\mathcal{T}(x_{3,n}, x_{3,0}; E; \psi_{n-1}, \ldots, \psi_0) = \prod_{k=0}^{n-1} \mathcal{T}_k(x_{3,k+1}, x_{3,k}; E; \psi_k), \tag{5.16}$$

with one mixing matrix $\mathcal{M}_k$ for each domain. The transition probability of observing a photon / ALP beam in the state $\rho_{\text{final}}$ after the crossing of $n$ magnetic domains reads

$$P_{\text{final}} = \text{Tr}(\rho_{\text{final}}\mathcal{T}(x_{3,n}, x_{3,0}; E; \psi_{n-1}, \ldots, \psi_0)\rho(x_{3,0})\mathcal{T}^\dagger(x_{3,n}, x_{3,0}; E; \psi_{n-1}, \ldots, \psi_0)). \tag{5.17}$$

Equipped with this formula, the photon transition probability $P_{\gamma\gamma}$ is defined as the sum of the transition probabilities from an initially unpolarized pure photon state $\rho_{\text{unpol}} = 1/2\text{diag}(1, 1, 0)$ to the final polarization states $\rho_{11} = \text{diag}(1, 0, 0)$ and $\rho_{22} = \text{diag}(0, 1, 0)$:

$$P_{\gamma\gamma} = P_{11} + P_{22} = \text{Tr}\left[(\rho_{11} + \rho_{22})\mathcal{T}\rho_{\text{unpol}}\mathcal{T}^\dagger\right]. \tag{5.18}$$

Without absorption, $\mathcal{T}$ is unitary and it is easy to show that $P_{\gamma\gamma} \geq 1/2$ is always true for an initially unpolarized photon beam (see Appendix E).

## 5.2 Magnetic field configurations and scenarios

As the photon / ALP beam propagates towards Earth, it crosses different regions of plasma and magnetic field configurations. The following environments are considered, ordered by increasing distance from Earth:

1. The Galactic magnetic field of the Milky Way (GMF).

2. The intergalactic magnetic field (IGMF).

3. The magnetic field inside a galaxy cluster (intracluster magnetic field, ICMF) in the vicinity of the emitting source.

The goal is to find the magnetic field configuration within current observational bounds which results in a maximal photon-ALP mixing. In this way, a lower limit on $g_{a\gamma}$ can be derived. The observational evidence and model assumptions for each region are discussed in the following subsections. In principle, magnetic fields can be probed through Faraday rotation measurements, observation of synchrotron radiation, and, mainly in the Milky Way, Zeeman splitting and absorption and emission from magnetically aligned dust grains (see, e.g., Noutsos, 2012, for a review). Faraday rotation causes a change of the polarization angle, $\phi = \lambda^2(\mathrm{RM}) + \phi_0$, compared to the initial polarization $\phi_0$, and the effect increases with the square of the wavelength $\lambda$. The effect scales with the rotation measure (RM), the line of sight integral over the $B$ field parallel to the propagation direction multiplied with the ambient electron number density. The synchrotron emission depends on the magnetic field transversal to the line of sight and the degree of polarization can be used as a probe for the structure of the magnetic field (e.g., Widrow, 2002).
The origin of cosmic magnetic fields is under debate (see, e.g., Widrow, 2002; Kulsrud & Zweibel, 2008, for reviews). The current paradigm is that seed fields are initially produced and subsequently amplified. Seed fields can result from the Biermann battery mechanism (Biermann, 1950) during structure formation. It follows from the idea that an electric field is created to counteract the charge separation due to gas pressure. If the pressure gradient and the particle number density are not collinear, a magnetic field will be created as well (e.g., Govoni & Feretti, 2004). This can happen in shock fronts, stars, or in accretion disks in AGN that expel plasma and the frozen-in $B$ field in jets. Another possibility is that the seed fields are created in the electroweak or QCD phase transition (e.g., Widrow, 2002, and references therein). Possible amplification mechanism include the standard $\alpha$–$\omega$ dynamo (e.g., Parker, 1979) or turbulences (e.g., Kulsrud & Anderson, 1992).

### 5.2.1 Magnetic field of the Milky Way

The regular component of the $B$ field of the Milky Way, coherent over galactic scales, will be described with the analytical GMF model presented in Jansson & Farrar (2012a). The model consists of three components: a disk, a halo, and a so-called X component; and it predicts a field strength of the order $O(\mu\mathrm{G})$. The model parameters were determined with a $\chi^2$-minimization utilizing the data of the WMAP7 synchrotron emission maps and Faraday rotation measurements of extragalactic sources. Compared to previous models (e.g., Pshirkov *et al.*, 2011), a relatively large field strength and extent is predicted for the halo and X component which leads to a comparatively large photon-ALP conversion probability in certain regions in the sky.

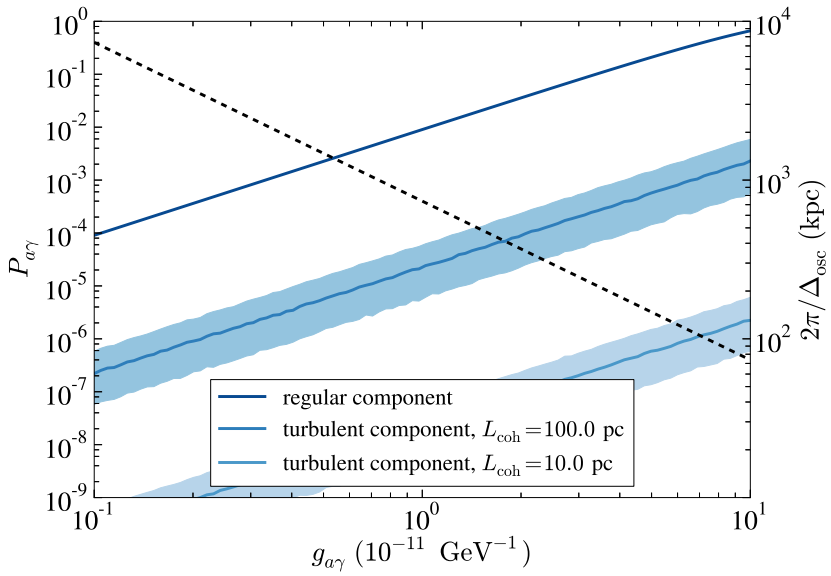


**FIGURE 5.1:** Oscillation of a monochromatic ALP beam with $E = 1\,\text{TeV}$ into an unpolarized photon beam in the regular and turbulent component of the GMF. For the turbulent field, coherence lengths of 10 pc and 100 pc are assumed and the resulting magnetic field strength follows from Eq. (5.19). A source position at RA = 64.22 and DEC = 1.09 (consistent with the blazar 1ES 0414+009) is chosen and the path length through the GMF is $\sim 50\,\text{kpc}$. The mean electron density along the line of sight is derived from the NE2001 code with $\overline{n}_e \approx 0.66\,\text{cm}^{-3}$. For the turbulent field, 5000 realization are simulated, 68 % of which result in the shaded areas, whereas the solid lines depict the median values. The dashed line shows the oscillation length in units of kpc as a function of the photon-ALP coupling for the mean $B$ field and mean electron density crossed by the beam.

The turbulent field is presented in Jansson & Farrar (2012b). It is modeled with a purely random and a striated component, where the latter one follows the regular field on large scales but randomly changes its sign on small scales. The root mean square (rms) values of the turbulent field are found to be in general larger than the field strengths of the regular component. The model does not make any predictions of the coherence length of the turbulences. These are believed to be of the order of $O(10\,\text{pc})$ and the magnetic energy spectrum integrated up to a scale $s$ can be described by (e.g., Han *et al.*, 2004; Mirizzi *et al.*, 2007)

$$\frac{\langle|\mathbf{B}|^2\rangle}{8\pi} = B_{\rm rms}^2 \left(\frac{s}{s_{\rm max}}\right)^{\alpha-1} . \tag{5.19}$$

For scales between 4 pc and 80 pc, the slope $\alpha$ is not well determined but probably lies between the Kolmogorov value ($\alpha = 5/3$) and $\alpha = 2/3$ with $s_{\max} = 1\,\mathrm{kpc}$ and $B_{\mathrm{rms}} \approx 5\,\mu\mathrm{G}$ (Han *et al.*, 2004; Minter & Spangler, 1996). For these values, the conversion probability of a pure ALP beam into an unpolarized photon beam in a random field is calculated and compared to the regular component (see Figure 5.1). The random field is assumed to have a domain-like structure with constant $B_{\mathrm{rms}}$ but randomly changing orientation. It is found to be approximately three orders of magnitude below the value for the regular component for a coherence length $s = 100\,\mathrm{pc}$ due to the large oscillation length $2\pi/\Delta_{\mathrm{osc}}$ of the ALP, where

$$\Delta_{\mathrm{osc}} = [(\Delta_a - \Delta_{\parallel})^2 + 4\Delta_{a\gamma}^2]^{1/2}, \tag{5.20}$$

which is of the order $O(100\,\mathrm{kpc})$. Even though this is a simplified approach, as the regular and turbulent component can strictly speaking not be disentangled, it justifies that the latter component will be neglected in the following.
For each extragalactic VHE-$\gamma$-ray source, the conversion probability is evaluated along the line of sight where it is assumed that the GMF is constant and homogeneous on a length scale of 100 pc. It was checked that smaller values for the domain length do not alter the results. Moreover, the density of the thermal electron plasma is calculated with the NE2001 code (in accordance with Jansson & Farrar, 2012a) which predicts densities of the order of $10^{-1}\,\mathrm{cm}^{-3}$ (Cordes & Lazio, 2002). A summary of the magnetic field components can be found in Appendix F together with the necessary projection of the GMF onto the line of sight in order to calculate the magnetic field transversal to the photon direction. Figure 5.2 shows an all-sky map in galactic coordinates with the conversion probability of a pure ALP beam into photons in the regular component of the Jansson & Farrar GMF model.

### 5.2.2 Intergalactic magnetic field

In contrast to the GMF, little is known about the intergalactic magnetic field. From the observational side, only upper limits exist on the field strength, which constrain the IGMF at $z = 0$ to a few $10^{-9}\,\mathrm{G}$ (Kronberg, 1994). Blasi *et al.* (1999) find $B^0_{\mathrm{IGMF}} \equiv B_{\mathrm{IGMF}}(z = 0) \lesssim 6 \times 10^{-9}\,\mathrm{G}$ for a coherence length of $\lambda^c_{\mathrm{IGMF}} = 50\,\mathrm{Mpc}$ using Faraday rotation measurements of quasars. However, large scale structure formation with magnetic field amplification and cosmic ray deflection simulations suggest smaller values no larger than $B^0_{\mathrm{IGMF}} = 2 \times 10^{-12}\,\mathrm{G}$ (Dolag *et al.*, 2005) or $B^0_{\mathrm{IGMF}} \approx 10^{-11}\,\mathrm{G}$ in voids (Sigl *et al.*, 2004). The morphology of the IGMF is not known either and the most simple assumption is a domain-like structure which is also adopted here. The field strength is constant in each cell and only grows with cosmic expansion, i.e. $B_{\mathrm{IGMF}}(z) = B^0_{\mathrm{IGMF}}(1 + z)^2$, but the orientation changes randomly from one cell to another. The domain length is given by $\lambda^c_{\mathrm{IGMF}}$. As shown in Wouters & Brun (2012), adopting a Kolmogorov-type turbulence spectrum instead

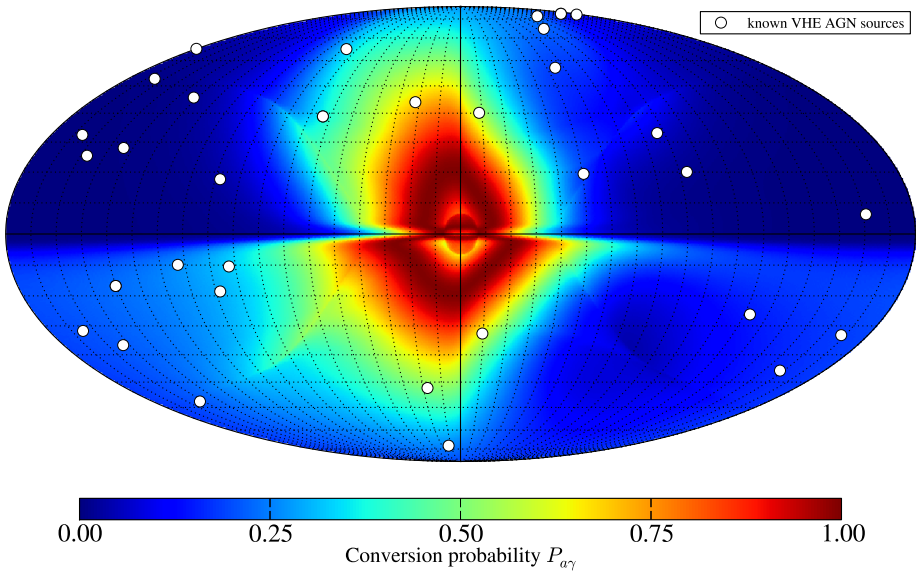


**FIGURE 5.2:** Healpix representation (Górski *et al.*, 2005, with $N_{\mathrm{side}} = 256$) of the conversion probability of a pure ALP beam into an unpolarized photon beam entering the Milky Way and propagating towards Earth. The assumed photon-ALP coupling is $g_{a\gamma} = 5 \times 10^{-11}\,\mathrm{GeV}^{-1}$, for ALPs with energy of $E = 1\,\mathrm{TeV}$. The conversion probability is close to one in the vicinity of the galactic center due to the strong $B$ fields of the halo and X component. Also shown are the positions of known extragalactic VHE sources (white bullets).

of the simple domain structure has negligible effects on the results. In principle, the same procedure is followed here as presented in de Angelis *et al.* (2011), with the exception that the assumption of a strong mixing is dropped.

A scan over a logarithmic grid with $100 \times 100$ pixels in the $(\lambda^{c}_{\mathrm{IGMF}}, B^{0}_{\mathrm{IGMF}})$ space is performed to determine the most optimistic magnetic field setup. For each grid point, the photon survival probability is calculated with Eq. (5.18) for 5000 realizations of the orientation of $B_{\mathrm{IGMF}}$ for a fixed source distance $z = 0.536$, energy $E = 0.574\,\mathrm{TeV}$ (this combination of $z$ and $E$ corresponds to an optical depth of $\tau = 4$ with the EBL model of Kneiske & Dole, 2010, henceforth KD model), an ALP mass $m_a = 0.1\,\mathrm{neV}$, and two different values of the coupling. Only the conversion in the intergalactic magnetic field with absorption due to the EBL of the KD model is taken into account. The impact of the photon-ALP conversions is

quantified with the boost factor $\mathcal{B}$, defined by

$$\mathcal{B} = \tilde{P}_{\gamma\gamma} / \exp(-\tau_{\gamma\gamma}), \tag{5.21}$$

where $\tilde{P}_{\gamma\gamma}$ is the median of the distribution of photon survival probabilities. The median is preferred over the mean value since the distribution of $P_{\gamma\gamma}$ is highly skewed (see below). The result is shown for two different values of the photon-ALP coupling in the top row of Figure 5.3. As one would naively expect, for a large coupling of $g_{a\gamma} = 5 \times 10^{-11}\,\mathrm{GeV}^{-1}$ (top-right panel) the boost factor increases with increasing $B^0_{\mathrm{IGMF}}$ and increasing $\lambda^c_{\mathrm{IGMF}}$ up to a value of $10^{0.4} \approx 2.5$. For even higher values, the boost factor starts to decrease again and shows an oscillatory behavior. This feature was already observed by de Angelis *et al.* (2011): If the conversion probability becomes too high, the photon fraction in the beam is large at all times; but at the same time, the photon flux is attenuated by the interaction with the EBL. As a consequence, $\mathcal{B}$ declines, and one is tempted to choose the values of $\lambda^c_{\mathrm{IGMF}}$ and $B^0_{\mathrm{IGMF}}$ from within the 0.4 contour. The situation changes, however, if $g_{a\gamma}$ is decreased (top-left panel) by more than an order of magnitude to $10^{-12}\mathrm{GeV}^{-1}$. The entire region of $\mathcal{B} > 0$ is shifted towards higher values in the $(\lambda^c_{\mathrm{IGMF}}, B^0_{\mathrm{IGMF}})$ plane. Without any *a priori* assumption about values of the ALP mass and coupling, it is thus advisable to select the maximum values of $\lambda^c_{\mathrm{IGMF}}$ and $B^0_{\mathrm{IGMF}}$ that are allowed by observations and it is settled for $\lambda^c_{\mathrm{IGMF}} = 50\,\mathrm{Mpc}$ and $B^0_{\mathrm{IGMF}} = 5\,\mathrm{nG}$. For the thermal electron density in the intergalactic medium, a typical value of $n_{\mathrm{el,\,IGM}} = 10^{-7}\,\mathrm{cm}^{-3}$ is adopted, derived from the baryon density measured with WMAP (Jarosik *et al.*, 2011).

### 5.2.3 Intracluster magnetic fields

In contrast to intergalactic magnetic fields, the existence of intracluster magnetic fields is well established. Synchrotron emission of the intracluster medium together with Faraday rotation measurements at radio frequencies have led to the common picture that turbulent magnetic fields of the order of $O(\mu\mathrm{G})$ fill the cluster volume (e.g., Govoni & Feretti, 2004; Feretti *et al.*, 2012, for reviews and typical values of the model parameters used below). The turbulence is usually described with a Kolmogorov-type spectrum, or with the simpler cell-like structure which is again used here. There is evidence that the magnetic field strength follows the radial profile of the thermal electron distribution $n_{\mathrm{el,\,ICM}}$ in the cluster,

$$B_{\mathrm{ICMF}}(r) = B^0_{\mathrm{ICMF}} \left( n_{\mathrm{el,\,ICM}}(r) / n^0_{\mathrm{el,\,ICM}} \right)^{\eta}, \tag{5.22}$$

with typical values $0.5 \lesssim \eta \lesssim 1$ and central magnetic fields up to $\sim 10\,\mu\mathrm{G}$ in the most massive clusters. The thermal electron density is described by

$$n_{\mathrm{el,\,ICM}}(r) = n^0_{\mathrm{el,\,ICM}} \left(1 + r/r_{\mathrm{core}}\right)^{-3\beta/2}, \tag{5.23}$$

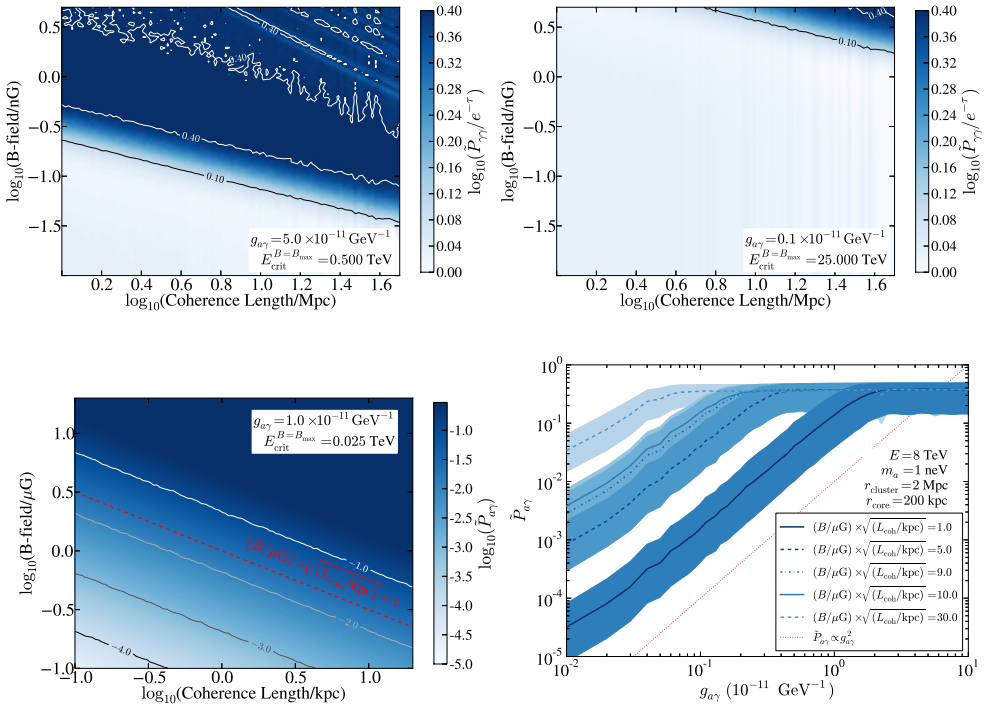


**FIGURE 5.3:** Parameter space scan in the $(\lambda_c, B_0)$ plane. Top row: Photon-ALP-conversion in the IGMF. The color map displays the boost factor of the median of all simulated $B_{\mathrm{IGMF}}$-field realizations; see Eq. (5.21). The adopted values for the coupling (Left column: large couplings; Right column: small couplings) are displayed in the figure together with the critical energy above which the conversion occurs in the strong mixing regime. Bottom row: Conversion in the ICMF. In the left panel, the color coding shows the fraction of the initial photon beam that is converted to ALPs (median over all realizations). The median of the conversion probability is constant for constant values of $B_0 \times \sqrt{L_{\mathrm{coh}}}$, as indicated by the red dashed line. The bottom-right panel displays the dependence of $\tilde{P}_{a\gamma}$ on the coupling $g_{a\gamma}$ for different values of $B_0 \times \sqrt{L_{\mathrm{coh}}}$. In this panel, 68 % of all $B$-field realizations for each $B_0 \times \sqrt{L_{\mathrm{coh}}}$ value fall into the corresponding shaded regions. See text for further details.

with characteristic values of $\beta = 2/3$ and $r_{\mathrm{core}} = 200\,\mathrm{kpc}$. The coherence length is usually assumed to be comparable to galactic scales of the order of 10 kpc. As before, a grid scan over the $(\lambda^c_{\mathrm{ICMF}}, B^0_{\mathrm{ICMF}})$ plane is performed in order to determine the parameters that maximize the photon-ALP conversions. A cluster with a radius of 2 Mpc is assumed together with $\eta = 0.5$. Instead of the boost factor, the fraction of ALPs, $P_{a\gamma}$, in the final state [i.e., $\rho_{\mathrm{final}} = \rho_{33} = \mathrm{diag}(0, 0, 1)$] is shown in the bottom row of Figure 5.3 for an initially unpolarized pure photon

beam, $P_{a\gamma} = \mathrm{Tr}(\rho_{33}\mathcal{T}\rho_{\mathrm{unpol}}\mathcal{T}^{\dagger})$. Again, 5000 $B_{\mathrm{ICMF}}$-field realizations are simulated, and the median $\tilde{P}_{a\gamma}$ is computed. The more ALPs leave the cluster the stronger the effect will be on the VHE spectra because more ALPs can convert back into photons in the GMF and enhance the observed flux. The bottom-left panel of Fig. 5.3 clearly shows that more ALPs are produced for stronger magnetic fields and longer coherence lengths for a photon-ALP coupling strength of $g_{a\gamma} = 10^{-11}\mathrm{GeV}^{-1}$. Interestingly, the conversion probability is constant for constant values of $B_0 \times \sqrt{L_{\mathrm{coh}}}$ (red dashed line), and $\tilde{P}_{a\gamma}$ increases quadratically with growing coupling strength until the maximum probability of $\sim 1/3$ is reached (bottom-right panel of Fig. 5.3). Not surprisingly, the maximum is reached for smaller couplings for larger values of $B_0 \times \sqrt{L_{\mathrm{coh}}}$. Thus, for an optimistic scenario, a central ICMF value of $B_0 = 10\,\mu\mathrm{G}$ with a coherence length of 10 kpc is chosen and it is assumed that the VHE-emitting AGN is located at the center of a galaxy cluster. The core thermal electron density is taken to be $n^0_{\mathrm{el,\,ICM}} = 10^{-2}\,\mathrm{cm}^{-3}$.

### 5.2.4 Magnetic field scenarios

Now that the most optimistic values for the different magnetic fields are identified, four scenarios are presented for which the effect of photon-ALP oscillations on VHE-$\gamma$-ray spectra will be investigated. In all four configurations, the conversion in the GMF is included.

1. In the first scenario, called *general source* hereafter, no specific environment is assumed for the ALP production and only the conversion in the GMF is included. Instead, an initial beam polarization $\rho_{\mathrm{init}} = 1/3\,\mathrm{diag}(e^{-\tau}, e^{-\tau}, 1)$ is considered. This situation corresponds to a maximal mixing in some turbulent magnetic field inside or around the source and a subsequent attenuation of the photon fraction of the beam. In this general scheme, one is not forced to apply some sort of averaging over the many possible orientations of the random magnetic field.

2. In a second configuration, named *optimistic ICM*, it is optimistically assumed that *all* VHE $\gamma$-ray-emitting AGN are located at the center of galaxy clusters of a 2 Mpc radius. The magnetic field changes over the distance from the cluster core as in Eq. (5.22) with a central magnetic field of $B^0_{\mathrm{ICMF}} = 10\,\mu\mathrm{G}$ and a coherence length of $\lambda^c_{\mathrm{ICMF}} = 10\,\mathrm{kpc}$. Any conversion in the intergalactic magnetic field is neglected, as well as any attenuation of the photon flux by local radiation fields inside the galaxy cluster. Upon exit of the galaxy cluster, the photon beam will be attenuated by the interaction with the EBL whereas the ALP fraction propagates unhampered over the entire distance to the Milky Way. In the GMF, ALPs and photons can again convert into each other.

3. Thirdly, it will be assumed that no AGN is affected by the photon-ALP conversion inside a galaxy cluster but, on the other hand, the intergalactic field

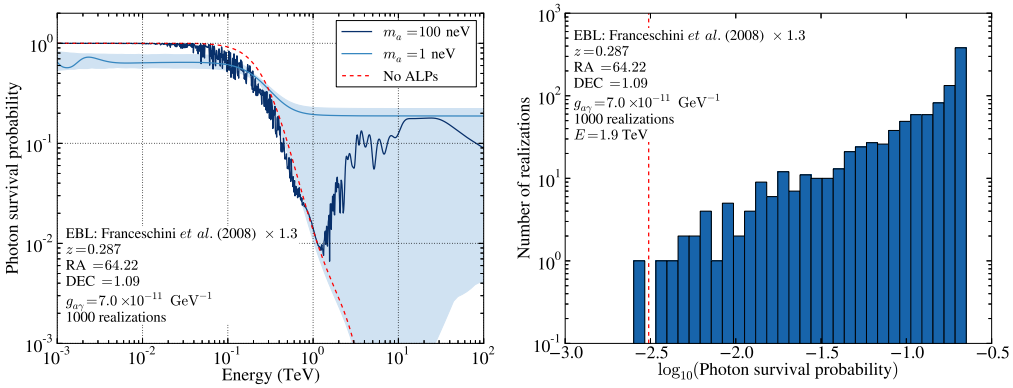


**FIGURE 5.4:** Left panel: Photon survival probability with and without the contribution of ALPs. The effect of ALPs is demonstrated for two particular realizations of the random magnetic field for two different ALP masses (solid blue lines). The light-blue shaded region shows the entire region of $P_{\gamma\gamma}$ covered by 1000 realizations of $B_{\rm ICMF}$. The reduced survival probability at low energies is due to the photon-ALP mixing in the GMF which sets in between 100 MeV and 1 GeV. Right panel: Histogram of all realizations of $B_{\rm ICMF}$ for a fixed $\gamma$-ray energy of 1.9 TeV and an ALP mass of 1 neV. The survival probability without ALPs is again shown as a red dashed line.

will be taken to its most optimistic values, i.e., $B^0_{\rm IGMF} = 5\,{\rm nG}$ and $\lambda^c_{\rm IGMF} = 50\,{\rm Mpc}$. This setup is labeled *optimistic IGMF* and is basically the same as the one considered in, e.g., de Angelis *et al.* (2011) apart from the complete energy-dependent treatment applied here.

4. Finally, a set of more conservative model parameters is chosen to study both the conversion in the IGMF and ICMF. The parameters are conservative in the sense that they are not as close to the observational bounds as in the optimistic scenarios introduced above. Only the AGN listed in Table 1 of Horns *et al.* (2012) are assumed to be located inside a galaxy cluster. As their position relative to the cluster core in unknown, a constant ICMF of $1\,\mu$G is assumed. Furthermore, a value of $r_{\rm cluster} = 2/3\,{\rm Mpc}$ is adopted as the distance that photons propagate through the intra-cluster medium[1]. The value of the IGMF is motivated by simulations of large scale structure formations (Sigl *et al.*, 2004; Dolag *et al.*, 2005). This framework will be called *fiducial*.

All scenarios are analyzed with two EBL models, namely the model of Franceschini *et al.* (2008, FRV model) and the lower limit prediction of the KD model. The

[1]This value is motivated by the following reasoning: if an AGN is placed randomly inside a sphere with a radius of 2 Mpc and one computes the distance to the edge of the sphere, the median distance that a photon travels through the sphere is found to be approximately 2/3 Mpc for a large number of simulations ($10^4$).

**TABLE 5.1:** Model parameters for the different magnetic field scenarios. In frameworks including the conversion inside galaxy clusters, the beam is assumed to travel the distance $r_{\mathrm{cluster}}$ through the volume filled with a $B$ field. In the *optimistic ICM* scenario, the $B$ field varies as in Eq. (5.22). All AGN are assumed to be located at the center of a cluster. In the *fiducial* case, the magnetic field and thermal electron density are assumed to be constant throughout the cluster volume. Only AGN listed in Table 1 of Horns *et al.* (2012) are assumed to lie within galaxy clusters. See text for further details.

| Name | IGMF | | | ICM | | | | | |
|---|---|---|---|---|---|---|---|---|---|
| | $B^0_{\mathrm{IGMF}}$ (nG) | $\lambda^c_{\mathrm{IGMF}}$ (Mpc) | $n^0_{\mathrm{el,IGM}}$ ($\times 10^{-7}\,\mathrm{cm}^{-3}$) | $B^0_{\mathrm{ICMF}}$ ($\mu$G) | $\lambda^c_{\mathrm{ICMF}}$ (kpc) | $r_{\mathrm{cluster}}$ (Mpc) | $n^0_{\mathrm{el,ICM}}$ ($\times 10^{-3}\,\mathrm{cm}^{-3}$) | $r_{\mathrm{core}}$ (kpc) | $\eta$ |
| *general source* | Only conversion in GMF, but $\rho_{\mathrm{init}} = 1/3\,\mathrm{diag}(e^{-\tau}, e^{-\tau}, 1)$ | | | | | | | | |
| *optimistic IGMF* | 5 | 50 | 1 | ... | ... | ... | ... | ... | ... |
| *optimistic ICM* | ... | ... | ... | 10 | 10 | 2 | 10 | 200 | 0.5 |
| *fiducial* | 0.01 | 10 | 1 | 1 | 10 | 2/3 | 1 | ... | ... |

optical depth of the former is additionally scaled by a factor of $\sim 1.3$, as suggested by recent studies of VHE $\gamma$-ray spectra (H.E.S.S. Collaboration *et al.*, 2013). These two EBL models more or less bracket the range of the EBL density allowed by lower limits from galaxy number counts and upper limits derived from VHE-$\gamma$-ray spectra (cf. Chapter 2). Moreover, it was shown in Chapter 3 that these two models result in a high significance of the PPA; and it can be expected that comparably small photon-ALP couplings are able to reduce this tension significantly and, thus, to derive conservative lower limits on the photon-ALP coupling.

As an example, the effect of photon-ALP oscillations for the *optimistic ICM* scenario is illustrated in Figure 5.4 (left panel) for an extragalactic VHE source consistent with the position of the blazar 1ES 0414-009. The conversion into ALPs can increase the photon flux by several orders of magnitude, especially at high energies, compared to the case without ALPs. Higher ALP masses cause the strong mixing regime to be shifted towards higher energies, as shown by the blue and dark-blue lines [see also Eq. (5.11)]. Outside this regime, the transfer functions shows an oscillatory behavior. Some realizations can also result in an additional dimming of the photon flux, however, the majority of the simulations give an enhancement of the survival probability. The effect of ALPs becomes strongest for optical depths $\tau_{\gamma\gamma} \geqslant 2$. Interestingly, in this regime, the indication for an pair production anomaly is found in VHE $\gamma$-ray spectra (see Chapter 3). The distribution of the 1000 simulated values of $P_{\gamma\gamma}$ is highly skewed as shown in the right panel of Figure 5.4. All but one realization lead to an increased survival probability (the optical depth of the scaled FRV model is $\sim 6$ at 1.9 TeV).

The different scenarios and their corresponding model parameters are summarized in Table 5.1. The photon-ALP conversion inside the source is not explicitly taken into account here, but a possible contribution is accounted for in the *general source* scenario.

## 5.3 Probing the Opacity with VHE gamma-ray spectra

With the framework to calculate the photon survival probability $P_{\gamma\gamma}$ introduced in the previous sections, the observed VHE $\gamma$-ray spectra are corrected for absorption in the presence of ALPs. As it is not assumed that the photon-ALP conversions occur in the strong mixing regime, $P_{\gamma\gamma}$ can show a strong oscillatory behavior. Therefore, the $j$-th observed spectral point from a spectrum $i$ with a flux $\Phi_{ij}^{\mathrm{obs}}$ over an energy bin $\Delta E_{ij}$ with central energy $E_{ij}$ is corrected with an average transfer function,

$$\langle P_{\gamma\gamma}\rangle_{ij} = \frac{1}{\Delta E_{ij}} \int_{\Delta E_{ij}} \mathrm{d}E\, P_{\gamma\gamma}(E), \tag{5.24}$$

so that the absorption corrected flux $\Phi_{ij}$ is obtained by

$$\Phi_{ij} = \langle P_{\gamma\gamma}\rangle_{ij}^{-1}\, \Phi_{ij}^{\mathrm{obs}}. \tag{5.25}$$

In practice, the photon survival probability is calculated for 40 energies for each source and linearly interpolated in $\log_{10}(E)$ and $\log_{10}(P_{\gamma\gamma})$. This has been cross-checked for one $(m_a, g_{a\gamma})$ pair with 100 energies and the results are found to be compatible if only 40 energies are used.

The same technique as put forward as *Method 2* in Section 3.1.1 is used here to quantify the significance of the PPA in the presence of ALPs. Each spectrum $i$ with data points that correspond to $\tau_{\gamma\gamma}(z_i, E_{ij}) \geqslant 2$, i.e., the optical thick regime, is fitted with an analytical function $f_i(E)$. A list with all considered spectra that fulfill this criterion is shown in Table 5.2. The function $f_i(E)$ is either a power law, or, in case the fit probability is $p_{\mathrm{fit}}^{\mathrm{PL}} < 0.05$, a logarithmic parabola, compare Eq. (3.2). For each data point in the optical thick regime, the residual is calculated according to Eq. (3.6). Under the hypothesis that $P_{\gamma\gamma}$ gives a correct prediction of the opacity of the Universe to VHE $\gamma$-rays, the residuals in the optical thick regime should follow a Gaussian distribution with zero mean. This conjecture is checked with the $t$ test, for which the variable $t$ defined in Eq. (3.7) follows a $t$ distribution from which the significance (one-sided confidence interval) can be calculated. This method to quantify the accordance between model and data has several advantages. Firstly, the functions to parametrize the spectra do not depend on any particular blazar emission model, as no constraints on the photon index nor on the curvature are made during the fit. Most spectra are adequately described by these functions, as shown in Appendix A. Secondly, no extrapolation from the optical thin to the optical thick regime is required, and the statistical uncertainties of the measurement enter the significance test self-consistently.

Without the contribution of ALPs, one finds for the spectra listed in Table 5.2 a significance of $7.2 \times 10^{-6} \approx 4.3\,\sigma$ for the KD model and $2.3 \times 10^{-4} \approx 3.5\,\sigma$ for the scaled FRV model that the models do not describe the data. It might come as a surprise that the scaled FRV model gives a lower significance than the minimal

**TABLE 5.2:** List of VHE $\gamma$-ray spectra included in the analysis. The table shows the redshift of the source, the IACT experiment that measured it, the energy range covered by the spectrum and the number of data points in the optical thick regime for the optical depth given by the KD model and by the scaled version of the FRV model. The references are listed in Table 3.1.

| $j$ | Source | Redshift | Experiment | Energy range (TeV) | $N_{\tau \geqslant 2}$ ($\tau_{\gamma\gamma} = 1 \times \tau_{\mathrm{KD}}$) | $N_{\tau \geqslant 2}$ ($\tau_{\gamma\gamma} = 1.3 \times \tau_{\mathrm{FRV}}$) |
|---|---|---|---|---|---|---|
| 1 | Mrk 421 | 0.031 | HEGRA | 0.82 – 13.59 | 0 | 1 |
| 2 | Mrk 421 | 0.031 | HEGRA | 0.82 – 13.59 | 0 | 1 |
| 3 | Mrk 421 | 0.031 | H.E.S.S. | 1.12 – 17.44 | 0 | 2 |
| 4 | Mrk 421 | 0.031 | H.E.S.S. | 1.75 – 23.10 | 1 | 4 |
| 5 | Mrk 501[1] | 0.034 | HEGRA | 0.56 – 21.45 | 1 | 3 |
| 6 | 1ES 1950+650 | 0.048 | HEGRA | 1.59 – 10.00 | 0 | 1 |
| 7 | 1ES 1950+650 | 0.048 | HEGRA | 1.52 – 10.94 | 0 | 1 |
| 8 | PKS 2155-304[1] | 0.116 | H.E.S.S. | 0.23 – 2.28 | 0 | 2 |
| 9 | PKS 2155-304[1] | 0.116 | H.E.S.S. | 0.23 – 3.11 | 0 | 3 |
| 10 | PKS 2155-304[1] | 0.116 | H.E.S.S. | 0.22 – 4.72 | 0 | 6 |
| 11 | PKS 2155-304[1] | 0.116 | H.E.S.S. | 0.25 – 3.20 | 0 | 2 |
| 12 | RGB J0710+591 | 0.125 | VERITAS | 0.42 – 3.65 | 0 | 2 |
| 13 | H 1426+428 | 0.13 | HEGRA, CAT, WHIPPLE | 0.25 – 10.12 | 2 | 5 |
| 14 | 1ES 0229-200 | 0.140 | H.E.S.S. | 0.60 – 11.45 | 3 | 6 |
| 15 | H 2356-309 | 0.165 | H.E.S.S. | 0.18 - 0.92 | 0 | 1 |
| 16 | H 2356-309 | 0.165 | H.E.S.S. | 0.22 - 0.91 | 0 | 1 |
| 17 | H 2356-309 | 0.165 | H.E.S.S. | 0.23 - 1.71 | 0 | 1 |
| 18 | 1ES 1218+304 | 0.182 | VERITAS | 0.19 – 1.48 | 0 | 3 |
| 19 | 1ES 1101-232[1] | 0.186 | H.E.S.S. | 0.18 – 2.92 | 3 | 7 |
| 20 | 1ES 0347-121 | 0.188 | H.E.S.S. | 0.30 – 3.03 | 2 | 4 |
| 21 | RBS 0413 | 0.190 | VERITAS | 0.23 – 0.61 | 0 | 1 |
| 22 | 1ES 0414+009[1] | 0.287 | H.E.S.S. | 0.17 – 1.13 | 2 | 3 |
| 23 | 1ES 0414+009[1] | 0.287 | VERITAS | 0.23 – 0.61 | 0 | 1 |
| 24 | PKS 1222+21 | 0.432 | MAGIC | 0.08 – 0.35 | 0 | 1 |
| 25 | 3C 279 | 0.536 | MAGIC | 0.15 – 0.35 | 1 | 1 |
| 26 | 3C 279 | 0.536 | MAGIC | 0.08 – 0.48 | 1 | 2 |

[1] Assumed to be located in a galaxy cluster in the *fiducial* scenario (see Horns *et al.*, 2012, Table 1).

attenuation KD model. The reason for this is that more data points migrate into the optical thick regime as the EBL density increases. This leads to an overall residual distribution closer to a zero mean and shows the limitation of the method: as long as the overall fit to all spectra is acceptable, the entire residual distribution must scatter around zero (see Section 3.1.2 for further details).

In the following discussion, ALPs are included in the correction of the observed spectra. For this purpose, the transition probability for all four scenarios and the two different EBL models is calculated separately for each source listed in Table 5.2. This is necessary because each AGN has a different redshift (important for the attenuation) and a different position in the sky (influencing the conversion in the GMF). Furthermore, $P_{\gamma\gamma}$ is computed over a grid of equally spaced values in the $(\log_{10}(m_a), \log_{10}(g_{a\gamma}))$ space. For the coupling constant, the range $10^{-13}\,\mathrm{GeV}^{-1} \leqslant g_{a\gamma} \leqslant 10^{-10}\,\mathrm{GeV}^{-1}$ is chosen for all magnetic field frameworks. The upper bound is motivated by the bound set by the CAST experiment of $g_{a\gamma} < 8.8 \times 10^{-11}\,\mathrm{GeV}^{-1}$ (Andriamonje *et al.*, 2007, and Section 1.4), while for the lower bound the con-

tribution of ALPs is expected to become negligible. On the other hand, the range of the tested ALP masses differs in the different scenarios. It is determined by the critical energy given in Eq. (5.11) that should span an interval that includes the minimum and maximum energies of the VHE spectrum sample in Table 5.2, namely 0.08 TeV and 23.1 TeV. The different magnetic fields and thermal electron densities result in different mass ranges. For the *general source* and *optimistic ICM* configurations, a mass range of $1\,\mathrm{neV} \leqslant m_a \leqslant 10^3\,\mathrm{neV}$ is chosen; whereas for the *optimistic IGMF* setup, the smaller values of $B_{\mathrm{IGMF}}$ and the ambient density lead to a shift in the mass to $10^{-1.5}\,\mathrm{neV} \leqslant m_a \leqslant 10^{1.5}\,\mathrm{neV}$. In the combined *fiducial* scenario, it is settled for the intermediate range $10^{-0.5}\,\mathrm{neV} \leqslant m_a \leqslant 10^{2.5}\,\mathrm{neV}$. A resolution of the grid of $32 \times 32 = 1024$ points is selected in the particular ranges of $(\log_{10}(m_a), \log_{10}(g_{a\gamma}))$.
A complication is introduced by the random magnetic fields in the scenarios apart from the *general source* case. Since the exact orientation of the IGMF and ICMF in each domain is unknown, a large number $N_{\mathrm{sim}}$ of simulated random realizations is required. Here, $N_{\mathrm{sim}}$ will be set to 5000, and therefore for each $(m_a, g_{a\gamma})$ pair one ends up with 5000 values for the significance level of the $t$ test, $p_t$. One solution would be to compute the median (or mean) of the transfer function and afterwards calculate $p_t$. However, in the averaging process all information on the $p_t$ distribution is lost, and it is unclear if this certain value is statistically suitable to deduce a lower limit on $g_{a\gamma}$. Instead, the $p_t$ distribution is used to determine the $p_t$ value for which 95 % of all $B$-field realizations result in a worse compatibility of the particular framework with the data (i.e., those realizations that result in a smaller $p_t$ value). This particular significance is henceforth denoted as $p_{95}$. In summary, for each scenario, one now has one $p_{95}$ value for each grid point in the $(m_a, g_{a\gamma})$ space. The lower limit on $g_{a\gamma}$ is then defined as the contour line for which $p_{95} = 0.01$. In this way, $(m_a, g_{a\gamma})$ values are regarded to improve the compatibility between model and data if at least 5 % of the realizations give an accordance better than 1 %. For the two EBL models used here, this corresponds to a decrease of the significance of the PPA by a factor of $7.2 \times 10^{-4}$ (KD model) and $2.3 \times 10^{-2}$ (scaled FRV model).

## 5.4 Results

The results for the significance test introduced in the previous section are presented for each of the four scenarios developed in Section 5.2. The upper panels of of Figure 5.5 show the $p_t$ values for the *general source* configuration for the KD model (top-right panel) and the scaled FRV model (top-left panel). In this scenario, no random magnetic field is involved, and thus there is only one $p_t$ value for each pixel. The color coding and the contour lines show the $-\log_{10}(p_t)$ values and larger values of $p_t$ [smaller values of $-\log_{10}(p_t)$] represent a higher probability that the corresponding $t$ value is the result of a statistical fluctuation; i.e., a higher

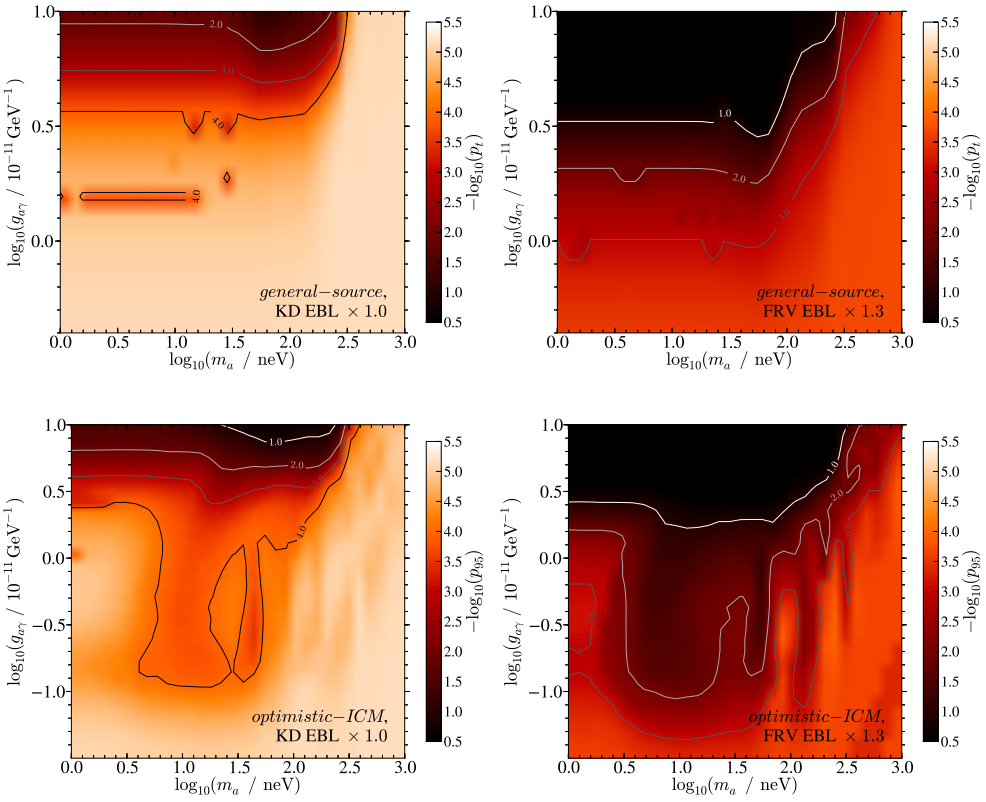


**Figure 5.5:** Significance map for the photon-ALP conversion in the $(m_a, g_{a\gamma})$ plane. Smaller values (brighter regions) indicate less accordance between the model and the data. Upper panel: $p_t$ values for the *general source* scenario, shown as $-\log_{10}(p_t)$. Lower panel: $p_{95}$ values for the *optimistic ICM* case. For each pixel, 5000 realizations of the random magnetic field are simulated and $p_{95}$ is determined from the resulting 5000 $p_t$ values (cf. Section 5.3). In the left column, the attenuation due to the interaction of VHE $\gamma$-rays with the EBL is given by the KD model, whereas in the right column the scaled FRV model is utilized. The maps are smoothed using a bilinear interpolation between the single $(m_a, g_{a\gamma})$ pixels.

probability that the transfer function is in accordance with the data. Clearly, the $p_t$ values increase with an increasing photon-ALP coupling. The lower limit on $g_{a\gamma}$ ($p_t = 0.01$ corresponds to the $-\log_{10}(p_t) = 2$ contour line) is $\sim 7.8 \times 10^{-11}\,\mathrm{GeV}^{-1}$ for the KD model- and $\sim 1.4 \times 10^{-11}\,\mathrm{GeV}^{-1}$ for the scaled FRV model, respectively, in the regime where the mixing becomes independent of the ALP mass at $m_a \lesssim 15\,\mathrm{neV}$. This mass marks the onset of the strong mixing regime (SMR) for all spectra in the environment of the Milky Way. For higher masses, the critical energy increases, and so does the number of spectral points outside the SMR. Higher couplings of $g_{a\gamma}$ are necessary to compensate this effect and to retain a low level of the

significance of the PPA. Above $m_a \gtrsim 250\,\mathrm{neV}$, the tested coupling does not lead to a reduction of the tension between the model and data in comparison to the no-ALPs case. These observations are valid for both EBL models.

A similar overall behavior is found in the *optimistic ICM* case (Figure 5.5, bottom-right panel: KD model; bottom-left panel: scaled FRV model). The color code now displays the $p_{95}$ values for the 5000 simulated realizations of the random ICMF in each pixel. Apart from the overall trend, peculiar regions are visible for the contour lines. In certain mass ranges, the lower limit contour for $g_{a\gamma}$ extends down to almost $g_{a\gamma} = 10^{-12}\,\mathrm{GeV}^{-1}$ using the scaled FRV model. These features are caused by the oscillatory behavior of $P_{\gamma\gamma}$ outside the SMR which affects the low-energy data points in the spectra. These data points usually have the best count statistics, smallest error bars, and the strongest influence on the overall spectral fit. The oscillations in the transfer function can lead to a correction that is strong in one energy bin but small in the adjacent bin. As a result, the spectral fit is altered and leads to residuals in the optical thick regime that are closer to zero for certain $(m_a, g_{a\gamma})$ pairs. Thus, it is expected that these features will change if more VHE spectra are included in a future analysis. Furthermore, the oscillations of the transfer function lead to a poor fit quality for the spectra with the best overall statistics [Mrk 421 (Tluczykont, 2011), Mrk 501 (Aharonian *et al.*, 1999b), and PKS 2155-304 (Aharonian *et al.*, 2007a)] and to a small overall fit probability (see Appendix A). This will lead to a broadening of the residual distribution and a possible overestimation of the $p_{95}$ values closer to 1. These features should not be taken as a preferred parameter region for ALPs to explain the opacity of the Universe.

In the *optimistic IGMF* scenario with the KD model, the only significant improvement over the no-ALP case is actually outside the SMR, as can be seen from Figure 5.6 (top-right panel). Note that the mass range in which the transition to the SMR occurs has now shifted to lower masses due to the smaller IGMF and ambient electron density compared to the intracluster case. With the attenuation of the scaled FRV model, the optimistic parameter choices for $B^0_{\mathrm{IGMF}}$ and $\lambda^c_{\mathrm{IGMF}}$ lead to a lower limit on $g_{a\gamma}$ as low as $\sim 3 \times 10^{-13}\,\mathrm{GeV}^{-1}$ (top-left panel of Figure 5.6).

The bottom row of Figure 5.6 displays the results for the more conservative parameter choice of the *fiducial*-framework. In this scenario, one cannot strictly speak about a lower limit on $g_{a\gamma}$ as neither the values of the magnetic fields nor the values for the coherence lengths are set to their observationally allowed upper limits. The $(m_a, g_{a\gamma})$ pairs that result in $p_{95} \geqslant 0.01$ can thus rather be seen as a preferred region in the parameter space if one tries to explain the opacity of the Universe with photon-ALP conversions. One has to keep in mind, though, that the majority of simulated $B$-field realization results in smaller $p_t$ values. Not surprisingly, one can conclude that the photon-ALP conversion in the IGMF is negligible, since the $p_{95} = 0.01$ contour line does not extend to lower values of $g_{a\gamma}$ at $m_a \approx 1\,\mathrm{neV}$, as observed in the *optimistic IGMF* case. Compared to the *optimistic ICM* case, the lower limit contour line has shifted towards higher values in $g_{a\gamma}$ because a smaller

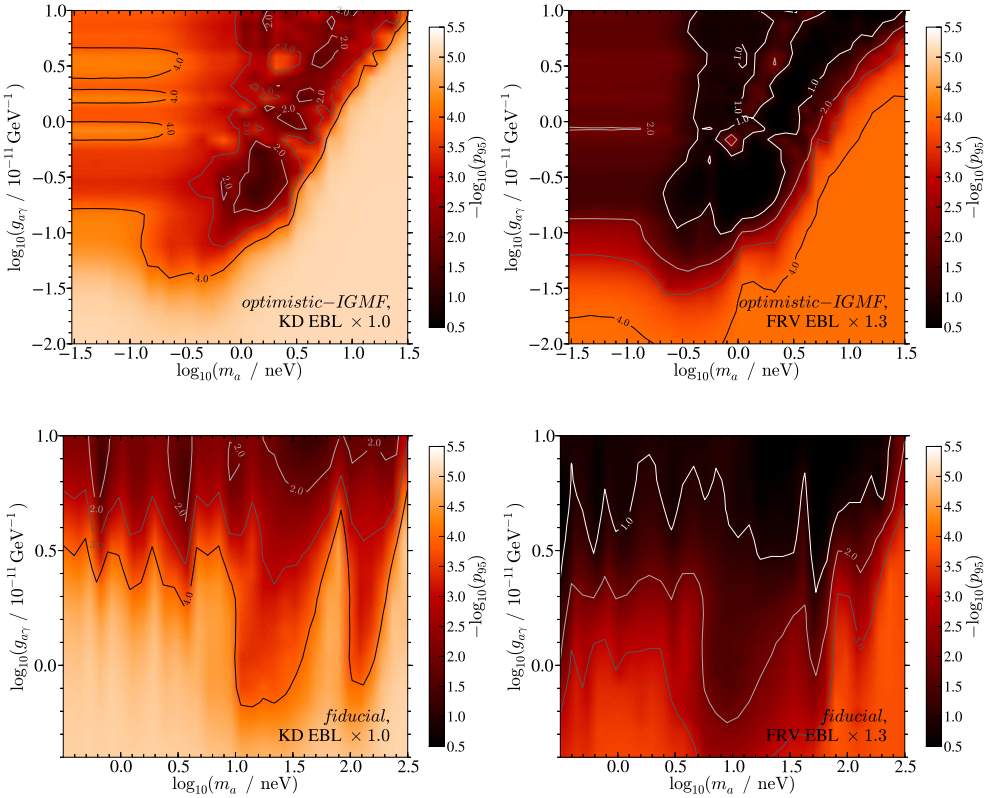


**Figure 5.6:** Significance maps for the photon-ALP conversion. Same as the bottom row in Fig. 5.5, but for the *optimistic IGMF* scenario (top row) and *fiducial* case (bottom row).

number of AGN is assumed to be located inside galaxy clusters. However, it has to be underlined that ALPs are still able to improve the accordance of the model with the data significantly.

From Figures 5.5 and 5.6 it is obvious that in the KD model higher values of the photon-ALP coupling are necessary to reduce the tension between model and data below the threshold of $p_{95} = 0.01$ (more stringent lower limits) than in the scaled FRV model. The reason for this is twofold: On the one hand, without ALPs, the absorption correction in the scaled FRV model is larger for high optical depths, which leads to higher residuals in some spectra. Lower photon-ALP couplings suffice in these cases to reduce the residuals. On the other hand, the significance of the PPA is lower in the scaled FRV model to begin with (cf. Section 5.3). Demanding the same decrease of the significance as in the FRV model without ALPs to the lower limit value ($2.3 \times 10^{-4}$ to 0.01) in the KD model-case results in a significance value of $\sim 3.1 \times 10^{-4}$, close to the $p_t = 10^{-4}$ contour line. Especially in the *optimistic IGMF* and *fiducial* scenarios this line is in good agreement with the $p_t = 10^{-2}$

contour line in the FRV model case.
VHE $\gamma$-ray spectra are subject to systematic uncertainties which can also affect the significance test used here. In Section 3.1.2, several sources of uncertainties in the quantification of the significance of the PPA are identified such as a selection bias of VHE sources, the uncertainty of the overall energy scale of IACTs, and spillover effects in the highest energy bins due to the limited energy resolution of IACTs. Including these effects leads in general to a reduction of the significance. The strongest reduction to $p_t \approx 2.0\,\sigma$ (scaled FRV model) is found if the last energy bins of all spectra are excluded from the analysis and the energy points are simultaneously scaled by $-15\,\%$ in energy (a conservative choice, as it was shown that a scaling of the order of $5\,\%$ is in better agreement with a cross correlation between IACTs and the *Fermi*-LAT; see Meyer *et al.*, 2010). This certainly poses a lower limit on the significance, as it seems unlikely that all VHE spectra are influenced by these systematics in the same way. Nevertheless, a lower limit of $p_{95} = 0.01$ with the inclusion of ALPs would not help to significantly improve the accordance between model and data in this case of a marginal indication. If ALPs were required at all, higher photon-ALP couplings would be necessary. However, the goal here is to set lower limits on $g_{a\gamma}$ if the PPA is not explained by invoking all systematic uncertainties on the VHE observations at once.
Figure 5.7 compares the lower limits derived here with current observational upper limits, regions of theoretical interest, and sensitivities of planned experiments. Only the lower limits for the scaled FRV model are shown, since they all lie below the limits derived with the KD model. The lower limits clearly extend below the stringent upper limits from the CAST experiment (dark shaded region; Andriamonje *et al.*, 2007). In the *optimistic IGMF* case, they also lie below the upper limit derived from the non-observation of prompt $\gamma$-rays from the supernova SN 1987a (gray shaded region; Brockway *et al.*, 1996; Grifols *et al.*, 1996). These $\gamma$-rays would be the result of ALPs reconverted in the GMF that are produced in the supernova explosion[2]. The dotted-dashed lines show theoretical upper limits on $g_{a\gamma}$ calculated from magnetic white dwarfs (mWDs; Gill & Heyl, 2011). Photon-ALP conversions lead to a linear polarization $P_L$ of the photon beam (Raffelt & Stodolsky, 1988), and by treating the current observations of mWDs as a limit, i.e., $P_L \lesssim 5\,\%$, one can derive a limit on the photon-ALP coupling. The different lines correspond to different values of the magnetic field strength of the mWDs and different values for the limit on $P_L$. Although the magnetic field and ambient density in the vicinity of mWDs are very different from the scenarios considered here, the mWD considerations turn out to be sensitive in the same $(m_a, g_{a\gamma})$ region as the VHE observations. Nevertheless, the limits use a $B$-field model inferred from one single mWD. If they are confirmed with future observations, they will strongly constrain the parameter space for ALPs that can potentially decrease the opacity of the Universe for VHE $\gamma$-rays. On the

[2]The limits should be considered as an order of magnitude estimate since they rely on some simplifications. For instance, a constant photon-ALP conversion probability in the GMF is assumed.

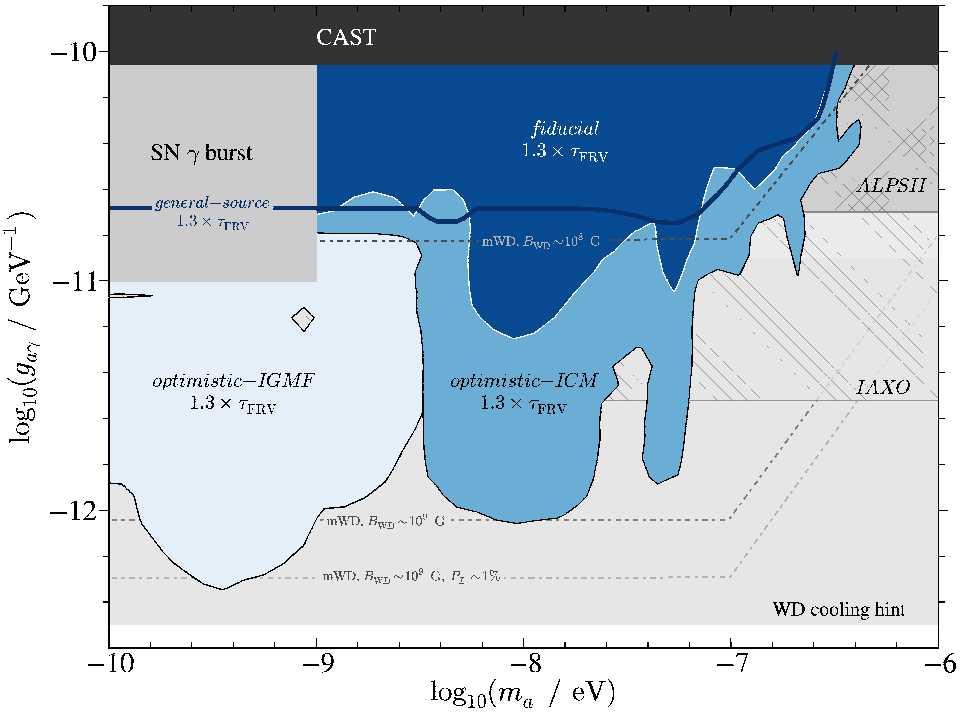


**FIGURE 5.7:** ALP parameter space with the lower limits on $g_{a\gamma}$ derived here. The lower limits for the different scenarios are displayed as blue shaded regions, or in the case of the *general source*-scenario, as a dark blue solid line. They are only shown for the scaled FRV model, so that the optical depth is given by $\tau_{\gamma\gamma} = 1.3 \times \tau_{\mathrm{FRV}}$. For comparison, upper limits, hints for theoretical preferred regions, and sensitivities of future experiments are also plotted. See text for further details.

other hand, ALPs could solely be responsible for the entire observed linear polarization. Consequently, the limits can also be regarded as a preferred parameter range for ALPs.

The lower limits of the optimistic scenarios extend into the preferred region for the ALP parameters to explain the white dwarf (WD) cooling problem. It is difficult with current theoretical models to satisfactorily reproduce the observed WD luminosity function. The production of ALPs, on the other hand, with a mass and coupling within the light-gray-shaded band in Figure 5.7[3] serves as an additional cooling mechanism for WD and can reduce the tension between current model predictions and data (Isern *et al.*, 2008). This issue is, however, subject to ongoing

[3] Isern *et al.* (2008) set bounds on the mass of the QCD axion or equivalently on the electron-axion coupling. This can be translated into a bound on the photon-axion coupling (Raffelt, 2008; Redondo, 2013) and consequently on the photon-ALP coupling. The values shown here are taken from Hewett *et al.* (2012).

discussion (Melendez *et al.*, 2012).
Interestingly, the ALP parameter space of the *fiducial*-scenario can be probed with planned experiments. The sensitivity forecasts for the improved Any Light Particle Search (ALPS II; Bähre *et al.*, 2013) and the International Axion Observatory (IAXO; Irastorza *et al.*, 2011) are displayed as a crosshatched and right-hatched region, respectively, in Figure 5.7. The lower limits derived here thus pose an additional physics case for these future experiments.
The lower limits derived here could be further relaxed if additional contributions to the GMF are realized in nature, such as a kiloparsec-scale magnetized wind (Everett *et al.*, 2008) that could further enhance the conversion probability. As noted at the end of Chapter 3, at the time being the sample of VHE spectra is dominated by sources with a redshift $0.1 \lesssim z \lesssim 0.2$ and is thus most sensitive to changes in the EBL density at near-infrared wavelengths. As a consequence, certain EBL model realizations exist for which the PPA is less significant and higher values of $g_{a\gamma}$ would be required to obtain a significant improvement over the situation without ALPs. One improvement would be to parametrize the EBL model independently (for instance, with splines, as done in Chapter 2) and recalculate the significances in the presence of ALPs. This is left for future investigations. Firm conclusions can only be drawn with future direct observations of the EBL and VHE measurements in the optical thick regime of both distant sources at several hundreds of GeV and nearby sources at several tens of TeV, which will also enable further tests of ALP scenarios. Several such observations have already been announced[4] and will become more feasible with the next generation of air shower experiments such as the Cherenkov Telescope Array (CTA; Actis *et al.*, 2011), the High Altitude Water Cherenkov Experiment (HAWC; Sinnis *et al.*, 2005), and the Hundred*i Square-km Cosmic ORigin Explorer (HiSCORE; Tluczykont *et al.*, 2011).
To conclude, the results are summarized as follows:

- Without absorption, the median of the photon-ALP conversion probability is constant for constant values of $B \times \sqrt{L_{\mathrm{coh}}}$ and increases quadratically with the coupling until it saturates at $\sim 1/3$.

- Including absorption, the median values show an oscillatory behavior for large $B \times \sqrt{L_{\mathrm{coh}}}$, as the photon fraction in the beam that can be attenuated is always high (as already noted by de Angelis *et al.*, 2011). This allows to identify the most optimistic $B$-field parameters for photon-ALP mixing in intracluster and intergalactic magnetic fields.

- If the indication of the PPA found in Chapter 3 is not attributed to systematic uncertainties that effect all spectra of all instruments, ALPs can ease the ten-

[4] For example, the detection of the distant BL Lac KUV 00311-1938 with H.E.S.S. or the observation of a flaring state of Markarian 421 with VERITAS were recently announced, see `http://tevcat.uchicago.edu/`

sion between model and data significantly. For optimistic *B*-field scenarios, this is achieved for couplings $g_{a\gamma} \gtrsim 10^{-12}\,\mathrm{GeV}^{-1}$ (*optimistic IGMF* case and *optimistic ICM* case). More fiducial parameters yield $g_{a\gamma} \gtrsim 2 \times 10^{-11}\,\mathrm{GeV}^{-1}$ (*fiducial* case). These results include the contribution of the GMF and a full energy dependent treatment of the oscillations.

- These first lower limits on $g_{a\gamma}$ derived from VHE $\gamma$-ray observations are well in reach of future laboratory experiments as ALPS II and IAXO and reach into the region of the parameter space favored for an additional WD cooling mechanism (Isern *et al.*, 2008).

- The lower limits are worsened outside the strong mixing regime, as the oscillatory behavior of the transfer function leads to small fit probabilities. On the other hand, this behavior can be used to search for ALPs or to constrain the parameter space (as suggested by Wouters & Brun, 2012).

# 6 Summary and outlook

In this thesis, the opacity of the Universe for high and very high energy (HE and VHE) $\gamma$-rays originating from cosmological sources has been studied. The opacity arises through the attenuation of $\gamma$-rays through the interactions with photons at ultraviolet to far infrared wavelengths of the extragalactic background light (EBL). Constraints on the EBL photon density have been derived in an analysis of 22 VHE spectra from 19 different blazars in conjunction with data taken in the first 2 years of operation of the Large Area Telescope (LAT) on board the *Fermi* satellite. The *Fermi*-LAT measures the considered spectra of active galactic nuclei (AGN) at energies where absorption is negligible. Consequently, the spectral slope determined from *Fermi*-LAT observations serves as a limiting value for the absorption-corrected slope at VHE, if an overall concave shape of the intrinsic spectrum is assumed. This relaxes the need to make specific theoretical assumptions on the intrinsic photon index at VHE. Blazars are known to be variable in time, thus either simultaneous measurements with imaging air Cherenkov telescopes (IACTs) and the *Fermi*-LAT, or, if unavailable, the most conservative measured values for the intrinsic blazar spectrum have been used. With the further assumption of concave spectra in the VHE band, upper limits on the EBL photon density have been derived which are independent of specific EBL models and span roughly three orders of magnitude in wavelength from $0.4\,\mu$m to $100\,\mu$m. The EBL intensity is limited below $5\,\mathrm{nW\,m^2\,sr^{-1}}$ at mid-infrared wavelengths, close to the lower limits derived from galaxy number counts. The calculation of the upper limits also accounts for the evolution of the EBL density with redshift and for the possible formation of electromagnetic cascades. A novel exclusion criterion for EBL densities has been introduced, which relies on the assumption that the VHE luminosity of blazars should not exceed the Eddington luminosity.

Based on the spectral data obtained, it has been investigated whether current EBL models predict an overcorrection of VHE $\gamma$-ray spectra in the regime where the exponential flux suppression exceeds two e-foldings corresponding to an optical depth $\tau_{\gamma\gamma} \geqslant 2$. For this purpose, VHE spectra of sources with unambiguous redshift determination have been corrected for absorption under the assumption of various EBL models. Special emphasis is placed on the EBL model of Kneiske & Dole (2010, KD model), which results in a minimal attenuation at TeV energies and follows closely the lower limits on the EBL density in the infrared regime derived

from galaxy number counts. The overcorrection has been searched for with two statistical tests: The absorption-corrected energy bins of the spectra in the $\tau_{\gamma\gamma} < 1$ regime are fitted with an analytical function and the fit is extrapolated to data points with $\tau_{\gamma\gamma} \geqslant 1$. Subsequently, the ratios between the absorption-corrected measured flux and the flux obtained from the extrapolation are calculated. The distribution of ratios in the regimes $1 \leqslant \tau_{\gamma\gamma} < 2$ and $\tau_{\gamma\gamma} \geqslant 2$ are compared with the Kolmogorov-Smirnov (KS) test. In a second test, all absorption-corrected data points of each spectrum are included in fit. The mean of the fit-residual distribution for data points with $\tau_{\gamma\gamma} \geqslant 2$ is compared to an expected mean of 0 using the Student's *t* test.

For the KD model, an indication for a reduced opacity of the Universe, coined *pair-production anomaly* (PPA), with a significance $3.9\,\sigma$ and $4.3\,\sigma$ has been found consistently for the KS test and *t* test, respectively. Several systematics influencing this result have been studied, and the unknown absolute energy calibration together with the limited energy resolution of IACTs have been identified as the major uncertainty. However, it seems unlikely that all studied spectra are influenced by these systematics in the same way.

A complementary search for the PPA has been conducted with *Fermi*-LAT data collected in the first 4.3 years of operation. To this end, photons above 10 GeV have been associated with AGN with known redshift which are listed in the second (2 year) *Fermi*-LAT source catalog (2FGL). Sources with one or more associated photons with an energy resulting in $\tau_{\gamma\gamma} \geqslant 1$ have been further analyzed to determine the intrinsic unattenuated spectrum. From the extrapolation to higher energies, the expected number of photons beyond $\tau_{\gamma\gamma} \geqslant 1$ and $\tau_{\gamma\gamma} \geqslant 2$ has been calculated and compared to the number of observed photons. Each analyzed source constitutes an independent hypothesis test, so that multi-trial factors have to be taken into account. Combining the results from all sources including trial factors results in no significant deviation in the case all sources with an associated $\tau_{\gamma\gamma} \geqslant 1$ photon are considered. If the sample is limited to sources with an associated $\tau_{\gamma\gamma} \geqslant 2$ photon, an indication of $3.7\,\sigma$ is found that the predicted EBL absorption is too strong. In total, $\sim 400$ AGN that are listed in the 2FGL with sufficiently large redshift to emit a photon in the optical thick regime in the energy range of the *Fermi*-LAT. It has been studied how the detected 20 (6) photons below 500 GeV with an optical depth $\tau_{\gamma\gamma} \geqslant 1$ ($\tau_{\gamma\gamma} \geqslant 2$) compare to the expected number of photons from these AGN. Recalculating this number, an indication for a PPA is only found if the intrinsic spectra are modeled with curved spectra rather than simple power laws (the curved intrinsic spectrum results in a lower number of expected photons at higher energies).

The possibility that conversions of photons into hypothetical axion-like particles (ALPs) can explain the indication for the PPA has been addressed in detail. Since the conversion probability depends on the strength and orientation of the ambient magnetic field, different environments are examined including galaxy clusters, the intergalactic medium, and the Milky Way. In the first two regions, the magnetic fields are modeled with a domain-like structure, the field being constant and ran-

domly orientated in each cell. Without photon absorption, the photon-ALP conversion in such fields scales with the square of the photon-ALP coupling, $g_{a\gamma}$, and increases with increasing values of $B \times \sqrt{L_{\rm coh}}$, with the field strength $B$ and the coherence length $L_{\rm coh}$ (equal to the domain size). It has also been shown analytically that for an initially unpolarized pure photon beam, the ALP fraction in the beam can never exceed 1/2. Values close to the observational bounds for the intergalactic magnetic field and values equal to measurements of the intracluster magnetic fields in the most massive clusters allow, for the first time, to derive lower limits on $g_{a\gamma}$ from VHE $\gamma$-ray observations. The resulting bound is $g_{a\gamma} \gtrsim 10^{-12}\,\mathrm{GeV}^{-1}$. For more conservative $B$-field parameters in a sense that they are not equal to observational bounds, the limit $g_{a\gamma} \gtrsim 2\times10^{-11}\,\mathrm{GeV}^{-1}$ is obtained, well in range for detection with the future experiments ALPS II and IAXO.

A straightforward extension of the presented work is the application of the photon-ALP oscillation framework[1] developed in Chapter 5 to *Fermi*-LAT data. The first result of this application is shown in the panels of Figure 6.1. For the analysis, the extrapolation of the intrinsic LAT spectrum (discussed in Chapter 3.2) includes photon-ALP oscillations. The post-trial probability, $P_{\rm PPA,\,post-trial}$, to detect the observed photons is calculated with the EBL model of Franceschini *et al.* (2008, FRV model) and in the *general source* scenario (cf. Section 5.2) for two values of $g_{a\gamma}$. In this scenario, the initial photon polarization matrix necessary to compute the photon survival probability from Eq. (5.18) is chosen to be $\rho_{\rm init} = 1/3\,\mathrm{diag}(e^{-\tau_{\gamma\gamma}}, e^{-\tau_{\gamma\gamma}}, 1)$. This means that already a large fraction of the beam has converted into ALPs. A low ALP mass of $m_a = 0.01\,\mathrm{neV}$ is assumed to ensure the onset of the strong mixing regime below the energy range of the *Fermi*-LAT, i.e., $E_{\rm crit} \lesssim 100\,\mathrm{MeV}$ [cf. Eq. (5.11)]. This implies that the intrinsic flux normalization determined from a fit to *Fermi*-LAT data (see Section 3.2.2) has to be upscaled by a factor of $3/2$ since one third of the photons emitted by the source has already converted into ALPs. When applied to blazars that are firmly associated ($P_{\rm src} > 0.9$) with a high optical depth photon (HOP), photon-ALP oscillations result in an increased probability to observe the detected photons above an EBL normalization $\alpha = 1$, especially for photon-ALP couplings close to current limits. For values of $g_{a\gamma}$ close to the lower limits of the *general source*-scenario (cf. Figure 5.5), an increase is still observed which is, however, less pronounced (see Figure 6.1). This analysis can be extended in the future to include the other $B$-field scenarios considered in Chapter 5. It will be interesting to examine those $B$-field realizations that maximize the photon survival probability. In this way, it can be investigated by how much photon-ALP oscillations can increase the probability of observing the three photons with $\tau_{\gamma\gamma} \geqslant 2$.

This first result demonstrates that photon-ALP conversions can significantly affect the number of expected photons observed with the *Fermi*-LAT. Nevertheless, its current sensitivity is insufficient to give a definitive answer on the nature of the

[1] The photon-ALP conversion code written in `python` will be made publicly available at `https://github.com/me-manu/Phot-ALPs`.

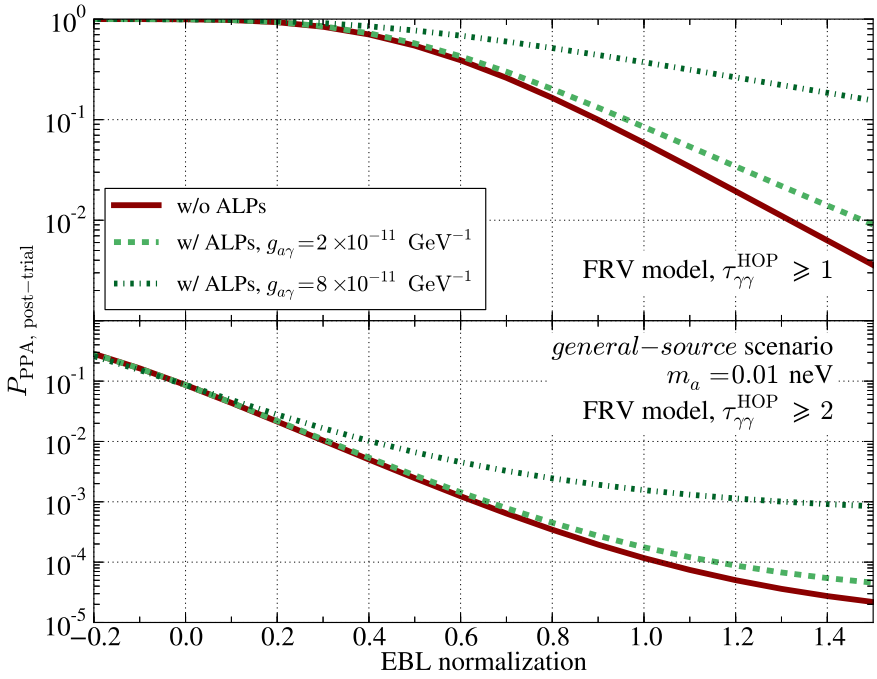


**Figure 6.1:** Post-trial probability of the PPA including photon-ALP conversions. Top panel: All blazars listed in Table 3.3 are included with a firmly associated ($P_{\mathrm{src}} > 0.9$) HOP with $\tau_{\gamma\gamma} \geqslant 1$. Bottom panel: only the three AGN are included that have a $\tau_{\gamma\gamma} \geqslant 2$ associated HOP with $P_{\mathrm{src}} > 0.9$.

PPA. This might change in the future with the updated *Pass 8* instrumental response functions that promise an increase of 15 – 20 % in acceptance at high energies and an energy reconstruction up to 3 TeV (Atwood *et al.*, 2013).

It should be noted that the search for an regenerated $\gamma$-ray flux due to photon-ALP conversions is not limited to the absorption due to the EBL. In principle, any environment in which the optical depth for $\gamma$-rays is high and magnetic fields are present can be used to test the ALP scenario. For example, any conversion inside an AGN has been neglected in the analysis in Chapter 5. In FSRQs, the attenuation of $\gamma$-rays can be severe [equivalent to a high compactness, $\ell_c$, defined in Eq. (1.8)] due to the high photon density of the broad line region (BLR), requiring that the emission zone is outside the BLR (Tavecchio *et al.*, 2011b). This might not be necessary in the presence of ALPs (Tavecchio *et al.*, 2012). Furthermore, including ALPs might reduce the large Doppler factors, $\delta_{\mathrm{D}} \gtrsim 60$, needed to explain the minute-scale time variability observed in PKS 2155-304 (Aharonian *et al.*, 2007a).

A different approach would be to search for the transition from the weak to the strong mixing regime around $E_{\mathrm{crit}}$ [cf. Eq. (5.11)] in IACT or *Fermi*-LAT spectra.

**TABLE 6.1:** The five *Fermi*-LAT detected pulsars with minimal photon survival probability $P_{\gamma\gamma}$ in the strong mixing regime. A photon-ALP coupling of $g_{a\gamma} = 5 \times 10^{-11}\,\mathrm{GeV}^{-1}$ is assumed. Also given are the pulsar position in galactic longitude and latitude $(l, b)$, the pulsar distance $d$, and its detection significance between 100 MeV and 100 GeV as listed in the 2FGL.

| Pulsar name | $l$ (degrees) | $b$ (degrees) | $d$ (kpc) | $P_{\gamma\gamma}$ | Significance |
|---|---|---|---|---|---|
| J1112-6103 | 291.22 | -0.46 | 30.00 | 0.861 | $11.33\,\sigma$ |
| J0248+6021 | 136.90 | 0.70 | 23.23 | 0.875 | $17.33\,\sigma$ |
| J2021+3651 | 75.22 | 0.11 | 18.88 | 0.865 | $95.01\,\sigma$ |
| J2030+3641 | 76.12 | -1.44 | 11.17 | 0.900 | $17.07\,\sigma$ |
| J0218+4232 | 139.51 | -17.53 | 5.85 | 0.931 | $26.69\,\sigma$ |

For instance, the transition could show up as a "step" in *Fermi*-LAT pulsar spectra (such a spectral feature has also been discussed, e.g., by Hochmuth & Sigl, 2007; Sánchez-Conde *et al.*, 2009). The strength of the feature should depend on the pulsar distance[2] and its position due to the different Galactic magnetic field (GMF) along each line of sight. Given the $\mu$G field strength of the coherent GMF, such a search would be sensitive to an ALP mass around 1 neV for couplings of the order of $g_{a\gamma} \sim 10^{-11}\mathrm{GeV}^{-1}$. The photon survival probability for the strong mixing regime in the GMF is shown in the all-sky map in Figure 6.2. Positions of *Fermi*-LAT detected pulsars are also marked in this figure. The most promising sources to study the photon-ALP oscillations are distant pulsars with a line of sight close to the Galactic center (maximizing the effect of ALPs) detected with a high significance (for high quality spectra). The five pulsars with a minimal photon survival probability are listed in Table 6.1.

More generally, further observations in the optical thick regime will give a more definite answer on the PPA. Such measurements will also help to constrain the EBL further, especially at optical and far-infrared wavelengths where the limits depend on just a few (or even only one) AGN spectra. At (mid-) infrared wavelengths, the large number of spectra considered in this work ensures robust limits against potential biases in individual spectra. Several observations of blazars in the optical thick regime have already been made. The BL Lac KUV 00311-1938 at a redshift of $z > 0.506$ has been observed with H.E.S.S. between 2010 and 2011 (Becherini *et al.*, 2012a). The major flare of Mkn 421 in 2010 has been detected with VERITAS yielding a preliminary spectrum from $\sim 200$ GeV to energies larger than 20 TeV (Fortson *et al.*, 2012). This measurement is particularly interesting for EBL constraints at far-infrared wavelengths. Recently, a lower limit on the redshift ($z \geqslant 0.6035$) of PKS 1424+240 has been published, suggesting that the VERITAS observations of this blazar (Acciari *et al.*, 2010a) extend to optical depths $\tau_{\gamma\gamma} \gtrsim 5$

[2] The pulsar distances are obtained from the ATNF pulsar catalog, `http://www.atnf.csiro.au/people/pulsar/psrcat/`.

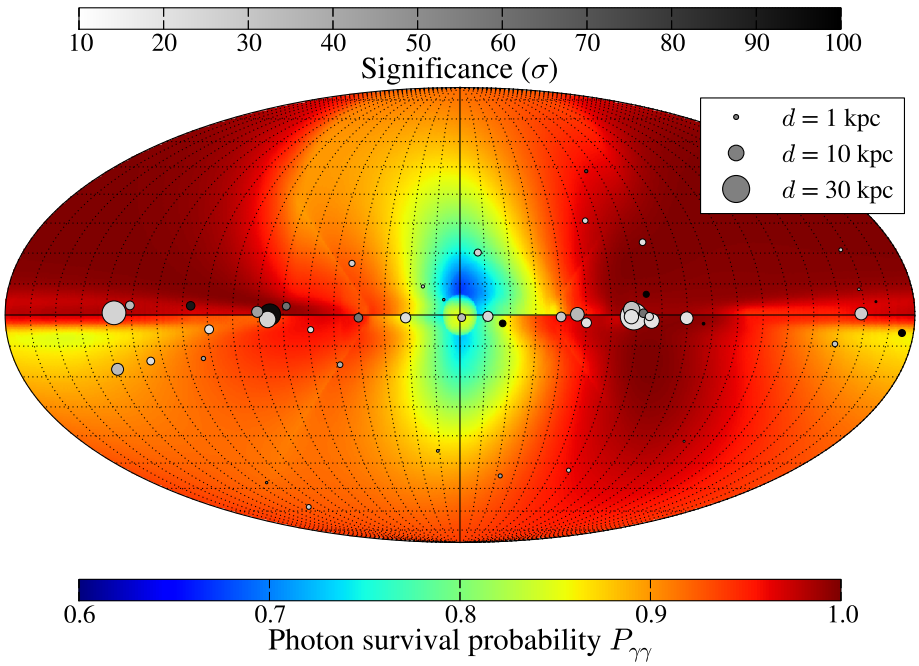


**FIGURE 6.2:** All-sky map of the photon survival probability in photon-ALP oscillations in the GMF. The color scale corresponds to the survival probability for photons with $E \gg E_{\rm crit}$ originating from a source at a distance of 8.5 kpc. A photon-ALP coupling of $g_{a\gamma} = 5 \times 10^{-11}$ GeV$^{-1}$ is chosen. The markers show positions of pulsars listed in the 2FGL. The marker sizes scale with the pulsar distances. The marker color scales with the detection significance given in the 2FGL (see upper color bar).

(Furniss *et al.*, 2013). These measurement can be easily integrated in the analyses presented in this work.

After the ongoing commissioning, the second phase of the H.E.S.S. experiment will lower the energy threshold of the array to $\sim$ 30 GeV in single telescope and $\sim$ 50 GeV in stereoscopic observations (Becherini *et al.*, 2012b), enabling the measurement of the intrinsic and absorbed part of AGN spectra simultaneously. In this respect, the prospects for the planned Cherenkov Telescope Array (CTA; Actis *et al.*, 2011) are even more promising for studying ALPs and EBL absorption. The array will incorporate three different sizes of IACTs to cover an energy range from tens of GeV up to $\sim$ 100 TeV with an energy resolution of the order of 10 – 15 %, a temporal resolution down to seconds, and an angular resolution on the arcmin scale. The projected sensitivity is a factor of $\sim$ 10 better than that of currently operating IACTs. From the analysis presented in Inoue *et al.* (2010), Mazin *et al.* (2013) estimated that about 100 new AGN can be detected within the first 5 years of CTA operation. This demonstrates that CTA observations will pave the way for disentan-

gling source intrinsic spectral features from the EBL imprints on the spectra. CTA telescopes will have a rapid slewing capability (180° in 20 s) promising the detection of $\sim 1$ gamma-ray bursts per year (Mazin *et al.*, 2013). With the observation of these bright transient phenomena, the EBL density can potentially be constrained up to redshifts of $z \gtrsim 4$ (Mazin *et al.*, 2013).
If at one point the EBL upper limits fall below the lower limits from galaxy number counts, processes beyond the Standard Model might offer a solution. It has been shown here that photon-ALP mixing seems to be the most viable candidate, as the spectra are altered in a $\tau_{\gamma\gamma}$ dependent way. Doro *et al.* (2013) have studied the CTA performance of detecting the regenerated photon flux from photon-ALP oscillations from a source with the same spectrum and redshift as PKS 1222+21 observed with MAGIC (Aleksić *et al.*, 2011a). The authors only consider the conversion in the IGMF with a field strength of 0.1 nG and assume that the spectrum extends up to 2 TeV. MAGIC detected the source in a flaring state that lasted for $\sim 30$ minutes. If at some point a similar event lasting for 5 hours was observed with CTA, coupling constants down to $\sim 10^{-16}\,\mathrm{GeV}^{-1}$ could be probed for an ALP with a mass of 1 neV. These calculations could be refined with the framework introduced in this work, including the mixing in the GMF and inside galaxy clusters.
Within the Standard Model, electromagnetic cascades initiated by cosmic rays could also explain the regenerated photon flux and the indication for the PPA. In such a scenario, a large fraction of the blazar luminosity must be transferred to the acceleration of cosmic rays. Furthermore, a future observation of a short-term variability of AGN in the $\tau_{\gamma\gamma} \gtrsim 2$ regime would be in contradiction with the expectations from the cascade.
Complementary to constraints on the EBL density obtained from $\gamma$-rays, the *James Webb Space telescope* scheduled to be launched in late 2018[3], will measure the EBL with unprecedented sensitivity at near infrared wavelengths (Gardner *et al.*, 2006). Such measurements will also shed further light on the nature of the PPA.

[3] See, e.g., `http://www.jwst.nasa.gov/`.

# A Fit qualities for VHE $\gamma$-ray spectra in the optical thick regime

This appendix summarizes the spectral fits to the very high energy (VHE) spectra which are used in Chapter 3 to calculate the significance of the pair-production anomaly. For the model of Kneiske & Dole (2010, KD model) of the extragalactic background light (EBL), the fits to the optical thin part of each spectrum that contains data points corresponding to $\tau_{\gamma\gamma} \geqslant 2$ are shown in Figure A.1. Spectra are excluded which have only one data point in the optical thin regime, since no intrinsic spectrum can be derived (the spectrum of 1ES 0229+200 and one spectrum of 3C 279). All $\chi^2$-values indicate that the optical thin spectra are well described with the chosen analytical functions as most $p_{\text{fit}}$ values are close to one. The bottom panels display the ratios $R$ defined in Eq. (3.3) used for the Kolmogorov-Smirnov test.

Figure A.2 shows again the spectra with data points in the $\tau_{\gamma\gamma} \geqslant 2$ regime, but this time the entire energy range is included in the determination of the best-fit parameters. The fit residuals [cf. Eq. (3.6)] are displayed in the bottom panels. Again, the fit probabilities are close to one for most spectra. The only exceptions are the spectrum of Mkn 501 and one spectrum of 3C 279. The former spectrum is measured with high accuracy resulting in very small statistical errors. It is dominated by its systematical uncertainties (see gray band in Figure 10 in Aharonian *et al.*, 1999b) which are not included here. The spectrum of 3C 279 consist only of three data points, making a power law the only meaningful fitting function.

The $\chi^2$- and $p_{\text{fit}}$-values for the fit of the entire energy range are summarized in Table A.1 for the KD model and additionally the EBL model of Franceschini *et al.* (2008) (FRV model) scaled by 1.3 as used in Chapter 5. The combined $\chi^2$-values translate into satisfactory overall fit probabilities of $p_{\text{fit}} = 0.160$ and $p_{\text{fit}} = 0.303$ for the KD model and FRV model, respectively.

In Chapter 5, the effect of photons mixing with axion-like particles (ALPs) is included in the de-absorption of the observed VHE spectra. In this case, the fit qualities are poor ($p_{\text{fit}} \ll 1$) in the transition to the strong mixing regime (SMR), i.e., for energies below $E_{\text{crit}}$, defined in Eq. (5.11). The corresponding high $\chi^2$-values are dominated by a few spectra only (as in the no-ALPs case), namely those with high count statistics and consequently small error bars. The largest contributions come

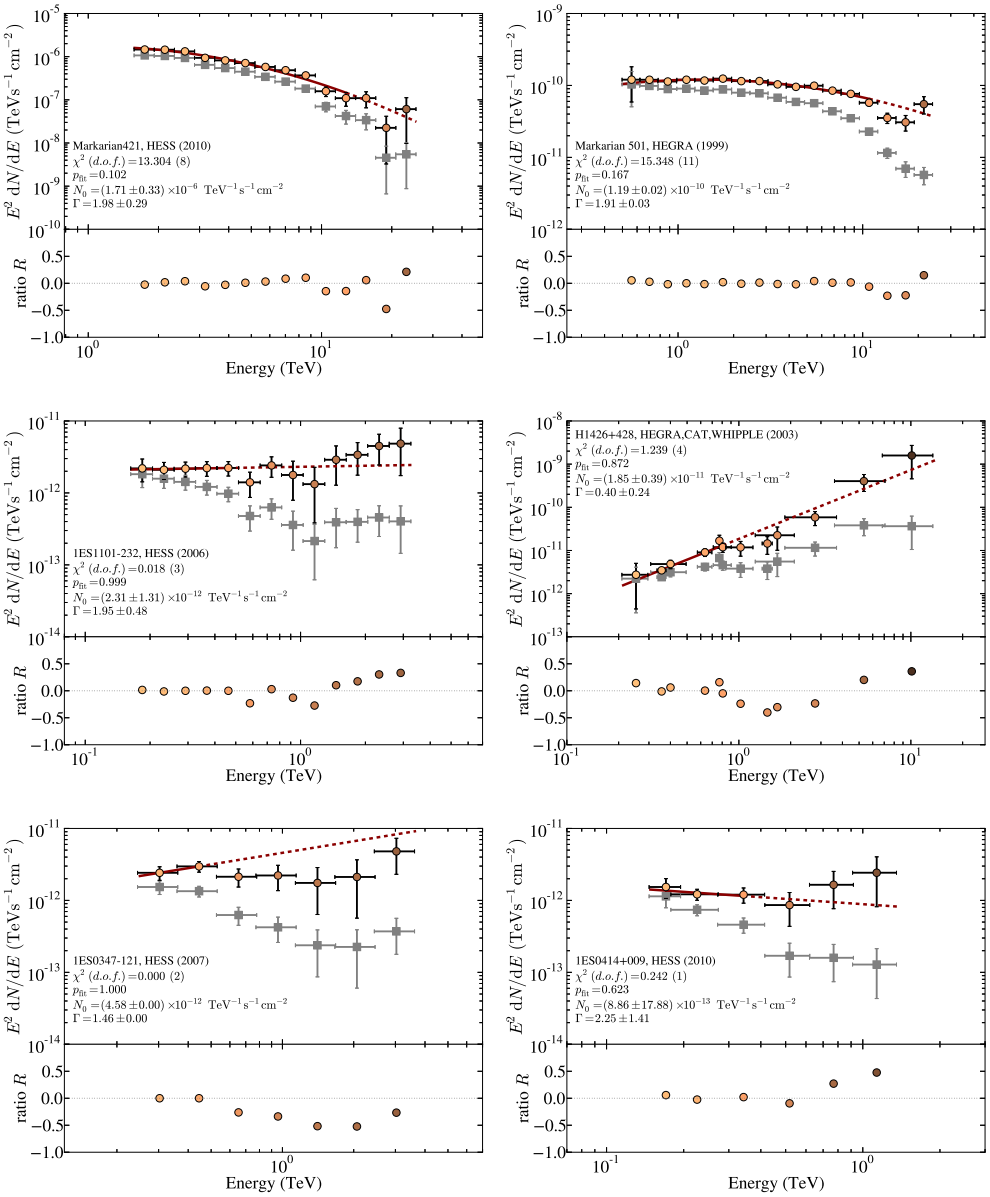


**Figure A.1:** Top panels: VHE spectra with data points in the optical thick regime. The color coding of the absorption-corrected data points scale with the optical depth. Observed data points are shown in gray. The best-fit values and the corresponding $\chi^2$- and $p_{\rm fit}$-values are also shown, the fit is represented by the solid line, the extrapolation by the dashed line. Lower panels: ratios between the (extrapolated) fits and absorption-corrected data points defined in Eq. (3.3).

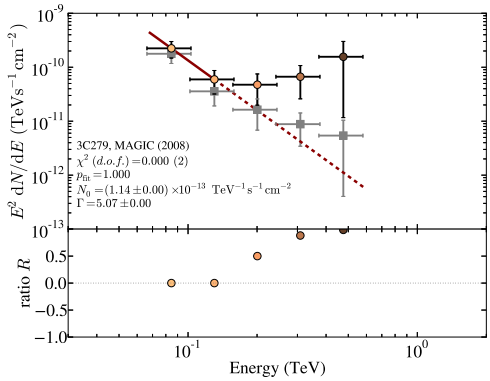


**FIGURE A.1:** Continued.

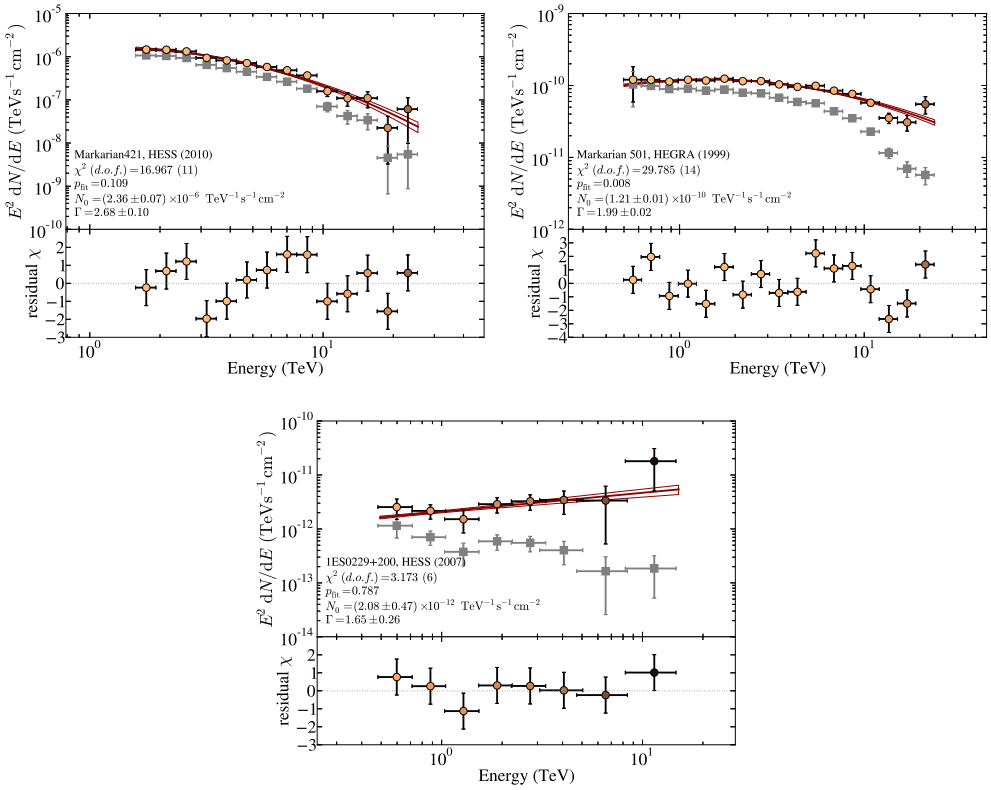


**FIGURE A.2:** Top panel: De-absorbed VHE spectra with data points in the $\tau_{\gamma\gamma} \geqslant 2$ regime (KD model). The corresponding spectral fits over the whole energy range are shown as dark red butterflies. The color scale of the absorption corrected data points scales with the optical depth. The observed data points are shown in gray. Lower panel: Fit residuals.

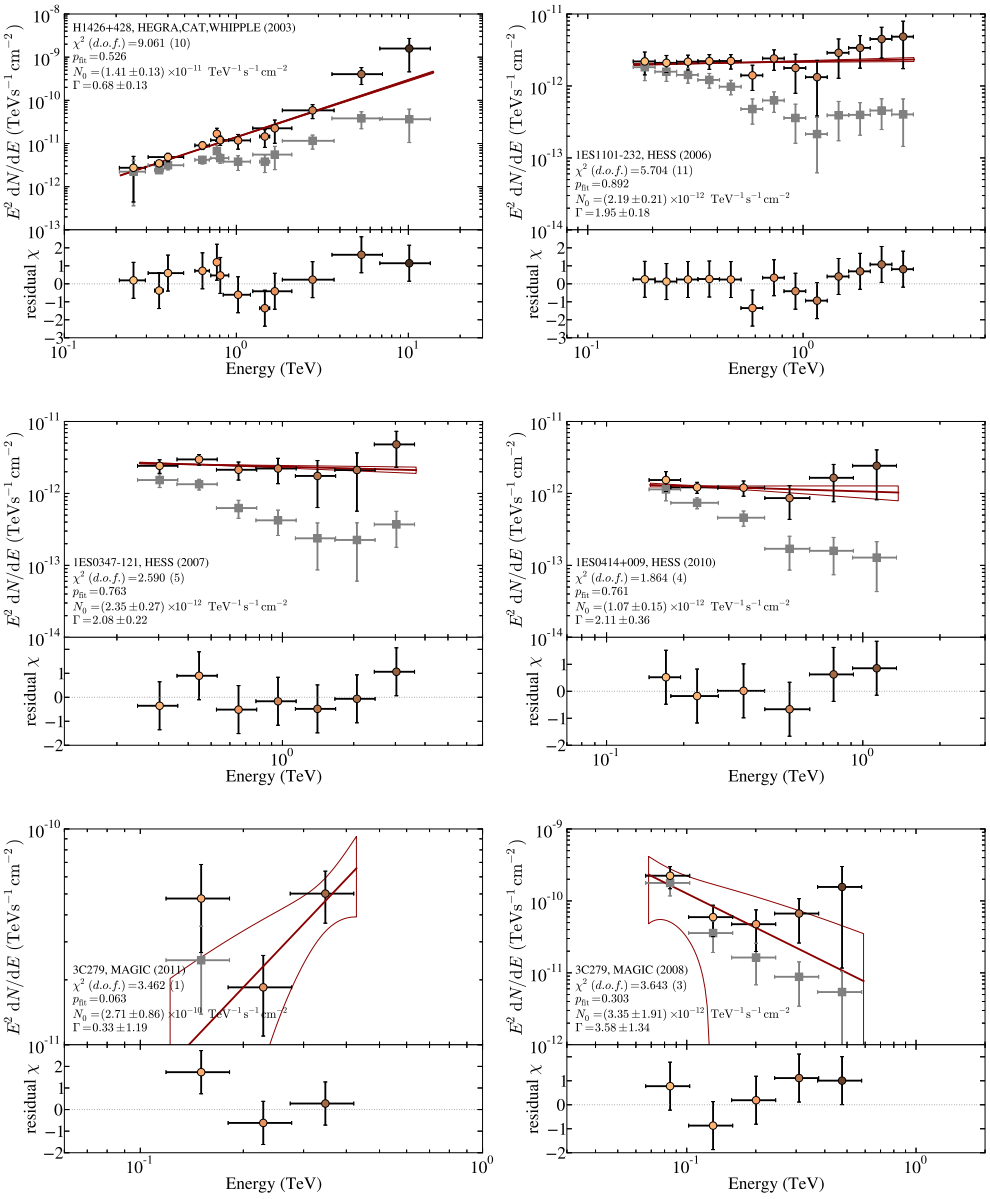


**FIGURE A.2:** Continued.

**TABLE A.1:** List of fit qualities for all VHE $\gamma$-ray spectra if no ALPs are included in the de-absorption of the spectra. The table shows the $\chi^2$-values, the degrees of freedom (d.o.f.), and the resulting fit probabilities $p_{\text{fit}}$ for the KD model and the scaled FRV model. See Table 3.1 for the references of each spectrum.

| $j$ | Source | Experiment | Fit function[1] | $\chi^2$ (d.o.f.) $\tau_{\gamma\gamma} = 1 \times \tau_{\text{KD}}$ | $p_{\text{fit}}$ | $\chi^2$ (d.o.f.) $\tau_{\gamma\gamma} = 1.3 \times \tau_{\text{FRV}}$ | $p_{\text{fit}}$ |
|---|---|---|---|---|---|---|---|
| 1 | Mkn 421 | HEGRA | LP | ... | ... | 4.10 (7) | 0.768 |
| 2 | Mkn 421 | HEGRA | PL | ... | ... | 8.75 (8) | 0.364 |
| 3 | Mkn 421 | H.E.S.S. | LP | ... | ... | 14.75 (10) | 0.142 |
| 4 | Mkn 421 | H.E.S.S. | LP, PL[2] | 16.97 (11) | 0.109 | 13.95 (12) | 0.304 |
| 5 | Mkn 501 | HEGRA | LP | 29.78 (14) | 0.008 | 38.55 (14) | 0.000 |
| 6 | 1ES 1950+650 | HEGRA | PL | ... | ... | 0.78 (3) | 0.854 |
| 7 | 1ES 1950+650 | HEGRA | PL | ... | ... | 7.89 (6) | 0.247 |
| 8 | PKS 2155-304 | H.E.S.S. | PL | ... | ... | 9.57 (7) | 0.215 |
| 9 | PKS 2155-304 | H.E.S.S. | PL | ... | ... | 8.34 (8) | 0.401 |
| 10 | PKS 2155-304 | H.E.S.S. | LP | ... | ... | 11.48 (14) | 0.648 |
| 11 | PKS 2155-304 | H.E.S.S. | PL | ... | ... | 5.46 (3) | 0.141 |
| 12 | RGB J0710+591 | VERITAS | PL | ... | ... | 2.00 (3) | 0.573 |
| 13 | H 1426+428 | HEGRA, CAT, WHIPPLE | PL | 9.06 (10) | 0.526 | 9.33 (10) | 0.501 |
| 14 | 1ES 0229-200 | H.E.S.S. | PL | 3.17 (6) | 0.787 | 3.86 (6) | 0.695 |
| 15 | H 2356-309 | H.E.S.S. | PL | ... | ... | 3.56 (6) | 0.735 |
| 16 | H 2356-309 | H.E.S.S. | PL | ... | ... | 4.20 (6) | 0.649 |
| 17 | H 2356-309 | H.E.S.S. | PL | ... | ... | 3.70 (6) | 0.717 |
| 18 | 1ES 1218+304 | VERITAS | PL | ... | ... | 2.33 (5) | 0.802 |
| 19 | 1ES 1101-232 | H.E.S.S. | PL | 5.70 (11) | 0.892 | 6.83 (11) | 0.813 |
| 20 | 1ES 0347-121 | H.E.S.S. | PL | 2.59 (5) | 0.763 | 2.30 (5) | 0.807 |
| 21 | RBS 0413 | VERITAS | PL | ... | ... | 0.02 (2) | 0.988 |
| 22 | 1ES 0414+009 | H.E.S.S. | PL | 1.86 (4) | 0.761 | 2.95 (4) | 0.567 |
| 23 | 1ES 0414+009 | VERITAS | PL | ... | ... | 0.51 (2) | 0.776 |
| 24 | PKS 1222+21 | MAGIC | PL | ... | ... | 0.24 (3) | 0.971 |
| 25 | 3C 279 | MAGIC | PL | 3.46 (1) | 0.063 | 3.95 (1) | 0.047 |
| 26 | 3C 279 | MAGIC | PL | 3.64 (3) | 0.303 | 4.48 (3) | 0.214 |
| **Combined** | | | | 76.25 (65) | 0.160 | 173.88 (165) | 0.303 |

[1] PL = power law, LP = logarithmic parabola.
[2] The spectrum is fitted with a logarithmic parabola in the KD model and with a power law in the FRV model, respectively.

from the spectra of Mrk 421 (Tluczykont, 2011) and Mrk 501 (Aharonian *et al.*, 1999b), for the KD model, and, additionally, the spectrum of PKS 2155-304 (Aharonian *et al.*, 2007a) for the FRV model. Again, these spectra are dominated by their systematic uncertainties which are not included here.

The reason for the large contribution of these spectra to the total $\chi^2$-values is the oscillatory behavior of the photon survival probability [see Eq. (5.18)] outside the SMR. As a result of the oscillations, the fit residuals also scatter strongly around zero and give rise to a low fit probability. If the spectra with high statistics are removed from the samples, the $\chi^2$/d.o.f. values are close to one for all tested values of the ALP mass $m_a$ and the coupling to photons $g_{a\gamma}$.

The fits to most spectra in the $(m_a, g_{a\gamma})$ parameter space are acceptable. In the case of a small overall fit probability, the lower limits on $g_{a\gamma}$ are pushed towards lower values as the residual distribution broadens (see the discussion in Chapter 5).

# B Galactic VHE $\gamma$-ray spectra used to cross check the pair production anomaly

In Section 3.1.2 galactic very high energy (VHE) spectra are used as a control sample to ensure that an indication of a pair-production anomaly is not mimicked by an instrumental effect. This Appendix lists the utilized galactic spectra in Table B.1 together with their corresponding energy range and reference.

**Table B.1:** Galactic VHE spectra used to cross check the indication of the pair-production anomaly.

| $i$[1] | Source | Instrument | Energy range (TeV) |
|---|---|---|---|
| 1 | J1800-240B | H.E.S.S. | 0.31 – 2.31 |
| 2 | W28 | H.E.S.S. | 0.41 – 1.73 |
| 3 | CTB 37A | H.E.S.S. | 0.47 – 13.77 |
| 4 | CTB 37B | H.E.S.S. | 0.42 – 1.27 |
| 5 | CTB 37B | H.E.S.S. | 0.37 – 3.66 |
| 6 | Crab | H.E.S.S. | 0.52 – 30.50 |
| 7 | Crab | MAGIC | 0.08 – 6.94 |
| 8 | Crab | HEGRA | 0.31 – 37.62 |

[1] *References*: (1) Aharonian *et al.* (2008c); (2) Aharonian *et al.* (2008c); (3) Aharonian *et al.* (2008b); (4) Aharonian *et al.* (2006e); (5) Aharonian *et al.* (2008a); (6) Aharonian *et al.* (2006d); (7) Albert *et al.* (2008c); (8) Aharonian *et al.* (2004); (9) Celik (2008); (10) Aharonian *et al.* (2005e); (11) Aharonian *et al.* (2009d); (12) Albert *et al.* (2006d); (13) Aharonian *et al.* (2006e); (14) Aharonian *et al.* (2006e); (15) Aharonian *et al.* (2006e); (16) Aharonian *et al.* (2006e); (17) H.E.S.S. Collaboration *et al.* (2011a); (18) Aharonian *et al.* (2007d); (19) Aharonian *et al.* (2008c); (20) Aharonian *et al.* (2006e); (21) Aharonian *et al.* (2007d); (22) Aharonian *et al.* (2006e); (23) Albert *et al.* (2006c); (24) Aharonian *et al.* (2006e); (25) Aharonian *et al.* (2006e); (26) Albert *et al.* (2006f); (27) Aharonian *et al.* (2006e); (28) Aharonian *et al.* (2009a); (29) Aharonian *et al.* (2006b); (30) Aharonian *et al.* (2006b); (31) Albert *et al.* (2008a); (32) Albert *et al.* (2009); (33) Anderhub *et al.* (2009a); (34) Acciari *et al.* (2008b); (35) Albert *et al.* (2006g); (36) Acciari *et al.* (2009c); (37) Aharonian *et al.* (2009e); (38) Aharonian *et al.* (2005b); (39) Aharonian *et al.* (2009b); (40) Aharonian *et al.* (2005a); (41) Aharonian *et al.* (2007f); (42) Aharonian *et al.* (2007h); (43) Acero *et al.* (2010); (44) Acero *et al.* (2010); (45) Aharonian *et al.* (2007b); (46) H.E.S.S. Collaboration *et al.* (2011b); (47) H.E.S.S. Collaboration *et al.* (2011b)

| | | | |
|---|---|---|---|
| 9 | Crab | VERITAS | 0.31 – 6.17 |
| 10 | G 0.9+0.1 | H.E.S.S. | 0.23 – 6.16 |
| 11 | Galactic Center | H.E.S.S. | 0.28 – 32.36 |
| 12 | Galactic Center | MAGIC | 0.60 – 14.94 |
| 13 | J1616-508 | H.E.S.S. | 0.38 – 18.24 |
| 14 | J1634-471 | H.E.S.S. | 0.32 – 2.16 |
| 15 | J1640-465 | H.E.S.S. | 0.28 – 2.93 |
| 16 | J1708-410 | H.E.S.S. | 0.38 – 4.73 |
| 17 | J1708-443 | H.E.S.S. | 0.91 – 19.08 |
| 18 | J1718-385 | H.E.S.S. | 1.22 – 33.20 |
| 19 | J1800-240A | H.E.S.S. | 0.31 – 1.73 |
| 20 | J1804-216 | H.E.S.S. | 0.19 – 10.78 |
| 21 | J1809-193 | H.E.S.S. | 0.36 – 33.07 |
| 22 | J1813-178 | H.E.S.S. | 0.32 – 22.05 |
| 23 | J1813-178 | MAGIC | 0.50 – 7.98 |
| 24 | J1825-137 | H.E.S.S. | 0.20 – 42.92 |
| 25 | J1834-087 | H.E.S.S. | 0.27 – 2.95 |
| 26 | J1834-087 | MAGIC | 0.18 – 1.81 |
| 27 | J1837-069 | H.E.S.S. | 0.22 – 16.45 |
| 28 | J1908+06 | H.E.S.S. | 0.38 – 14.75 |
| 29 | Kookaburra (Pulsar) | H.E.S.S. | 0.39 – 24.45 |
| 30 | Kookaburra (Rabbit) | H.E.S.S. | 0.39 – 15.43 |
| 31 | LSI+61 303 | MAGIC | 0.36 – 4.94 |
| 32 | LSI+61 303 | MAGIC | 0.36 – 2.56 |
| 33 | LSI+61 303 | MAGIC | 0.36 – 2.56 |
| 34 | LSI+61 303 | VERITAS | 0.61 – 0.73 |
| 35 | LSI+61 303 | MAGIC | 0.22 – 4.34 |
| 36 | LSI+61 303 | VERITAS | 0.78 – 3.08 |
| 37 | PSR B1259-63 | H.E.S.S. | 1.40 – 50.87 |
| 38 | PSR B1259-63 | H.E.S.S. | 0.46 – 2.46 |
| 39 | RCW86 | H.E.S.S. | 0.90 – 18.91 |
| 40 | RX J0852.0-4622 (Vela Junior) | H.E.S.S. | 0.53 – 12.00 |
| 41 | RX J0852.0-4622 (Vela Junior) | H.E.S.S. | 0.37 – 15.83 |
| 42 | RX J1713.7-3946 | H.E.S.S. | 0.33 – 81.26 |
| 43 | SN 1006 | H.E.S.S. | 0.29 – 5.55 |
| 44 | SN 1006 | H.E.S.S. | 0.23 – 15.70 |
| 45 | Westerlund 2 | H.E.S.S. | 0.79 – 10.67 |
| 46 | Westerlund 2 (J1023-575) | H.E.S.S. | 0.79 – 10.67 |
| 47 | Westerlund 2 (J1026-582) | H.E.S.S. | 1.27 – 23.51 |

# C Light curves of AGN associated with a high optical depth photon

The variability of the active galactic nuclei (AGN) associated with a high optical depth photon (HOP, photon energy and source redshift result in $\tau_{\gamma\gamma} \geqslant 1$, see Section 3.2.1) is analyzed by calculating the light curves of the intrinsic spectrum, i.e., in the energy range 1 GeV – $E_{99}$ (see Section 3.2.2 for the definition of $E_{99}$).
The light curves are derived using the `python` implementation of the unbinned analysis chain of the *Fermi science tools*. The best-fit values of the intrinsic spectrum and sources within a 15° radius of the entire considered time range (the $\sim$ 4.3 years of *Fermi*-LAT operation) serve as input parameters for each time bin. All sources are described by power laws and the spectral indices are frozen to their initial values. Only the power-law normalizations of sources within an angular distance of 4° from the central sources and the normalizations of the two background components (galactic diffuse and isotropic) are allowed to vary during the fit. A binning of three weeks is chosen for all AGN. Upper limits are derived if the $TS$ value in the corresponding time bin falls below 4. The results for all AGN listed in Table 3.3 are shown in Figure C.1 in descending order with the optical depth of the associated HOP.

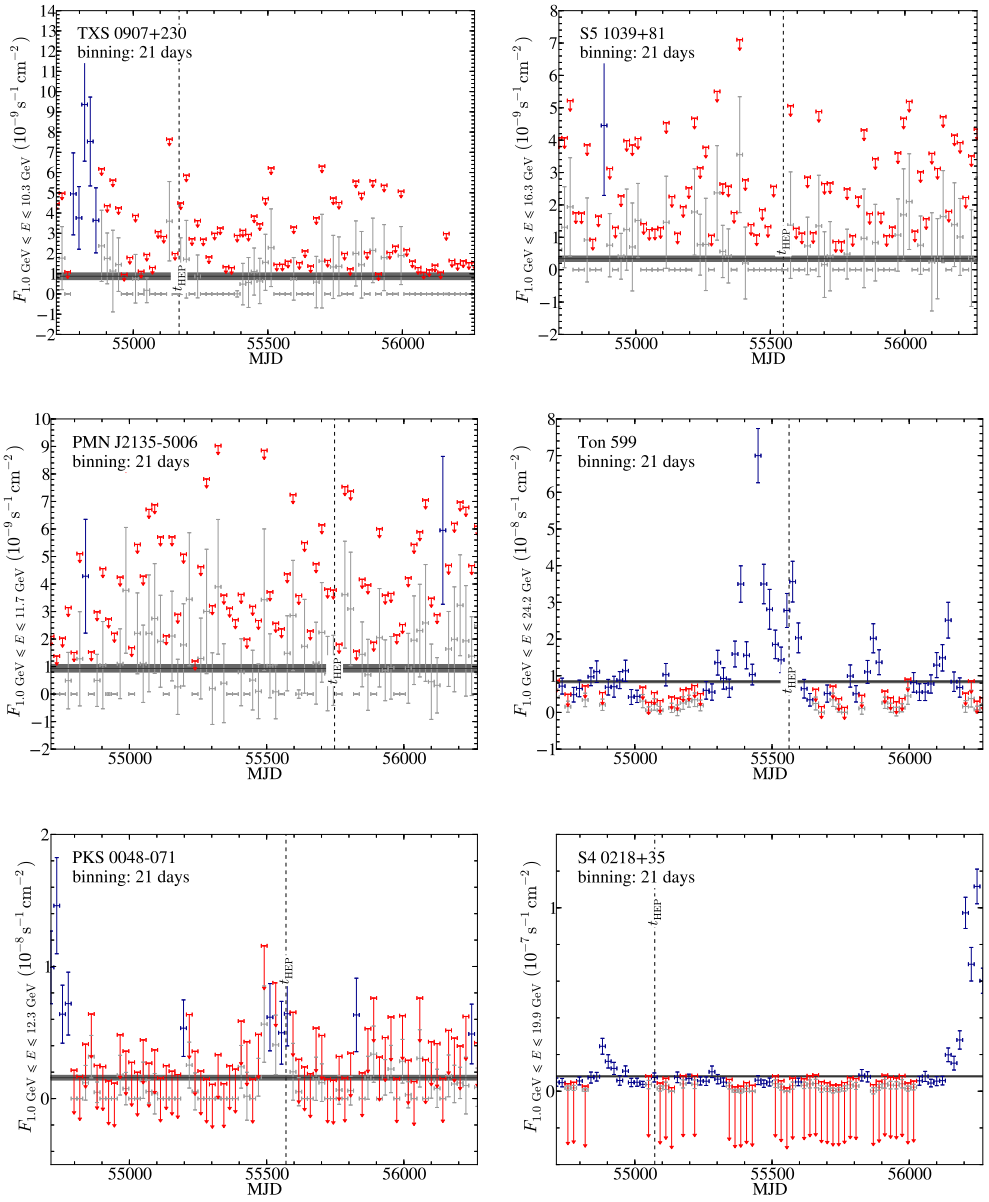


**Figure C.1:** Light curves of the intrinsic spectra of the AGN associated with a HOP. Flux points are shown in blue. For time bins where $TS < 4$, flux points are depicted in gray and $2\,\sigma$ upper limits on the flux are derived (red arrows). The arrival time of the HOP is shown as a dashed vertical line and the horizontal gray band indicates the integrated average flux.

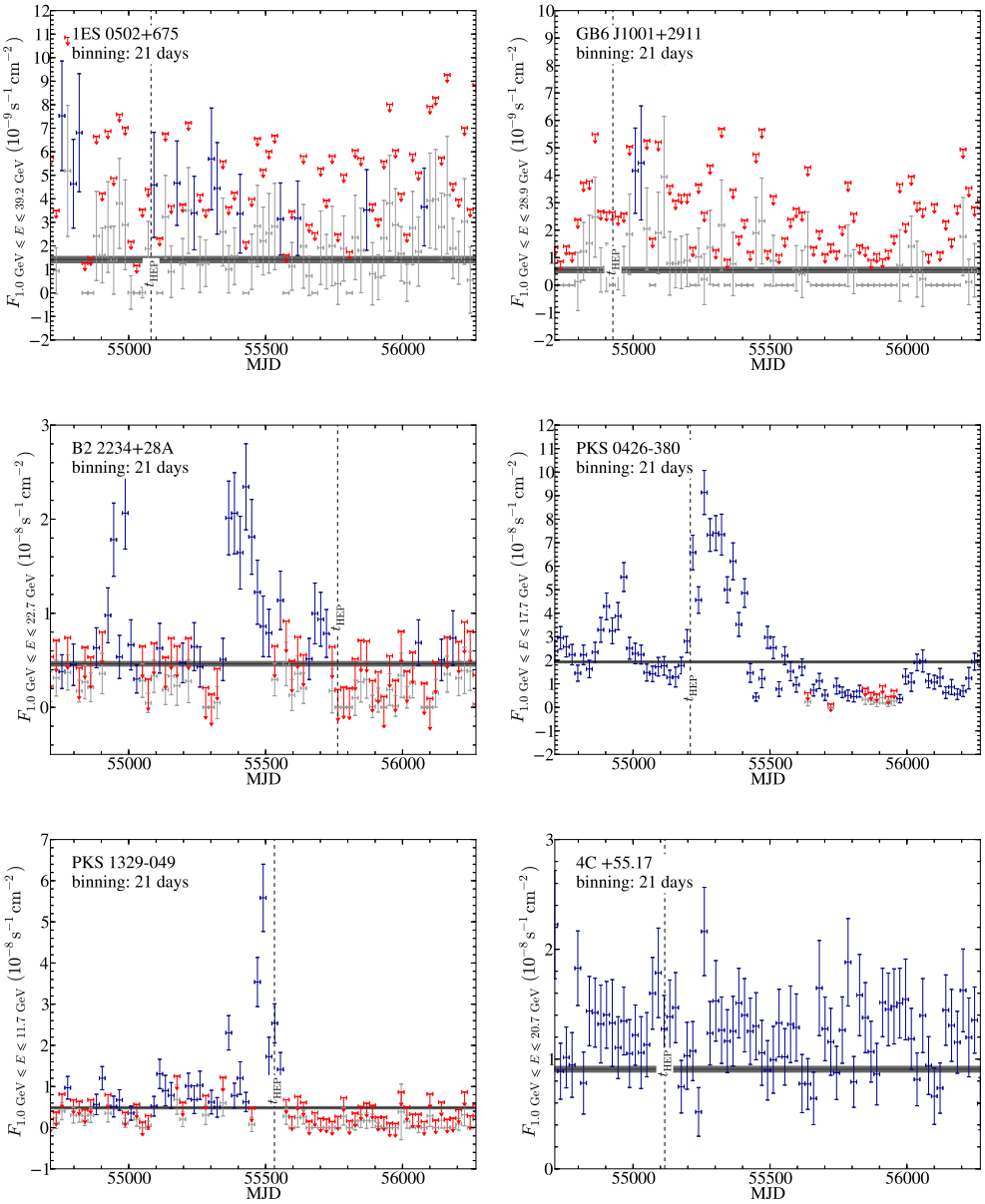


**FIGURE C.1:** Continued.

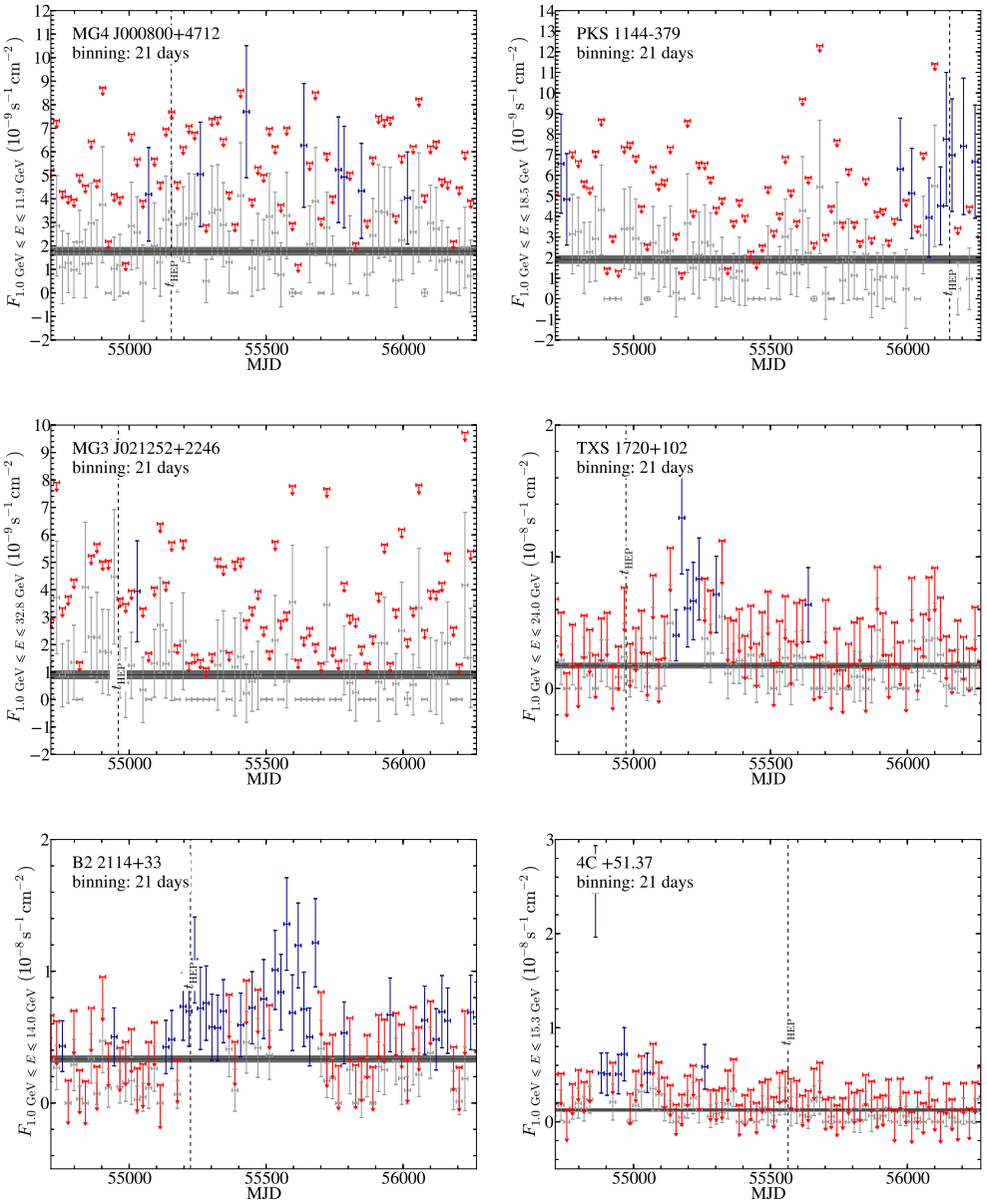


**FIGURE C.1:** Continued.

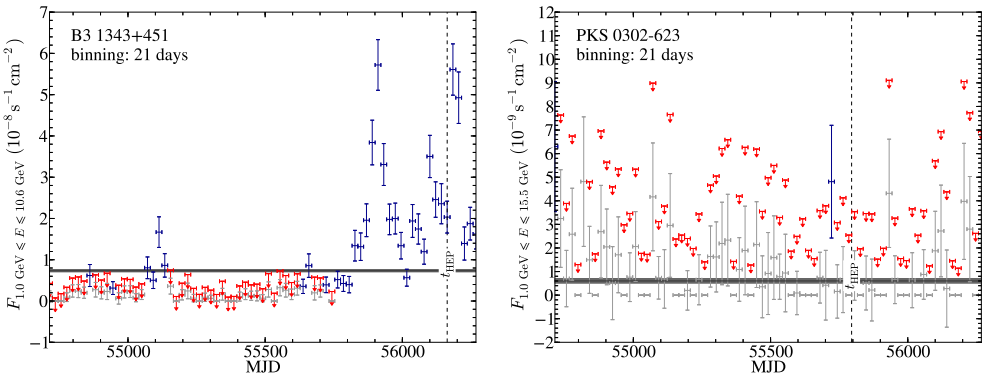


**FIGURE C.1:** Continued.

# D Solution to the equation of motion of photon-ALP oscillations

In this appendix, the equation of motion for the conversion of photons into axion-like particles (ALPs) given by Eq. (5.5) is solved in terms of the transfer matrix $\mathcal{T}(x_3, 0; E)$ for one domain of a constant homogeneous magnetic field. The general case of oscillations outside the strong-mixing regime is considered [energy $E < E_{\rm crit}$, see Eq. (5.11)], and the possibility is included that photons are lost due to pair production. The calculation will be similar to the case of the strong mixing regime, presented, e.g., in de Angelis *et al.* (2011). From Eq. (5.6), the mixing matrix can be written as

$$\mathcal{M}_0 = \begin{pmatrix} t + iw & 0 & 0 \\ 0 & u + iw & v \\ 0 & v & s \end{pmatrix}, \tag{D.1}$$

so that $t = \Delta_\perp$, $u = \Delta_\parallel$, $w = 1/(2\lambda_\gamma)$, $s = \Delta_a$, and $v = \Delta_{a\gamma}$. The eigenvalues $\lambda$ of this matrix are determined by solving $\det(\mathcal{M}_0 - \lambda I) = 0$, which gives,

$$\lambda_1 = t + iw, \tag{D.2}$$

$$\lambda_{2/3} = \frac{1}{2}\left(s + u + iw \mp D\right), \tag{D.3}$$

with $D = \sqrt{[s - (u + iw)]^2 + 4v^2}$. The transfer matrix is found with the ansatz

$$\mathcal{T}(x_3, 0; E; \psi = 0) = \sum_{j=1}^{3} e^{i\lambda_j x_3} T_j(E; \psi = 0), \tag{D.4}$$

where $\psi$ denotes the angle between the $x_2$ direction and the transverse component of the $B$-field, $\mathbf{B}_\perp$. The $T_j$ are determined with Eq. (A17-A19) in de Angelis *et al.* (2011),

$$T_1(\psi = 0) = \begin{pmatrix} 1 & 0 & 0 \\ 0 & 0 & 0 \\ 0 & 0 & 0 \end{pmatrix}, \tag{D.5}$$

and

$$T_2(E;\psi=0) = \begin{pmatrix} 0 & 0 & 0 \\ 0 & \frac{s-(u+iw)+D}{2D} & -\frac{v}{D} \\ 0 & -\frac{v}{D} & \frac{-s+(u+iw)+D}{2D} \end{pmatrix}, \tag{D.6}$$

$$T_3(E;\psi=0) = \begin{pmatrix} 0 & 0 & 0 \\ 0 & \frac{-s+(u+iw)+D}{2D} & \frac{v}{D} \\ 0 & \frac{v}{D} & \frac{s-(u+iw)+D}{2D} \end{pmatrix}. \tag{D.7}$$

The similarity transformation of Eq. (5.14) yields the final result for the transfer matrix for arbitrary angles of $\psi$,

$$V(\psi)\quad T_1(\psi=0)\quad V^\dagger(\psi) = \begin{pmatrix} \cos^2\psi & -\sin\psi\cos\psi & 0 \\ -\sin\psi\cos\psi & \sin^2\psi & 0 \\ 0 & 0 & 0 \end{pmatrix}, \tag{D.8}$$

$$V(\psi)\quad T_2(\psi=0)\quad V^\dagger(\psi) = \begin{pmatrix} \frac{s-(u+iw)+D}{2D}\sin^2\psi & \frac{s-(u+iw)+D}{2D}\sin\psi\cos\psi & -\frac{v}{D}\sin\psi \\ \frac{s-(u+iw)+D}{2D}\sin\psi\cos\psi & \frac{s-(u+iw)+D}{2D}\cos^2\psi & -\frac{v}{D}\cos\psi \\ -\frac{v}{D}\sin\psi & -\frac{v}{D}\cos\psi & \frac{-s+(u+iw)+D}{2D} \end{pmatrix}, \tag{D.9}$$

$$V(\psi)\quad T_3(\psi=0)\quad V^\dagger(\psi) = \begin{pmatrix} \frac{-s+(u+iw)+D}{2D}\sin^2\psi & \frac{-s+(u+iw)+D}{2D}\sin\psi\cos\psi & \frac{v}{D}\sin\psi \\ \frac{-s+(u+iw)+D}{2D}\sin\psi\cos\psi & \frac{-s+(u+iw)+D}{2D}\cos^2\psi & \frac{v}{D}\cos\psi \\ \frac{v}{D}\sin\psi & \frac{v}{D}\cos\psi & \frac{s-(u+iw)+D}{2D} \end{pmatrix}, \tag{D.10}$$

in accordance with the result obtained by de Angelis *et al.* (2011).

# E Theoretical bound on the photon survival probability in photon-ALP oscillations

In the following, it will be proven that the photon survival probability, $P_{\gamma\gamma}$, introduced in Eq. (5.18), is always larger than $1/2$ for an initially unpolarized photon beam. For the proof, a photon beam propagating in the $x_3$ direction in a turbulent magnetic field is considered. Neglecting absorption, the oscillations of photons into axion-like particles (ALPs) can be described with the unitary transfer matrix $\mathcal{T}$. If the initial photon beam is unpolarized, the density matrix is given by $\rho_i = 1/2\mathrm{diag}(1,1,0)$. The probability for ALPs in the final state is

$$P_{\gamma a} = \mathrm{Tr}\left[\rho_{aa}\mathcal{T}\rho_i\mathcal{T}^\dagger\right], \tag{E.1}$$

with $\rho_{aa} = \mathrm{diag}(0,0,1)$. Let $t_{ij}$ denote the entries of $\mathcal{T}$ with $i,j = x,y,a$, then an explicit calculation gives

$$P_{\gamma\gamma} = \frac{1}{2}\left(|t_{xx}|^2 + |t_{xy}|^2 + |t_{yx}^2| + |t_{yy}|^2\right), \tag{E.2}$$

$$P_{\gamma a} = \frac{1}{2}\left(|t_{ax}|^2 + |t_{ay}|^2\right). \tag{E.3}$$

It follows from the unitarity of the transfer matrix, $\mathcal{T}\mathcal{T}^\dagger = \mathcal{T}^\dagger\mathcal{T} = 1$, that

$$|t_{xx}|^2 + |t_{yx}|^2 + |t_{ax}|^2 = 1, \tag{E.4}$$

$$|t_{xy}|^2 + |t_{yy}|^2 + |t_{ay}|^2 = 1, \tag{E.5}$$

$$|t_{xa}|^2 + |t_{ya}|^2 + |t_{aa}|^2 = 1, \tag{E.6}$$

and equally for $\{i \leftrightarrow j\}$. Inserting these relations into Eqs. (E.2) and (E.3) one arrives at

$$P_{\gamma\gamma} = 1 - \frac{1}{2}\left(|t_{ax}|^2 + |t_{ay}|^2\right) = 1 - P_{\gamma a} = 1 - \frac{1}{2}\left(1 - |t_{aa}|^2\right) \geqslant \frac{1}{2}, \tag{E.7}$$

and, thus, $P_{\gamma a} \leqslant 1/2$.

Including absorption, the transfer matrix is not unitary anymore. However, the numerical simulations in Chapter 5 show that the result still holds. This has been independently confirmed by Daniele Montanino.

# F The Galactic magnetic field in heliocentric spherical coordinates

The model of Jansson & Farrar (2012a) is used to describe the regular galactic magnetic field of the Milky Way (GMF) and to compute the conversion probability of photons into axion-like particles (ALPs) and vice versa. As discussed in Chapter 5, ALPs only mix with the magnetic field component transversal to the propagation direction. The projection of the $B$ field onto the line of sight is best calculated if the magnetic field is given in heliocentric spherical coordinates. This requires the transformation of the magnetic field originally given in galactocentric cylindrical coordinates $(\rho, \phi, z)$ to heliocentric spherical coordinates, $(s, l, b)$, with $s$ the distance from the sun, and $(l, b)$ the galactic longitude and latitude, respectively. The corresponding calculation is presented here, together with additional details on the GMF model. First, the components of the GMF are briefly summarized (see Jansson & Farrar, 2012a, for further details in references therein):

Disk Component. This component is confined to the ($x$,$y$) plane. For distances from the Galactic center (GC) $\rho < 3\,\mathrm{kpc}$, the field strength is set to zero, while for $3\,\mathrm{kpc} \leqslant \rho \leqslant 5\,\mathrm{kpc}$ the field is constant with a value of $b_{\mathrm{ring}}$ and has only a azimuthal (i.e., $\phi$-) component. Up to the maximum distance of 20 kpc, the field is modeled with 8 arms of a logarithmic spiral that intersect the negative $x$-axis according to the equation $\rho = r_{-x} \exp[(\phi - 270°)/\tan(90° - i)]$, with the opening angle $i = 11.5°$ (note that there is a misprint in the manuscript: $(\phi - 270°)$ has to be divided by and not multiplied with the tan-expression). Each ring has its own field strength, $b_j$, $j = 1, \ldots, 8$, and the $\rho$ and $\phi$ components are given by

$$B_{\rho,\mathrm{disk}}(\rho, \phi, z) = b_j \sin i \left(\frac{5\,\mathrm{kpc}}{\rho}\right) L(z, h_{\mathrm{disk}}, w_{\mathrm{disk}}) \tag{F.1}$$

$$B_{\phi,\mathrm{disk}}(\rho, \phi, z) = b_j \cos i \left(\frac{5\,\mathrm{kpc}}{\rho}\right) L(z, h_{\mathrm{disk}}, w_{\mathrm{disk}}) \tag{F.2}$$

$$B_z = 0, \tag{F.3}$$

where the extension of $\mathbf{B}_{\rm disk}$ is modeled with $h_{\rm disk}$ and $w_{\rm disk}$ entering through

$$L(z,h,w) = \left[1+\exp\left(\frac{|z|-h}{w}\right)\right]^{-1}. \tag{F.4}$$

HALO COMPONENT. The halo component is completely toroidal with different field strengths ($B_n$, $B_s$) and radial extensions ($\rho_n$, $\rho_s$) north and south of the Galactic plane:

$$B_{\phi,\rm halo}(\rho,z) = \exp(-|z|/z_0)L(z,h_{\rm disk},w_{\rm disk}) \times \begin{cases} B_n(1-L(\rho,\rho_n,w_{\rm halo})), & \text{if} \quad z>0, \\ B_s(1-L(\rho,\rho_s,w_{\rm halo})), & \text{if} \quad z<0. \end{cases} \tag{F.5}$$

X COMPONENT. In addition to the halo component, the X component contributes to the field outside the galactic plane with a radial and $z$ component. The field has a constant elevation angle $\Theta_{\rm X}^0 = \sphericalangle(\rho,z)$ for distances $\rho > \rho_{\rm X}^c$. For these radii, the field strength varies as $b_{\rm X}(\rho_p)\rho_p/\rho$, where $\rho_p = \rho - |z|/\tan(\Theta_{\rm X}^0)$ and $b_{\rm X}(\rho_p) = B_{\rm X}\exp(-\rho_p/\rho_{\rm X})$. Below $\rho_{\rm X}^c$, which is left free during the fit, the elevation angle $\Theta_{\rm X}$ increases until it reaches 90° for $\rho = 0$. In this regime, the field strength decreases as $b_{\rm X}(\rho_p)(\rho_p/\rho)^2$ with

$$\rho_p = \frac{\rho\rho_p}{\rho_{\rm X}^c + |z|/\tan(\Theta_{\rm X}^0)}, \tag{F.6}$$

$$\Theta_X(\rho,z) = \arctan\left(\frac{|z|}{\rho-\rho_p}\right). \tag{F.7}$$

In total, this component has four free parameters: $B_{\rm X}$, $\Theta_{\rm X}^0$, $\rho_{\rm X}$, and $\rho_{\rm X}^c$. The magnetic field components are given by

$$B_{\rho,\rm X} = b_{\rm X} \times \begin{cases} \cos\Theta_{\rm X}, & \text{if} \quad z>0, \\ \cos(90^\circ-\Theta_{\rm X}), & \text{if} \quad z<0, \end{cases} \tag{F.8}$$

$$B_{z,\rm X} = b_{\rm X} \times \begin{cases} \sin\Theta_{\rm X}, & \text{if} \quad z>0, \\ \sin(90^\circ-\Theta_{\rm X}), & \text{if} \quad z<0, \end{cases} \tag{F.9}$$

where $\Theta_{\rm X}$ has to be replaced by $\Theta_{\rm X}^0$ if $\rho > \rho_{\rm X}^c$. Additionally, for the central region with $\sqrt{\rho^2+z^2} < 1\,\text{kpc}$, the X component is set to 0.

The values for the free parameters are subsequently determined by a best fit of $\mathbf{B}_{\rm GMF} = \mathbf{B}_{\rm disk} + \mathbf{B}_{\rm halo} + \mathbf{B}_{\rm X}$ to the WMAP7 Galactic synchrotron emission map and over 40,000 rotation measures, and the best-fit parameters can be found on Table 1 of Jansson & Farrar (2012a). The model is chosen such that $\nabla\cdot\mathbf{B}_{\rm GMF} = 0$. The implementation of the GMF model is shown in Figure F.1, and shows perfect

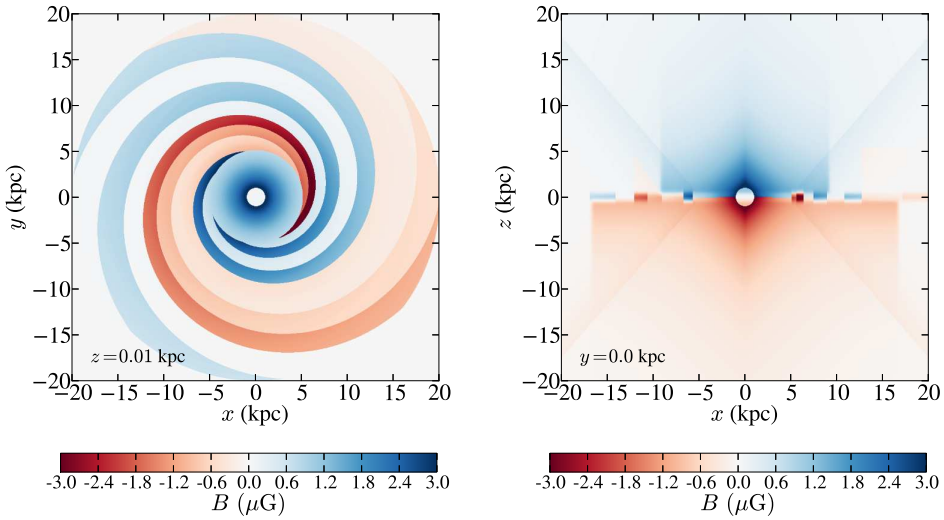


**FIGURE F.1:** Right panel: $(x, y)$ plane of the GMF for $z = 0.01\,\text{kpc}$. Left panel: $(x, z)$ plane of the GMF for $y = 0\,\text{kpc}$. The blobs at $z = 0\,\text{kpc}$ correspond to the disk component of the GMF. The color coding gives the field strength $\sqrt{|\mathbf{B}_{\text{GMF}}|^2}$ with negative values if the $\phi$-component is oriented clockwise. The sun is located at $x = -8.5\,\text{kpc}$ and $y = z = 0\,\text{kpc}$.

agreement with the results presented in Figure 5 and 7 of Jansson & Farrar (2012a).

For the photon-ALP conversion probability, one has to know the magnetic field along the line of sight pointing to an extragalactic source. Thus, the cylindrical galactocentric coordinates are best expressed as heliocentric spherical coordinates $(s, l, b)$. Letting $d = -8.5\,\text{kpc}$ denote the position of the sun in Cartesian galactocentric coordinates, the two coordinate systems are related via

$$\rho = \sqrt{s^2 \cos^2 b + d^2 + 2s \cos l \cos b}, \tag{F.10}$$

$$\phi = \arctan\left(\frac{s \sin l \cos b}{s \cos l \cos b + d}\right), \tag{F.11}$$

$$z = s \sin b. \tag{F.12}$$

Furthermore, only the magnetic field transversal to the photon propagation direction, $\hat{\mathbf{s}}$, contributes to photon-ALP mixing. This component is found by rewriting both the unit vectors of the heliocentric spherical coordinates and the magnetic field in terms of the translational invariant Cartesian basis, $(\hat{\mathbf{x}}, \hat{\mathbf{y}}, \hat{\mathbf{z}})$,

$$\hat{\mathbf{s}} = \cos l \cos b \hat{\mathbf{x}} + \sin l \cos b \hat{\mathbf{y}} + \sin b \hat{\mathbf{z}}, \tag{F.13}$$

$$\hat{\mathbf{b}} = \cos l \sin b \hat{\mathbf{x}} + \sin l \sin b \hat{\mathbf{y}} - \cos b \hat{\mathbf{z}}, \tag{F.14}$$

$$\hat{\mathbf{l}} = -\sin l \hat{\mathbf{x}} + \cos l \hat{\mathbf{y}}, \tag{F.15}$$

and

$$\mathbf{B} = [B_\rho \cos\phi - B_\phi \sin\phi]\hat{\mathbf{x}} + [B_\rho \sin\phi + B_\phi \cos\phi]\hat{\mathbf{y}} + B_z\hat{\mathbf{z}}. \tag{F.16}$$

With these expressions, it is now possible to compute the projections of $\mathbf{B}_{\mathrm{GMF}}$ onto the unit vectors $(\hat{\mathbf{s}}, \hat{\mathbf{b}}, \hat{\mathbf{l}})$ of the heliocentric coordinate system:

$$B_s \equiv \langle \mathbf{B}, \hat{\mathbf{s}} \rangle = \cos b[B_\rho \cos(l-\phi) + B_\phi \sin(l-\phi)] + B_z \sin b, \tag{F.17}$$

$$B_t \equiv \langle \mathbf{B}, \hat{\mathbf{b}} \rangle = \sin b[B_\rho \cos(l-\phi) + B_\phi \sin(l-\phi)] + B_z \cos b, \tag{F.18}$$

$$B_u \equiv \langle \mathbf{B}, \hat{\mathbf{l}} \rangle = B_\rho \sin(l-\phi) + B_\phi \cos(\phi - l). \tag{F.19}$$

Only the $B_t$ and $B_u$ component contribute to the photon-ALP oscillations.
The maximum distance $s_{\max}$ traveled by a $\gamma$-ray through the Milky Way also depends on the position of source. It has to obey the relations $\rho < \rho_{\max} = 20\,\mathrm{kpc}$ and $z \lesssim 50\,\mathrm{kpc}$. Inserting the relations for $\rho$ and $z$ from Eqs. (F.10) and (F.12) yields

$$s_{\max} = \min\left[\frac{1}{\cos b}\left(-d\cos l + \sqrt{d^2\cos^2 l - d^2\cos^2 b + \rho_{\max}}\right), \frac{z_{\max}}{|\sin b|}\right]. \tag{F.20}$$

# Publication list

## Publications used in this thesis

### Peer-reviewed publications

- **Meyer, M.**; Horns, D.; Raue, M., *First lower limits on the photon - axion-like particle coupling from very high energy $\gamma$-ray observations*. Physical Review D, vol. 87, Issue 3, id. 035027 (2013).
  Chapter 5 is based on this publication. I did all calculations, co-developed the idea, and wrote the manuscript.

- Horns, D.; Maccione, L.; **Meyer, M.**; Mirizzi, A.; Montanino, D.; Roncadelli, M., *Hardening of TeV gamma spectrum of active galactic nuclei in galaxy clusters by conversions of photons into axion-like particles*. Physical Review D, vol. 86, Issue 7, id. 075024 (2012).
  I developed a code for photon-ALPs oscillations in galaxy clusters and the Galactic magnetic field (GMF) model of Jansson & Farrar (2012a). It was used to cross check the results of the paper and to produce the all-sky map for the conversion probability. I also wrote parts of the manuscript. The framework for the photon-ALP oscillations in the GMF is outlined in Chapter 5 and further described in Appendix F.

- **Meyer, M.**; Raue, M.; Mazin, D.; Horns, D., *Limits on the extragalactic background light in the Fermi era*. Astronomy & Astrophysics, Volume 542, id.A59 (2012).
  Chapter 2 is based on this publication. I performed all calculations and wrote the manuscript. I had the idea to include the cascade formation in the calculations.

- Horns, D. & **Meyer, M.**, *Indications for a pair-production anomaly from the propagation of VHE gamma-rays*. Journal of Cosmology and Astroparticle Physics, Issue 02, id. 033 (2012).
  Chapter 3.1 discusses the results of this publication for which I co-developed the idea and independently did all calculations. I proof-read the manuscript.

### Conference proceedings

- **Meyer, M.**; Horns, D.; Raue, M, *Revisiting the Indication for a low opacity Universe for very high energy gamma-rays*. 8th Patras Workshop on Axions, WIMPs and WISPs, 18-22 July, Chicago, IL, USA.
  I performed the calculations included in Chapter 3.1 and wrote the manuscript.

- **Meyer, M.**; Horns, D.; Raue, M, *Indications for a low opacity universe from Fermi-LAT data*. 5th International Symposium on High-Energy Gamma-Ray Astronomy (Gamma2012), 9-13 July, Heidelberg, Germany.
  I wrote the manuscript and did all calculations. Chapter 3.2 uses the presented method.

## Further publications

### Peer-reviewed publications

- Raue, M. & **Meyer, M.**, *Probing the peak of the star formation rate density with the extragalactic background light.* Monthly Notices of the Royal Astronomical Society, Volume 426, Issue 2, pp. 1097-1106 (2012).

- **Meyer, M.**; Horns, D.; Zechlin, H.-S., *The Crab Nebula as a standard candle in very high-energy astrophysics*. Astronomy & Astrophysics, Volume 523, id.A2 (2010).

### Conference proceedings

- **Meyer, M.**; Horns, D.; Maccione, L.; Mirizzi, A.; Montanino, D.; Roncadelli, M., *The effect of photon-axion-like particle conversions in galaxy clusters on very high energy gamma-ray spectra*. 8th Patras Workshop on Axions, WIMPs and WISPs, 18-22 July, Chicago, IL, USA.

- **Meyer, M.**; Raue, M; Mazin, D.; Horns, D., *Limits on the extragalactic background light in the Fermi era*. 5th International Symposium on High-Energy Gamma-Ray Astronomy (Gamma2012), 9-13 July, Heidelberg, Germany.

- Zanin, Roberta, et al. (including **Meyer, M.**), *MAGIC measurement of the Crab Nebula spectrum over three decades in energy*. 32nd International Conference on Cosmic Rays (ICRC) 2011, 11-18 August 2011, Beijing, China.

- Horns, D. & **Meyer, M.**, *Very high energy optical depth of the universe*. 12th International Conference on Topics in Astroparticle and Underground Physics (TAUP), 5-9 September 2011, Munich, Germany.

- **Meyer, M.** & Horns, D., *Indications for a suppression of pair production at very high energies*. 7th Patras Workshop on Axions, WIMPs and WISPs, 26 June - 1 July 2011, Mykonos, Greece.

- **Meyer, M.**; Raue, M.; Mazin, D., *Influence of the cosmological evolution of the EBL on the limits derived from VHE gamma-ray blazar observations*. Beamed and Unbeamed Gamma-rays from Galaxies, 11-15 April 2011, Olos, Finland.

- **Meyer, M.** & Horns, D., *Indications for a transparent universe at very high energies*. Beamed and Unbeamed Gamma-rays from Galaxies, 11-15 April 2011, Olos, Finland.

- **Meyer, M.** & Horns, D., *On the transparency of the universe*. Cosmic Radiation Fields: Sources in the early Universe, 9-12 November 2010, Hamburg, Germany.

- **Meyer, M.**; Horns, D.; Zechlin, H.-S., *Cross Calibration of Imaging Air Cherenkov Telescopes with Fermi*. The 2009 Fermi Symposium, 2-5 November 2009, Washington D.C., USA.

# Acknowledgements

*At a time when science plays such a powerful role in the life of society, when the destiny of the whole of mankind may hinge on the results of scientific research, it is incumbent on all scientists to be fully conscious of that role, and conduct themselves accordingly. I appeal to my fellow scientists to remember their responsibility to humanity.*

Joseph Rotblat

First of all, I would like to thank my supervisors Prof. Dieter Horns and Dr. Martin Raue for giving me the opportunity to work on the fascinating topics covered in this thesis. Their enthusiasm and ideas have helped me tremendously to improve my work and to interpret the results obtained during the last three years. I felt always encouraged to tackle new problems and questions. They also made it possible for me to present my work to the scientific community at various conferences and workshops.
Furthermore, I am grateful to Dr. Andreas Ringwald for co-refereeing my thesis and my defense, and to Prof. Marcus Brüggen for also refereeing my defense.
I am much obliged to Dieter Horns, Martin Raue, Alessandro Mirizzi, Josefa Becerra, Andrei Lobanov, and Martin Tluczykont for their helpful comments on the manuscript. For language editing I would like to thank Roberto Sibbel, Inken Carsten, Nils Neubert, and Nelly Nguyen. Moreover, I am very grateful for the excellent collaboration with Marco Roncadelli and Girgio Galanti during my stay in Pavia. It was also a great pleasure for me to work with Alessandro Mirizzi, Daniele Montanino, Luca Maccione, Marco Roncadelli, and Daniel Mazin on the different manuscripts that found their way into this thesis.
I gratefully acknowledge the help from the *Fermi* help desk especially from Jeremy S. Perkings and the help from Ronnie Jansson with his GMF model.
My stay on the H.E.S.S. site would not have been the same without Ramin Marx. I would also like to thank Albert Jahnke and Toni Hanke for their support during the H.E.S.S. shift.
I will deeply miss the excellent and joyful working atmosphere with my colleagues in Hamburg. First of all, I thank my office mates Milton Fernandes and Max Kastendieck, and also Hannes Zechlin, Nelly Nguyen, Björn Opitz, Attila Abramowski,

Alexander Gewering-Peine, Andreas Maurer, Family Spies, and the whole Hamburg group for creating this unique work climate.
I am thankful for the IT support by Rainer Peter Feller and the whole IT team of the University of Hamburg.
Furthermore, I am grateful to the various authors of the EBL models used in this work for making their models publicly available. This work has made extensive use of the `python` modules `scipy`, `numpy`, `matplotlib`, `minuit`, `healpy`, `pyfits`, and `kapteyn`, as well as the NE2001 code, `gnuplot`, NASA's Astrophysics Data System (ADS), Arxiv, and google. Simulations were performed on the DESY BIRD cluster.
Moreover, I thank the state excellence cluster "Connecting Particles with the Cosmos" at the university of Hamburg.
Last but not least, I would like to thank Svea and my family for their never ending support.

# BIBLIOGRAPHY


ABBOTT, L. F., & SIKIVIE, P. 1983. A cosmological bound on the invisible axion. *Physics Letters B*, **120**(Jan.), 133–136.

ABDO, A. A., ACKERMANN, M., AJELLO, M., *et al.* 2009a. A limit on the variation of the speed of light arising from quantum gravity effects. *Nature*, **462**(Nov.), 331–334.

ABDO, A. A., ACKERMANN, M., AJELLO, M., *et al.* 2009b. Fermi large area telescope observations of the cosmic-ray induced $\gamma$-ray emission of the Earth's atmosphere. *Phys. Rev. D*, **80**(12), 122004.

ABDO, A. A., ACKERMANN, M., AJELLO, M., *et al.* 2010a. A change in the optical polarization associated with a $\gamma$-ray flare in the blazar 3C279. *Nature*, **463**, 919–923.

ABDO, A. A., ACKERMANN, M., AJELLO, M., *et al.* 2010b. Fermi Large Area Telescope Constraints on the Gamma-ray Opacity of the Universe. *Astrophys. J.*, **723**, 1082–1096.

ABDO, A. A., ACKERMANN, M., AJELLO, M., *et al.* 2010c. Spectrum of the Isotropic Diffuse Gamma-Ray Emission Derived from First-Year Fermi Large Area Telescope Data. *Physical Review Letters*, **104**(10), 101101.

ABDO, A. A., ACKERMANN, M., AGUDO, I., *et al.* 2010d. The Spectral Energy Distribution of Fermi Bright Blazars. *Astrophys. J.*, **716**(June), 30–70.

ABDO, A. A., ACKERMANN, M., AJELLO, M., *et al.* 2011a. Fermi Gamma-ray Space Telescope Observations of the Gamma-ray Outburst from 3C454.3 in November 2010. *Astrophys. J., Lett.*, **733**, L26.

ABDO, A. A., ACKERMANN, M., AJELLO, M., *et al.* 2011b. Insights into the High-energy $\gamma$-ray Emission of Markarian 501 from Extensive Multifrequency Observations in the Fermi Era. *Astrophys. J.*, **727**(Feb.), 129–+.

ABDO, A. A., ACKERMANN, M., AJELLO, M., *et al.* 2011c. Insights into the High-energy $\gamma$-ray Emission of Markarian 501 from Extensive Multifrequency Observations in the Fermi Era. *Astrophys. J.*, **727**(Feb.), 129.

ABEL, S. A., GOODSELL, M. D., JAECKEL, J., *et al.* 2008. Kinetic mixing of the photon with hidden U(1)s in string phenomenology. *Journal of High Energy Physics*, **7**(July), 124.

ACCIARI, V., ALIU, E., ARLEN, T., *et al.* 2009a. Discovery of Very High Energy Gamma-ray Radiation from the BL Lac 1ES 0806+524. *Astrophys. J., Lett.*, **690**(Jan.), L126–L129.

ACCIARI, V. A., ALIU, E., BEILICKE, M., *et al.* 2008a. VERITAS Discovery of >200 GeV Gamma-Ray Emission from the Intermediate-Frequency-Peaked BL Lacertae Object W Comae. *Astrophys. J., Lett.*, **684**(Sept.), L73–L77.

Acciari, V. A., Beilicke, M., Blaylock, G., *et al.* 2008b. VERITAS Observations of the $\gamma$-Ray Binary LS I +61 303. *Astrophys. J.*, **679**(June), 1427–1432.

Acciari, V. A., Aliu, E., Aune, T., *et al.* 2009b. Multiwavelength Observations of a TeV-Flare from W Comae. *Astrophys. J.*, **707**(Dec.), 612–620.

Acciari, V. A., Aliu, E., Arlen, T., *et al.* 2009c. Multiwavelength Observations of LS I +61degree 303 with Veritas, Swift, and RXTE. *Astrophys. J.*, **700**(Aug.), 1034–1041.

Acciari, V. A., Aliu, E., Arlen, T., *et al.* 2009d. VERITAS Observations of the BL Lac Object 1ES 1218+304. *Astrophys. J.*, **695**(Apr.), 1370–1375.

Acciari, V. A., Aliu, E., Arlen, T., *et al.* 2010a. Discovery of Very High Energy Gamma Rays from PKS 1424+240 and Multiwavelength Constraints on Its Redshift. *Astrophys. J., Lett.*, **708**(Jan.), L100–L106.

Acciari, V. A., Aliu, E., Arlen, T., *et al.* 2010b. The Discovery of $\gamma$-Ray Emission from the Blazar RGB J0710+591. *Astrophys. J., Lett.*, **715**(May), L49–L55.

Acero, F., Aharonian, F., Akhperjanian, A. G., *et al.* 2009. Detection of Gamma Rays from a Starburst Galaxy. *Science*, **326**(5956), 1080–1082.

Acero, F., Aharonian, F., Akhperjanian, A. G., *et al.* 2010. First detection of VHE $\gamma$-rays from SN 1006 by HESS. *Astron. Astrophys.*, **516**(June), A62.

Ackermann, M., Ajello, M., Allafort, A., *et al.* 2011. The Second Catalog of Active Galactic Nuclei Detected by the Fermi Large Area Telescope. *Astrophys. J.*, **743**(Dec.), 171.

Ackermann, M., Ajello, M., Atwood, W. B., *et al.* 2012a. Fermi-LAT Observations of the Diffuse $\gamma$-Ray Emission: Implications for Cosmic Rays and the Interstellar Medium. *Astrophys. J.*, **750**(May), 3.

Ackermann, M., Ajello, M., Albert, A., *et al.* 2012b. The Fermi Large Area Telescope on Orbit: Event Classification, Instrument Response Functions, and Calibration. *Astrophys. J., Sup.*, **203**(Nov.), 4.

Ackermann, M., Ajello, M., Allafort, A., *et al.* 2012c. The Imprint of the Extragalactic Background Light in the Gamma-Ray Spectra of Blazars. *Science*, **338**(Nov.), 1190–.

Ackermann, M., Ajello, M., Albert, A., *et al.* 2013. Search for Gamma-ray Spectral Lines with the Fermi Large Area Telescope and Dark Matter Implications.

Actis, M., Agnetta, G., Aharonian, F., *et al.* 2011. Design concepts for the Cherenkov Telescope Array CTA: an advanced facility for ground-based high-energy gamma-ray astronomy. *Experimental Astronomy*, **32**, 193–316.

Aharonian, F., Akhperjanian, A., Beilicke, M., *et al.* 2002a. Variations of the TeV energy spectrum at different flux levels of Mkn 421 observed with the HEGRA system of Cherenkov telescopes. *Astron. Astrophys.*, **393**(Oct.), 89–99.

Aharonian, F., Akhperjanian, A., Beilicke, M., *et al.* 2003a. Detection of TeV gamma-rays from the BL Lac 1ES 1959+650 in its low states and during a major outburst in 2002. *Astron. Astrophys.*, **406**(July), L9–L13.

Aharonian, F., Akhperjanian, A., Beilicke, M., *et al.* 2003b. Observations of H1426+428 with HEGRA. Observations in 2002 and reanalysis of 1999&2000 data. *Astron. Astrophys.*, **403**(May), 523–528.

Aharonian, F., Akhperjanian, A., Beilicke, M., *et al.* 2003c. Observations of H1426+428 with HEGRA. Observations in 2002 and reanalysis of 1999&2000 data. *Astron. Astrophys.*, **403**(May), 523–528.

Aharonian, F., Akhperjanian, A., Beilicke, M., *et al.* 2004. The Crab Nebula and Pulsar between 500 GeV and 80 TeV: Observations with the HEGRA Stereoscopic Air Cerenkov Telescopes. *Astrophys. J.*, **614**(Oct.), 897–913.

Aharonian, F., Akhperjanian, A. G., Bazer-Bachi, A. R., *et al.* 2005a. Detection of TeV $\gamma$-ray emission from the shell-type supernova remnant RX J0852.0-4622 with HESS. *Astron. Astrophys.*, **437**(July), L7–L10.

Aharonian, F., Akhperjanian, A. G., Aye, K.-M., *et al.* 2005b. Discovery of the binary pulsar PSR B1259-63 in very-high-energy gamma rays around periastron with HESS. *Astron. Astrophys.*, **442**(Oct.), 1–10.

Aharonian, F., Akhperjanian, A. G., Aye, K.-M., *et al.* 2005c. H.E.S.S. observations of PKS 2155-304. *Astron. Astrophys.*, **430**(Feb.), 865–875.

Aharonian, F., Akhperjanian, A. G., Bazer-Bachi, A. R., *et al.* 2005d. Multi-wavelength observations of PKS 2155-304 with HESS. *Astron. Astrophys.*, **442**(Nov.), 895–907.

Aharonian, F., Akhperjanian, A. G., Aye, K.-M., *et al.* 2005e. Very high energy gamma rays from the composite SNR G 0.9+0.1. *Astron. Astrophys.*, **432**(Mar.), L25–L29.

Aharonian, F., Akhperjanian, A. G., Bazer-Bachi, A. R., *et al.* 2006a. A low level of extragalactic background light as revealed by $\gamma$-rays from blazars. *Nature*, **440**(Apr.), 1018–1021.

Aharonian, F., Akhperjanian, A. G., Bazer-Bachi, A. R., *et al.* 2006b. Discovery of the two "wings" of the Kookaburra complex in VHE $\gamma$-rays with HESS. *Astron. Astrophys.*, **456**(Sept.), 245–251.

Aharonian, F., Akhperjanian, A. G., Bazer-Bachi, A. R., *et al.* 2006c. Discovery of very high energy $\gamma$-ray emission from the BL Lacertae object H 2356-309 with the HESS Cherenkov telescopes. *Astron. Astrophys.*, **455**(Aug.), 461–466.

Aharonian, F., Akhperjanian, A. G., Bazer-Bachi, A. R., *et al.* 2006d. Observations of the Crab nebula with HESS. *Astron. Astrophys.*, **457**(Oct.), 899–915.

Aharonian, F., Akhperjanian, A. G., Bazer-Bachi, A. R., *et al.* 2006e. The H.E.S.S. Survey of the Inner Galaxy in Very High Energy Gamma Rays. *Astrophys. J.*, **636**(Jan.), 777–797.

Aharonian, F., Akhperjanian, A. G., Bazer-Bachi, A. R., *et al.* 2007a. An Exceptional Very High Energy Gamma-Ray Flare of PKS 2155-304. *Astrophys. J., Lett.*, **664**(Aug.), L71–L74.

Aharonian, F., Akhperjanian, A. G., Bazer-Bachi, A. R., *et al.* 2007b. Detection of extended very-high-energy $\gamma$-ray emission towards the young stellar cluster Westerlund 2. *Astron. Astrophys.*, **467**(June), 1075–1080.

Aharonian, F., Akhperjanian, A. G., Bazer-Bachi, A. R., *et al.* 2007c. Detection of VHE gamma-ray emission from the distant blazar 1ES 1101-232 with HESS and broadband characterisation. *Astron. Astrophys.*, **470**(Aug.), 475–489.

Aharonian, F., Akhperjanian, A. G., Bazer-Bachi, A. R., *et al.* 2007d. Discovery of two candidate pulsar wind nebulae in very-high-energy gamma rays. *Astron. Astrophys.*, **472**(Sept.), 489–495.

Aharonian, F., Akhperjanian, A. G., Barres de Almeida, U., *et al.* 2007e. Discovery of VHE $\gamma$-rays from the distant BL Lacertae 1ES 0347-121. *Astron. Astrophys.*, **473**(Oct.), L25–L28.

Aharonian, F., Akhperjanian, A. G., Bazer-Bachi, A. R., *et al.* 2007f. H.E.S.S. Observations of the Supernova Remnant RX J0852.0-4622: Shell-Type Morphology and Spectrum of a Widely Extended Very High Energy Gamma-Ray Source. *Astrophys. J.*, **661**(May), 236–249.

Aharonian, F., Akhperjanian, A. G., Barres de Almeida, U., *et al.* 2007g. New constraints on the mid-IR EBL from the HESS discovery of VHE $\gamma$-rays from 1ES 0229+200. *Astron. Astrophys.*, **475**(Nov.), L9–L13.

Aharonian, F., Akhperjanian, A. G., Bazer-Bachi, A. R., *et al.* 2007h. Primary particle acceleration above 100 TeV in the shell-type supernova remnant <ASTROBJ>RX J1713.7-3946</ASTROBJ> with deep HESS observations. *Astron. Astrophys.*, **464**(Mar.), 235–243.

Aharonian, F., Akhperjanian, A. G., Barres de Almeida, U., *et al.* 2008a. Chandra and HESS observations of the supernova remnant CTB 37B. *Astron. Astrophys.*, **486**(Aug.), 829–836.

Aharonian, F., Akhperjanian, A. G., Barres de Almeida, U., *et al.* 2008b. Discovery of a VHE gamma-ray source coincident with the supernova remnant CTB 37A. *Astron. Astrophys.*, **490**(Nov.), 685–693.

Aharonian, F., Akhperjanian, A. G., Bazer-Bachi, A. R., *et al.* 2008c. Discovery of very high energy gamma-ray emission coincident with molecular clouds in the W 28 (G6.4-0.1) field. *Astron. Astrophys.*, **481**(Apr.), 401–410.

Aharonian, F., Akhperjanian, A. G., Barres de Almeida, U., *et al.* 2008d. Discovery of VHE $\gamma$-rays from the high-frequency-peaked BL Lacertae object RGB J0152+017. *Astron. Astrophys.*, **481**(Apr.), L103–L107.

Aharonian, F., Buckley, J., Kifune, T., & Sinnis, G. 2008e. High energy astrophysics with ground-based gamma ray detectors. *Reports on Progress in Physics*, **71**(9), 096901.

Aharonian, F., Akhperjanian, A. G., Anton, G., *et al.* 2009a. Detection of very high energy radiation from HESS J1908+063 confirms the Milagro unidentified source MGRO J1908+06. *Astron. Astrophys.*, **499**(June), 723–728.

Aharonian, F., Akhperjanian, A. G., de Almeida, U. B., *et al.* 2009b. Discovery of Gamma-Ray Emission From the Shell-Type Supernova Remnant RCW 86 With Hess. *Astrophys. J.*, **692**(Feb.), 1500–1505.

Aharonian, F., Akhperjanian, A. G., Anton, G., *et al.* 2009c. Simultaneous Observations of PKS 2155-304 with HESS, Fermi, RXTE, and Atom: Spectral Energy Distributions and Variability in a Low State. *Astrophys. J., Lett.*, **696**(May), L150–L155.

Aharonian, F., Akhperjanian, A. G., Anton, G., *et al.* 2009d. Spectrum and variability of the Galactic center VHE $\gamma$-ray source HESS J1745-290. *Astron. Astrophys.*, **503**(Sept.), 817–825.

Aharonian, F., Akhperjanian, A. G., Anton, G., *et al.* 2009e. Very high energy $\gamma$-ray observations of the binary PSR B1259-63/SS2883 around the 2007 Periastron. *Astron. Astrophys.*, **507**(Nov.), 389–396.

Aharonian, F., Essey, W., Kusenko, A., & Prosekin, A. 2013. TeV gamma rays from blazars beyond z=1? *Phys. Rev. D*, **87**(6), 063002.

Aharonian, F. A. 2000. TeV gamma rays from BL Lac objects due to synchrotron radiation of extremely high energy protons. *Nature*, **5**, 377–395.

Aharonian, F. A., Coppi, P. S., & Voelk, H. J. 1994. Very high energy gamma rays from active galactic nuclei: Cascading on the cosmic background radiation fields and the formation of pair halos. *Astrophys. J., Lett.*, **423**, L5–L8.

Aharonian, F. A., Akhperjanian, A. G., Andronache, M., *et al.* 1999a. Observations of MKN 421 during 1997 and 1998 in the energy range above 500 GeV with the HEGRA stereoscopic Cherenkov telescope system. *Astron. Astrophys.*, **350**(Oct.), 757–764.

Aharonian, F. A., Akhperjanian, A. G., Barrio, J. A., *et al.* 1999b. The time averaged TeV energy spectrum of MKN 501 of the extraordinary 1997 outburst as measured with the stereoscopic Cherenkov telescope system of HEGRA. *Astron. Astrophys.*, **349**(Sept.), 11–28.

Aharonian, F. A., Timokhin, A. N., & Plyasheshnikov, A. V. 2002b. On the origin of highest energy gamma-rays from Mkn 501. *Astron. Astrophys.*, **384**, 834–847.

Aharonian, F. A., Khangulyan, D., & Costamante, L. 2008f. Formation of hard very high energy gamma-ray spectra of blazars due to internal photon-photon absorption. *Mon. Not. R. Astron. Soc.*, **387**, 1206–1214.

Ahlers, M., Gies, H., Jaeckel, J., Redondo, J., & Ringwald, A. 2007. Light from the hidden sector: Experimental signatures of paraphotons. *Phys. Rev. D*, **76**(11), 115005.

Albert, J., Aliu, E., Anderhub, H., *et al.* 2006a. Discovery of Very High Energy Gamma Rays from 1ES 1218+30.4. *Astrophys. J., Lett.*, **642**(May), L119–L122.

Albert, J., Aliu, E., Anderhub, H., *et al.* 2006b. Discovery of Very High Energy $\gamma$-Rays from Markarian 180 Triggered by an Optical Outburst. *Astrophys. J., Lett.*, **648**(Sept.), L105–L108.

Albert, J., Aliu, E., Anderhub, H., *et al.* 2006c. MAGIC Observations of Very High Energy $\gamma$-Rays from HESS J1813-178. *Astrophys. J., Lett.*, **637**(Jan.), L41–L44.

Albert, J., Aliu, E., Anderhub, H., *et al.* 2006d. Observation of Gamma Rays from the Galactic Center with the MAGIC Telescope. *Astrophys. J., Lett.*, **638**(Feb.), L101–L104.

Albert, J., Aliu, E., Anderhub, H., *et al.* 2006e. Observation of Very High Energy Gamma-Ray Emission from the Active Galactic Nucleus 1ES 1959+650 Using the MAGIC Telescope. *Astrophys. J.*, **639**(Mar.), 761–765.

Albert, J., Aliu, E., Anderhub, H., *et al.* 2006f. Observation of VHE Gamma Radiation from HESS J1834-087/W41 with the MAGIC Telescope. *Astrophys. J., Lett.*, **643**(May), L53–L56.

Albert, J., Aliu, E., Anderhub, H., *et al.* 2006g. Variable Very-High-Energy Gamma-Ray Emission from the Microquasar LS I +61 303. *Science*, **312**(June), 1771–1773.

Albert, J., Aliu, E., Anderhub, H., *et al.* 2007a. Discovery of Very High Energy $\gamma$-Ray Emission from the Low-Frequency-peaked BL Lacertae Object BL Lacertae. *Astrophys. J., Lett.*, **666**(Sept.), L17–L20.

Albert, J., Aliu, E., Anderhub, H., *et al.* 2007b. Discovery of Very High Energy $\gamma$-Rays from 1ES 1011+496 at z = 0.212. *Astrophys. J., Lett.*, **667**(Sept.), L21–L24.

Albert, J., Aliu, E., Anderhub, H., *et al.* 2007c. Observation of Very High Energy $\gamma$-Rays from the AGN 1ES 2344+514 in a Low Emission State with the MAGIC Telescope. *Astrophys. J.*, **662**(June), 892–899.

Albert, J., Aliu, E., Anderhub, H., *et al.* 2007d. Observations of Markarian 421 with the MAGIC Telescope. *Astrophys. J.*, **663**(July), 125–138.

Albert, J., Aliu, E., Anderhub, H., *et al.* 2008a. Multiwavelength (Radio, X-Ray, and $\gamma$-Ray) Observations of the $\gamma$-Ray Binary LS I +61 303. *Astrophys. J.*, **684**(Sept.), 1351–1358.

Albert, J., Aliu, E. Anderhub, H., *et al.* 2008b. Very-High-Energy gamma rays from a Distant Quasar: How Transparent Is the Universe? *Science*, **320**(June), 1752–.

Albert, J., Aliu, E., Anderhub, H., *et al.* 2008c. VHE $\gamma$-Ray Observation of the Crab Nebula and its Pulsar with the MAGIC Telescope. *Astrophys. J.*, **674**(Feb.), 1037–1055.

Albert, J., Aliu, E., Anderhub, H., *et al.* 2009. Periodic Very High Energy $\gamma$-Ray Emission from LS I +61degree303 Observed with the MAGIC Telescope. *Astrophys. J.*, **693**(Mar.), 303–310.

Aleksić, J., Anderhub, H., Antonelli, L. A., *et al.* 2010. MAGIC TeV gamma-ray observations of Markarian 421 during multiwavelength campaigns in 2006. *Astron. Astrophys.*, **519**(Sept.), A32+.

Aleksić, J., Antonelli, L. A., Antoranz, P., *et al.* 2011a. MAGIC Discovery of Very High Energy Emission from the FSRQ PKS 1222+21. *Astrophys. J., Lett.*, **730**(Mar.), L8+.

Aleksić, J., Antonelli, L. A., Antoranz, P., *et al.* 2011b. MAGIC Observations and multiwavelength properties of the quasar 3C 279 in 2007 and 2009. *Astron. Astrophys.*, **530**(June), A4.

Aleksić, J., Alvarez, E. A., Antonelli, L. A., *et al.* 2012. Discovery of VHE $\gamma$-ray emission from the BL Lacertae object B3 2247+381 with the MAGIC telescopes. *Astron. Astrophys.*, **539**(Mar.), A118.

Aliu, E., Anderhub, H., Antonelli, L. A., *et al.* 2009. Discovery of a Very High Energy Gamma-Ray Signal from the 3C 66A/B Region. *Astrophys. J., Lett.*, **692**(Feb.), L29–L33.

Aliu, E., Aune, T., Beilicke, M., *et al.* 2011. Multiwavelength Observations of the Previously Unidentified Blazar RX J0648.7+1516. *Astrophys. J.*, **742**(Dec.), 127.

Aliu, E., Archambault, S., Arlen, T., *et al.* 2012a. Discovery of High-energy and Very High Energy $\gamma$-Ray Emission from the Blazar RBS 0413. *Astrophys. J.*, **750**(May), 94.

Aliu, E., Archambault, S., Arlen, T., *et al.* 2012b. Multiwavelength Observations of the AGN 1ES 0414+009 with VERITAS, Fermi-LAT, Swift-XRT, and MDM. *Astrophys. J.*, **755**(Aug.), 118.

Amelino-Camelia, G., & Ahluwalia, D. V. 2002. Relativity in Spacetimes with Short-Distance Structure Governed by an Observer-Independent (Planckian) Length Scale. *International Journal of Modern Physics D*, **11**, 35–59.

Amelino-Camelia, G., Ellis, J., Mavromatos, N. E., Nanopoulos, D. V., & Sarkar, S. 1998. Tests of quantum gravity from observations of $\gamma$-ray bursts. *Nature*, **393**(June), 763–765.

An, H., Pospelov, M., & Pradler, J. 2013a. Dark Matter Detectors as Dark Photon Helioscopes. *ArXiv e-prints*, Apr.

An, H., Pospelov, M., & Pradler, J. 2013b. New stellar constraints on dark photons. *ArXiv e-prints*, Feb.

Anderhub, H., Antonelli, L. A., Antoranz, P., *et al.* 2009a. Correlated X-Ray and Very High Energy Emission in the Gamma-Ray Binary LS I +61 303. *Astrophys. J., Lett.*, **706**(Nov.), L27–L32.

Anderhub, H., Antonelli, L. A., Antoranz, P., *et al.* 2009b. Simultaneous Multiwavelength Observation of Mkn 501 in a Low State in 2006. *Astrophys. J.*, **705**(Nov.), 1624–1631.

Anderson, T. W., & Darling, D. A. 1954. A Test of Goodness-of-Fit. *Journal of the American Statistical Association*, **49**, 765–769.

Andriamonje, S., Aune, S., Autiero, D., CAST Collaboration, *et al.* 2007. An improved limit on the axion photon coupling from the CAST experiment. *JCAP*, **4**, 10.

Arias, P., Cadamuro, D., Goodsell, M., *et al.* 2012. WISPy cold dark matter. *JCAP*, **6**(June), 13.

Asano, K., & Inoue, S. 2007. Prompt GeV-TeV Emission of Gamma-Ray Bursts Due to High-Energy Protons, Muons and Electron-Positron Pairs. *Astrophys.J.*, **671**, 645–655.

Atwood, W., Albert, A., Baldini, L., *et al.* 2013. Pass 8: Toward the Full Realization of the Fermi-LAT Scientific Potential. *ArXiv e-prints*, Mar.

Atwood, W. B., Abdo, A. A., Ackermann, M., *et al.* 2009. The Large Area Telescope on the Fermi Gamma-Ray Space Telescope Mission. *Astrophys. J.*, **697**, 1071–1102.

Bähre, R., Döbrich, B., Dreyling-Eschweiler, J., *et al.* 2013. Any Light Particle Search II – Technical Design Report. *ArXiv e-prints*, Feb.

Baixeras, C., Bastieri, D., Bigongiari, C., *et al.* 2004. Commissioning and first tests of the MAGIC telescope. *Nuclear Instruments and Methods in Physics Research A*, **518**(Feb.), 188–192.

Barnes, J. E., & Hernquist, L. E. 1991. Fueling starburst galaxies with gas-rich mergers. *Astrophys. J., Lett.*, **370**(Apr.), L65–L68.

Becherini, Y., Boisson, C., Cerruti, M., & H. E. S. S. Collaboration. 2012a (Dec.). Discovery of VHE $\gamma$-ray emission from the very distant BL Lac KUV 00311-1938 by H.E.S.S. *Pages 490–493 of:* Aharonian, F. A., Hofmann, W., & Rieger, F. M. (eds), *American Institute of Physics Conference Series*. American Institute of Physics Conference Series, vol. 1505.

Becherini, Y., Punch, M., & H. E. S. S. Collaboration. 2012b (Dec.). Performance of HESS-II in multi-telescope mode with a multi-variate analysis. *Pages 741–744 of:* Aharonian, F. A., Hofmann, W., & Rieger, F. M. (eds), *American Institute of Physics Conference Series*. American Institute of Physics Conference Series, vol. 1505.

Begelman, M. C., Blandford, R. D., & Rees, M. J. 1984. Theory of extragalactic radio sources. *Reviews of Modern Physics*, **56**(Apr.), 255–351.

Benbow, W. 2005 (Feb.). The Status and Performance of H.E.S.S. *Pages 611–616 of:* Aharonian, F. A., Völk, H. J., & Horns, D. (eds), *High Energy Gamma-Ray Astronomy*. American Institute of Physics Conference Series, vol. 745.

Berezinsky, V., Gazizov, A. Z., & Grigorieva, S. I. 2002. Signatures of AGN model for UHECR. *ArXiv Astrophysics e-prints*, Oct.

Berezinsky, V., Gazizov, A., & Grigorieva, S. 2006. On astrophysical solution to ultrahigh energy cosmic rays. *Phys. Rev. D*, **74**(4), 043005.

Beringer, J., Arguin, J.-F., Barnett, R. M., *et al.* 2012. Review of Particle Physics. *Phys. Rev. D*, **86**(1), 010001.

Bertone, G., Hooper, D., & Silk, J. 2005. Particle dark matter: evidence, candidates and constraints. *physical report*, **405**(Jan.), 279–390.

Biermann, L. 1950. Über den Ursprung der Magnetfelder auf Sternen und im interstellaren Raum (miteinem Anhang von A. Schlüter). *Zeitschrift Naturforschung Teil A*, **5**, 65.

Blandford, R. D., & Levinson, A. 1995. Pair cascades in extragalactic jets. 1: Gamma rays. *Astrophys.J.*, **441**, 79–95.

Blandford, R. D., & Payne, D. G. 1982. Hydromagnetic flows from accretion discs and the production of radio jets. *Mon. Not. R. Astron. Soc.*, **199**(June), 883–903.

Blandford, R. D., & Znajek, R. L. 1977. Electromagnetic extraction of energy from Kerr black holes. *Mon. Not. R. Astron. Soc.*, **179**(May), 433–456.

Blasi, P., Burles, S., & Olinto, A. V. 1999. Cosmological Magnetic Field Limits in an Inhomogeneous Universe. *Astrophys. J., Lett.*, **514**, L79–L82.

Błażejowski, M., Sikora, M., Moderski, R., & Madejski, G. M. 2000. Comptonization of Infrared Radiation from Hot Dust by Relativistic Jets in Quasars. *Astrophys. J.*, **545**(Dec.), 107–116.

Bloom, S. D., & Marscher, A. P. 1996. An Analysis of the Synchrotron Self-Compton Model for the Multi–Wave Band Spectra of Blazars. *Astrophys. J.*, **461**, 657–+.

Blumenthal, G. R., & Gould, R. J. 1970. Bremsstrahlung, Synchrotron Radiation, and Compton Scattering of High-Energy Electrons Traversing Dilute Gases. *Reviews of Modern Physics*, **42**, 237–271.

Bonnoli, G., Ghisellini, G., Foschini, L., *et al.* 2011. The $\gamma$-ray brightest days of the blazar 3C 454.3. *Mon. Not. R. Astron. Soc.*, **410**, 368–380.

Böttcher, M. 2010. Models for the Spectral Energy Distributions and Variability of Blazars. *ArXiv e-prints*, June.

Böttcher, M., Dermer, C. D., & Finke, J. D. 2008. The Hard VHE $\gamma$-Ray Emission in High-Redshift TeV Blazars: Comptonization of Cosmic Microwave Background Radiation in an Extended Jet? *Astrophys. J., Lett.*, **679**(May), L9–L12.

Brandt, S. 1999. *Data analysis : statistical and computational methods for scientists and engineers*.

Bregeon, J., Charles, E., & Wood, M. 2013. Fermi-LAT data reprocessed with updated calibration constants. *ArXiv e-prints*, Apr.

Brockway, J. W., Carlson, E. D., & Raffelt, G. G. 1996. SN 1987A gamma-ray limits on the conversion of pseudoscalars. *Physics Letters B*, **383**, 439–443.

Broderick, A. E., Chang, P., & Pfrommer, C. 2012. The Cosmological Impact of Luminous TeV Blazars. I. Implications of Plasma Instabilities for the Intergalactic Magnetic Field and Extragalactic Gamma-Ray Background. *Astrophys. J.*, **752**(June), 22.

Cadamuro, D., & Redondo, J. 2012. Cosmological bounds on pseudo Nambu-Goldstone bosons. *JCAP*, **2**(Feb.), 32.

Celik, O. 2008. Observations of the Crab Nebula and Pulsar with VERITAS. *Pages 847–850 of: International Cosmic Ray Conference*. International Cosmic Ray Conference, vol. 2.

Celotti, A., & Fabian, A. C. 1993. The Kinetic Power and Luminosity of Parsecscale Radio Jets - an Argument for Heavy Jets. *Mon. Not. R. Astron. Soc.*, **264**, 228.

Chelouche, D., Koester, B. P., & Bowen, D. V. 2007. The Dust Content of Galaxy Clusters. *Astrophys. J., Lett.*, **671**, L97–L100.

Cicoli, M., Goodsell, M. D., & Ringwald, A. 2012. The type IIB string axiverse and its low-energy phenomenology. *Journal of High Energy Physics*, **10**, 146.

Cleveland, W. S. 1979. Robust Locally Weighted Regression and Smoothing Scatterplots. *Journal of the American Statistical Association*, **74**(368), 829–836.

Coleman, S., & Glashow, S. L. 1999. High-energy tests of Lorentz invariance. *Phys. Rev. D*, **59**(11), 116008.

Colladay, D., & Kostelecký, V. A. 1998. Lorentz-violating extension of the standard model. *Phys. Rev. D*, **58**(11), 116002.

Cordes, J. M., & Lazio, T. J. W. 2002. NE2001.I. A New Model for the Galactic Distribution of Free Electrons and its Fluctuations. *ArXiv Astrophysics e-prints*.

Csáki, C., Kaloper, N., Peloso, M., & Terning, J. 2003. Super-GZK photons from photon axion mixing. *JCAP*, **5**(May), 5.

Cucchiara, A., Levan, A.J., Fox, D.B., *et al.* 2011. A Photometric Redshift of z $\sim$ 9.4 for GRB 090429B. *Astrophys.J.*, **736**, 7.

Curtis, H. D. 1918. Descriptions of 762 Nebulae and Clusters Photographed with the Crossley Reflector. *Publications of Lick Observatory*, **13**, 9–42.

Dai, Z. G., Zhang, B., Gou, L. J., Mészáros, P., & Waxman, E. 2002. GeV Emission from TeV Blazars and Intergalactic Magnetic Fields. *Astrophys. J., Lett.*, **580**, L7–L10.

Davies, J. M., & Cotton, E. S. 1957. Design of the quartermaster solar furnance. *J. Solar Energy Sci. Eng.*, **1**, 16–21.

de Angelis, A., Roncadelli, M., & Mansutti, O. 2007. Evidence for a new light spin-zero boson from cosmological gamma-ray propagation? *Phys. Rev. D*, **76**(12), 121301.

De Angelis, A., Mansutti, O., Persic, M., & Roncadelli, M. 2009. Photon propagation and the very high energy $\gamma$-ray spectra of blazars: how transparent is the Universe? *Mon. Not. R. Astron. Soc.*, **394**, L21–L25.

de Angelis, A., Galanti, G., & Roncadelli, M. 2011. Relevance of axionlike particles for very-high-energy astrophysics. *Phys. Rev. D*, **84**(10), 105030.

de Boor, C. 1978. *A practical guide to splines*.

Dermer, C. D., & Menon, G. 2009. *High Energy Radiation from Black Holes: Gamma Rays, Cosmic Rays, and Neutrinos*.

Dermer, C. D., & Schlickeiser, R. 1993. Model for the High-Energy Emission from Blazars. *Astrophys. J.*, **416**(Oct.), 458.

Dermer, C. D., Schlickeiser, R., & Mastichiadis, A. 1992. High-energy gamma radiation from extragalactic radio sources. *Astron. Astrophys.*, **256**(Mar.), L27–L30.

Dermer, C. D., Sturner, S. J., & Schlickeiser, R. 1997. Nonthermal Compton and Synchrotron Processes in the Jets of Active Galactic Nuclei. *Astrophys. J., Sup.*, **109**, 103–+.

Dermer, C. D., Cavadini, M., Razzaque, S., *et al.* 2011. Time Delay of Cascade Radiation for TeV Blazars and the Measurement of the Intergalactic Magnetic Field. *Astrophys. J., Lett.*, **733**, L21+.

Di Matteo, T., Springel, V., & Hernquist, L. 2005. Energy input from quasars regulates the growth and activity of black holes and their host galaxies. *Nature*, **433**(Feb.), 604–607.

Dine, M., & Fischler, W. 1983. The not-so-harmless axion. *Physics Letters B*, **120**(Jan.), 137–141.

Djannati-Atai , A., Piron, F., Barrau, A., *et al.* 1999. Very High Energy Gamma-ray spectral properties of MKN 501 from CAT Čerenkov telescope observations in 1997. *Astron. Astrophys.*, **350**(Oct.), 17–24.

Dolag, K., Grasso, D., Springel, V., & Tkachev, I. 2005. Constrained simulations of the magnetic field in the local Universe and the propagation of ultrahigh energy cosmic rays. *JCAP*, **1**, 9.

Dolag, K., Kachelriess, M., Ostapchenko, S., & Tomàs, R. 2009. Blazar Halos as Probe for Extragalactic Magnetic Fields and Maximal Acceleration Energy. *Astrophys. J.*, **703**, 1078–1085.

Dolag, K., Kachelriess, M., Ostapchenko, S., & Tomàs, R. 2011. Lower Limit on the Strength and Filling Factor of Extragalactic Magnetic Fields. *Astrophys. J., Lett.*, **727**, L4+.

Domínguez, A., Primack, J. R., Rosario, D. J., *et al.* 2011. Extragalactic background light inferred from AEGIS galaxy-SED-type fractions. *Mon. Not. R. Astron. Soc.*, **410**, 2556–2578.

Dondi, L., & Ghisellini, G. 1995. Gamma-ray-loud blazars and beaming. *Mon. Not. R. Astron. Soc.*, **273**(Apr.), 583–595.

Donnert, J., Dolag, K., Lesch, H., & Müller, E. 2009. Cluster magnetic fields from galactic outflows. *Mon. Not. R. Astron. Soc.*, **392**, 1008–1021.

Doro, M., Conrad, J., Emmanoulopoulos, D., *et al.* 2013. Dark matter and fundamental physics with the Cherenkov Telescope Array. *Astroparticle Physics*, **43**(Mar.), 189–214.

Dwek, E., & Barker, M. K. 2002. The Cosmic Radio and Infrared Backgrounds Connection. *Astrophys. J.*, **575**(Aug.), 7–11.

Dwek, E., & Krennrich, F. 2005. Simultaneous Constraints on the Spectrum of the Extragalactic Background Light and the Intrinsic TeV Spectra of Markarian 421, Markarian 501, and H1426+428. *Astrophys. J.*, **618**, 657–674.

Dwek, E., & Krennrich, F. 2013. The extragalactic background light and the gamma-ray opacity of the universe. *Astroparticle Physics*, **43**(Mar.), 112–133.

Dwek, E., Arendt, R. G., & Krennrich, F. 2005. The Near-Infrared Background: Interplanetary Dust or Primordial Stars? *Astrophys. J.*, **635**, 784–794.

Ehret, K., Frede, M., Ghazaryan, S., *et al.* 2009. Resonant laser power build-up in ALPS–A light shining through a wall experiment. *Nuclear Instruments and Methods in Physics Research A*, **612**(Dec.), 83–96.

Ehret, K., Frede, M., Ghazaryan, S., *et al.* 2010. New ALPS results on hidden-sector lightweights. *Physics Letters B*, **689**(May), 149–155.

Ellis, J., & Mavromatos, N. E. 2013. Probes of Lorentz violation. *Astroparticle Physics*, **43**(Mar.), 50–55.

Ellis, J., Mavromatos, N. E., & Nanopoulos, D. V. 2000. Quantum-Gravitational Diffusion and Stochastic Fluctuations in the Velocity of Light. *General Relativity and Gravitation*, **32**(Jan.), 127–144.

Elyiv, A., Neronov, A., & Semikoz, D. V. 2009. Gamma-ray induced cascades and magnetic fields in the intergalactic medium. *Phys. Rev. D*, **80**(2), 023010–+.

Essey, W., & Kusenko, A. 2010. A new interpretation of the gamma-ray observations of distant active galactic nuclei. *Astroparticle Physics*, **33**, 81–85.

Essey, W., & Kusenko, A. 2012. On Weak Redshift Dependence of Gamma-Ray Spectra of Distant Blazars. *Astrophys. J., Lett.*, **751**(May), L11.

Essey, W., Kalashev, O. E., Kusenko, A., & Beacom, J. F. 2010. Secondary Photons and Neutrinos from Cosmic Rays Produced by Distant Blazars. *Physical Review Letters*, **104**(14), 141102–+.

Essey, W., Kalashev, O., Kusenko, A., & Beacom, J. F. 2011. Role of Line-of-sight Cosmic-ray Interactions in Forming the Spectra of Distant Blazars in TeV Gamma Rays and High-energy Neutrinos. *Astrophys. J.*, **731**, 51–+.

Everett, J. E., Zweibel, E. G., Benjamin, R. A., *et al.* 2008. The Milky Way's Kiloparsec-Scale Wind: A Hybrid Cosmic-Ray and Thermally Driven Outflow. *Astrophys. J.*, **674**, 258–270.

Fanaroff, B. L., & Riley, J. M. 1974. The morphology of extragalactic radio sources of high and low luminosity. *Mon. Not. R. Astron. Soc.*, **167**(May), 31P–36P.

Fath, E. A. 1909. The spectra of some spiral nebulae and globular star clusters. *Lick Observatory Bulletin*, **5**, 71–77.

Fazio, G. G., & Stecker, F. W. 1970. Predicted High Energy Break in the Isotropic Gamma Ray Spectrum: a Test of Cosmological Origin. *Nature*, **226**(Apr.), 135–136.

Fazio, G. G., Ashby, M. L. N., *et al.* 2004. Number Counts at 3 $\mu$m $< \lambda <$ 10 $\mu$m from the Spitzer Space Telescope. *Astrophys. J., Sup.*, **154**, 39–43.

Feretti, L., Giovannini, G., Govoni, F., & Murgia, M. 2012. Clusters of galaxies: observational properties of the diffuse radio emission. *Astron. Astrophys. Review*, **20**, 54.

Fermi, E. 1949. On the Origin of the Cosmic Radiation. *Physical Review*, **75**(Apr.), 1169–1174.

Fichtel, C. E., Hartman, R. C., Kniffen, D. A., *et al.* 1975. High-energy gamma-ray results from the second small astronomy satellite. *Astrophys. J.*, **198**(May), 163–182.

Finke, J. D. 2013. Compton Dominance and the Blazar Sequence. *Astrophys. J.*, **763**(Feb.), 134.

Finke, J. D., Razzaque, S., & Dermer, C. D. 2010. Modeling the Extragalactic Background Light from Stars and Dust. *Astrophys. J.*, **712**(Mar.), 238–249.

Fisher, R. A. 1925. Theory of Statistical Estimation. *Proceedings of the Cambridge Philosophical Society*, **22**, 700.

Fixsen, D. J., Cheng, E. S., Gales, J. M., Mather, J. C., Shafer, R. A., & Wright, E. L. 1996. The Cosmic Microwave Background Spectrum from the Full COBE FIRAS Data Set. *Astrophys. J.*, **473**(Dec.), 576.

Fortson, L., VERITAS Collaboration, & Fermi-LAT Collaborators. 2012 (Dec.). Results from VERITAS observations on the giant flare from Mrk 421 in February 2010. *Pages 514–517 of:* Aharonian, F. A., Hofmann, W., & Rieger, F. M. (eds), *American Institute of Physics Conference Series*. American Institute of Physics Conference Series, vol. 1505.

Fossati, G., Maraschi, L., Celotti, A., *et al.* 1998. A unifying view of the spectral energy distributions of blazars. *Mon. Not. R. Astron. Soc.*, **299**(Sept.), 433–448.

Franceschini, A., Elbaz, D., Fadda, D., & Cesarsky, C. J. 2002. The AGN Contribution to the Cosmic Infrared Background: Steps towards Measuring the Gravitational vs. Stellar Global Energy Budget. *Page 229 of:* Maiolino, R., Marconi, A., & Nagar, N. (eds), *Issues in Unification of Active Galactic Nuclei*. Astronomical Society of the Pacific Conference Series, vol. 258.

Franceschini, A., Rodighiero, G., & Vaccari, M. 2008. Extragalactic optical-infrared background radiation, its time evolution and the cosmic photon-photon opacity. *Astron. Astrophys.*, **487**, 837–852.

Furniss, A., Williams, D. A., Danforth, C., *et al.* 2013. The Firm Redshift Lower Limit of the Most Distant TeV-detected Blazar PKS 1424+240. *Astrophys. J., Lett.*, **768**(May), L31.

Galaverni, M., & Sigl, G. 2008. Lorentz Violation for Photons and Ultrahigh-Energy Cosmic Rays. *Physical Review Letters*, **100**(2), 021102.

Gall, D., & for the VERITAS Collaboration. 2009. Multi-wavelength Observations of Markarian 501. *ArXiv e-prints*, Dec.

Gambini, R., & Pullin, J. 1999. Nonstandard optics from quantum space-time. *Phys. Rev. D*, **59**(12), 124021.

Gardner, J. P., Mather, J. C., Clampin, M., *et al.* 2006. The James Webb Space Telescope. *Space Science Reviews*, **123**(Apr.), 485–606.

Georganopoulos, M., & Kazanas, D. 2003. Decelerating flows in TeV blazars: a resolution to the bl lac - fr I unification problem. *Astrophys.J.*, **594**, L27–L30.

Georganopoulos, M., Sambruna, R. M., Kazanas, D., Cillis, A. N., Cheung, C. C., Perlman, E. S., Blundell, K. M., & Davis, D. S. 2008. A Novel Method for Measuring the Extragalactic Background Light: Fermi Application to the Lobes of Fornax A. *Astrophys. J., Lett.*, **686**, L5–L8.

Georganopoulos, M., Finke, J. D., & Reyes, L. C. 2010. A Method for Setting Upper Limits to the Extragalactic Background Light with Fermi-lat and TeV Observations of Blazars. *Astrophys. J., Lett.*, **714**, L157–L161.

Ghisellini, G. 2011 (Sept.). Extragalactic relativistic jets. *Pages 180–198 of:* Aharonian, F. A., Hofmann, W., & Rieger, F. M. (eds), *American Institute of Physics Conference Series*. American Institute of Physics Conference Series, vol. 1381.

Ghisellini, G., & Madau, P. 1996. On the origin of the gamma-ray emission in blazars. *Mon.Not.Roy.Astron.Soc.*, **280**, 67–76.

Ghisellini, G., & Tavecchio, F. 2008. Rapid variability in TeV blazars: the case of PKS2155-304. *Mon. Not. R. Astron. Soc.*, **386**(May), L28–L32.

Giacconi, R., Kellogg, E., Gorenstein, P., *et al.* 1971. An X-Ray Scan of the Galactic Plane from UHURU. *Astrophys. J., Lett.*, **165**(Apr.), L27.

Gill, R., & Heyl, J. S. 2011. Constraining the photon-axion coupling constant with magnetic white dwarfs. *Phys. Rev. D*, **84**(8), 085001.

Gilmore, R. C., Somerville, R. S., Primack, J. R., & Domínguez, A. 2012. Semi-analytic modelling of the extragalactic background light and consequences for extragalactic gamma-ray spectra. *Mon. Not. R. Astron. Soc.*, **422**(June), 3189–3207.

Giommi, P., Padovani, P., Polenta, G., *et al.* 2012. A simplified view of blazars: clearing the fog around long-standing selection effects. *Mon. Not. R. Astron. Soc.*, **420**(Mar.), 2899–2911.

Giunti, C., & Kim, C. W. 1998. Coherence of neutrino oscillations in the wave packet approach. *Phys. Rev. D*, **58**(1), 017301.

Goldhaber, A. S., & Nieto, M. M. 1971. Terrestrial and Extraterrestrial Limits on The Photon Mass. *Reviews of Modern Physics*, **43**(July), 277–296.

Gondolo, P., & Raffelt, G. G. 2009. Solar neutrino limit on axions and keV-mass bosons. *Phys. Rev. D*, **79**(10), 107301.

Goodsell, M., Jaeckel, J., Redondo, J., & Ringwald, A. 2009. Naturally light hidden photons in LARGE volume string compactifications. *Journal of High Energy Physics*, **11**(Nov.), 27.

Górski, K. M., Hivon, E., Banday, A. J., Wandelt, B. D., Hansen, F. K., Reinecke, M., & Bartelmann, M. 2005. HEALPix: A Framework for High-Resolution Discretization and Fast Analysis of Data Distributed on the Sphere. *Astrophys. J.*, **622**(Apr.), 759–771.

Gould, R. J., & Schréder, G. 1966. Opacity of the Universe to High-Energy Photons. *Physical Review Letters*, **16**, 252–254.

Gould, R. J., & Schréder, G. P. 1967. Opacity of the Universe to High-Energy Photons. *Physical Review*, **155**(Mar.), 1408–1411.

Govoni, F., & Feretti, L. 2004. Magnetic Fields in Clusters of Galaxies. *International Journal of Modern Physics D*, **13**, 1549–1594.

Greisen, K. 1966. End to the Cosmic-Ray Spectrum? *Physical Review Letters*, **16**(Apr.), 748–750.

Grifols, J. A., Massó, E., & Toldrà, R. 1996. Gamma Rays from SN 1987A due to Pseudoscalar Conversion. *Physical Review Letters*, **77**, 2372–2375.

Guy, J., Renault, C., Aharonian, F. A., Rivoal, M., & Tavernet, J.-P. 2000. Constraints on the cosmic infra-red background based on BeppoSAX and CAT spectra of Markarian 501. *Astron. Astrophys.*, **359**, 419–428.

H. E. S. S. collaboration : F. Aharonian, Akhperjanian, A. G., Anton, G., *et al.* 2010. Discovery of VHE gamma-rays from the BL Lac object PKS 0548-322. *ArXiv e-prints*, June.

Han, J. L., Ferriere, K., & Manchester, R. N. 2004. The Spatial Energy Spectrum of Magnetic Fields in Our Galaxy. *Astrophys. J.*, **610**(Aug.), 820–826.

Hartman, R. C., Bertsch, D. L., Bloom, S. D., *et al.* 1999. The Third EGRET Catalog of High-Energy Gamma-Ray Sources. *Astrophys. J., Sup.*, **123**(July), 79–202.

Hauser, M. G., & Dwek, E. 2001. The Cosmic Infrared Background: Measurements and Implications. *Ann. Rev. Astron. Astrophys.*, **39**, 249–307.

Hauser, M. G., Arendt, R. G., *et al.* 1998. The COBE Diffuse Infrared Background Experiment Search for the Cosmic Infrared Background. I. Limits and Detections. *Astrophys. J.*, **508**, 25–43.

Heitler, W. 1954. *Quantum theory of radiation*.

Helou, G., Soifer, B. T., & Rowan-Robinson, M. 1985. Thermal infrared and nonthermal radio - Remarkable correlation in disks of galaxies. *Astrophys. J., Lett.*, **298**(Nov.), L7–L11.

Hermsen, W., Swanenburg, B. N., Bignami, G. F., *et al.* 1977. New high energy gamma-ray sources observed by COS B. *Nature*, **269**(Oct.), 494.

Hess, V. F. 1912. Über Beobachtungen der durchdringenden Strahlung bei sieben Freiballonfahrten. *Phys. Zeitschr.*, **13**, 1084.

HESS Collaboration, Abramowski, A., Acero, F., Aharonian, F., *et al.* 2010a. Multi-wavelength observations of H 2356-309. *Astron. Astrophys.*, **516**(June), A56+.

HESS Collaboration, Acero, F., Aharonian, F., Akhperjanian, A. G., *et al.* 2010b. PKS 2005-489 at VHE: four years of monitoring with HESS and simultaneous multi-wavelength observations. *Astron. Astrophys.*, **511**(Feb.), A52+.

H.E.S.S. Collaboration, Abramowski, A., Acero, F., *et al.* 2011a. Detection of very-high-energy $\gamma$-ray emission from the vicinity of PSR B1706-44 and G 343.1-2.3 with H.E.S.S. *Astron. Astrophys.*, **528**(Apr.), A143.

H.E.S.S. Collaboration, Abramowski, A., Acero, F., Aharonian, F., *et al.* 2011b. Revisiting the Westerlund 2 field with the HESS telescope array. *Astron. Astrophys.*, **525**(Jan.), A46.

H.E.S.S. Collaboration, Abramowski, A., Acero, F., Aharonian, F., *et al.* 2012. Discovery of hard-spectrum $\gamma$-ray emission from the BL Lacertae object 1ES 0414+009. *Astron. Astrophys.*, **538**(Feb.), A103.

H.E.S.S. Collaboration, Abramowski, A., Acero, F., Aharonian, F., *et al.* 2013. Measurement of the extragalactic background light imprint on the spectra of the brightest blazars observed with H.E.S.S. *Astron. Astrophys.*, **550**(Feb.), A4.

Hewett, J. L., Weerts, H., Brock, R., Butler, J. N., Casey, B. C. K., Collar, J., de Gouvea, A., Essig, R., Grossman, Y., Haxton, W., & et al. 2012. Fundamental Physics at the Intensity Frontier, Fig. 6-1. *ArXiv e-prints*.

Hillas, A. M. 1985 (Aug.). Cerenkov light images of EAS produced by primary gamma. *Pages 445–448 of:* Jones, F. C. (ed), *International Cosmic Ray Conference*. International Cosmic Ray Conference, vol. 3.

Hinton, J. A. 2004. The status of the HESS project. *New Astronomy Reviews*, **48**(Apr.), 331–337.

Hinton, J. A., & Hofmann, W. 2009. Teraelectronvolt astronomy. *Ann.Rev.Astron.Astrophys.*, **47**, 523–565.

Hochmuth, K. A., & Sigl, G. 2007. Effects of axion-photon mixing on gamma-ray spectra from magnetized astrophysical sources. *Phys. Rev. D*, **76**(12), 123011.

Hofmann, W., Jung, I., Konopelko, A., *et al.* 1999. Comparison of techniques to reconstruct VHE gamma-ray showers from multiple stereoscopic Cherenkov images. *Astroparticle Physics*, **12**(Nov.), 135–143.

Holdom, B. 1986. Heavy quarks and electroweak symmetry breaking. *Physical Review Letters*, **57**(Nov.), 2496–2499.

Hooper, D., & Profumo, S. 2007. Dark matter and collider phenomenology of universal extra dimensions. *physical report*, **453**(Dec.), 29–115.

Horiuchi, S., Beacom, J. F., & Dwek, E. 2009. Diffuse supernova neutrino background is detectable in Super-Kamiokande. *Phys. Rev. D*, **79**(8), 083013.

Horns, D. 2005. Large zenith angle observations of Mkn 421 with H.E.S.S. *Page 319 of: International Cosmic Ray Conference*. International Cosmic Ray Conference, vol. 4.

Horns, D., & Meyer, M. 2012. Indications for a pair-production anomaly from the propagation of VHE gamma-rays. *JCAP*, **2**, 33.

Horns, D., Maccione, L., Meyer, M., *et al.* 2012. Hardening of TeV gamma spectrum of AGNs in galaxy clusters by conversions of photons into axion-like particles. *ArXiv e-prints*.

Huan, H., Weisgarber, T., Arlen, T., & Wakely, S. P. 2011. A New Model for Gamma-Ray Cascades in Extragalactic Magnetic Fields. *Astrophys. J., Lett.*, **735**, L28+.

Inoue, Y., Totani, T., & Mori, M. 2010. Prospects for a Very High-Energy Blazar Survey by the Next-Generation Cherenkov Telescopes. *Publ. Astron. Soc. Japan*, **62**(Aug.), 1005–.

Inoue, Y., Inoue, S., Kobayashi, M. A. R., *et al.* 2012. Extragalactic Background Light from Hierarchical Galaxy Formation: Gamma-ray Attenuation up to the Epoch of Cosmic Reionization and the First Stars. *ArXiv e-prints*, Dec.

Irastorza, I. G., Avignone, F. T., Caspi, S., *et al.* 2011. Towards a new generation axion helioscope. *JCAP*, **6**, 13.

Isern, J., García-Berro, E., Torres, S., & Catalán, S. 2008. Axions and the Cooling of White Dwarf Stars. *Astrophys. J., Lett.*, **682**, L109–L112.

Itzykson, C., Zuber, J.-B., & Higgs, P. 1984. Quantum Field Theory. *Physics Today*, **37**, 80.

Jacob, U., & Piran, T. 2008. Inspecting absorption in the spectra of extra-galactic gamma-ray sources for insight into Lorentz invariance violation. *Phys. Rev. D*, **78**(12), 124010–+.

Jaeckel, J., & Ringwald, A. 2010. The Low-Energy Frontier of Particle Physics. *Annual Review of Nuclear and Particle Science*, **60**, 405–437.

Jaeckel, J., Redondo, J., & Ringwald, A. 2008. Signatures of a Hidden Cosmic Microwave Background. *Physical Review Letters*, **101**(13), 131801.

James, F. 1998. *MINUIT Reference Manual (CERN Program Library Long Writeup D506)*.

Jansky, K. G. 1933. Radio Waves from Outside the Solar System. *Nature*, **132**(July), 66.

Jansson, R., & Farrar, G. R. 2012a. A New Model of the Galactic Magnetic Field. *Astrophys. J.*, **757**, 14.

Jansson, R., & Farrar, G. R. 2012b. The Galactic Magnetic Field. *Astrophys. J., Lett.*, **761**(Dec.), L11.

Jarosik, N., Bennett, C. L., Dunkley, J., *et al.* 2011. Seven-year Wilkinson Microwave Anisotropy Probe (WMAP) Observations: Sky Maps, Systematic Errors, and Basic Results. *Astrophys. J., Sup.*, **192**, 14.

Jelley, J. V. 1966. High-Energy $\gamma$-Ray Absorption in Space by a 3.5K Microwave Field. *Physical Review Letters*, **16**, 479–481.

Jungman, G., Kamionkowski, M., & Griest, K. 1996. Supersymmetric dark matter. *physical report*, **267**(Mar.), 195–373.

Kachelriess, M., Ostapchenko, S., & Tomàs, R. 2012. ELMAG: A Monte Carlo simulation of electromagnetic cascades on the extragalactic background light and in magnetic fields. *Computer Physics Communications*, **183**(Apr.), 1036–1043.

Kashlinsky, A. 2005. Cosmic infrared background and early galaxy evolution [review article]. *physical report*, **409**, 361–438.

Katarzyński, K., Sol, H., & Kus, A. 2001. The multifrequency emission of Mrk 501. From radio to TeV gamma-rays. *Astron. Astrophys.*, **367**(Mar.), 809–825.

Katarzyński, K., Ghisellini, G., Tavecchio, F., *et al.* 2006. Hard TeV spectra of blazars and the constraints to the infrared intergalactic background. *Mon. Not. R. Astron. Soc.*, **368**, L52–L56.

Kifune, T. 1999. Invariance Violation Extends the Cosmic-Ray Horizon? *Astrophys. J., Lett.*, **518**(June), L21–L24.

Kim, J. E. 1979. Weak-interaction singlet and strong CP invariance. *Physical Review Letters*, **43**(July), 103–107.

Kirk, J. G., & Duffy, P. 1999. TOPICAL REVIEW: Particle acceleration and relativistic shocks. *Journal of Physics G Nuclear Physics*, **25**(Aug.), 163.

Kneiske, T. M., & Dole, H. 2010. A lower-limit flux for the extragalactic background light. *Astron. Astrophys.*, **515**, A19+.

Kneiske, T. M., Mannheim, K., & Hartmann, D. H. 2002. Implications of cosmological gamma-ray absorption. I. Evolution of the metagalactic radiation field. *Astron. Astrophys.*, **386**, 1–11.

Kneiske, T. M., Bretz, T., Mannheim, K., & Hartmann, D. H. 2004. Implications of cosmological gamma-ray absorption. II. Modification of gamma-ray spectra. *Astron. Astrophys.*, **413**, 807–815.

Krawczynski, H., & Treister, E. 2013. Active galactic nuclei – the physics of individual sources and the cosmic history of formation and evolution. *Frontiers of Physics*, Apr.

Krawczynski, H., Coppi, P. S., & Aharonian, F. 2002. Time-dependent modelling of the Markarian 501 X-ray and TeV gamma-ray data taken during 1997 March and April. *Mon. Not. R. Astron. Soc.*, **336**, 721–735.

Krennrich, F., Bond, I. H., Bradbury, S. M., *et al.* 2002. Discovery of Spectral Variability of Markarian 421 at TeV Energies. *Astrophys. J., Lett.*, **575**(Aug.), L9–L13.

Kronberg, P. P. 1994. Extragalactic magnetic fields. *Reports on Progress in Physics*, **57**, 325–382.

Kronberg, P. P., & Simard-Normandin, M. 1976. New evidence on the origin of rotation measures in extragalactic radio sources. *Nature*, **263**, 653–656.

Kroupa, P., Weidner, C., Pflamm-Altenburg, J., *et al.* 2011. The stellar and sub-stellar IMF of simple and composite populations. *ArXiv e-prints*, Dec.

Kulsrud, R. M., & Anderson, S. W. 1992. The spectrum of random magnetic fields in the mean field dynamo theory of the Galactic magnetic field. *Astrophys. J.*, **396**(Sept.), 606–630.

Kulsrud, R. M., & Zweibel, E. G. 2008. On the origin of cosmic magnetic fields. *Reports on Progress in Physics*, **71**(4), 046901.

Kuo, T. K., & Pantaleone, J. 1989. Neutrino oscillations in matter. *Reviews of Modern Physics*, **61**(Oct.), 937–980.

Kutyrev, A. S., Arendt, R., Dwek, E., *et al.* 2008 (Aug.). High efficiency near infrared spectrometer for zodiacal light spectral study. *In: Society of Photo-Optical Instrumentation Engineers (SPIE) Conference Series*. Society of Photo-Optical Instrumentation Engineers (SPIE) Conference Series, vol. 7014.

Lee, S., Olinto, A. V., & Sigl, G. 1995. Extragalactic Magnetic Field and the Highest Energy Cosmic Rays. *Astrophys. J., Lett.*, **455**, L21.

Lefa, E., Rieger, F. M., & Aharonian, F. 2011a. Formation of Very Hard Gamma-Ray Spectra of Blazars in Leptonic Models. *Astrophys. J.*, **740**, 64.

Lefa, E., Aharonian, F. A., & Rieger, F. M. 2011b. "Leading Blob" Model in a Stochastic Acceleration Scenario: The Case of the 2009 Flare of Mkn 501. *Astrophys. J., Lett.*, **743**, L19.

Longair, M. S. 2011. *High Energy Astrophysics*.

Maccione, L., Liberati, S., & Sigl, G. 2010. Ultrahigh-Energy Photons as Probes of Lorentz Symmetry Violations in Stringy Space-Time Foam Models. *Physical Review Letters*, **105**(2), 021101.

Madau, P., & Pozzetti, L. 2000. Deep galaxy counts, extragalactic background light and the stellar baryon budget. *Mon. Not. R. Astron. Soc.*, **312**, L9–L15.

Maier, G., Acciari, V. A., Amini, R., & et al. 2008. VERITAS: Status and Latest Results. *Pages 1457–1460 of: International Cosmic Ray Conference*. International Cosmic Ray Conference, vol. 3.

Mankuzhiyil, N., Persic, M., & Tavecchio, F. 2010. High-frequency-peaked BL Lacertae Objects as Spectral Candles to Measure the Extragalactic Background Light in the Fermi and Air Cherenkov Telescopes Era. *Astrophys. J., Lett.*, **715**, L16–L20.

Mannheim, K. 1993. The proton blazar. *Astron. Astrophys.*, **269**(Mar.), 67–76.

Mannheim, K., & Biermann, P. L. 1992. Gamma-ray flaring of 3C 279 - A proton-initiated cascade in the jet? *Astron. Astrophys.*, **253**(Jan.), L21–L24.

Maraschi, L., Ghisellini, G., & Celotti, A. 1992. A jet model for the gamma-ray emitting blazar 3C 279. *Astrophys. J., Lett.*, **397**(Sept.), L5–L9.

Marscher, A. P., & Gear, W. K. 1985. Models for high-frequency radio outbursts in extragalactic sources, with application to the early 1983 millimeter-to-infrared flare of 3C 273. *Astrophys. J.*, **298**(Nov.), 114–127.

Martini, P., Mulchaey, J. S., & Kelson, D. D. 2007. The Distribution of Active Galactic Nuclei in Clusters of Galaxies. *Astrophys. J.*, **664**(Aug.), 761–776.

Massaro, E., Giommi, P., Leto, C., *et al.* 2009. Roma-BZCAT: a multifrequency catalogue of blazars. *Astron. Astrophys.*, **495**(Feb.), 691–696.

Matsumoto, T., Matsuura, S., Murakami, H., *et al.* 2005. Infrared Telescope in Space Observations of the Near-Infrared Extragalactic Background Light. *Astrophys. J.*, **626**, 31–43.

Mattingly, D. 2008. Have we tested Lorentz invariance enough? *ArXiv e-prints*, Feb.

Matute, I., La Franca, F., Pozzi, F., *et al.* 2006. Active galactic nuclei in the mid-IR. Evolution and contribution to the cosmic infrared background. *Astron. Astrophys.*, **451**, 443–456.

Maurer, A., Raue, M., Kneiske, T., *et al.* 2012. Dark Matter Powered Stars: Constraints from the Extragalactic Background Light. *Astrophys. J.*, **745**(Feb.), 166.

Mazin, D., & Raue, M. 2007. (MR07) New limits on the density of the extragalactic background light in the optical to the far infrared from the spectra of all known TeV blazars. *Astron. Astrophys.*, **471**, 439–452.

Mazin, D., Raue, M., Behera, B., *et al.* 2013. Potential of EBL and cosmology studies with the Cherenkov Telescope Array. *Astroparticle Physics*, **43**(Mar.), 241–251.

Melendez, B., Miller Bertolami, M., & Althaus, L. 2012. Revisiting the Impact of Axions in the Cooling of White Dwarfs. *ArXiv e-prints*, Sept.

Mészáros, P. 2013. Gamma ray bursts. *Astroparticle Physics*, **43**(Mar.), 134–141.

Meyer, M., Horns, D., & Zechlin, H.-S. 2010. The Crab Nebula as a standard candle in very high-energy astrophysics. *Astron. Astrophys.*, **523**(Nov.), A2.

Meyer, M., Horns, D., & Raue, M. 2012a (Dec.). Indications for a low opacity universe from Fermi-LAT data. *Pages 598–601 of:* Aharonian, F. A., Hofmann, W., & Rieger, F. M. (eds), *American Institute of Physics Conference Series*. American Institute of Physics Conference Series, vol. 1505.

Meyer, M., Raue, M., Mazin, D., & Horns, D. 2012b. Limits on the extragalactic background light in the Fermi era. *Astron. Astrophys.*, **542**, A59.

Meyer, M., Horns, D., & Raue, M. 2012c. Revisiting the Indication for a low opacity Universe for very high energy gamma-rays. *ArXiv e-prints*, Nov.

Meyer, M., Horns, D., & Raue, M. 2013. First lower limits on the photon-axion-like particle coupling from very high energy gamma-ray observations. *Phys. Rev. D*, **87**(3), 035027.

Miniati, F., & Elyiv, A. 2012. Relaxation of Blazar Induced Pair Beams in Cosmic Voids: Measurement of Magnetic Field in Voids and Thermal History of the IGM. *ArXiv e-prints*, Aug.

Minter, A. H., & Spangler, S. R. 1996. Observation of Turbulent Fluctuations in the Interstellar Plasma Density and Magnetic Field on Spatial Scales of 0.01 to 100 Parsecs. *Astrophys. J.*, **458**(Feb.), 194.

Mirizzi, A., & Montanino, D. 2009. Stochastic conversions of TeV photons into axion-like particles in extragalactic magnetic fields. *JCAP*, **12**, 4–+.

Mirizzi, A., Raffelt, G. G., & Serpico, P. D. 2007. Signatures of axionlike particles in the spectra of TeV gamma-ray sources. *Phys. Rev. D*, **76**(2), 023001.

Mirizzi, A., Redondo, J., & Sigl, G. 2009a. Constraining resonant photon-axion conversions in the early universe. *JCAP*, **8**(Aug.), 1.

Mirizzi, A., Redondo, J., & Sigl, G. 2009b. Microwave background constraints on mixing of photons with hidden photons. *JCAP*, **3**(Mar.), 26.

Mücke, A., & Protheroe, R. J. 2000 (June). Modeling the April 1997 flare of Mkn 501. *Pages 149–153 of:* Dingus, B. L., Salamon, M. H., & Kieda, D. B. (eds), *American Institute of Physics Conference Series*. American Institute of Physics Conference Series, vol. 515.

Mücke, A., & Protheroe, R. J. 2001. A proton synchrotron blazar model for flaring in Markarian 501. *Astroparticle Physics*, **15**, 121–136.

Mücke, A., Protheroe, R. J., Engel, R., Rachen, J. P., & Stanev, T. 2003. BL Lac objects in the synchrotron proton blazar model. *Astroparticle Physics*, **18**, 593–613.

Murase, K., Dermer, C. D., Takami, H., & Migliori, G. 2012. Blazars as Ultra-high-energy Cosmic-ray Sources: Implications for TeV Gamma-Ray Observations. *Astrophys. J.*, **749**(Apr.), 63.

Mushotzky, R. F., Cowie, L. L., Barger, A. J., & Arnaud, K. A. 2000. Resolving the extragalactic hard X-ray background. *Nature*, **404**(Mar.), 459–464.

Myers, R. C., & Pospelov, M. 2003. Ultraviolet Modifications of Dispersion Relations in Effective Field Theory. *Physical Review Letters*, **90**(21), 211601.

Neronov, A., & Semikoz, D. V. 2009. Sensitivity of $\gamma$-ray telescopes for detection of magnetic fields in the intergalactic medium. *Phys. Rev. D*, **80**(12), 123012–+.

Neronov, A., & Vovk, I. 2010. Evidence for Strong Extragalactic Magnetic Fields from Fermi Observations of TeV Blazars. *Science*, **328**, 73–.

Neronov, A., Semikoz, D., & Vovk, I. 2011. High Galactic latitude Fermi sources of $\gamma$-rays with energies above 100 GeV. *Astron. Astrophys.*, **529**(May), A59.

Neronov, A., Semikoz, D., & Taylor, A. M. 2012a. Very hard gamma-ray emission from a flare of Mrk 501. *Astron. Astrophys.*, **541**(May), A31.

Neronov, A., Semikoz, D. V., Taylor, A. M., & Vovk, I. 2012b. Very-high-energy gamma-ray emission from high-redshift blazars. *ArXiv e-prints*, July.

Netzer, H. 2008. Ionized gas in active galactic nuclei. *New Astronomy Reviews*, **52**(Aug.), 257–273.

Nikishov, A. I. 1962. Absorption of high-energy photons in the Universe. *Sov. Phys. JETP*, **14**, 393–394.

Nolan, P. L., Abdo, A. A., Ackermann, M., *et al.* 2012. (2FGL) Fermi Large Area Telescope Second Source Catalog. *Astrophys. J., Sup.*, **199**, 31.

Noutsos, A. 2012. The Magnetic Field of the Milky Way from Faraday Rotation of Pulsars and Extragalactic Sources. *Space Science Reviews*, **166**(May), 307–324.

Nussinov, S. 1976. Solar neutrinos and neutrino mixing. *Physics Letters B*, **63**(July), 201–203.

Okun, L. B. 1982. The limits of electrodynamics - Paraphotons. *Zhurnal Eksperimentalnoi i Teoreticheskoi Fiziki*, **83**(Sept.), 892–898.

Orr, M. R., Krennrich, F., & Dwek, E. 2011. Strong New Constraints on the Extragalactic Background Light in the Near- to Mid-infrared. *Astrophys. J.*, **733**, 77–+.

Parker, E. N. 1979. *Cosmical magnetic fields: Their origin and their activity*.

Peacock, J. A. 1999. *Cosmological Physics*.

Peccei, R. D. 2008. The Strong CP Problem and Axions. *Pages 3–540 of:* Kuster, M., Raffelt, G., & Beltrán, B. (eds), *Axions*. Lecture Notes in Physics, Berlin Springer Verlag, vol. 741.

Peccei, R. D., & Quinn, H. R. 1977. CP conservation in the presence of pseudoparticles. *Physical Review Letters*, **38**, 1440–1443.

Peebles, P. J. E. 1993. *Principles of Physical Cosmology*.

Pei, Y. C., Fall, S. M., & Hauser, M. G. 1999. Cosmic Histories of Stars, Gas, Heavy Elements, and Dust in Galaxies. *Astrophys. J.*, **522**(Sept.), 604–626.

Penzias, A. A., & Wilson, R. W. 1965. A Measurement of Excess Antenna Temperature at 4080 Mc/s. *Astrophys. J.*, **142**(July), 419–421.

Pimbblet, K. A., Shabala, S. S., Haines, C. P., *et al.* 2013. The drivers of AGN activity in galaxy clusters: AGN fraction as a function of mass and environment. *Mon. Not. R. Astron. Soc.*, **429**(Feb.), 1827–1839.

Plaga, R. 1995. Detecting intergalactic magnetic fields using time delays in pulses of $\gamma$-rays. *Nature*, **374**(Mar.), 430–432.

Planck Collaboration, Ade, P. A. R., Aghanim, N., Armitage-Caplan, C., *et al.* 2013. Planck 2013 results. XVI. Cosmological parameters. *ArXiv e-prints*, Mar.

Popov, V. 1999. On the experimental search for photon mixing. *Turkish Journal of Physics*, **23**(May), 943–950.

Preskill, J., Wise, M. B., & Wilczek, F. 1983. Cosmology of the invisible axion. *Physics Letters B*, **120**(Jan.), 127–132.

Press, W. H., Teukolsky, S. A., Vetterling, W. T., & Flannery, B. P. 2002. *Numerical recipes in C++ : the art of scientific computing*.

Prosekin, A., Essey, W., Kusenko, A., & Aharonian, F. 2012. Time Structure of Gamma-Ray Signals Generated in Line-of-sight Interactions of Cosmic Rays from Distant Blazars. *Astrophys. J.*, **757**(Oct.), 183.

Protheroe, R. J., & Stanev, T. 1993. Electron-Photon Cascading of Very High-Energy Gamma-Rays in the Infrared Background. *Mon. Not. R. Astron. Soc.*, **264**, 191–+.

Pshirkov, M. S., Tinyakov, P. G., Kronberg, P. P., & Newton-McGee, K. J. 2011. Deriving the Global Structure of the Galactic Magnetic Field from Faraday Rotation Measures of Extragalactic Sources. *Astrophys. J.*, **738**, 192.

Punch, M., Akerlof, C. W., Cawley, M. F., *et al.* 1992. Detection of TeV photons from the active galaxy Markarian 421. *Nature*, **358**(Aug.), 477.

Rachen, J. P., & Mészáros, P. 1998. Photohadronic neutrinos from transients in astrophysical sources. *Phys. Rev. D*, **58**(12), 123005.

Raffelt, G., & Stodolsky, L. 1988. Mixing of the photon with low-mass particles. *Phys. Rev. D*, **37**, 1237–1249.

Raffelt, G. G. 1996. *Stars as laboratories for fundamental physics : the astrophysics of neutrinos, axions, and other weakly interacting particles*.

Raffelt, G. G. 2008. Astrophysical Axion Bounds, e.g. Section 4.2. *Page 51 of:* Kuster, M., Raffelt, G., & Beltrán, B. (eds), *Axions*. Lecture Notes in Physics, Berlin Springer Verlag, vol. 741.

Rando, R. 2009. Post-launch performance of the Fermi Large Area Telescope. *ArXiv e-prints*, July.

Raue, M. 2007. *New constraints on the density of the extragalactic background light and the discovery of TeV gamma-rays from the BL Lac 1ES 0347-121 and the extended source HESS J1023-575*. Ph.D. thesis, University of Hamburg.

Raue, M. 2010. Searching for an extragalactic background light attenuation signature in the Fermi/LAT 1st year catalog data. *Astron. Astrophys.*, **520**, A34+.

Raue, M., & Mazin, D. 2008. Optical Depth for VHE $\gamma$-RAYS from Distant Sources from a Generic EBL Density. *International Journal of Modern Physics D*, **17**, 1515–1520.

Raue, M., & Mazin, D. 2011. EBL studies with ground-based VHE gamma-ray detectors: Current status and potential of next-generation instruments. *ArXiv e-prints*.

Raue, M., & Meyer, M. 2012. Probing the peak of the star formation rate density with the extragalactic background light. *ArXiv e-prints*.

Raue, M., Kneiske, T., & Mazin, D. 2009. First stars and the extragalactic background light: how recent $\gamma$-ray observations constrain the early universe. *Astron. Astrophys.*, **498**, 25–35.

Razzaque, S., Dermer, C. D., & Finke, J. D. 2009. The Stellar Contribution to the Extragalactic Background Light and Absorption of High-Energy Gamma Rays. *Astrophys. J.*, **697**(May), 483–492.

Razzaque, S., Dermer, C. D., & Finke, J. D. 2012. Lower Limits on Ultrahigh-energy Cosmic Ray and Jet powers of TeV Blazars. *Astrophys. J.*, **745**(Feb.), 196.

Redondo, J. 2008. Helioscope bounds on hidden sector photons. *JCAP*, **7**(July), 8.

Redondo, J. 2013. *private communication*.

Rees, M. J. 1998. Astrophysical Evidence for Black Holes. *Page 79 of:* Wald, R. M. (ed), *Black Holes and Relativistic Stars*.

Rieger, F. M., de Ona-Wilhelmi, E., & Aharonian, F. A. 2013. TeV Astronomy. *ArXiv e-prints*, Feb.

Riordan, E. M., Krasny, M. W., Lang, K., *et al.* 1987. Search for short-lived axions in an electron-beam-dump experiment. *Physical Review Letters*, **59**(Aug.), 755–758.

Rossi, B. 1952. *High Energy Particles*.

Sánchez-Conde, M. A., Paneque, D., Bloom, E., *et al.* 2009. Hints of the existence of axionlike particles from the gamma-ray spectra of cosmological sources. *Phys. Rev. D*, **79**(12), 123511.

Savolainen, T., Homan, D. C., Hovatta, T., Kadler, M., Kovalev, Y. Y., Lister, M. L., Ros, E., & Zensus, J. A. 2010. Relativistic beaming and gamma-ray brightness of blazars. *Astron. Astrophys.*, **512**(Mar.), A24.

Schlickeiser, R., Ibscher, D., & Supsar, M. 2012. Plasma Effects on Fast Pair Beams in Cosmic Voids. *Astrophys. J.*, **758**(Oct.), 102.

Schmidt, M. 1963. 3C 273 : A Star-Like Object with Large Red-Shift. *Nature*, **197**(Mar.), 1040.

Seyfert, C. K. 1943. Nuclear Emission in Spiral Nebulae. *Astrophys. J.*, **97**(Jan.), 28.

Shao, L., & Ma, B.-Q. 2010. Lorentz Violation Effects on Astrophysical Propagation of Very High Energy Photons. *Modern Physics Letters A*, **25**, 3251–3266.

Shaw, M. S., Romani, R. W., Cotter, G., *et al.* 2013. Spectroscopy of the Largest Ever $\gamma$-Ray-selected BL Lac Sample. *Astrophys. J.*, **764**(Feb.), 135.

Shifman, M. A., Vainshtein, A. I., & Zakharov, V. I. 1980. Can confinement ensure natural CP invariance of strong interactions? *Nuclear Physics B*, **166**(Apr.), 493–506.

Sigl, G., Miniati, F., & Ensslin, T. A. 2004. Cosmic Magnetic Fields and Their Influence on Ultra-High Energy Cosmic Ray Propagation. *Nuclear Physics B Proceedings Supplements*, **136**, 224–233.

Sikivie, P. 2008. Axion Cosmology. *Page 19 of:* Kuster, M., Raffelt, G., & Beltrán, B. (eds), *Axions*. Lecture Notes in Physics, Berlin Springer Verlag, vol. 741.

Sikora, M., Begelman, M. C., & Rees, M. J. 1994. Comptonization of diffuse ambient radiation by a relativistic jet: The source of gamma rays from blazars? *Astrophys. J.*, **421**(Jan.), 153–162.

Simet, M., Hooper, D., & Serpico, P. D. 2008. Milky Way as a kiloparsec-scale axionscope. *Phys. Rev. D*, **77**(6), 063001.

Simha, V., & Steigman, G. 2008. Constraining the early-Universe baryon density and expansion rate. *JCAP*, **6**(June), 16.

Sinnis, G., Smith, A., & McEnery, J. E. 2005. Hawc:. a Next Generation All-Sky VHE Gamma-Ray Telescope. *Page 1068 of:* Novello, M., Perez Bergliaffa, S., & Ruffini, R. (eds), *The Tenth Marcel Grossmann Meeting. On recent developments in theoretical and experimental general relativity, gravitation and relativistic field theories.*

Somerville, R. S., Gilmore, R. C., Primack, J. R., & Domínguez, A. 2012. Galaxy properties from the ultraviolet to the far-infrared: $\Lambda$ cold dark matter models confront observations. *Mon. Not. R. Astron. Soc.*, **423**(July), 1992–2015.

Stecker, F. W. 2003. Constraints on Lorentz invariance violating quantum gravity and large extra dimensions models using high energy $\gamma$-ray observations. *Astroparticle Physics*, **20**(Nov.), 85–90.

Stecker, F. W., & Glashow, S. L. 2001. New tests of Lorentz invariance following from observations of the highest energy cosmic /$\gamma$-rays. *Astroparticle Physics*, **16**(Oct.), 97–99.

Stecker, F. W., & Scully, S. T. 2009. Is the Universe More Transparent to Gamma Rays Than Previously Thought? *Astrophys. J., Lett.*, **691**, L91–L94.

Stecker, F. W., de Jager, O. C., & Salamon, M. H. 1992. TeV gamma rays from 3C 279 - A possible probe of origin and intergalactic infrared radiation fields. *Astrophys. J., Lett.*, **390**, L49–L52.

Stecker, F. W., Baring, M. G., & Summerlin, E. J. 2007. Blazar $\gamma$-Rays, Shock Acceleration, and the Extragalactic Background Light. *Astrophys. J., Lett.*, **667**(Sept.), L29–L32.

Strumia, A., & Vissani, F. 2006. Neutrino masses and mixings and... *ArXiv High Energy Physics - Phenomenology e-prints*, June.

Su, M., Slatyer, T. R., & Finkbeiner, D. P. 2010. Giant Gamma-ray Bubbles from Fermi-LAT: Active Galactic Nucleus Activity or Bipolar Galactic Wind? *Astrophys. J.*, **724**(Dec.), 1044–1082.

Sun, W.-H., & Malkan, M. A. 1989. Fitting improved accretion disk models to the multiwavelength continua of quasars and active galactic nuclei. *Astrophys. J.*, **346**(Nov.), 68–100.

Svensson, R. 1987. Non-thermal pair production in compact X-ray sources - First-order Compton cascades is soft radiation fields. *Mon. Not. R. Astron. Soc.*, **227**, 403–451.

Tadhunter, C. 2008. An introduction to active galactic nuclei: Classification and unification. *New Astronomy Reviews*, **52**(Aug.), 227–239.

Tagliaferri, G., Foschini, L., Ghisellini, G., *et al.* 2008. Simultaneous Multiwavelength Observations of the Blazar 1ES 1959+650 at a Low TeV Flux. *Astrophys. J.*, **679**(June), 1029–1039.

Tanaka, Y. T., Stawarz, Ł., Thompson, D. J., *et al.* 2011. Fermi Large Area Telescope Detection of Bright $\gamma$-Ray Outbursts from the Peculiar Quasar 4C +21.35. *Astrophys. J.*, **733**, 19.

Tavecchio, F., & Ghisellini, G. 2008. The spectrum of the broad-line region and the high-energy emission of powerful blazars. *Mon. Not. R. Astron. Soc.*, **386**(May), 945–952.

Tavecchio, F., Ghisellini, G., Ghirlanda, G., *et al.* 2009. The hard TeV spectrum of 1ES 0229+200: new clues from Swift. *Mon. Not. R. Astron. Soc.*, **399**, L59–L63.

Tavecchio, F., Ghisellini, G., Foschini, L., *et al.* 2010. The intergalactic magnetic field constrained by Fermi/Large Area Telescope observations of the TeV blazar 1ES0229+200. *Mon. Not. R. Astron. Soc.*, **406**, L70–L74.

Tavecchio, F., Ghisellini, G., Bonnoli, G., & Foschini, L. 2011a. Extreme TeV blazars and the intergalactic magnetic field. *Mon. Not. R. Astron. Soc.*, **414**, 3566–3576.

Tavecchio, F., Becerra-Gonzalez, J., Ghisellini, G., *et al.* 2011b. On the origin of the $\gamma$-ray emission from the flaring blazar PKS 1222+216. *Astron. Astrophys.*, **534**(Oct.), A86.

Tavecchio, F., Roncadelli, M., Galanti, G., & Bonnoli, G. 2012. Evidence for an axion-like particle from PKS 1222+216? *ArXiv e-prints*.

Taylor, A. M., Vovk, I., & Neronov, A. 2011. Extragalactic magnetic fields constraints from simultaneous GeV-TeV observations of blazars. *Astron. Astrophys.*, **529**(May), A144.

Thompson, D. J., Bertsch, D. L., Fichtel, C. E., *et al.* 1993. Calibration of the Energetic Gamma-Ray Experiment Telescope (EGRET) for the Compton Gamma-Ray Observatory. *Astrophys. J., Sup.*, **86**(June), 629–656.

Tluczykont, M. 2011. H.E.S.S. Observations of strong flaring activity of Mrk421 in February 2010. *ArXiv e-prints*, June.

Tluczykont, M., Hampf, D., Horns, D., *et al.* 2011. The ground-based large-area wide-angle $\gamma$-ray and cosmic-ray experiment HiSCORE. *Advances in Space Research*, **48**, 1935–1941.

Tridon, D. B., Schweizer, T., Goebel, F., *et al.* 2010. The MAGIC-II gamma-ray stereoscopic telescope system. *Nuclear Instruments and Methods in Physics Research A*, **623**(Nov.), 437–439.

Unsöld, A., & Baschek, B. 2002. *Der neue Kosmos. Einführung in die Astronomie und Astrophysik*.

Urry, C. M., & Padovani, P. 1995. Unified Schemes for Radio-Loud Active Galactic Nuclei. *Publ.. Astron. Soc. Pac.*, **107**, 803–+.

Urry, C. M., Scarpa, R., O'Dowd, M., *et al.* 2000. The Hubble Space Telescope Survey of BL Lacertae Objects. II. Host Galaxies. *Astrophys. J.*, **532**, 816–829.

VERITAS Collaboration, Acciari, V. A., Aliu, E., Arlen, T., *et al.* 2009. A connection between star formation activity and cosmic rays in the starburst galaxy M82. *Nature*, **462**(Dec.), 770–772.

Vincent, P. 2005. H.E.S.S. Phase II. *Page 163 of: International Cosmic Ray Conference*. International Cosmic Ray Conference, vol. 5.

Wagner, R. M. 2008. Synoptic studies of 17 blazars detected in very high-energy $\gamma$-rays. *Mon. Not. R. Astron. Soc.*, **385**, 119–135.

Wagner, S. J., & H.E.S.S. Collaboration. 2010 (Feb.). Detection of VHE Gamma-ray Emission from a Type 1 Quasar. *Page 27.06 of: AAS/High Energy Astrophysics Division 11*. AAS/High Energy Astrophysics Division, vol. 11.

Weekes, T. C., Cawley, M. F., Fegan, D. J., *et al.* 1989. Observation of TeV gamma rays from the Crab nebula using the atmospheric Cerenkov imaging technique. *Astrophys. J.*, **342**(July), 379–395.

Weinberg, S. 1978. A new light boson? *Physical Review Letters*, **40**, 223–226.

Weniger, C. 2012. A tentative gamma-ray line from Dark Matter annihilation at the Fermi Large Area Telescope. *JCAP*, **8**(Aug.), 7.

Widrow, L. M. 2002. Origin of galactic and extragalactic magnetic fields. *Reviews of Modern Physics*, **74**, 775–823.

Wilczek, F. 1978. Problem of strong P and T invariance in the presence of instantons. *Physical Review Letters*, **40**, 279–282.

Wilks, S. S. 1938. The large-sample distribution of the likelihood ratio for testing composite hypotheses. *Annals of Mathematical Statistics*, **9**, 60–62.

Williams, E. R., Faller, J. E., & Hill, H. A. 1971. New Experimental Test of Coulomb's Law: A Laboratory Upper Limit on the Photon Rest Mass. *Physical Review Letters*, **26**(Mar.), 721–724.

Woo, J.-H., Urry, C. M., van der Marel, R. P., *et al.* 2005. Black Hole Masses and Host Galaxy Evolution of Radio-Loud Active Galactic Nuclei. *Astrophys. J.*, **631**, 762–772.

Wouters, D., & Brun, P. 2012. Irregularity in gamma ray source spectra as a signature of axionlike particles. *Phys. Rev. D*, **86**(4), 043005.

Zacharopoulou, O., Khangulyan, D., Aharonian, F. A., & Costamante, L. 2011. Modeling the Hard TeV Spectra of Blazars 1ES 0229+200 and 3C 66A with an Internal Absorption Scenario. *Astrophys. J.*, **738**, 157–+.

Zatsepin, G. T., & Kuz'min, V. A. 1966. Upper Limit of the Spectrum of Cosmic Rays. *Soviet Journal of Experimental and Theoretical Physics Letters*, **4**(Aug.), 78.

Zavattini, E., Zavattini, G., Ruoso, G., *et al.* 2008. New PVLAS results and limits on magnetically induced optical rotation and ellipticity in vacuum. *Phys. Rev. D*, **77**(3), 032006.

Zechlin, H.-S. 2009. *New Constraints on Hidden Photons using Very High Energy Gamma-Rays from the Crab Nebula*. Ph.D. thesis, University of Hamburg. `http://www.iexp.uni-hamburg.de/groups/astroparticle/de/forschung/zechlin_diplom.pdf`.

Zechlin, H.-S., Horns, D., & Redondo, J. 2008 (Dec.). New Constraints on Hidden Photons using Very High Energy Gamma-Rays from the Crab Nebula. *Pages 727–730 of:* Aharonian, F. A., Hofmann, W., & Rieger, F. (eds), *American Institute of Physics Conference Series*. American Institute of Physics Conference Series, vol. 1085.